ugr | Universidad de Granada

SIGNAL PROCESSING-BASED IDENTIFICATION OF PATHOLOGY USING ULTRASONICS

BY:

Nicolas Bochud

A THESIS SUBMITTED TO:

University of Granada

ADVISORS:

Guillermo Rus Carlborg & Ángel M. Gómez García

Department of Structural Mechanics & Hydraulic Engineering ,
University of Granada
Granada (Spain)

January 2014

Signal processing-based identification of pathology using ultrasonics

Summary

Nondestructive evaluation is an emerging technology that enables to raise the safety and lifespan of nowadays structures, as well as to characterize advanced materials and biomaterials in medical science. Ultrasound is currently one of the most frequently used nondestructive inspection techniques, since it has been proven to provide effective and reliable results at relatively low cost for the estimation of the quality and structural functionality of a material, and for the characterization of its mechanical properties. Indeed, ultrasonic nondestructive evaluation is a well-established method to obtain physically relevant parameters to characterize pathologies in isotropic homogeneous materials. Pathologies are here understood as material's defects or consistency change, which altered the linear and/or nonlinear mechanical properties of materials. However, ultrasonic signals obtained from multilayered materials (composites, tissue-engineered products, biomaterials, etc.) require special care in signal interpretation (i.e. multiple and overlapping ultrasonic echoes) due to their structural complexity.

For competitive pathology assessment and quality control of stratified materials, quantitative non-destructive evaluation techniques based on the use of theoretical models of the ultrasonic wave propagation have been developed to extract additional information from experimental measurements. Despite the structural complexity of those materials, relative simple models are required for efficient and real-time monitoring of their structure health. Consequently, the complexity of the signals recorded by the transducers suggests to directly compare the experimental measurements with the theoretical results, with the purpose of extracting quantitative information from damage or consistency changes. A possible approach to solve this problem is provided by the model-based estimation procedure. However, conventional model-based estimation procedure developed in the mechanical engineering community are not attractive from a practical point of view (e.g. imperfections of the acquisition system, excessive computational resources, model uncertainties, etc.). In response to those problems, some procedures have been developed in the information technology community to enhance both the reliability and the quantitative pathology-informational content of ultrasonic signals obtained from conventional nondestructive evaluation systems. Therefore, in this thesis, we intent to unify the grounds implied in both areas by developing efficient and novel methods for practical applications on layered media, facing towards the optimization of the performance of such estimation procedure.

In particular, we present a general framework that relies on an advanced model-based estimation procedure to nondestructively evaluate pathologies using ultrasonics, which incorporates and adapts classical signal processing and modeling techniques to extract relevant features from the ultrasonic signals and enhance the signal interpretation. The main contributions of this dissertation concern the modeling approaches developed within this procedure to cope with the wave propagation in multilayered media. We first revisit a conventional approach known as the Transfer Matrix formalism to review the theoretical grounding for our dissertation and obtain a formulation that offers us the possibility of extending this method to more complex problems. Alternatively, signal modeling has also been proven to be an useful tool to characterize damaged materials under ultrasonic nondestructive evaluation. Consequently, we introduce a novel digital signal model for ultrasonic nondestructive evaluation of multilayered materials. This model borrows concepts from lattice filter theory, and bridges them to the physics involved in the wave-material interactions. In addition, we demonstrate that this digital model has several advantages with respect to purely physics-based models or classical spectral estimation approaches. Finally, we propose an extension of these two models to deal with the classical nonlinear constitutive behavior of such layered materials. Indeed, nonlinear mechanical properties may vary several orders of magnitude with damage, opposed to the marginal variation of linear properties. For this reason, it is proposed as an ultrasonic signature that may be more sensitive to early damage.

In a further part, the development of consistent optimization strategies and the obtaining of relevant experimental observations necessary to achieve a performant model-based estimation procedure are also contemplated. In particular, we introduce the context and motivation of the employed materials, describing their potential and the challenge that they offer from a structural viewpoint, and focusing on the requirement of efficient ultrasonic nondestructive evaluation techniques to identify their damage mechanisms. In addition, we present the specimens tested and the experimental configurations used to analyze them. Finally, we provide the theoretical background for the inverse problem and system identification approaches used for characterizing the pathologies of the introduced specimens.

The developed models are finally compared and validated with experimental measurements obtained from multilayered media that consist of traditional materials. Once validated, those models are tested using several applications of practical interest, including:

- ▷ The detection and identification of impact and fatigue damages in carbon fiber-reinforced polymers plates. In this case, both contact and immersion measurements are performed.
- ▷ The monitoring of tissue-engineered materials using a embedded ultrasonic system. This novel system is first validated on a gelation process, and then used to characterize a fibrin-agarose based construct for artificial tissue development.

From a theoretical point of view, the proposed digital signal model opens new perspectives in developing models for ultrasonic nondestructive evaluation, since it represents the material as a digital filter with sparse coefficients by merging concepts both from the mechanics and the signal theory. As a consequence, this model preserves both the strengths of purely physics-based models and (heuristic) parametric signals models. From a practical point of view, this model demonstrates its ability to simulate multilayered materials. In addition, it can be successfully inserted in a model-based estimation procedure to monitor the mechanical properties of relatively complex layered materials.

The presented monitoring technique achieves for the first time the reconstruction of multiple damages in carbon fiber-reinforced polymer plates from a single measurement. In contrast to other studies, the pathologies are not identified by considering the time-of-flight or the broadband ultrasound attenuation, but by reconstructing the complete waveform. Moreover, the damage multiplicity does not only appear at several locations but simultaneously in different forms. The other encouraging results on tissue-engineered materials suggest that this methodology previously developed for structural applications could be further applied in the field of biomedical engineering.

Resumen

LLa evaluación no destructiva es una tecnología emergente que permite aumentar la longevidad y fiabilidad de las estructuras de hoy en día, así como la caracterización de materiales avanzados y biomateriales en las ciencias médicas. Los ultrasonidos son en este momento una de las técnicas no destructivas de inspección más frecuentemente empleadas, ya que han demostrado que proporcionan resultados efectivos y fiables a un coste relativamente bajo, para estimar la calidad y el estado general de un material, así como para la caracterización de sus propiedades mecánicas. De hecho, la evaluación no destructiva ultrasónica es un método establecido para obtener parámetros físicos relevantes de cara a caracterizar patologías en medios isótropos y homogéneos. Por concepto de patología entendemos la presencia de defectos o cambios de consistencia en un material, que alteran las propiedades mecánicas lineales y no lineales del mismo. Sin embargo, las señales ultrasónicas obtenidas a partir de materiales estratificados (materiales compuestos, cultivos tisulares artificiales, materiales biológicos, etc.) requieren una atención particular a la hora de interpretar las señales (a saber múltiples ecos ultrasónicos solapados) debido a su complejidad estructural.

Para una evaluación competitiva de una patología y un control de calidad de los materiales estratificados, se han desarrollado técnicas de evaluación no destructiva ultrasónica cuantitativa, basándose en el uso de modelos teóricos de propagación de ondas ultrasónicas para extraer información adicional de las medidas experimentales. A pesar de la complejidad estructural de dichos materiales, se requieren modelos relativamente sencillos para una monitorización eficiente y en tiempo real de la salud estructural. Por consiguiente, la complejidad de las señales capturadas por los sensores nos ha llevado a comparar directamente las medidas experimentales con los resultados teóricos, con el propósito de extraer información cuantitativa de los defectos o de los cambios de consistencia. Un posible planteamiento para resolver este tipo de problema nos lo proporciona el *procedimiento de estimación basado en modelos*. Sin embargo, los *procedimientos de estimación basados en modelos* convencionales desarrollados en el ámbito de la ingeniería mecánica pueden carecer de atractivo desde una perspectiva práctica (por ejemplo debido a las imperfecciones del sistema de adquisición, el exceso de recursos computacionales, o las incertidumbres del modelo, etc.). En respuesta a esos problemas, se han desarrollado procedimientos alternativos en la comunidad de la tecnología de la información para realzar tanto la fiabilidad como el contenido cuantitativo acerca de las patologías de las señales ultrasónicas obtenidas a partir de

sistemas convencionales de evaluación no destructiva. Por lo tanto, en esta tesis, intentamos unificar los fundamentos de amabas áreas con el objeto de desarrollar métodos innovadores y eficientes para aplicaciones prácticas de evaluación no destructiva ultrasónica de medios estratificados, con el fin de enfrentarnos a la optimización del rendimiento de este tipo de procedimiento de estimación.

En particular, en esta investigación presentamos un procedimiento general que se fundamenta en un método avanzado de estimación basado en modelos para la evaluación no-destructiva ultrasónica de patologías, que incorpora y adapta técnicas clásicas de procesamiento y modelado de señales para extraer características relevantes de las señales ultrasónicas y realzar la interpretación de esas señales. Las principales contribuciones de este trabajo conciernen a los modelos desarrollados para dicho procedimiento de cara a resolver los problemas asociados con la propagación de ondas en materiales estratificados. En primer lugar, reconsideramos un planteamiento clásico conocido como el formalismo de la Matriz de Transferencia con la intención de revisar los fundamentos teóricos de nuestra investigación y obtener una formulación que nos permita extender ese método a problemas más complejos. Por otra parte, se ha demostrado que el *modelado de señal* es una herramienta útil para caracterizar materiales defectuosos bajo el concepto de evaluación no destructiva ultrasónica. Por lo tanto, introducimos un modelado de señal digital novedoso para la evolución no destructiva ultrasónica de materiales estratificados. Este modelo toma prestado conceptos de la teoría de filtros en celosía y los relaciona con la física involucrada en la interacción de las ondas con el material. Adicionalmente, demostramos que este modelo digital tiene numerosas ventajas frente a modelos puramente físicos o planteamientos de estimación espectral clásicos. Finalmente, proponemos una ampliación de esos dos modelos mencionados anteriormente, para introducir la no linealidad clásica en el comportamiento constitutivo de esos materiales.

En la siguiente parte del trabajo, se contempla el desarrollo de estrategias de optimización consistentes, así como la obtención de conjuntos de observaciones experimentales relevantes para lograr un método de estimación basado en un modelo de calidad. En particular, introducimos el contexto y la motivación de los materiales empleados, describimos su potencial y el reto que ofrecen desde una perspectiva estructural, y destacamos los requisitos de técnicas ultrasónicas eficientes para identificar los mecanismos de daño de dichos materiales. Adicionalmente, presentamos los especímenes testados y las configuraciones experimentales empleadas para analizarlos. Por último, proporcionamos la base teórica para definir los planteamientos sobre el problema inverso y la identificación de sistema empleados para caracterizar patologías de los especímenes.

Los métodos desarrollados han sido comparados y validados con medidas experimentales obtenidas a partir de medios estratificados formados por materiales tradicionales. Una vez validados, esos modelos han sido probados en aplicaciones de interés práctico, incluyendo:

- ▷ La detección e identificación de defectos generados por impacto y fatiga cíclica en placas de fibra de carbono. En ese caso, hemos llevado a cabo medidas en contacto y en inmersión.
- ▷ La monitorización de tejidos artificiales empleando un sistema ultrasónico embebido. Ese sistema innovador se valida en primer lugar con un proceso de solidificación de un gel y más adelante se usa para caracterizar el desarrollo de un tejido artificial basado en un constructo de fibrina agarosa.

Desde una perspectiva teórica, el modelado de señal digital propuesto abre nuevas perspectivas para el desarrollo de modelos para la evaluación no destructiva ultrasónica, ya que representa el material como un filtro digital con coeficientes sparse uniendo conceptos de la mecánica de sólidos y de la teoría de la señal. Por consiguiente, ese modelo preserva las ventajas tanto de modelos basados esencialmente en la física como de modelos paramétricos de señales (heurísticos). Desde una perspectiva práctica, ese modelo demuestra su habilidad para simular la propagación de ondas en medios estratificados. Adicionalmente, este modelo se puede insertar en un procedimiento de estimación basado en modelos de forma satisfactoria para monitorizar las propiedades mecánicas de materiales estratificados particularmente complejos.

La técnica de monitorización que presentamos ha permitido lograr por primera vez la reconstrucción de múltiples daños en placas de fibra de carbono a partir de una sola medida. A diferencia de otros estudios, las patologías no se identifican considerando el tiempo de vuelo o la atenuación ultrasónica de banda ancha, sino reconstruyendo la forma de onda completa. Además, los múltiples daños no solo aparecen a distintas posiciones del material, sino simultáneamente de forma distinta. Los otros resultados alentadores sobre cultivos tisulares artificiales sugieren que esa metodología previamente desarrollada para aplicaciones estructurales pueda aplicarse más a fondo en otros ámbitos de la ingeniería biomédica.

Acknowledgments

First of all, I would like to thank the two advisors responsible for the direction of my thesis, Dr. Guillermo Rus Carlborg, head of the Nondestructive Evaluation Laboratory of the Department of Structural Mechanics and Hydraulic Engineering, and Dr. Ángel M. Gómez, lecturer at the the Department of Signal Theory, Networking and Communications. They have played an imperative role in the success of this dissertation, joining and confronting their respective expertise in fields of apparently such distinct nature. In particular, I thank the first one for his permanent dedication to the investigation and for teaching and passing me down this vision, whereas I thank the second one for his patience, guidance, rigor and constructive suggestions over the course of these years. Also I thank Prof. Dr. Antonio M. Peinado Herreros, as the main investigator of the project that embraces this dissertation and as supervisor of my Master thesis, for his guidance and availability during those years. In addition, I also thank Dr. Quentin Grimal and Prof. Dr. Pascal Laugier for supervising my research stay at the *Laboratoire d'Imagerie Paramétrique*, for sharing their expertise on bone quantitative ultrasound, and for counting on me for future collaborations. Finally, I thank all my colleagues of the Nondestructive Evaluation Laboratory for making the everyday life at the lab enjoyable, and particularly for supporting me over the last few months.

I would like to thank the Consejería de Economía, Innovación y Ciencia de la Junta de Andalucia, Spain, for the FPI grant, being part of the project no. P08-TIC-03911, that allowed me to take part to the Master in Multimedia Systems, and particularly to investigate within this interdisciplinary research area during three years. In addition, I acknowledge the Spanish Ministerio de Economía y Competitividad for project DPI2010-17065, and Junta de Andalucía for projects P11CTS-8089 and GGI3000IDIB, whose funding enabled me to take part to numerous international congresses.

Abbreviations

AE	Acoustic emission
APM	Approximated Prony method
AR	Autoregressive
BEM	Boundary element method
BFGS	Broyden-Fletcher-Goldfarb-Shanno
BG	Bernoulli-Gaussian
BMD	Bone mineral density
BUA	Broadband ultrasonic attenuation
CAN	Contact acoustic nonlinearity
CFRP	Carbon fiber-reinforced polymers
DFT	Discrete Fourier transform
DFTF	Discrete-time Fourier transform
DMEM	Dulbecco's modified Eagle's medium
EM	Expectation maximization
EWVD	Enhanced Wigner-Ville distribution
FBG's	fiber Bragg gratings
FBS	Fetal bovine serum
FD	Finite-difference
FDTD	Finite-difference time-domain
FEM	Finite element method
FIR	Finite impulse response
FFT	Fast Fourier transform
FP	Forward problem
FRP	Fiber-reinforced polymers
FSFS	Forward sequential feature selection
FT	Fourier transform
GA	Genetic Algorithm
GFRP	Glass fiber-reinforced polymers
GM	Global matrix
HOS	Higher-order statistics
ICA	Independent component analysis
IDFT	Inverse discrete Fourier transform

IFFT	Inverse fast Fourier transform
IP	Inverse problem
IR	Impulsive response
LDA	Linear discriminant analysis
LPC	Linear predictive coding
LS	Least squares
LTI	Linear time-invariant
MLE	Maximum likelihood estimation
MP	Matching pursuit
MAP	Maximum a posteriori
NDE	Nondestructive evaluation
NLS	Nonlinear least squares
NTM	Nonlinear transfer matrix
NWLS	Nonlinear weighted least squares
NZ	Number of non-zero coefficients
PBS	Phosphate buffered saline
PCA	Principal component analysis
PDF	Probability density function
PIP	Probabilistic inverse problem
PM	Prony method
PMMA	Poly(methyl methacrylate)
QNDE	Quantitative nondestructive evaluation
RMS	Root mean square
SAGE	Space alternating generalized expectation
SAW	Surface acoustic waves
SD	Sparse deconvolution
SDM	Specimen's digital model
SHM	Structure health monitoring
SM	Stiffness matrix
SNR	Signal-to-noise ratio
SSP	Split-spectrum processing
STFT	Short-time Fourier transform
SVD	Single value decomposition
TDOA	Time-difference of arrival
TM	Transfer matrix
TOA	Time-of-arrival
TOF	Time-of-flight
WT	Wavelet transform
WVD	Wigner-Ville distribution

List of Symbols

Symbol	Description
n	Sample index
N	Number of samples
$x(n)$	Discrete-time input signal
$y(n)$	Discrete-time output signal
M	Decimation factor
$e(n)$	Discrete-time error
$w(n)$	Analysis window
L	Window length
$X(\omega)$	Spectrum of the input signal
$Y(\omega)$	Spectrum of the output signal
$H(\omega)$	Frequency response
$H(\omega_k)$	Sampled version of the frequency response
$H(z)$	Discrete-time transfer function
$A(z)$	Polynomial expression in z
p	Model order
G	Filter gain
a_k	All-pole filter coefficients
b_k	All-zero filter coefficients
E	Error energy
R	Autocorrelation function
$c(n)$	Real cepstrum
$\hat{c}(n)$	Complex cepstrum
$\hat{c}_a(n)$	Complex cepstrum of the sequence a_k
$\delta(n)$	Unitary impulse
$l(n)$	Liftering window
$\sigma_c(n)$	Standart deviation of the cepstral coefficients
$\mathfrak{F}$	Fourier transform
$\mathfrak{F}^{-1}$	Inverse Fourier transform

Symbol	Description
u_i	Cartesian components of the displacement vector
σ_{ij}	Cartesian components of the stress tensor
ε_{ij}	Cartesian components of the strain tensor
δ_{ij}	Kronecker symbol
M	Number of material layers
$u(x, \Omega)$	Displacement (expressed in the frequency-domain)
$u^f(x, \Omega)$	Forward-propagating displacement component
$u^b(x, \Omega)$	Backward-propagating displacement component
$\boldsymbol{\mathcal{U}}_i(x, \Omega)$	State vector of a layer i
$\boldsymbol{\mathcal{D}}_{i,i+1}$	Discontinuity matrix of a layer i
$\boldsymbol{\mathcal{P}}_i(\Omega)$	Propagation matrix of a layer i
$\boldsymbol{\mathcal{T}}_i(\Omega)$	Transfer matrix of a layer i
$\boldsymbol{\mathcal{T}}(\Omega)$	Complete transfer matrix
$\mathcal{T}_{ij}(\Omega)$	Elements of the complete transfer matrix
$\boldsymbol{T}^{(k)}$	Discrete version of the complete transfer matrix
$\mathcal{H}(\Omega)$	Frequency response at frequency Ω (complex scalar number)
$H(\omega)$	Complete frequency response
$H(\omega_k)$	Sampled version of the frequency response $\mathcal{H}(\omega)$
$\det(\ldots)$	Determinant
$X_i(\omega)$	Input of the two-port diagram for a layer i
$Y_i(\omega)$	Output of the two-port diagram for a layer i
$\boldsymbol{U}_i(\omega)$	Output vector of a layer i
$\boldsymbol{T}_i(\omega)$	Frequency response of a layer i
$\boldsymbol{T}(\omega)$	Total frequency response
$T_{ij}(\omega)$	Elements of the total frequency response
G_r	Gain (reflection)
G_t	Gain (transmission)
$\langle P \rangle$	Average power per unit area
$H_i(\omega)$	Intra-layer frequency response of a layer i
m_i	Delay of a layer i
G_{α_i}	Gain (attenuation)
$H_i^D(z)$	Discrete-time transfer function a layer i
$H^D(z)$	Complete discrete-time transfer function
m_i	Integer delay of a layer i
$P_M(G_\alpha, z)$, $Q_M(G_\alpha, z)$	Polynomial expressions in z
$N(z)$	Numerator of a transfer function
$D(z)$	Denominator of a transfer function
Λ	Thickness-equivalent sample delay
$\boldsymbol{\mathcal{U}}_i^{(1)}(x, \Omega)$	State vector of first-order of a layer i
$\boldsymbol{\mathcal{D}}_{i,i+1}^{(1)}(\Omega)$	First-order discontinuity matrix of a layer i
$\mathcal{D}_{i,jk}^{(1)}$	Linear elements of the first-order discontinuity matrix of a layer i
$\mathcal{D}_{i,jk}^{(1)}(\Omega)$	Nonlinear frequency-dependent elements of the first-order discontinuity matrix of a layer i

Symbol	Description
$\boldsymbol{\mathcal{P}}_i^{(1)}(\Omega)$	First-order discontinuity matrix of a layer i
$\eta_i(\Omega)$	Cumulative element of the first-order propagation matrix of a layer i
$\boldsymbol{\mathcal{T}}_i^{(1)}(\Omega)$	First-order transfer matrix of a layer i
$\boldsymbol{\mathcal{T}}^{(1)}(\Omega)$	Complete transfer matrix of first-order
$\mathcal{T}_{ij}^{(1)}(\Omega)$	Elements of the complete transfer matrix of first-order
$\mathcal{H}^{(1)}(\Omega)$	Frequency response of first-order at frequency Ω (complex scalar number)
$\boldsymbol{\mathcal{T}}_{\beta\to 0}^{(1)}(\Omega)$	Linearized complete transfer matrix of first-order
$\boldsymbol{T}^{(i)}(\omega_k)$	Discrete version of the first-order transfer matrix of a layer i
$H_i^{(0)}(\omega)$	Intra-layer frequency response of a layer i for the fundamental waves
$H_i^{(1)}(\omega)$	Intra-layer frequency response of a layer i for the second harmonics
$H_i^{NL}(\omega)$	Nonlinear intra-layer frequency response of a layer i
$\boldsymbol{T}_i^{(1)}(\omega)$	First-order frequency response of a layer i
$\boldsymbol{T}^{(1)}(\omega)$	Total frequency of first-order response
$T_{ij}^{(1)}(\omega)$	Elements of the total frequency response of first-order
$R_M(G_\alpha, z), S_M(G_\alpha, z), V_M(G_\alpha, z)$	Polynomial expressions in z
$H^{(1)}(z)$	Complete discrete-time transfer function of first-order
$\boldsymbol{\theta}$	Damage model parameters
$y(n)$	Observed output signal
$\tilde{y}(n)$, $y^{(\boldsymbol{\theta})}(n)$	Modeled output signal
$\boldsymbol{y}$	Feature vector of the observed output signal
$\boldsymbol{y}^{(\boldsymbol{\theta})}$	Feature vector of the modeled output signal
$\boldsymbol{r}^{(\boldsymbol{\theta})}$	Residual vector
$f^{(\boldsymbol{\theta})}$	Cost functional (for gradient-based algorithms)
$\hat{f}^{(\boldsymbol{\theta})}$	Cost functional (for global search algorithms)
$\hat{\boldsymbol{\theta}}$	Estimated damage model parameters
N_p	Number of individuals in a population
N_g	Number of generations
P_s	Fraction of surviving individuals
P_t	Probability of tournament
P_c	Probability of crossover
P_m	Probability of mutation
S_m	Scale of mutation
N_r	Number of measurement repetitions
N_d	Number of damage class
$R(i, j)$	Confusion table
$e_w(n)$	Whitening error
ρ	Model fitness measure

Symbol	Description
$\mathcal{M}$	Set of model parameters
$\mathfrak{M}$	Manifold of possible value
$\mathcal{C}$	Model class
$\mathcal{O}$	Observations
$p(\dots)$	Probability
$p^0(\dots)$	Probability to prior data
$p^m(\dots)$	Probability of the model
$\mathcal{N}$	Gaussian distribution
k_j	Normalization constants
$J(\mathcal{M})$	Misfit function
$\hat{\mathcal{M}}$	Estimated model parameters

Symbol	SI	Description
ρ	[kg/m^3]	Density
λ	[Pa]	Lamé's first constant
μ	[Pa]	Lamé's second constant
β	[-]	Nonlinear elastic coefficient of first-order
δ	[-]	Nonlinear elastic coefficient of second-order
E	[Pa]	Young modulus
E^*	[Pa]	Dynamic modulus
$\bar{E}$	[Pa]	Storage modulus
$\tilde{E}$	[Pa]	Loss modulus
$\tan(\delta)$	[-]	Loss tangent
ν	[-]	Poisson ratio
c, c_p	[m/s]	Longitudinal wave velocity
Z	[Ω]	Material impedance
A, B	[m]	Displacement's amplitude
γ	[1/m]	Wave number
t	[s]	Time variable
x	[m]	Space variable
a	[m]	Thickness
α	[Np/m]	Attenuation coefficient
d	[m]	Position
T	[s]	Period
Ω	[rd/s]	Continuous-time frequency
ω	[rd/sample]	Discrete-time frequency
ω_k	[rd/sample]	DFT frequency
F_s	[Hz]	Sampling frequency
F_c	[Hz]	Central frequency of a transducer
B	[Hz]	Bandwidth
err	[%]	Classification error
w_{err}	[%]	Weighted error rate

Man braucht wirklich nicht viel darüber zu reden, es ist den meisten Menschen heute ohnehin klar, dass die Mathematik wie ein Dämon in alle Anwendungen unseres Lebens gefahren ist. Vielleicht glauben nicht alle diese Menschen an die Geschichte vom Teufel, dem man eine Seele verkaufen kann; aber alle Leute die von der Seele etwas verstehen müssen, weil sie als Geistlichen, Historiker und Künstler gute Einkünfte daraus beziehen, bezeugen es, dass sie von der Mathematik ruiniert worden sei und dass die Mathematik die Quelle eines bösen Verstandes bilde, der den Menschen zwar zum Herrn der Erde, aber zum Sklaven der Maschine mache [...]. Damit war später für sie bewiesen, dass die Mathematik, Mutter der exakten Naturwissenschaft, Grossmutter der Technik, auch Erzmutter jenes Geistes ist, aus dem schliesslich Giftgase und Kampfflieger aufgestiegen sind.

In Unkenntnis dieser Gefahren lebten eigentlich nur die Mathematiker selbst un ihre Schüler, die Naturforscher, die von alledem so wenig in ihrer Seele verspürten wie Rennfahrer, die fleissig darauf los treten und nichts in der Welt bemerken wie das Hinterrad ihres Vordermanns. Von Ulrich dagegen konnte man mit Sicherheit das eine sagen, dass er die Mathematik liebte, wegen der Menschen, die sie nicht ausstehen mochten. Er war weniger wissenschaftlich als menschlich verliebt in die Wissenschaft. Er sah, dass sie in allen Fragen, wo sie sich für zuständig hält, anders denkt als gewöhnliche Menschen. Wenn man statt wissenschaftlicher Anschauungen Lebensanschauung setzen würde, satt Hypothese Versuch und statt Wahrheit Tat, so gäbe es kein Lebenswerk eines ansehnlichen Naturforschers oder Mathematikers, das an Mut und Umsturzkraft nicht die grössten Taten der Geschichte weit übertreffen würde.

Der Mann ohne Eigenschaften
Robert Musil, 1930

No es necesario dar muchas vueltas a esto; hoy día parece evidente a la mayor parte de los hombres que la matemática se ha mezclado como un demonio en todas las facetas de nuestra vida. No todas creen en la historia del diablo al que se puede vender el alma, pero al menos aquellos que entienden algo del asunto, por llevar el título de clérigos, historiadores o artistas y perciben, como tales, buenos beneficios, atestiguan que la matemática les ha arruinado y que ella ha sido el origen de una razón perniciosa que, a la vez que ha proclamado el hombre señor del mundo, lo ha hecho también esclavo de la máquina [...]. Para ellos ha quedado demostrado más tarde que la matemática, madre de las ciencias exactas, abuela de la técnica, fue también matriz de aquel espíritu que engendró los gases asfixiantes y los aviones de combate.

En desconocimiento de estos peligros vivían sólo los matemáticos y sus discípulos: los físicos, a quienes de tales cuestiones les llegaba al alma tan poco como a un ciclista chuparruedas, que aprieta a correr hacia la meta y no ve del mundo más que la circunferencia trasera del contrincante que le precede. De Ulrich, en cambio, se podía asegurar una cosa con certeza, que amaba la matemática en consideración a aquellos que no la podían ni ver. Estaba enamorado de la ciencia por motivos más humanos que científicos. Veía que ella, en todo cuanto creía de su competencia, discurría de distinto modo que los hombres vulgares. Si se pudiera reemplazar opinión científica por concepto de la vida, hipótesis por tentativa, y verdad por hecho, la obra de un buen físico o matemático superaría en intrepidez y fuerza revolucionaria a las mayores proezas de la historia.

El hombre sin atributos
Robert Musil, 1930

Contents

List of Figures

Part I

INTRODUCTION

1

Context and motivation

Nondestructive evaluation (NDE) is an emerging technology that enables to raise the remaining life and reliability of nowadays structures, as well as to characterize advanced materials and biomaterials in medical science. Typically, four levels of NDE are considered: (1) the detection of the presence of a pathology (*healthy/malignant?*), (2) the localization of that pathology (*where?*), (3) the identification and quantification of that pathology (*which kind of pathology?* and *how much does it alter the properties?*), and (4) the influence of such a pathology on the remaining life of the structure (*how long?*). The concept of pathology is here understood in a broad sense, that ranges from defects in a structural material to consistency changes in a biomaterial. Thus, a pathology can be defined as the deviation from the nominal behavior of a dynamical system, which is often associated with changes of its properties that may gradually evolve in time. The pathologies may be benign or malignant depending on their impact on the structural components reliability and operating conditions [1]. Consequently, failures in complex mechanical systems could be averted if the malignant pathologies are detected at an early stage. Ultrasound is currently one of the most frequently used NDE inspection techniques, since it has been proven to provide effective and reliable results at relatively low cost for the estimation of the quality and general condition of a material, and for the characterization of its mechanical properties. Ultrasound pulses are noninvasive and non-ionizing mechanical waves, whose propagation is governed by the theory of elasticity, and are therefore directly related to the mechanical properties, which are responsible for the final integrity and quality of the inspected material.

Important research areas related to ultrasonic NDE frequently involve the study of the wave interactions within multilayered structures. The interest of an accurate identification

of multilayered materials properties is constantly growing, since they are encountered in a wide range of applications. In engineering applications, this concerns for instance the detection of poor cohesion and adhesion in joints, the measurement of elastic properties and thickness of layered materials, and the detection of damage in composites [2]. In material science developments, some layered materials are the products of synthetic chemistry and consist of a large class of compounds formed by metals, ceramics, and polymers [3]. In biomedical research, layered tissue mimicking fluids are developed and must have properties similar to amniotic fluid and typical soft tissue [4]. It also has been shown that the complex architecture of trabecular bone can be modeled as a simplified stratified medium of alternating solid and liquid layers [5, 6]. In the semiconductor industry, a large number of objects/components have multilayered structures, such as modern microelectronic packages, semiconductors, and thin/thick films [7].

In ultrasound-based inspection techniques, the received ultrasonic signal responses are evaluated to retrieve information about the inspected media. Thus, for competitive damage assessment and quality control of stratified materials, quantitative non-destructive evaluation (QNDE) techniques based on the use of theoretical models of the ultrasonic wave propagation have been developed to extract additional information from experimental measurements [8]. Despite the structural complexity of those materials (spatial heterogeneity of the mechanical properties, multiple damage mechanisms, dispersion, etc.), relative simple models are required for efficient and real-time monitoring of the health of the structure in which those materials are located. Indeed, the complexity of the signals recorded by the transducers suggests to directly compare the experimental measurements with theoretical results, with the purpose of extracting quantitative information from damage or consistency changes. A possible approach to solve this problem is provided by the model-based inverse problem (IP) framework, whose general outline was given by Tarantola [9]. The solution of an IP identification approach is commonly defined in terms of the minimization of a cost functional consisting in the discrepancy between the experimental observations and the numerically predicted results [10]. Generally, the model parameters are found such that the l_2-norm of the residual (the difference between the observed signal and the predicted one) is minimized.

Generally, two key aspects of the model-based IP framework are fundamental: (1) An appropriate understanding and modeling of the interactions between ultrasonic waves and multilayered media are required; and (2) the model parameters extracted from the measurements should be sensitive enough to reveal the pathologies (that is, damage or consistency changes) that manifest in the specimen under inspection, and minimally sensitive to the measurements noise and model uncertainties. Despite the potential strength of the model-based IP framework for NDE of multilayered materials, parts of its structure could not be attractive from a practical point of view: For a fast convergence of the minimization algorithm, this method requires precise and reliable observations. However, due to their

structural complexity, multilayered materials require a special treatment in ultrasonic signal interpretation. The random nature of the signal generation, the imperfections of the acquisition system, as well as the difficulties in understanding and analyzing multiple and overlapping ultrasonic echoes may have a drastic influence on the performance of the inversion scheme. Additionally, an accurate characterization of pathologies usually require the determination of numerous model parameters, at the cost of excessive computational resources.

In response to those problems, tremendous emphasis has been directed towards identifying procedures that enhance both the reliability and the quantitative informational content of signals obtained from conventional NDE systems [11]. Part of this emphasis has focused on the adaptation of advanced signal processing concepts to NDE problems, which have already been successfully applied in other scientific fields such as electrical engineering, speech recognition or geophysics. Among others, those procedures have given raise to the development of heuristic inverse problems, based on empirical models (trained over empirical data, in contrast to phenomenological approaches relying on underlying physical processes). The absence of a direct link between the physical process and the empirical model allows one to investigate the feasibility of using blind signal models (e.g. the modeling of ultrasonic signals using an autoregressive model [12]). Most of the heuristic techniques devoted to material characterization aim at mapping the signal space (e.g. time-domain) into a smaller-dimensional feature space. Pattern recognition techniques can then be used for identifying or classifying the damage by examining this feature space. Nonetheless, this consumes a huge amount of experimental data and requires an expensive training process. Moreover, the mapping process does usually not provide a satisfying understanding of the relations between the extracted features and the underlying mechanical properties that characterize the damage.

In this thesis, we intend to give solutions to those problems by developing efficient and novel methods for practical ultrasonic NDE applications on layered media. Concretely, we propose to combine the strength of both the phenomenological and empirical approaches, by inserting signal processing and modeling strategies with physical sense into a model-based estimation procedure. Before proposing a concise literature review and introducing the theoretical basis of this dissertation, the following chapter exposes the objectives of the present thesis to provide an idea of the potential of its contributions.

In order to separate the theoretical background, contributions, methodology and the results, this thesis is divided into five parts:

Part I already introduced the context and motivation of this thesis in the present chapter. In **Chapter 2**, the objectives are carefully described in order to provide an idea of the potential of the proposed contributions. A concise literature review is provided in **Chapter**

3, whereas **Chapter 4** introduces the theoretical basis of this dissertation.

Part II describes the main contributions of this dissertation. **Chapter 5** presents the underlying concept of the model-based estimation procedure. In **Chapter 6**, we expose the theoretical development of the Transfer Matrix (TM) formalism for ultrasonic wave propagation in multilayered structures. Then, an alternative model for multilayered materials, which borrows concepts from lattice filter theory and bridge them with the physics involved in the wave-material interactions is presented in **Chapter 7**. Finally, in **Chapter 8**, we propose two models that extend the ones developed in Chapters 6 and 7, in order to cope with the nonlinear constitutive behavior of multilayered structures.

Part III describes the materials and methods used over the course of this thesis. **Chapter 9** includes the experimental configuration used to analyze the tested specimens. In addition, this chapter also provides the theoretical background for the inverse problem and system identification approaches used for characterizing the pathologies of the introduced specimens.

Part IV presents the results obtained with the proposed models, and discusses several applications related to the identification of pathology in multilayered specimens. Four different applications are developed: Firstly, **Chapter 10** evaluates our novel digital modeling of the specimen. In a first experiment, we propose a synthetic comparison with a standard approach based on the TM formalism. Then, an experimental validation with measurements obtained from multilayered specimens consisting of traditional materials is reported. Secondly, **Chapter 11** investigates different robust parametrization approaches for damage detection in carbon fiber-reinforced polymer (CFRP) plates. Those are a classical spectral estimation approach, and sparse and physics-based digital signal models. In addition, in **Chapter 12**, we study a model-based estimation procedure for damage identification in CFRP plates. Two kind of damage mechanisms and different experimental approaches are investigated. Finally, **Chapter 13** described a probabilistic inverse problem for ultrasonic monitoring of tissue-engineered materials. First, a proposed embedded ultrasonic system is validated on a gelation process, and then applied to show its potential for monitoring a fibrin-agarose based construct for artificial tissue development.

Finally, Part V presents a discussion of the strength and limitations of the proposed contributions, and comment some aspects of the ongoing works currently under development at our laboratory.

2 Objectives

Anticipating and characterizing pathologies in advanced materials and bio-materials is a challenging problem. Ultrasonic non-destructive evaluation is a well-established method to obtain physically relevant parameters to identify pathologies in isotropic homogeneous materials. However, due to their structural complexity, layered materials require special care in signal interpretation. Model-based estimation procedure and signal modeling strategies are thus proposed to improve the pathology identification. On this basis, the concrete objectives of the present thesis are:

- ◇ To formulate a model-based estimation procedure to improve the identification of pathologies in layered systems. Side-objectives are to obtain relevant experimental data by performing measurements using traditional and emerging ultrasonic techniques and to formulate the optimization problem in a convenient way.
- ◇ To develop a digital modeling of the specimen for ultrasonic waves which propagates normally through a stratified structure. A side objective is to review the formulation and implementation of the conventional Transfer Matrix method for that case, to provide a physics-based comparison.
- ◇ To extend those models for wave propagation through nonlinear layered media, by accounting for classical nonlinear constitutive behavior.

3

Literature review

The underlying methodology of a model-based inverse problem generally consists of three parts: An (1) experimental setup to monitor in real-time the interactions between the ultrasonic waves and the multilayered specimen under inspection, a (2) forward modeling that simulates the wave-material interactions, and finally an (3) inverse problem procedure based on optimization algorithms to reconstruct the structural variations due to pathologies which may occur during the monitored process. Since these three parts can benefit from advanced signal processing and modeling techniques, the emphasis throughout this review is on ultrasonic NDE-oriented signal processing theory and methods.

The literature review is organized as follows: Section 3.1 briefly describes two of the most widely used ultrasonic testing methods, and discusses their limitations for inspecting multilayered structures. In Section 3.2, we present an overview of ultrasonic NDE signal processing techniques, focusing on detection enhancement problems, and defect characterization and classification. Section 3.3 outlines the model-based estimation framework, describing a wide range of modeling approaches for ultrasonic wave propagation in layered media. In addition, some optimization algorithms for system identification are presented. Finally, some fundaments of emerging nonlinear ultrasound techniques are introduced in Section 3.4, since they may have merit for characterizing layered media. The focus all over this review is mainly on two kinds of promising multilayered materials, those are carbon-fiber reinforced polymers (CFRP) and biomaterials (e.g. tissue-equivalent media).

3.1 Experimental NDE

In modern ultrasonic NDE applications, a wide range of techniques has been developed for imaging defect location and sizing, including pulse-echo, through-transmission, guided waves, time-of-flight diffraction, scanning acoustic microscopy, laser ultrasonic imaging, or harmonic imaging. However, a review of the extensive literature on experimental ultrasound-based techniques is beyond the scope of this thesis. Here, we briefly comment on two of the most conventional ultrasonic testing modes that include pulse-echo and through-transmission techniques, and stress their pros and cons for evaluating multilayered materials.

For the pulse-echo mode, one transducer acts as transmitter-receiver, and this method thus requires that the waves travel twice through the sample thickness. When the ultrasonic waves encounter a damaged interface, the reflected energy in the form of pulse-echo amplitude is distinct from that in an undamaged situation. However, for multilayered materials, this method can hardly distinguish multiple damages. When the layer thickness is less than or comparable to the wavelength of the ultrasonic transducer, the reflected echoes from the front and back layer interfaces can overlap. Thus, confusion can be caused in case of either multiple defects or superimposed back-wall signals due to incompetent range resolution [13]. The usual approach to prevent overlaps is to increase the transducer frequency and/or decrease the pulse width. However, there are several situations where this approach is not an option, because high-frequency waves suffer from high attenuation during propagation, resulting in low penetration [14]. This method can also be combined with two-dimensional scanning, thus obtaining three-dimensional images of the specimen. In principle, this method should enable the determination of the depth of a defect, but due to the limited bandwidth of the instrumentation and the very strong echo from the front surface of the layered media, the signals reflected by intrinsic boundaries are masked by interferences. The information about the depth of the defect can then be extracted but only by using additional post-processing of the ultrasonic signals. As an alternative, through-transmission methods can be considered, since they usually only require one travel through the sample.

For the through-transmission mode, two transducers are used: The transmitter is placed on one side of the sample, whereas the receiver is placed on the reverse side of the sample. When the ultrasonic waves encounter defects on their path, the signal attenuates and thus reveals their presence. Typically, the ultrasound waves only travel once through the sample thickness, hence the wave attenuation is lower for the through-transmission mode than for the pulse-echo mode. Nonetheless, for through-transmission testing, the transducers installation (on the testing facility) undergoes several limitations. For instance, the need for accessing to both sides of the testing sample limits the application of through-transmission methods for on-site NDE inspections. Additionally, for local contact measurements, the variability of the transducers alignment with respect to the expected damage location can

alter the received signals, and thus their interpretation. On the other hand, immersion measurements requires two transducers to be mounted on the tank equipped with motion controller system for C-scans, but most available commercial C-scan immersion systems are designed to handle only one transducer [15]. One further disadvantage of this method is that it does not possess a resolution across the sample and it is impossible to determine between which layers the defects is located. As a consequence, important defect features can be missed or wrong located. In order to prevent those inconveniences, an alternative low-frequency through-transmission setup has been proposed (known as sub-wavelength technique), where a longitudinal waves are transmitted through layers, whose size is much smaller than the wavelength of the transmitter [16].

In principle, classical time-of-flight (TOF) methods could be adapted for ultrasonic NDE of layered media. However, for the purpose of identifying small thicknesses, the required frequency is very high, and the cost of these methods become prohibitive. For instance, in the case of composites, high-frequency waves begin to interact with micro-structural details (individual plies or fibers, resin-rich regions, etc.) which interfere with the damage characterization process. It is therefore essential to employ advanced signal enhancement techniques to extract useful diagnostic information from the measured ultrasonic NDE signals.

3.2 Overview of ultrasonic NDE-oriented signal processing

Ultrasonic NDE of multilayered structures undergoes some specific problems. A first problem is the high attenuation due to scattering of ultrasonic waves and multiple reflections inside the samples caused by the different acoustic impedances of the layers or the possible presence of defects. The scattering by microstructure components of a material causes serious difficulties in the detection of discontinuities, as it reduces the signal-to-noise ratio (SNR). A second problem is penetration through multiple interfaces with high acoustic impedance changes. A third challenge is the axial resolution for detecting delamination and cracks at closely spaced interfaces, whose size is small in comparison to the wavelength of the emitted wave (sub-wavelength resolution). Indeed, when the layer thickness is less than or comparable to the wavelength of the transmitted wave, the multiple echoes can overlap and make the ultrasonic signal interpretation difficult. The different propagation modes, diffraction and dispersive attenuation make the interpretation of ultrasonic signals even more complex. In addition, ultrasonic echoes are often contaminated by noise generated from both the imperfections of the acquisition system and the propagation path through the inspected materials, which can hide the echoes caused by a possible defect [7]. The last commonly occurring problem is associated with the amount of data generated by an ultrasonic inspection of a specimen [17]. When a scan is performed, a time-domain waveform must be acquired at each spatial point. For even moderately sized specimens, the amount of data acquired is large, and the complete waveform can hardly be retained and displayed for each

measured point on the specimen. One common approach to resolve this problem is to reduce the waveform to a simple root mean square (rms)-value, which is generally displayed as a gray level on a two-dimensional plot. However, one obvious drawback to this method is the lack of detailed information about the flaw, since the location of (multiple) defects in a stack-up of layers cannot be isolated from these data.

The need for overcoming the aforementioned problems, accurately interpreting large volumes of inspection data, and minimizing errors due to human factors motivated the use of signal processing and classification techniques. Typically, such a NDE system that incorporates signal processing and classification techniques is divided in three steps: (1) The extraction of parameters from the ultrasonic signals, which should be sensitive enough to reveal defects, and minimally sensitive to the noise of the measurement system, (2) an optimal representation of the features vector, by means of dimensionality reduction while retaining the discriminatory information, and (3) the definition of the algorithm of classification. The available bibliography is basically restricted to two topics, namely the enhancement of detection (noise reduction and echoes enhancement), and the defect characterization for signal classification. Since the eighties, those methods have been increasingly used to provide enhancement techniques for ultrasonic imaging, especially for elastography imaging (B-scans) or conventional C-scans. However, the processing of signals directly obtained from the ultrasonic transducers (A-scans) has been scarcely addressed. As the focus of this dissertation is on 1D ultrasonic signals, we make no attempt to review any of the 2D imaging techniques here. Concretely, we intent to give an overview on the signal processing methods that have been applied to ultrasonic signals, starting from relative simple time and frequency-domain approaches, while ending up with more complex approaches including redundant and sparse signal representations.

3.2.1 Enhancement of detection

Ultrasonic signals are often contaminated by noise and/or artifacts originated from both the measurement system (e.g. transducers and instrumentation) and the material under inspection. Consequently, noise places a fundamental limit on the detection of small defects and the measurement accuracy. To increase the probability of defect detection and to decrease the probability of false alarm, a number of signal processing techniques have been applied for noise reduction and enhancement of detected echoes.

In many applications, the noise is generally assumed to be an uncorrelated Gaussian random variable, with zero mean and a band-limited power spectral density function [18]. On the one hand, in areas where the measurements are repeatable, such as ultrasonic NDE, the SNR can be improved by signal averaging, since the specimen-dependent part of the signal remains the same for all measurements (and thus after averaging), whereas the disturbances can be reduced since they are randomly generated in each individual measurement.

Nevertheless, a small random time-shift may be present due to imperfections of the measurement system or unstable conditions in the propagation path, causing signal misalignment in the time-domain. Under these conditions, the process of signal averaging results in a signal shape distortion. Grennberg and Sandell [19] proposed a signal averaging method based on the Hilbert-transform correlation to obtain a higher SNR without signal distortion. Time delays of all the samples can also be estimated by the cross-correlation method, so that the signals can be aligned on the time axis for better averaging. On the other hand, one can design a filter in the frequency-domain, and by focusing on a frequency-band of interest, it is possible to suppress effects of the noise out this band over the time-domain signal.

However, for highly scattering materials, there is another type of noise called structural or grain noise, which is produced by the microstructures/grain boundaries of the inspected material. Each grain behaves like a scattering center, producing an echo that is isolated or superimposed with other echoes coming from other grains which can hide the echoes produced by a possible defect. Grain noise will exhibit a small-scale correlation and can be erroneously associated to defects. This noise is coherent with the emitted signal and cannot be eliminated by conventional techniques such as classical filtering (e.g. time-domain smoothing or frequency-domain filtering) or temporal averaging [20]. The major drawback of the time-domain processing is that it provides poor measurement accuracy, particularly when the echoes overlap. Therefore, it is often advantageous to process the signal in a transformed domain which allows highly flexible operations. In this case, a conventional approach for filtering out grain noise consists of observing the frequency spectrum of the ultrasonic signal, and particularly its power density spectrum. Indeed, one can assume that the echoes caused by the flaw differ in spectral content from those due to the background scattering noise. An optimal approach is to use a Wiener filter, which operates on the spectral differences between the two distinct signal contributions. Unfortunately, the Wiener filter requires a prior knowledge of the power spectral densities of both the noise and flaw echoes [21]. Autoregressive analysis has also been used as an alternative approximation to enhance ultrasonic signals. Wang *et al.* [12] used second and third-order autoregressive (AR) models to evaluate the spectral shift in grain signals by utilizing features such as resonating frequency, maximum energy frequency or AR-coefficients. On the other hand, Izquierdo *et al.* [20] presented a method that considers the time-varying spectral content of the received echoes, based on a time-varying autoregressive model of the structural noise.

Alternatively, deconvolution techniques may be useful to separate the signature of the material under investigation (i.e. the impulse response of the system) from the spurious response of the measurement system (i.e. electronic system, ultrasonic transducers, and additive noise). The first proposals to solve the deconvolution problem in ultrasonic NDE used classical techniques, such as the Wiener filter, spectral extrapolation, estimation of the least squares [22], or homomorphic deconvolution by computation of the cepstrum [23]. Nonetheless, those conventional deconvolution techniques are sensitive to the additive

Gaussian noise and yield a minimum phase defect signature which contradicts the non-minimum phase property of ultrasonic signals. Thus, higher-order statistics (HOS)-based deconvolution methods have been developed to provide blind deconvolution techniques, avoiding any prior information on the signal noise or defect [24, 25].

However, in all these techniques, the signals are analyzed either in the time-domain or in the frequency-domain. It is noteworthy that an ultrasonic signal is usually a broad-band pulse modulated at the center frequency of the transducer, and is therefore time and frequency-limited. For this reason, the utilization of a time-frequency analysis, where the signal is decomposed both in the time and frequency-domain by means of the short-time Fourier transform (STFT), could be more appropriate. The added complexity of describing the originally 1D time-domain signal as a 2D representation results in a redundant signal representation, which can be advantageously used to improve the interpretation of the experimental data [26]. Time-frequency representation of ultrasonic signals is thus a useful tool for simultaneous characterization in time and frequency, in particular for detecting and characterizing dispersive effects and flaw echoes in high scattering materials [27].

Among the time-frequency analysis techniques, the Wigner-Ville distribution (WVD) has been used for the characterization of materials and localization of flaws. In particular, it has been applied to distinguish echoes from a crack from the noisy echoes generated by the scattered ultrasonic waves through the material grains [28]. However, due to the inability of reducing the cross-terms, useful information is always hidden, and it is therefore necessary to preprocess the signals before applying WVD. To get around it, Wu *et al.* [29] recently proposed an enhanced Wigner-Ville distribution (EWVD) for ultrasonic NDE of thin composite plates, based on the chirplet decomposition and signal elimination. Hence, useless echoes that affect the representation of flaws are conveniently eliminated from the WVD. In order to enhance the flaw visibility, a frequency diverse statistical filtering technique known as split-spectrum processing (SSP) was developed [30]. In this technique, the received ultrasonic wide-band signal is divided into a set of narrow-band signals using a bank of bandpass filters, in which nonlinear post-processing is applied to obtain a reconstructed signal less affected by noise [31]. Recently, SSP has been proposed for its ability to resolve echoes associated with delaminations in CFRP detected by ultrasonic methods [32, 33]. However, this technique is sensitive to the parameters of the filter bank, such as the center frequencies and bandwidth, and is consequently very difficult to employ in practical applications [7].

As an alternative to SSP, the Wavelet Transform (WT) has also been utilized to improve ultrasonic flaw detection in noisy environment. In contrast to SSP, the WT uses a constant relative bandwidth, resulting in a filter bank with a self-adjusting window structure that can display the temporal variation of the signal's spectral components with varying resolutions [26]. This property of the WT is extremely useful for detecting flaw echoes embedded in background noise, and the WT has thus widely been used for ultrasonic NDE of materials for pulse detection and noise suppression, both in its continuous [34, 35] and discrete form [36, 37]. Although this procedure may seem similar to thresholding the signal in the time

or frequency-domain, WT thresholding results in minimal averaging or smoothing of the signal in the time or frequency-domain, because each time-frequency contribution of the original signal is considered locally in the time-frequency domain. However, the operation can fail if the noise is correlated. Some efforts have been made to palliate this limitation of the wavelet thresholding. One is to utilize a 'level-dependent' soft threshold for a signal with stationary correlated noise [38]. Another is to use overcomplete and sparse signal representation techniques to cope with the ultrasonic flaw detection and noise suppression problem [39].

Indeed, redundant and sparse signal representations have drawn a lot of research attention over the past decade. Ultrasonic signals acquired from a multilayered structure generally consists of a limited number of echoes, since the layered structure contains a limited number of abrupt impedance changes. Consequently, the ultrasonic signal can be assumed to have a sparse representation [40]. A common approach is to use a linear time-invariant (LTI) model to describe the propagation of the ultrasonic wave inside a layered material, assuming that the echoes of the received signal are delayed and attenuated replica of the transmitted pulse corrupted by noise [41]. A widespread application of sparse signal representation that offers great advantages is sparse deconvolution (SD) [42, 43], which benefits to ultrasonic echo detection, defect sizing and noise suppression [7]. This technique is nowadays recognized as the state-of-the-art denoising technique.

The aforementioned techniques are usually employed as preprocessing steps (i.e. noise suppression or echoes enhancement) for damage classification or system identification procedures. In addition, most of these studies are restricted to backscattering approaches. Generally, these techniques are based on the assumption that the ultrasonic output signal results from the convolution of the input signal with the impulsive response (IR) of the specimen, plus an additive noise. They are then applied in an heuristic way, without an explicit physics-based model which bridges the extracted signal features to the mechanical and geometrical properties of the material, and thus a precise physical interpretation remains often unavailable. Although the sparse representation considerably improves this approach, as most of the parameters are forced to be zero, the lack of a physical interpretation is still present, since prior knowledge on the number of non-zero parameters is generally unavailable.

3.2.2 Defect characterization and signal classification

A number of signal processing methods have been proposed to classify defects detected by ultrasonic signals, such as pattern recognition techniques. Other related proposals dealt with the feasibility of using physical features from time and frequency representations of signals for flaw characterization, including maximum amplitude of the signal, pulse duration, waveform kurtosis, and rise and fall times [44]. A comparison of feature-based classifiers for ultrasonic structural health monitoring has recently been performed by Michaels *et al.* [45].

An essential element in NDE systems is the analysis of the captured signal, by means of a robust parameter extraction, in order to obtain relevant information from the tested specimen [46]. In some cases, the extracted signal parameters can be processed again to reduce the dimensionality of the feature vectors, in order to achieve the pursued information about the specimen [47, 48]. For a real-time system, the number of features used in the classification process needs to be reduced, since the computational burden of classification increases with those. Consequently, the fewest number of features which yield the highest correct classification of the materials should be selected [49].

Principal component analysis (PCA) has been widely used for extracting features from the defects in ultrasonic classification systems, since PCA gives an optimal linear transform for reducing the dimension of a data set providing uncorrelated components. In addition, noise may be reduced, as the data not contained in the first principal components may be mostly due to noise. Khelil *et al.* [50] extracted wavelets parameters from ultrasonic signals, and then obtained an optimized attribute vector applying PCA, which enabled them to discriminate between planar and volumetric defects. In another related proposal, Ramuhalli *et al.* [51] extended the PCA method to analyze 2D data for generating a reduced dimensional feature vector for classification of B-scan images. Alternatively, the classical linear discriminant analysis (LDA) has also been applied. LDA attempts to express dependent variables as a linear combination of a small amount of features, in order to characterize or separate two or more classes of pathologies or defects. Signal parameters, such as wave velocity, dominant frequency, and signal attenuation were estimated, and then preprocessed by LDA obtaining a good fitting for archaeological period classification [52]. Another traditional approach is to take the wavelet transforms of the ultrasound signals, and then to use a subset of the coefficients as features for the classifier. To determine these optimal features, Meyer *et al.* [49] applied a forward sequential feature selection (FSFS) algorithm which retains the lowest number of features required to obtain the highest system performance. The single value decomposition (SVD) of the Hankel data matrix (obtained by assuming that the discrete output data from the system can be represented by a state space model) has also been employed to determine the position of defects in laminated materials [17].

Independent component analysis (ICA) is a relatively new method in which the goal is to find a linear representation of non-Gaussian data so that the components are statistically independent, or as independent as possible. Recently, ICA has been used for enhancement of ultrasonic flaw detection and noise suppression. For instance, ICA has been used for the diagnosis of the material consolidation status and for the determination of the thickness material profiles in restoration of historical buildings [53]. This recent contribution suggests that ICA may have a great potential to separate the multiple echoes in an ultrasonic signal obtained from a multilayered structure.

Once a set of optimum features has been selected, a suitable classifier is needed to classify the waveforms. A number of supervised and unsupervised classification algorithms such as K-means clustering algorithm, fuzzy C-means, distance-based recognition systems

[54], threshold-based decision [28, 55], Bayes' decision rule [49] and neural networks [56, 52] have been proposed for classifying signals. The success of all traditional classification algorithms depends heavily on the availability of an adequate and representative set of training examples, whose acquisition is often very expensive and time consuming. However, real defects in industry are very complicated, so that in practical ultrasonic NDE applications, accurately classifying defects remains a big challenge for current techniques. In addition, in those cases, the main objective is usually the minimization of type-I errors (that is, to avoid detecting damage that does not exist), and only a few proposals look for more specific information of the material [36, 31]. Finally, except the recent works by Hägglund *et al.* [57, 58] for classification of thin bonding layers within three-layered materials, proposals on the classification of complex damage mechanisms in multilayered specimens are inexistent.

3.3 Model-based estimation

Accurate estimation of the ultrasonic echo pattern is essential in determining the propagation path properties, i.e the layered structures that compose the specimen under inspection and the possible presence of defects (location, size, orientation, and microstructure). Many ultrasonic testing applications are based on the estimation of the time-of-arrival (TOA), time-of-flight (TOF), time-difference of arrival (TDOA), or the broadband ultrasonic attenuation (BUA) of ultrasonic echoes. However, the estimation of those characteristics undergoes severe limitations when dealing with complex media (e.g. layered material properties, frequency-dependent attenuation, dispersion effects, etc.). Thus, the extraction of this information requires models that explain the formation of echoes. This problem has been addressed in a number of ways, and gave raise to the so-called model-based estimation procedure which generally consists of two steps: (1) The formulation of a reliable model that idealizes the measurements of the ultrasonic wave-material interactions, and whose model parameters can be linked to the physical properties of the layers, and (2) the use of an optimization algorithm to estimate those model parameters. The model-based estimation procedure offers a convenient solution for (i) reconstructing unknown material properties, (ii) monitoring (i.e identify and quantify) a medium whose properties changes over time, (iii) restoration of the output signal in the presence of significant noise by deconvolution, and (iv) for resolving closely-spaced overlapping echoes providing valuable applications such as the thickness sizing of thin layers.

It is noteworthy that investigations on model-based estimation for ultrasonic NDE applications have given raise to slightly different designations and developments, in accordance with the scientific community of which the researchers stem. In the engineering community, wave propagation models are usually *physics-based models* that strongly rely on the rational principles of continuum mechanics. The optimization is then performed using an *inverse problem* procedure, and so the overall problem approach received the name of *model-based inverse problem*. In contrast, in the information technology community (e.g. signal theory, telecommunication, electrodynamics, etc.), those models are typically *signal-based parametric*

models inspired by concepts from lattice filter theory or circuit models. The *estimation of the model parameters* using optimization algorithms is ordinarily understood as solving a problem under a *system identification approach*. Both denominations will be employed over the course of this work, depending from which perspective the research is conducted.

3.3.1 Ultrasonic wave modeling

Over the last decades, considerable attention has been given to the modeling of wave interactions with multilayered materials, in a number of diverse disciplines such as geophysics, electromagnetics, optics, and acoustics. An exhaustive review of the literature on this subject is beyond the scope of this thesis, and the reader is referred to the classic monograph by Brekhovskikh [59] for a concise review of the mathematical framework and physical phenomena related to this topic. Typically, the resolution of a model-based estimation procedure requires numerous evaluation of the model (i.e. the forward problem) to update the material properties over the optimization process. This characteristic promotes the use of efficient and low complexity models (preferably semi-analytical), and as a matter of fact makes almost unviable numerical methods, such as finite-difference time-domain (FDTD), finite element (FEM) and boundary elements (BEM) methods, due to their prohibitive computational costs for accurate material characterization [60]. Here, for sake of simplicity, the review is restricted to the one-dimensional modeling of ultrasonic waves that propagate with normal incidence through layered media.

Physics-based models

A method that describes ultrasonic waves in multilayered media with an arbitrary number of layers is desirable. Thus, modeling tools have generally been developed from matrix formulations, which combine the principles of continuum mechanics within each layer with the transmission conditions at the layer interfaces, resulting in a matrix description of the system in terms of its external boundaries (incoming and outgoing wave displacements) [2]. In the latter half of last century, such matrix formulations have evolved and given raise to numerous works, based on two quite different approaches and many variants which are in accepted use (differing usually in their implemented form).

To solve the problem of wave propagation through planar multilayered structures, a very systematic Transfer Matrix (TM) method (i.e. also referred to as a *propagator matrix* method) has been developed and has received considerable attention for a wide range of applications from researchers involved in NDE (e.g. acoustics, optics and geophysics). The wave motion of a physical system is usually represented by a set of state equations describing the dynamic state of certain physical variables. In this method, the solution to these equations is a transfer matrix which maps the field variables from one layer to the next. The interface boundary conditions are automatically satisfied by multiplying the individual transfer matrices, and thus one just has to impose the appropriate boundary conditions to the remaining two surfaces [61]. The earliest development of the TM method for wave propagation in layered media was introduced by Thomson [62] , then extended by Haskell

[63] in the early fifties, and furthered afterwards by Gilbert and Backus [64]. During the following decades, this theoretical framework has given rise to numerous works almost entirely devoted to seismological applications. First attempts oriented to applications in the ultrasonic field arose in the late seventies [65, 66], and peaked in the early nineties, as indicates the meticulous review by Lowe [2]. Among others, these developments principally addressed the introduction of wave attenuation in the TM approach [67, 68], and its extension to anisotropic media [69, 70, 71], to cylindrically layered media [72, 73] and to multilayered anisotropic poro-elastic media [74]. Other related proposals adapted TM method to periodically stratified media composed of alternating elastic solid and ideal fluid layers [75] and to anisotropic periodically multilayered media [76]. Most of these works dedicated much effort to predict the transmitted waveforms, but it may also be useful to predict the transfer function of the material. This slightly different approach has lead to some alternative models for adhesively-bonded joints [77, 78] that are rather variants of the TM method than innovative approaches.

Although the TM approach is applicable in principle, its direct implementation has been found to suffer from numerical instabilities, particularly when considering layers of large thickness and high-frequency ultrasound. The cause of this problem is the poor conditioning of the transfer matrices when performing multiplications that combine both decaying and growing terms (i.e. small precision errors amplified by the exponential terms) [79]. Many modifications of the original transfer matrix have been proposed to palliate this precision problem. One common approach, known as the delta-operator technique, is to retain the concept of transfer matrices but to rearrange the equations to avoid that they become ill-conditioned [80, 68, 81, 82]. Such a technique preserves the advantage of a low complexity transfer matrix system but unfortunately fails to keep the conceptual simplicity of the Thomson-Haskell formulation. In addition, for propagation through anisotropic media, this technique requires the computation of large-order delta matrices and the derivation of many analytical expressions [83]. In an other related approach, Hosten [84] suggested to perform certain numerical test to limit those large *frequency-thickness* product values that ultimately cancel each other, in order to restore the stability of the system without loss of precision. More recently, Balasubramaniam [85] proposed an approximation algorithm that numerically truncates those higher values by imposing a maximum threshold for the exponential terms, thus limiting the error amplification and propagation. Although this approximation does not compromise the computational cost of the original TM approach, the truncation strongly depends upon the assigned threshold value, and is thus highly application-dependent.

As an alternative to the TM approach for a computationally stable solution, the Global Matrix (GM) method was introduced by Knopoff [86], and has been well documented [87, 88, 89]. In this method, a large single matrix represents the whole system, and is assembled by simultaneous matching of the boundary conditions at each layer interface. This technique is robust and can be implemented easily. However, this approach involves a

global banded matrix whose size increases with the number of layers, and thus unfortunately leads to considerable amount of memory storage and computation time when the system comprises many layers [2]. Among the recent contributions, it is worth to mention the stiffness matrix (SM) method which presents several advantages over the conventional TM method, and whose basis was already provided by Kausel and Roësset [90] in the early eighties. This method operates with total stresses and displacements via the stiffness matrix applied in a recursive algorithm, reduces the solution to a global banded linear system of equations, and is more convenient to incorporate imperfect interfaces. This approach has been successfully proven to resolve the numerical instability of the TM method [91, 92], and naturally provided the framework for developing recursive asymptotic method [93, 94]. A rigorous comparison of the numerical stability between the TM and the SM methods is given by Balasubramaniam *et al.* [95]. Although the SM method has been demonstrated to be computationally stable for large layer thickness, it becomes inaccurate and nearly singular when the layer thickness reduces toward zero. As a consequence, Tan [96] recently proposed an hybrid compliance-stiffness matrix method for stable analysis of elastic wave propagation in multilayered anisotropic media. As the SM method, this approach is able to eliminate the numerical instability of the TM method, and also preserves the convenience for incorporating imperfect interfaces. However, it has the advantage of remaining well-conditioned and accurate even for zero or small thicknesses.

Communication theory inspired models

Alternatively, wave propagation phenomena in layered systems have also been studied by considering only general principles about delay, continuity and energy conservation, and somehow leaving behind knowledge about physics and differential equations. This approach has given raise to a generic framework, that could be applicable to such diverse wave types as sound and water waves, light in thin films, normal incident elastic waves (both pressure and shear types), electromagnetic waves, transmission lines, and electrical ladder networks [97]. Within this framework, multilayered wave-interactions have been mostly described using concepts drawn from communication theory, since the resulting transmitted and reflected waves can be connected to equivalent circuit models and/or lattice filter theory. Here, we briefly review these two families of models.

Under certain assumptions, the characterization of layered materials can be well represented by means of equivalent models based on electric circuits [98]. An equivalent circuit may be understood as the modeling of a mechanical system based on the electric network theory, that is a one-dimensional model that describes the analogue electrical characteristics of an acoustic structure. The voltage and current in the equivalent system stand for stress and velocity of the material particles, respectively. The reason circuit analog models are good for wave propagation problems in stratified structures, is that they are exact for one-dimensional wave propagation (and thus serve as basis for validating numerical models) regardless of whether considering acoustic or electromagnetic waves, and provide a powerful means of computing the response of the system, such as reflection and transmission

coefficients [99, 100]. For instance, transmission lines have been used to represent the propagation of plane longitudinal waves in generally isotropic layered media [3]. In a similar proposal, Ghorayeb *et al.* [101] achieved a complete simulation of a dental ultrasound-system with its associated driver-receiver electronics, by incorporating the transducers, the focusing lens and the different tooth layers in a model based on transmission line theory. In the same vain, Challis *et al.* [102] proposed to simulate wave propagation in lossy materials with mechanical properties which vary gradually in the spatial dimension, by using electric circuit transmission line analogs to the viscoelastic mechanical system. Alternatively, Vogt and Ermert *et al.* [103] employed a linear ultrasonic two-port network model analog to conventional electrical networks to reconstruct layered media, which consist of discrete layers connected in series. The multiple reflections are considered by a stepwise estimation and secession of network elements. However, despite the conveniency of equivalent circuit models to reduce the computational cost for numerical evaluation, this approach becomes complicated under conditions less restrictive than those used here (e.g. attenuation, dispersion, nonlinearity) and requires a reasonable background in electronics.

The lattice filter theory has been routinely used in making acoustic tube models for the analysis and synthesis of speech, with the layer recursions being mathematically equivalent to the Levinson lattice recursions of linear prediction. It also found application in geophysical deconvolution, inverse scattering problems for oil exploration or the probing of tissue by ultrasound [104]. The Goupillaud specialization [105], i.e. elastic layers of equal-wave travel time, has been often used in geophysical applications to model wave propagation in inhomogeneous media. Despite the long history of mathematical developments for Goupillaud-type media, some recent proposals employed an innovative digital representation of the wave propagation in multilayered elastic media, by considering the bonded structure as an acoustic filter by means of the z-transform [106]. Among them, Velo *et al.* [107] developed a finite trigonometric series representation for the stress in a multilayered Goupillaud-type elastic strip, achieved by means of a z-transform method. As a result, they were able to identify optimal layered designs which provide the smallest stress amplitude. Gazonas *et al.* [108] derived the resonance frequency spectrum for an m-layered Goupillaud-type elastic medium, obtaining analytical stress solutions from a coupled first-order system of difference equations also using z-transform methods. Their results suggest that the natural frequency spectrum depends on the layer impedance ratios and is inversely proportional to the equal wave travel time for each layer. Nonetheless, the Goupillaud characteristics are unrealistic for many practical applications, since the layers of inhomogeneous materials does usually not have equal-wave travel time.

Signal-based parametric models

Over the past two decades, signal modeling and parameter estimation for detecting and estimating multiple interfering echoes has been a main subject of study in the field of ultrasonic imaging. To this end, parametric signal models have been developed, since they offer several advantages over heuristic approaches (see Section 3.2) directly applied over

experimental data: (1) High-resolution parameter estimates can be achieved, (2) the accuracy of the estimation can be evaluated, and (3) an analytical relationship between model parameters and physical parameters of the system can be established.

A common approach to address this problem is to approximate the output signal by a Bernoulli-Gaussian (BG) model [109, 110, 111], whose model parameters can be linked to the physical properties of reflectors and frequency characteristics of the propagation path, by assuming that the output signal is made of echoes that are time-shifted, amplitude-scaled, and noise-corrupted version of the input signal. Implicit to this method is the assumption that the desired system response is a spike train with unknown amplitudes and locations, where the number of spikes is considered to be unknown. In addition, there is no assumption or statistical knowledge imposed on the amplitude and locations of the spikes. Among the first proposed approaches, Demirli *et al.* [112] modeled ultrasonic backscattered echoes in terms of superimposed Gaussian echoes corrupted by noise. In this model, each Gaussian echo is a nonlinear function of a set of parameters that are sensitive to the echo shape, e.g. the echo bandwidth, time-of-arrival, center frequency, amplitude, and phase. These parameters have intuitive meanings for an ideal surface reflector in a homogeneous propagation path. The TOA is related to the location of the reflector, whereas the bandwidth factor determines the bandwidth of the echo or the time duration of the echo in the time-domain. On the other hand, the center frequency is governed by the transducer center frequency and the frequency characteristics of the propagation path. Finally, the specific amplitude and phase of the echo account for the impedance, size, and orientation of the reflector. Nonetheless, this model is not valid for any kind of signal waveform and one must have an accurate prior information of the input signal's appearance [113].

Dealing with thin layers or long input signal's time-support implies that the output signal consists of several reverberant and overlapping echoes. Hence, a parametrization of the layered structure instead of each echo is preferable, since the total number of parameters in the model can be kept small and is independent of the number of observable echoes. In that vein, Hägglund *et al.* [57] proposed a parametric modeling of the received ultrasound waveform, to be used for flaw detection in layered media. The model structure is chosen so that all dynamics of the waveform is captured by a small number of parameters. The material is modeled using a continuous AR-model with parameters connected to physical properties, related to the thicknesses of the material layers and the reflection coefficients given by the layer boundaries. The effects of dispersion and diffraction are assumed to be negligible and the different materials are considered to be lossless. In a later work, Hägglund *et al.* [114] improved their continuous AR-model with further parameters connected to physical properties, including the attenuation inside the layers. Alternatively, Hägglund *et al.* [115] used a physics-based parametric layer model to analyze the multilayered material, where the parameters of the model are associated with physical properties (e.g. the reflection coefficients, the time-of-flight, and the attenuation) of each layer within the structure. It is noteworthy that this model is a slight variant of those described in the *physics-based models* section. The

main advantage using this model is that its complexity is connected to the number of layers rather than the number of observable echoes in the received ultrasonic waveform.

Finally, there are a number of uncertainties which cannot easily be described by a complete physics-based model, including certain material properties (e.g. the attenuation and dispersion) or subtle experimental setup characteristics (e.g. diffraction and misalignment effects). To cope with dynamics that the physical model is unable to handle, Martinsson *et al.* [116] proposed to use a combination of *hard* and *soft* modeling. As in [115], the *hard* (physical) model is applied to describe the multiple reflections and overlaps related to the specific measurement setup, while *soft* (empirical) models, in the form of finite impulse response (FIR) filters, are used to capture the unknown dispersion and attenuation effects from the layers, and to deal with unwanted diffraction and misalignment effects from the measurement setup. The main benefit of including soft models is that a complete representation of the waveform is possible, and the residual (i.e. mismatch between the modeled and observed waveform) only consists of measurement noise. On the other hand, the main drawback is that the number of parameters to estimate increases and the model has a loss in simplicity, so that the estimation algorithm requires higher computational resources and may suffer from numerical instability.

3.3.2 Inverse problem and estimation of the model parameters

In NDE of materials, the idea is that the ultrasonic data are related to the material properties through a known mathematical model. Generally, the mathematical model defines the forward problem in that it relates known material properties to the ultrasonic data. Thus, if experimentally measured ultrasonic data are available, computing the required material properties is just a matter of solving the inverse problem (IP), i.e. relating the known ultrasonic data to material properties using the inverse of the same model. However, although the forward approach might be relatively easy, the inverse scheme is often cumbersome, since IP's are usually highly nonlinear and hence, analytically intractable. Furthermore, the constraint of limited experimental data sets also increase the effort involved in the reconstruction. Consequently, numerical rather than closed-form solutions appear to be the practical answer for solving such nonlinear IP's. Therefore, formulating the identification IP in an optimization form is one of the most popular approach.

The optimization has been addressed in multiple ways, and a common approach is to formulate it as a nonlinear least-square problem. Generally, an ideal algorithm should cover several scopes, that are to (1) end up with a reasonably good approximation ('accuracy'), (2) achieve this with an affordable computational cost ('efficiency'), and (3) ensure the attainment of a (local) optimum ('convergence'). To this end, a broad spectrum of optimization techniques have been developed, ranging from local to global methods. A partial classification of them is depicted in Figure 3.1. Here, we briefly review the advantages and inconvenients of those methods, and the reader is referred to the survey on the methods for local unconstrained optimization provided by Dennis and Schnabel [117] for completeness.

The basic of those methods relies on the Newton's method, which is an iterative procedure that requires the computation of the gradient and the Hessian that arise when expressing the nonlinear function to optimize as a Taylor series expansion up to the second-order term. In the case that the gradient and the Hessian are not available, they can be calculated with finite-difference (FD) approximations. However, applying the Newton's method with an initial guess far from the optimum can deliver a quadratic model that does not properly represent the non-linear function or even lead to a non-positive definite Hessian matrix, therefore invalidating the convex quadratic model. Hence, to ensure the convergence starting from almost any initial guess, two families of strategies, termed globally convergent modifications of the Newton's method (e.g. line search and model trust region), have been devised. In identification IP's, the Hessian is however not easily available and its computation by FD's is expensive. Alternatively, the secant method is a class of algorithms that use cheaper ways of approximating the Hessian, usually by updating the approximate Hessian in the previous estimate. The best Hessian update is provided by the positive definite secant update or the Broyden-Fletcher-Goldfarb-Shanno (BFGS) method. Except the calculation of the Hessian by updating, the rest of the minimization algorithm remains as in the Newton's method, and so the aforementioned globally convergent modifications are also applicable to the secant method.

Local		Global
Optimization algorithms (Gauss-Newton, Quasi-Newton Secant, Levenberg-Marquardt, BFGS)	Simulated Annealing	Genetic and evolutionary algorithms
Linear and quadratic programming		Neural networks, Fuzzy inference
Kalman filter, projection filter		Random search

Figure 3.1: *A classification of optimization methods used to minimize the cost functional in an inverse problem approach*[1].

Newton's methods and the secant updates can be extended to the non-linear least square problem, taking advantage of its special structure. In that case, the non-linear residual function is expressed in terms of the Jacobian matrix. For instance, the Gauss-Newton method is based on approximating the Hessian by making use of the Jacobian, and is then solved by applying the Newton's method. This approximation increases the algorithm convergence, but has the disadvantage that it is not necessarily globally convergent, and that it is not well defined if the Jacobian does not have full column rank. Nonetheless, it can be shown that in the case that the Gauss-Newton's step is a descent direction, then the aforementioned globally convergent modifications can be applied, leading to the damped Gauss-Newton and Levenberg-Marquardt methods. The former is globally convergent although it may be very slow. In addition, this method is not well defined for non-full column rank Jacobian matrices. The latter is equivalent to the Gauss-Newton method modified by the model

[1]Reproduced and adapted from Rus and Gallego [118].

trust region approach, and improves the behavior of the algorithm for not full column rank Jacobian matrices. Since optimizations algorithms such as Gauss-Newton [119], Levenberg-Marquardt [120] or BFGS [121] are among the most popular in the literature to solve IP's, a brief summary of their characteristics is provided in Figure 3.2. Nonetheless, this corpus of methods are gradient-based techniques, and consequently have a high probability of entrapment at a local minimum for initial guesses that are not close to the global minimum. As an alternative, genetic algorithms (GA's) have hold a lot of promise in dealing with complex problems while requiring significantly few data, for searching such complex multimodal spaces for unique global optima. GA's are not gradient-based search techniques and no initial guesses are required. A deeper insight on GA's is given in Section 9.3.1.

	Gauss-Newton	Levenberg-Marquardt	BFGS
Convergence rate vs. probability of convergence	High convergence rate	Reasonable trade-off	High probability of convergence
Particularities	Good for local scope (near the solution)	Good for global scope (far from the solution)	Does not take advantage of the structure of the cost functional

Figure 3.2: *Characteristics summary of the optimization algorithms*[2].

There are relatively few works reported in the literature that deal with the estimation of material properties through judicious use of the experimentally obtained structural response and the response of the mathematical model of the structure. This is mainly due to the fact that most researchers focus their effort either in the experimental fields or in the modeling ones. For ultrasonic applications, we come across the same *duality* as for the models, depending whether the reported works stem from the engineering or information theory communities. In the engineering community, the *model-based IP* is usually solved for reconstructing altered mechanical properties of materials due to damage. Generally, the optimization algorithms are applied in a rather straightforward way, while the focus is on the physical interpretation of the reconstructed model parameters. In contrast, for researchers involved in the information theory, a thorough effort is made on the model parameters estimation and optimization algorithms during the *system identification approach*, at the cost of analyzing rather simple materials.

Model-based IP's

Since the nineties, a number of studies have been carried out to solve the inverse problem for thickness sizing of thin coatings and reconstructing the mechanical properties of damaged composites. In that vein, Kinra and Zhu [16] described a technique for ultrasonic NDE of a thin coating on a thick substrate. They developed an inverse algorithm, which utilizes the well-known Newton-Raphson method, to reconstruct the thickness and the phase velocity through a comparison of the theoretical and the measured transfer functions. Using this

[2]Reproduced and adapted from Rus and Gallego [118].

technique both the thickness and the wave velocity of the coating could be extracted from the same measurement without knowing either. In a similar proposal, Kinra *et al.* [122] presented an inverse algorithm, which utilizes either the Newton-Raphson or the Simplex method in conjunction with the incremental search method, to reconstruct simultaneously the thickness and phase velocity of the individual layers comprising three-layer specimens. The optimization was achieved by minimizing the difference between the theoretical and the experimental results in the frequency-domain in a mean squared sense. The most important conclusion of that preliminary work was that in addition to the magnitude spectrum, phase spectrum must be considered in the inverse problem. In another related proposal, Kinra and Iyer [123] used an inverse algorithm, which utilizes the well-known secant method [124] in conjunction with the method of least squares, to deduce any one of the four acoustical properties (thickness, wave velocity, density or attenuation) of a thin linear-viscoelastic plate (given the remaining three) through a comparison of between the experimentally obtained and theoretically predicted transfer function.

Alternatively, Balasubramaniam and Whitney [125] described an inverse technique for computing the material elastic constants from data acquired using an immersion through-transmission method for characterizing thick glass-epoxy composites. The group velocity was experimentally measured as a function of the energy propagation angle (group angle), from which the phase velocity was numerically computed as a function of the phase angle [126]. Then, the material constants were determined from phase velocity profiles using commercially available parameter identification software (SCIENTIST, MicroMath Scientific Software). In a similar approach, Balasubramaniam and Rao [127] employed an inverse technique based on genetic algorithms to reconstruct the material stiffness properties of unidirectional fiber-reinforced composites from obliquely incident ultrasonic bulk wave data.

As a drawback, it is worth to note that most of these works propose the simultaneous reconstruction of relatively few model parameters. In addition, some of the works dedicated to the resolution of IP's are purely theoretical, whereas they investigate the stability to noise by adding different distributions and amounts of synthetic random noise to noise-free data simulated by making use of the forward model. In light of these considerations, most of the actual IP solutions remain somehow far from practical applications, since real defects of multilayered media in industry are very complicated, i.e. damage may appear at several locations and simultaneously in different forms.

System identification approach

Independently of the previous works, a number of authors started to explore the merit of model-based system identification approaches for ultrasonic applications, by adapting classical methods originally developed for the analysis of speech or images. Investigations were conducted in various applications such as transducer pulse-echo wavelet estimation, subsample time delay estimation, and thickness sizing of thin layers. From the information processing viewpoint, the system identification is especially challenging when dealing with overlapping echoes (i.e. the layer dimension is small in comparison with the wavelength of

the input signal). In such a case, the discrimination and precise localization of the echoes is far from obvious. Another issue occurs when the noise level is high since echoes may be partly or completely drowned in noise due to the material attenuation. As described in Section 3.3.1, numerous authors modeled ultrasonic signals as the superposition of many Gaussian echoes corrupted by noise. The first approaches [128, 129] tended to decompose the observed data into their individual echoes and then to estimate the model parameters of each individual echo separably using the Expectation Maximization (EM) algorithm or the Space Alternating Generalized Expectation Maximization (SAGE) algorithm [130]. The translation of the complicated superimposed echoes estimation into isolated echo estimations provides computational versatility. In a similar proposal, Demirli and Saniie [112] addressed the estimation of those model parameters using the maximum likelihood estimation (MLE) principle, assuming that all of the parameters describing the shape of the echo are unknown but deterministic. When noise is considered as white Gaussian, the MLE problem simplifies to a least squares (LS) estimation problem. Nonetheless, the iterative LS optimization algorithms suffer from convergence problems and exponential growth in computation when the number of superimposed echoes increases. To overcome this problem, they proposed to use the EM-based algorithm. In a companion paper, Demirli and Saniie [131] showed that their method was able to perform deconvolution in the presence of significant noise, and could restore closely-spaced overlapping echoes beyond the resolution of the measuring system. Unfortunately, there is no guaranty that these iterative algorithms converge to the wanted optimum [41]. Furthermore, the EM algorithm converges very slowly [132], whereas the SAGE algorithm converges faster under certain conditions but becomes unstable for low SNR's [133].

Alternatively, Hägglund *et al.* [114] derived a MLE for estimating the parameters of the developed continuous AR-model to identify the properties of a thin three-layered structure. The noise on both the input and output ultrasonic signals is assumed to be white and Gaussian, implying that the MLE ends up in a Nonlinear Least Squares (NLS) problem. In addition, to achieve a faster iteration in the optimization process, analytical expressions for the gradient and the Hessian are derived. The iterative update of the models parameters to find the optimum is performed by using the Gauss-Newton linearization method. In a related proposal, Hägglund *et al.* [115] improved the MLE for estimating the model parameters by using the noise on both the input signals and the output signals to weight the modeling error, implying that the MLE ends up in a Nonlinear Weighted Least Squares (NWLS) problem [134]. According to Pintelon and Schoukens [135], the unknown model parameters are estimated from discrete Fourier-transformed data. In that case, the objective of the model parameters estimation is to find those that minimize the square of the error, weighted by the covariance matrix. In a similar approach, Martinsson *et al.* [116] also estimated the unknown model parameters from discrete Fourier transformed data using a NWLS fit. In contrast to his colleague, he proposed to use the Levenberg-Marquardt optimization method [136] to

maximize the likelihood function, taking advantage of its ability to expand the search space and handle ill-conditioned Hessians.

Among the emerging studies on sparse representation for ultrasonic signals, a common approach is to model the sparse reflectivity sequence as a BG model and to use a maximum a posteriori (MAP) estimation for reconstruction [111]. The latter author proposed a genetic algorithm for optimizing that criterion, motivated by the fact that the latter is non-convex (i.e. has more than one local minimum). Unfortunately, this leads to nonlinear and computationally expensive solutions. As a consequence, truly optimal reconstructions are unfeasible, but many sub-optimal methods have been devised [137, 138]. A possible way for improving the optimization is to add a regularizing term to the usual squared error cost function that will penalize non-sparse solutions [139]. In this context, Soussen *et al.* [43] addressed the sparse deconvolution as an inverse problem where the detection and estimation of the spikes are performed jointly, by explicitly taking into account that the reflectivity sequence is sparse. This can be achieved using either l_1 or l_0-norm regularization [140, 141]. In both cases, the inversion problem results in a numerical optimization problem. For the l_1 case, the optimization is continuous and can be solved by recent efficient algorithms [142]. On the other hand, for the l_0 case, the optimization problem turns into a combinatorial problem whose goal is to find a sparse configuration with a limited number of spikes yielding the best fit to the data. The matching pursuit (MP) algorithm has been widely used in many signal processing areas, and offers a robust approach for solving the sparse deconvolution problem. MP is is a greedy algorithm for performing sparse decomposition of a signal by splitting the signal into a linear expansion of waveforms selected from an overcomplete dictionary [143]. Due to their simple implementation and numerical efficiency, modified MP methods have recently seen the light in the NDE community [144, 145, 146]. In that vein, Guo *et al.* [40] proposed a method based on a MP algorithm to decompose an ultrasonic signal into elements of the Gabor dictionary to suppress noise and enhance flaws by using the sparse information to estimate the crack location and size. In an other related approach, Bossmann *et al.* [41] presented two sparse deconvolution methods for nondestructive testing. The first method is based on a (modified) MP algorithm [147], whereas the second uses the approximated Prony method (APM) [148]. Although greedy algorithms are relatively fast and have, therefore, been used extensively in practical applications, their performance is guaranteed only under very strict conditions. The reader is referred to the excellent review by Zhang and Harvey [7] for a deeper insight into the optimization algorithms for performing identification of (sparse) systems.

As a drawback, it is worth to mention the algorithms described in most of these works require an accurate initial guess for providing a precise parameter estimation. Some authors proposed to find the initial guess on the parameters from prior knowledge on the theoretical values of the material, but this is often not possible in practical applications. In addition, most of those works deal with rather simple and conventional materials, which consist of a

single or few homogeneous isotropic layers in an undamaged state.

Despite of the satisfying properties of a model-based approach, several general issues which should be taken into account are summarized as follows: (1) if the observed data are nonlinear functions of parameters, the inverse problem (parameter estimation) is also nonlinear and does not have an explicit solution; (2) the noise embedded in the observed signals can difficult the estimation of the true parameters value. Hence, the degradation caused by noise needs to be eliminated or quantified as uncertainty bounds on the estimated parameters; and (3) the number of model parameters may a priori not be known, and therefore the model-order selection needs to be combined in the estimation problem [131].

This void in the mechanical characterization and interpretation of materials may be overcome by adopting a probabilistic model-based inverse problem strategy, coupled with a stochastic model-class selection formulation [149]. This approach allows one to obtain not only the optimal parameters in a model class, but also the uncertainty associated with the parameter estimates (due to measurements noise, heterogeneous material properties, approximated mathematical model, unknown number of model parameters, etc.).

3.4 Nonlinear acoustics

In linear acoustics, the presence of structural inhomogeneities lead to phase and/or amplitude variation of the received signal whereas its frequency remains the same than that of the emitted signal. The majority of well-known acoustic phenomena (i.e. TOF and BUA) are associated with linear elastic material properties, and are described by a linear stress-strain relation (Hooke's law). In contrast, in nonlinear acoustics, when a sinusoidal ultrasonic wave at a given frequency is transmitted into a nonlinear medium, the fundamental wave distorts as it propagates, and therefore second and higher harmonics of the fundamental frequency are generated [150]. Those well-known acoustical manifestations of nonlinear behavior can be explained as follows: Due to the amplitude-dependent wave propagation velocity, the compression phase of a sinusoidal wave travels faster than the rarefaction phase, and thus the wave distorts after it has propagated for some distance through a nonlinear material being transformed into a saw-tooth wave. This steepening of the waveform in the time-domain causes an energy transfer from the fundamental frequency to higher harmonics. As a consequence, several higher harmonics can be observed as local maxima in the frequency-domain [151, 152].

Measurements of the amplitude of these harmonics thus provide a mean for extracting the coefficient of second and higher order terms in the nonlinear stress-strain relation, and deliver valuable information on the material degradation that uses to be far more sensitive than the linear acoustic properties. Measuring these amplitudes is commonly referred to as the finite-amplitude method, initially developed by Breazeale and Thompson [153]. The nonlinear coefficients are usually determined by measuring the second-harmonic generation and sometimes higher harmonics for the longitudinal waves, and can be used to characterize

acoustic nonlinear properties of gases, liquids, and solids. For this technique, the through-transmission mode in immersion is usually preferred. Instead of using two transducers, it is opportune to replace the receiver by a needle hydrophone (with a nearly linear frequency response), in order to conveniently measure the second and higher-harmonics. A finite-duration burst of (nearly) pure tone - typically around 20 cycles long - is launched towards the specimen, and the progress of some stationary peaks near the end of the tone-burst is followed and selected to compute the Fast Fourier Transform (FFT), and thus allows to obtain the second and higher-order harmonics amplitude.

In this dissertation, our goal is not to survey all papers published in this broad and rapidly growing area, but only to review some experimental and theoretical results that might be exploited in the present thesis. To this end, we provide some basis on the very restricted topic of classical nonlinear acoustics using the finite-amplitude method. First, we expose the underlying mechanisms of the elastic nonlinearity of materials. Then, some works that explore to the intrinsic nonlinearity of materials (that is the determination of the nonlinear elastic parameters) are reviewed, whereas a final subsection is devoted to studies that investigate the nonlinearity changes due to to material degradation.

3.4.1 Elastic nonlinearity of materials

The nonlinear elastic behavior of materials is an emergent and extremely rich topic, that has broad implications in material sciences, including rock physics and nondestructive evaluation [154]. There are actually two classes of material nonlinearities, which differentiate themselves both in intensity and origin of their nonlinear response [155]. The first class, called atomic nonlinear elasticity (also classical or Landau nonlinearity [156]), comprises most fluids, tissues and monocrystalline solids. In that case, the nonlinearity arises from the lattice anharmonicity of the interatomic/molecular potential, and is relatively weak because the intermolecular forces are extremely strong. The second class, called structural nonlinear elasticity (also mesoscopic/nanoscale or hysteretic/nonclassical nonlinearity [157]), involves heterogeneous and a wide range of consolidated materials (i.e. soils, cement, rocks, fluid-filled porous materials, bone, etc.). Those materials contain soft inclusions (e.g. cracks, pores, grain contacts, dislocations) embedded in a hard matrix (e.g. grains, crystals), producing a large nonlinear response. Manifestations of nonclassical nonlinearity include stress-strain hysteresis and discrete memory in quasi-static experiments, and specific dependencies of the harmonic amplitudes with respect to the drive amplitude, frequency-shift of the resonance curve, frequency mixing for multiple input signals, nonlinear attenuation and slow dynamic effects in dynamic wave experiments, which are remarkably different from those predicted by the classical theory.

Differences between nonclassical and classical nonlinear dynamic behavior include: (1) A downshift of the resonance frequency, proportional to the resonance amplitude in the nonclassical case versus a quadratic amplitude dependence in the classical case, (2) nonlinear attenuation versus amplitude independent attenuation, and (3) a quadratic amplitude dependence of the third harmonic versus cubic in the classical case [158]. Another striking

feature observed in the nonclassical nonlinear dynamic response of nonclassical materials is slow dynamics, i.e., the slow recovery of the linear material properties (wavespeed and attenuation) after a sample has been subjected to a force [159]. From the above manifestations, one can calculate a set of fundamental nonlinear parameters of the material and attempt to use them in order to infer the nature of the nonlinear response.

Classical acoustic nonlinearity is a direct measure of the material anharmonicity and it delivers unique information about the nonlinear behavior of the intermolecular lattice forces [160]. The nonlinear elastic properties of solids containing micro- and macro-defects (scaled from dislocations to volume inclusions) or structural changes may be manifested in specific types of acoustic nonlinearity, which can be used as a measure of the defectiveness of a material or the integrity of a product structure. Despite those different nonlinear mechanisms, a quantitative evaluation of elastic nonlinearity of any scale and type can be achieved by measurements of the classical nonlinear coefficients or some other parameters similar to them that are always proportional to the amplitudes of the higher harmonics generated [161]. The most frequently used experimental method for this purpose is the the finite-amplitude method.

3.4.2 Intrinsic material nonlinearity

First applications of nonlinear ultrasound using the finite-amplitude method were devoted to the experimental determination of the intrinsic nonlinear elastic properties of various fluids [162, 163], various solids, to investigate lattice structure [164] and dislocations in crystals [165, 166, 167], as well as various biological media at both the tissue and molecular level [168, 169, 170]. In addition, considerable theoretical progress in understanding nonlinear acoustic phenomena was also accomplished during that period. Indeed, the amplitude-dependent nonlinear effects can be described by the equations of state and continuity of the medium, resulting in nonlinear equations of motion. The nonlinear wave equation is usually obtained by including a nonlinear version of the Hooke's law (i.e. as a Taylor series expansion up to second or higher-order terms of the stress as function of the strain) in the equation of motion [171]. The solution to the nonlinear equation is then recovered by applying the perturbation theory [172]. As a result, second and higher-order harmonics are formed at some distance from a monochromatic source propagating in a nondissipative nonlinear medium, and their amplitude grow with the propagation distance (linearly for the second-order harmonic, quadratically for the third-oder one, and so on). It has been demonstrated that the n^{th} harmonic amplitude is proportional to the normalized Bessel function, and is known as the Fubini-Ghiron solution [162]. Also of interest is that purely longitudinal waves in elastic solids and nondissipative fluids are governed by an equation of motion of precisely the same form [173]. Nonetheless, this rather simple methodology assumes a lossless plane-wave propagation, so that neither diffraction nor attenuation and dispersion are taken into account for the determination of the nonlinear coefficients. In addition, most of the studies are restricted to the determination of the second-order harmonics only. Nevertheless, some subsequent studies considered the influence of higher-order harmonics [174],

incorporated the effects of attenuation, diffraction and dispersion [175, 176], or took into consideration the reflection and transmission coefficients for the fluid-solid interfaces (that is, when the measurements are performed in immersion) [177, 178].

Later, nonlinear acoustics has been used to investigate the elastic nonlinear effects in grained materials and rocks [179, 180] concerning their prospective applications in geology and seismology. In this context, Van den Abeele [181] presented a model that describes the interaction of frequency components in arbitrary pulsed elastic waves during one-dimensional propagation in an infinite medium with extreme nonlinear response. This model is based on the one-dimensional Green's function theory in combination with a perturbation method, and was initially developed for a general source function by McCall [182]. The solution is implemented numerically in an iterative procedure up to fourth-order nonlinear terms and allows one to include an arbitrary attenuation function. In a companion paper, they applied this theoretical model to laboratory data from dynamic wave experiments on a cylindrical rod of Berea sandstone [183]. As a result, abnormally efficient third-harmonic generation with respect to the existing Landau-theory and non-monotonic spectral distribution of the higher harmonics were observed, suggesting the need of including a further term into the nonlinear wave equation (i.e. because the constitutive relation not only depends on powers of the strain but also on the second derivative of the strain). The new phenomenological approach to describe these nonclassical phenomena is known as the Preisach-Mayergoyz space, developed in analogy with the treatment of magnetic hysteresis, and the reader is referred to the pioneer work of McCall and Guyer [184] for a detailed explanation. From then on, numerous works were dedicated to this exciting topic (see for instance references [185, 186, 187, 188], to name a few), whose review unfortunately remains beyond the scope of this dissertation.

Besides the various applications described above, another promising application of nonlinear acoustics is believed to be oriented to NDE purposes. An important reason for this prospect is that increasing nonlinear properties are always closely related to the amount and specific nature of defects in materials [189].

3.4.3 Wave-damage interactions

Most of these conventional ultrasonic NDE methods are very sensitive to gross defects, but much less sensitive to distributed micro-cracks, diffuse damage or material degradation. Furthermore, general degradation of strength is often found in apparently flawless materials [190]. It is well known that material failure is usually preceded by some kind of nonlinear mechanical behavior before significant plastic deformation or material damage occurs [191]. Therefore, the degree of material degradation can be evaluated by measuring the nonlinearity of the ultrasonic wave that propagates through the target material. Thus, one can expect that the magnitude of the second and higher-order harmonics will appear differently in normal and degraded material, when the same amplitude of wave and the same propagation distance is used. For instance, the finite-amplitude technique has been proven to be useful for nondestructive detection of defects in ceramics [192], concrete structures [193, 194],

composites [150], as well as fatigue cracks in metals, such as steels, titanium, and aluminum alloys [195, 196]. Such defects are due to internal stresses, micro-cracks, zero-volume disbonds, and usually precede the main cracking mechanisms and the subsequent failure of the material. The characteristics between such defects and common material heterogeneities (i.e. pores, grains, etc.) is that an internal interface separates the intact material and the inclusion. This contact interface can be either free (large pores, opened cracks), partially clamped ("clapping" mechanism between the states opened/closed cracks), or ideally bonded, and is thought to be mostly responsible for the high nonlinear behavior of degraded materials [197]. Therefore, a considerable number of authors have been involved in laboratory experiments to show that cracks and imperfect interfaces can behave in a nonlinear fashion [198, 199], and have thus opened new opportunities to detect partially closed cracks that may not be identified by conventional linear methods.

As a consequence, numerous theoretical studies have been dedicated to the modeling of those contact interfaces (known as contact acoustic nonlinearity (CAN)). First proposals considered boundary conditions that allow an interface to be either completely open or completely closed [200], but such a model can not provide a convincing description of the wave damage interactions involving a partially closed interface. For ideally bonded interfaces, a general approach to the boundary acoustic nonlinearity was first developed by Zhou and Shui [201], which showed that a weak nonlinear incident acoustic wave that interacts with an interface can generate strong reflected and transmitted harmonics. The theory was later extended to include the analysis of reflected and transmitted second-harmonics for an anisotropic interface [202]. In an other related proposal, Pecorari [203] presented a new set of boundary conditions to be enforced on an elastodynamic wave interacting with a nonlinear interface, focusing on the modeling of the nonlinear interaction of a bulk plane wave with a nominally flat interface formed by two rough surfaces in contact. The potential relevance of his model for evaluating partially closed interfaces was examined in a subsequent paper [204].

Despite the potential of such models for describing interfaces, the nonlinear mechanical behavior of layered media has been investigated using almost only homogenization approaches [205]. Since this approach does not directly consider the layer interfaces, it is limited in examining the global behavior of the material, neglecting the wave interactions that could be very important when identifying structural changes. Among the few works that take into account the propagation through nonlinear multilayers, it is worth to mention some proposals that investigate the possibility of modeling damaged interfaces in solids [206], the bond quality of adhesive layers [207], or layered liquid and tissue-equivalent media [208]. To our knowledge, the only model that straightforwardly formulated the one-dimensional nonlinear ultrasonic wave propagation through layered media is the proposal by Yun *et al.* [209], which extends[3] the Transfer Matrix method described in Section 3.3.1.

[3]This framework will be take up again in this dissertation for two reasons: (1) The original development has not been developed for NDE purposes, and has in the proposed form, a lack of applicability; and (2) the authors discovered that the original development war erroneous at some point.

In addition, proposals on signal modeling for nonlinear ultrasonic systems or IP's dealing with the reconstruction of nonlinear coefficients are virtually nonexistent in the literature.

4

Theoretical background

The aim of this chapter is to supply the theoretical basis on wave propagation phenomena and signal parametrization, that will be extensively used over the course of this thesis. Section 4.1 exposes the fundamental principles that give raise to the one-dimensional linear-elastic wave equation, and also provides an extension to cope with the nonlinear constitutive behavior of materials. Section 4.2 reviews a number of signal parametrization techniques that will be used to improve the inverse problem strategy over the course of this dissertation.

4.1 Ultrasonic wave propagation

This section presents the basis to understand the wave propagation in solids. In first place, we briefly go over the equations that govern the three-dimensional linear wave propagation phenomena, to end up with the one-dimensional linear-elastic wave equation. Then, we extend this equation to solids with nonlinear constitutive behavior and thoroughly examine its solution.

4.1.1 Governing equations of the linear wave propagation

The formulation of the dynamic equilibrium equations is obtained by applying the linear momentum theorem for each direction of the three-dimensional orthonormal basis [210]. This formulation is given in index notation as,

$$\rho u_{i,tt} = \sigma_{ij,j} \tag{4.1}$$

where ρ denotes the density of the medium in which the waves are propagating. The components u_i and σ_{ij}, with $i, j = x, y, z$, are the cartesian components of the displacement vector, and those of the stress tensor, respectively. The relations between the stress and the strain tensor are established by the constitutive law as,

$$\sigma_{ij} = \lambda \varepsilon_{kk} \delta_{ij} + 2\mu \varepsilon_{ij} \tag{4.2}$$

where ε_{ij}, with $i, j = x, y, z$, are the cartesian components of the strain tensor, and $\varepsilon_{kk} = \varepsilon_{xx} + \varepsilon_{yy} + \varepsilon_{zz}$ is the dilatation (change in volume per unit volume). The Kronecker symbol δ_{ij} is defined as,

$$\delta_{ij} = \begin{cases} 1 & \text{for} \quad i = j \\ 0 & \text{for} \quad i \neq j \end{cases} \tag{4.3}$$

where λ and μ are the Lamé constants, which describe the behavior of linear-elastic, isotropic materials. The relations between the Lamé constants and the engineering moduli are derived as,

$$\lambda = \frac{E\nu}{(1+\nu)(1-2\nu)} \quad , \quad \mu = \frac{E}{2(1+\nu)} \tag{4.4}$$

where E and ν denote the Young modulus and the Poisson ratio, respectively. The kinematic relations establish a relation between the displacement field and the strain tensor as,

$$\varepsilon_{ij} = \frac{1}{2}(u_{i,j} + u_{j,i}) \tag{4.5}$$

It can be shown that substituting Equations (4.2) and (4.5) into Equation (4.1) leads to the generalized three-dimensional linear wave equation for the displacement $u(\boldsymbol{x}, t)$. Since the present work only deals with one-dimensional plane wave propagation in elastic media, those equations can be reduced to the one-dimensional case, yielding a generalized one-dimensional linear wave equation for the displacement $u(x, t)$ as,

$$\frac{\partial^2 u}{\partial t^2} = c_p^2 \frac{\partial^2 u}{\partial x^2} \tag{4.6}$$

where c_p denotes the longitudinal (P-wave) wave propagation velocity.

4.1.2 Foundations of the nonlinear wave propagation

To highlight the fundamental effects of nonlinear elastic materials, the classical approach of the nonlinear theory of elasticity is briefly presented here (details can be found in [156]). Assuming that the nonlinear contributions (e.g. geometric) of the wave propagation equation are negligible compared to constitutive nonlinearity, the only equation that differs from the linear theory is the constitutive law expressed in Equation 4.2. Thus, the one-dimensional relation between the stress and the strain is established with the nonlinear version of the Hooke's law as,

$$\sigma = E\varepsilon(1 + \beta\varepsilon + \delta\varepsilon^2 + \ldots) \tag{4.7}$$

where β and δ denote the nonlinear elastic coefficients of first- and second-order, respectively. The generalized one-dimensional nonlinear wave equation for the displacement $u(x,t)$ can thus be written as,

$$\frac{\partial^2 u}{\partial t^2} = c_p^2 \frac{\partial^2 u}{\partial x^2}\left(1 + 2\beta\frac{\partial u}{\partial x} + 3\delta\left(\frac{\partial u}{\partial x}\right)^2 + \ldots\right) \tag{4.8}$$

This expression means that the displacement depends on linear and nonlinear potencies of the linear deformation $\frac{\partial u}{\partial x}$. This deformation can be generated from the wave itself (wave of finite amplitude), as well as from an extern load applied to the concern solid. Alternatively, Equation (4.8) can be written as,

$$\frac{\partial^2 u}{\partial t^2} = \left(c_L^2 + c_{NL}^2\right)\frac{\partial^2 u}{\partial x^2} \tag{4.9}$$

where c_L and c_{NL} denote the longitudinal linear and nonlinear wave propagation velocity, respectively. They are defined as,

$$c_L = c_p = \sqrt{\frac{\lambda + 2\mu}{\rho}} \quad , \quad c_{NL} = c_p\sqrt{2\beta\frac{\partial u}{\partial x} + 3\delta\left(\frac{\partial u}{\partial x}\right)^2 + \ldots} \tag{4.10}$$

Note that by setting $\beta = \delta = 0$, we recover the linear wave equation.

Analytically calculated perturbation solutions

Let us now solve the nonlinear wave equation up to the second-order nonlinearity. Applying the *perturbation method* [172] enables us to write the wave displacement as,

$$u = u_0 + u_1 + u_2 + \ldots \tag{4.11}$$

where u_0 denotes the zero-order perturbation solution which corresponds to the fundamental solution of the linear wave equation. The first-and second-order perturbation solutions are denoted by u_1 and u_2, respectively. For convenience of the mathematical formulation, let us define the displacements' first- and second-derivatives with respect to the x coordinate as $u' = \frac{\partial u}{\partial x}$ and $u'' = \frac{\partial^2 u}{\partial x^2}$, respectively, and the second time-derivative as $\ddot{u} = \frac{\partial^2 u}{\partial t^2}$. Since the effect of the nonlinear terms β and δ is small, an approximate solution can be obtained by iteration. For this purpose, let us insert Equation (4.11) into Equation (4.8),

$$\begin{aligned}
\ddot{u}_0 + \ddot{u}_1 + \ddot{u}_2 + \ldots &= c_p^2\left(u_0'' + u_1'' + u_2'' + \ldots\right) \\
&+ 2c_p^2\beta\left(u_0'' + u_1'' + u_2'' + \ldots\right)\left(u_0' + u_1' + u_2' + \ldots\right) \\
&+ 3c_p^2\delta\left(u_0'' + u_1'' + u_2'' + \ldots\right)\left(u_0' + u_1' + u_2' + \ldots\right)^2
\end{aligned} \tag{4.12}$$

This equation delivers various sub-equations, obtained by rearranging the terms according to the perturbation order. Hence,

$$\begin{aligned}
&\text{Zero-order:} && \ddot{u}_0 - c_p^2 u_0'' &&= 0 \\
&\text{First-order:} && \ddot{u}_1 - c_p^2 u_1'' &&= 2c_p^2 \beta u_0'' u_0' \\
&\text{Second-order:} && \ddot{u}_2 - c_p^2 u_2'' &&= 2c_p^2 \beta \left(u_1'' u_0' + u_0'' u_1'\right) + 3c_p^2 \delta u_0'' \left(u_0'\right)^2 \\
&\ldots
\end{aligned} \tag{4.13}$$

Consequently, u_0 is the solution to the linear wave equation, that is Equation (4.8) for $\beta = \delta = 0$, whose general solution can be stated as,

$$u_0 = \sum_{n=1}^{\infty} \left(A_0^{(n)} \sin\left(n\left(\gamma x - \Omega t\right)\right) + B_0^{(n)} \cos\left(n\left(\gamma x - \Omega t\right)\right) \right) \qquad (n \in \mathbb{R}) \tag{4.14}$$

where $\gamma = \Omega / c_p$ and Ω are the wave number and continuous-time frequency, respectively. By considering a monochromatic wave that propagates in a semi-infinite nonlinear elastic medium, the zero-order perturbation solution (4.14) can be simplified as,

$$u_0 = A_0 \sin\left(\gamma x - \Omega t\right) \tag{4.15}$$

Let then u_1 be the first-order perturbation solution to Equation (4.8). Inserting the zero-order perturbation solution (4.15) within the first-order perturbation Equation (4.13b) leads to,

$$u_1'' - \frac{1}{c_p^2} \ddot{u}_1 = \beta \gamma^3 A_0^2 \sin\left(2\left(\gamma x - \Omega t\right)\right) \tag{4.16}$$

Equation (4.16) has the form of a classical partial differential equation with an inhomogeneous part. It is well-known from the mathematical analysis, that when the inhomogeneous part is linearly dependent to the general solution of the homogeneous part, the solution approach for the particular solution of u_1 must be multiplied by a sufficiently large power of x to become linearly independent. Thus, a particular solution may be obtained by the method of *variations of parameters* as,

$$u_1 = A(x) \sin\left(2\left(\gamma x - \Omega t\right)\right) + B(x) \cos\left(2\left(\gamma x - \Omega t\right)\right) \tag{4.17}$$

where $A(x)$ and $B(x)$ represent space-dependent amplitudes of the first-order perturbation solution. Inserting Equation (4.17) into Equation (4.16) leads to a pair of equations obtained by *matching like coefficients* of the sine and cosine terms,

$$\begin{aligned}
B''(x) + 4\gamma A'(x) &= 0 \\
A''(x) - 4\gamma B'(x) &= \beta \gamma^3 A_0^2
\end{aligned} \tag{4.18}$$

Let us write the space-dependent amplitudes as linear functions $A(x) = A_1 x + A_2$ and $B(x) = B_1 x + B_2$, and insert them in Equation (4.18):

$$\begin{aligned} 4\gamma A_1 &= 0 \quad &\Rightarrow \quad A_1 &= 0 \\ -4\gamma B_1 &= \beta\gamma^3 A_0^2 \quad &\Rightarrow \quad B_1 &= -\frac{1}{4}\beta\gamma^2 A_0^2 \end{aligned} \tag{4.19}$$

Therefore, the first-order perturbation solution can be stated as,

$$u_1 = A_2 \sin\left(2\left(\gamma x - \Omega t\right)\right) + \left(B_2 - \frac{1}{4}\beta\gamma^2 A_0^2 x\right)\cos\left(2\left(\gamma x - \Omega t\right)\right) \tag{4.20}$$

where A_2 and B_2 are constants corresponding to complementary solutions of Equation (4.13b). The constants can be determined by the boundary condition ($u_1(0,t) = 0$) and the Sommerfeld radiation-type condition, which requires that the solution represents a wave propagating in the positive x-direction (no reflection may occur since the layer is considered as semi-infinite). However, setting $A_2 = B_2 = 0$ simplifies the analysis without significantly affecting its accuracy. Indeed, Hamilton and Blackstock [172] demonstrated that any term of the wave displacement perturbation solution that remains independent of x may be ignored, regardless of wether it stems from the complementary or particular solution. Hence,

$$u_1 = -\frac{1}{4}\beta\gamma^2 A_0^2 x \cos\left(2\left(\gamma x - \Omega t\right)\right) \tag{4.21}$$

As can be observed, the first-order perturbation solution is generated by the fundamental waves, whose amplitude accumulates with the propagation distance x. In this case, the nonlinear effect is essentially due to frequency-mixing between two spectral components, i.e. the double-frequency component (second harmonics) is generated by a mixing of the fundamental waves with themselves [185]. The general solution up to first-order perturbation is therefore stated as,

$$u(x,t) = u_0(x,t) + u_1(x,t) = A_0 \sin\left(\gamma x - \Omega t\right) - \frac{1}{4}\beta\gamma^2 A_0^2 x \cos\left(2\left(\gamma x - \Omega t\right)\right) \tag{4.22}$$

and corresponds to the results obtained by Van den Abeele [181][1] and Pantea *et al.* [211][2]. In contrast, the first-order perturbation solution provided by Jhang and Kim [190] seems to be erroneous[3].

[1] Note that he found that the nonlinear coefficient of first-order $\hat{\beta} = 8A_1/(\gamma^2 x A_0^2)$. However, be aware that the former makes use of a slightly different nonlinear wave equation where $\hat{\beta} = 2\beta$. It can be shown that both solutions are equivalent.

[2] Note that they made use of a slightly different nonlinear wave equation (negative nonlinear term) and zero-order solution (cosine instead of sine), which explain the slightly different result. It can be proven again that both solutions are equivalent.

[3] Even if they start from the same equation than us, their resulting solution factor $1/8$ instead of $1/4$ is wrong.

The second-order perturbation solution can be solved accordingly by inserting the zero and first-order perturbation solutions from Equations (4.15) and (4.21) within the second-order perturbation Equation (4.13c) as,

$$u_2'' - \frac{1}{c_p^2}\ddot{u}_2 = -2\beta\left(u_0''u_1' + u_1''u_0'\right) - 3\delta u_0''\left(u_0'\right)^2 \tag{4.23}$$

where,

$$\begin{aligned} u_0' &= \gamma A_0 \cos\left(\gamma x - \Omega t\right) \\ u_0'' &= -\gamma^2 A_0 \sin\left(\gamma x - \Omega t\right) \\ u_1' &= -\frac{1}{4}\beta\gamma^2 A_0^2 \cos\left(2\left(\gamma x - \Omega t\right)\right) + \frac{1}{2}\beta\gamma^3 A_0^2 x \sin\left(2\left(\gamma x - \Omega t\right)\right) \\ u_1'' &= \beta\gamma^3 A_0^2 \sin\left(2\left(\gamma x - \Omega t\right)\right) + \beta\gamma^4 A_0^2 x \cos\left(2\left(\gamma x - \Omega t\right)\right) \end{aligned} \tag{4.24}$$

Inserting Equations (4.24) in Equation (4.23), and making use of the trigonometric identities $\cos(3a) = \cos(a)(\cos^2(a) - 3\sin^2(a))$ and $\sin(3a) = \sin(a)(3\cos^2(a) - \sin^2(a))$ leads to,

$$\begin{aligned} u_2'' - \frac{1}{c_p^2}\ddot{u}_2 = &-\left(\frac{1}{2}\beta^2\gamma^5 x A_0^3 \cos\left(\gamma x - \Omega t\right) + \frac{3}{4}\left(\beta^2 - \delta\right)\gamma^4 A_0^3 \sin\left(\gamma x - \Omega t\right)\right. \\ &+ \left.\frac{3}{2}\beta^2\gamma^5 x A_0^3 \cos\left(3\left(\gamma x - \Omega t\right)\right) + \frac{1}{4}\left(5\beta^2 - 3\delta\right)\gamma^4 A_0^3 \sin\left(3\left(\gamma x - \Omega t\right)\right)\right) \end{aligned} \tag{4.25}$$

Following the aforementioned method of *variations of parameters*, a suitable approach for the particular solution of the second-order perturbation solution u_2 may be written as,

$$\begin{aligned} u_2 = &\; A(x)\sin\left(\gamma x - \Omega t\right) + B(x)\cos\left(\gamma x - \Omega t\right) \\ &+ C(x)\sin\left(3\left(\gamma x - \Omega t\right)\right) + D(x)\cos\left(3\left(\gamma x - \Omega t\right)\right) \end{aligned} \tag{4.26}$$

Inserting Equation (4.26) in Equation (4.25) leads to two pairs of uncoupled equations obtained by *matching like coefficients* of the sine and cosine terms,

$$\begin{aligned} B''(x) + 2\gamma A'(x) &= -\frac{1}{2}\beta^2\gamma^5 x A_0^3 \\ A''(x) - 2\gamma B'(x) &= -\frac{3}{4}\left(\beta^2 - \delta\right)\gamma^4 A_0^3 \\ D''(x) + 6\gamma C'(x) &= -\frac{3}{2}\beta^2\gamma^5 x A_0^3 \\ C''(x) - 6\gamma D'(x) &= -\frac{1}{4}\left(5\beta^2 - 3\delta\right)\gamma^4 A_0^3 \end{aligned} \tag{4.27}$$

Let us now write the space-dependent amplitudes as quadratic functions $K(x) = K_1x^2 + K_2x + K_3$, with $K = \{A, B, C, D\}$, and insert them in Equation (4.27):

$$\begin{aligned}
2B_1 + 2\gamma(2A_1x + A_2) &= -\frac{1}{2}\beta^2\gamma^5 x A_0^3 \quad \Rightarrow \quad A_1 = -\frac{1}{8}\beta^2\gamma^4 A_0^3 \\
2A_1 - 2\gamma B_2 &= -\frac{3}{4}\left(\beta^2 - \delta\right)\gamma^4 A_0^3 \quad \Rightarrow \quad B_2 = \frac{1}{4}\left(\beta^2 - \frac{3}{2}\delta\right)\gamma^3 A_0^3 \\
2D_1 + 6\gamma(2C_1x + C_2) &= -\frac{3}{2}\beta^2\gamma^5 x A_0^3 \quad \Rightarrow \quad C_1 = -\frac{1}{8}\beta^2\gamma^4 A_0^3 \\
2C_1 - 6\gamma D_2 &= -\frac{1}{4}(5\beta^2 - 3\delta)\gamma^4 A_0^3 \quad \Rightarrow \quad D_2 = \frac{1}{6}\left(\beta^2 - \frac{3}{4}\delta\right)\gamma^3 A_0^3
\end{aligned} \tag{4.28}$$

Therefore, the second-order perturbation solution can be stated as,

$$\begin{aligned}
u_2 &= \left(A_3 - \frac{1}{8}\beta^2\gamma^4 x^2 A_0^3\right)\sin(\gamma x - \Omega t) + \left(B_3 + \frac{1}{4}\left(\beta^2 - \frac{3}{2}\delta\right)\gamma^3 x A_0^3\right)\cos(\gamma x - \Omega t) \\
&+ \left(C_3 - \frac{1}{8}\beta^2\gamma^4 x^2 A_0^3\right)\sin(3(\gamma x - \Omega t)) + \left(D_3 + \frac{1}{6}\left(\beta^2 - \frac{3}{4}\delta\right)\gamma^3 x A_0^3\right)\cos(3(\gamma x - \Omega t))
\end{aligned} \tag{4.29}$$

where the constants K_3 corresponding to complementary solutions can be set to zero as done for the first-order perturbation solution (see Equations (4.20)-(4.21)). Hence,

$$\begin{aligned}
u_2 &= -\frac{1}{8}\beta^2\gamma^4 x^2 A_0^3\left(\sin(\gamma x - \Omega t) + \sin(3(\gamma x - \Omega t))\right) \\
&+ \frac{1}{4}\gamma^3 x A_0^3\left(\left(\beta^2 - \frac{3}{2}\delta\right)\cos(\gamma x - \Omega t) + \left(\frac{2}{3}\beta^2 - \frac{1}{2}\delta\right)\cos(3(\gamma x - \Omega t))\right)
\end{aligned} \tag{4.30}$$

As can be observed, the second-order perturbation solution is composed of two parts, which are both generated by interactions of the zero-order with the first-order perturbation solution. In this case, the nonlinear effect is essentially frequency mixing between three spectral components: The triple-frequency component (third harmonics) is generated by a *positive* mixing of the fundamental waves with the second harmonics (Ω+2Ω), while the resulting single-frequency component (first harmonics) is generated by a *negative* mixing of the fundamental waves with the second harmonics (2Ω-Ω).

The general solution up to second-order perturbation is easily obtained by combining Equation (4.30) with Equation (4.22) as,

$$\begin{aligned}
u(x,t) &= u_0(x,t) + u_1(x,t) + u_2(x,t) \\
&= A_0\sin(\gamma x - \Omega t) - \frac{1}{4}\beta\gamma^2 A_0^2 x\cos(2(\gamma x - \Omega t)) \\
&- \frac{1}{8}\beta^2\gamma^4 x^2 A_0^3\left(\sin(\gamma x - \Omega t) + \sin(3(\gamma x - \Omega t))\right) \\
&+ \frac{1}{4}\beta^2\gamma^3 x A_0^3\left(\cos(\gamma x - \Omega t) + \frac{2}{3}\cos(3(\gamma x - \Omega t))\right) \\
&- \frac{3}{8}\delta\gamma^3 x A_0^3\left(\cos(\gamma x - \Omega t) + \frac{1}{3}\cos(3(\gamma x - \Omega t))\right)
\end{aligned} \tag{4.31}$$

and corresponds to the results by Melngailis *et al.* [164][4] and Van den Abeele [181][5]. It is noteworthy that higher-order perturbation solutions could be found accordingly. The elementary relationships for the β, δ-model up to second-order perturbation solutions can be summarized as follows, looking at the individual spectral components and their dependence on distance x, frequency Ω, and amplitude A_0 of the fundamental waves [185]:

$$u_1(x,t) \propto \beta \left(\frac{\Omega}{c_p}\right)^2 A_0^2 x \quad , \quad u_2(x,t) \propto \begin{cases} \beta^2 \left(\frac{\Omega}{c_p}\right)^4 A_0^3 x^2 & \text{, if } \beta^2 \left(\frac{\Omega}{c_p}\right) x \gg |\delta| \\ \delta \left(\frac{\Omega}{c_p}\right)^3 A_0^3 x & \text{, if } \beta^2 \left(\frac{\Omega}{c_p}\right) x \ll |\delta| \end{cases} \tag{4.32}$$

Manifestations of nonlinear constitutive behavior

Let us finally consider a simple example to highlight the well-known acoustical manifestations of nonlinear constitutive behavior, i.e. the steepening of the waveform in the time-domain and the observation of higher harmonics as local maxima in the frequency-domain. To this end, we developed the model in Equation (4.31) up to 10 harmonics. For clarity, we refer to the first-order (one nonlinear parameter) Taylor series expansion as the β-model, and to the extended second-order expansion as the β, δ model. The input is a monochromatic continuous pressure wave at frequency $F = 5$ MHz and four drive displacement amplitudes (A_0, $2A_0$, $3A_0$, and $4A_0$, where $A_0 = 5$ nm). The propagation distance is $x = 20$ cm, and the linear wave velocity in the model is fixed to $c_p = 1500$ m/s (attenuation is neglected). Strain values of the wave responses can be obtained from those classical nonlinear models. The values of the nonlinear parameters are indicated in the figures below. Figure 4.1 depicts the linear case, where as expected the frequency of the output remains the same than that of the input. In addition, there is no amplitude-dependent propagation, so that the ratio between the amplitudes remains equivalent.

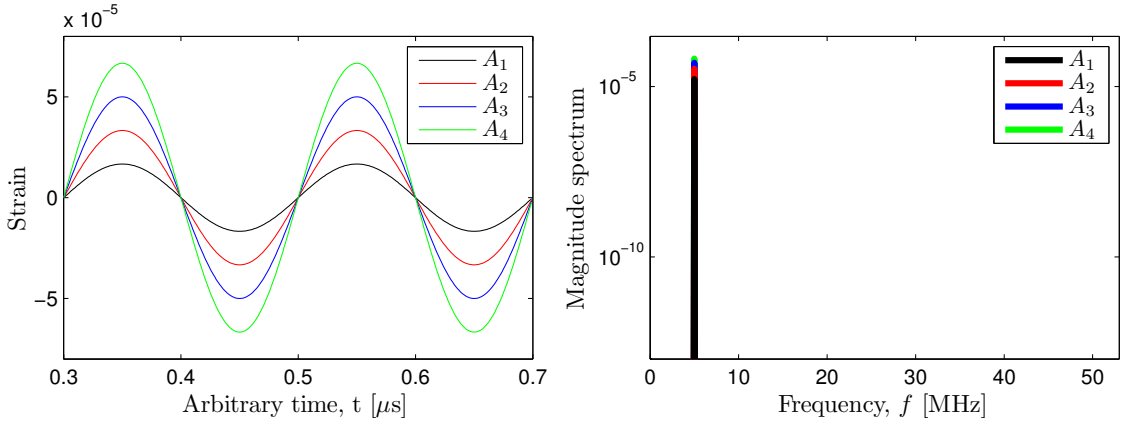

Figure 4.1: *Linear model ($\beta = \delta = 0$).*

[4]Note that in his proposed form, $a = 2\beta$ and $\delta = 0$.

[5]He found that the amplitude of the third harmonics (when neglecting δ) was $A_2 = \bar{\beta}^2 A_0^3 \gamma^4 x/32$ (with $\bar{\beta} = 2\beta$).

Figure 4.2 shows the β-model. As can be observed, an increase of the drive amplitude leads to increased asymmetry in the waveforms (i.e. saw-tooth form), which corresponds to a larger distribution of energy into higher-order harmonics. The harmonic energy contained in the spectral components tends to fall off rapidly and nearly exponentially as a function of the frequency [185].

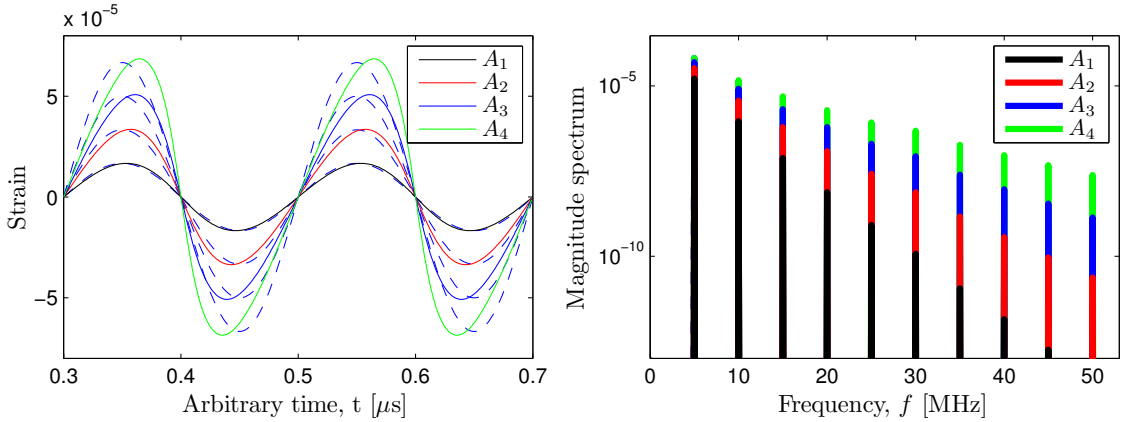

Figure 4.2: *Nonlinear β-model: $\beta = 5$ ($\delta = 0$).*

On the other hand, Figure 4.3 illustrates the β, δ-model with β set equal to zero and a positive δ-value. The distortion from a sinusoidal waveform increases with increasing drive amplitude, and the spectral components are characterized by the presence of odd harmonics, as predicted by Equation (4.31).

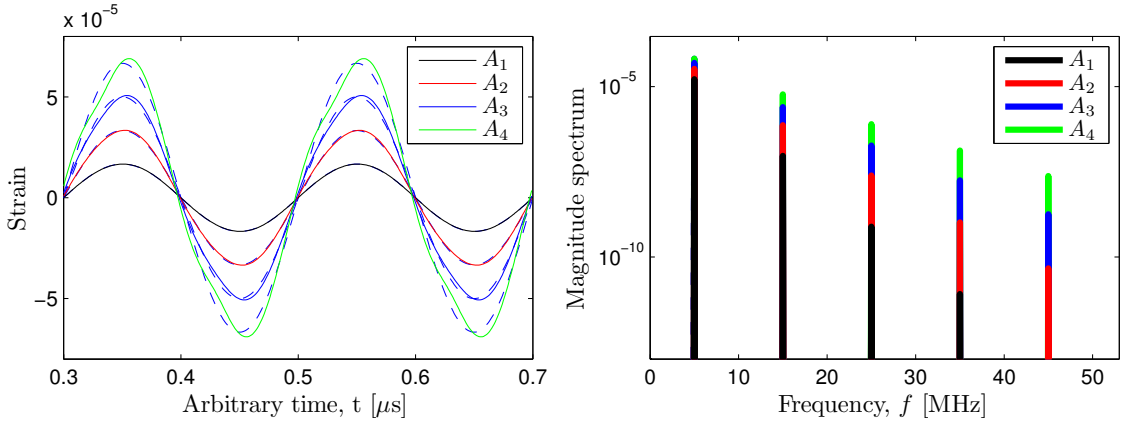

Figure 4.3: *Nonlinear β, δ-model: $\beta = 5$, $\delta = 20000$.*

Note also that the magnitude spectrum is identical for positive or negative δ-values, as depicted in Figure 4.4 for the largest input energy $4A_0$. Time-domain differences could however be observed in the phase-spectrum.

In addition, Figure 4.5 depicts the combination of first- and second-order nonlinearity (β, δ-model), for a positive δ-value which is much larger than β^2, since values for $|\delta|$ of one or two orders of magnitude larger than β^2 is typically required to visually alter the distorted waveform [185]. As can be observed, in that case the spectral components are made of both

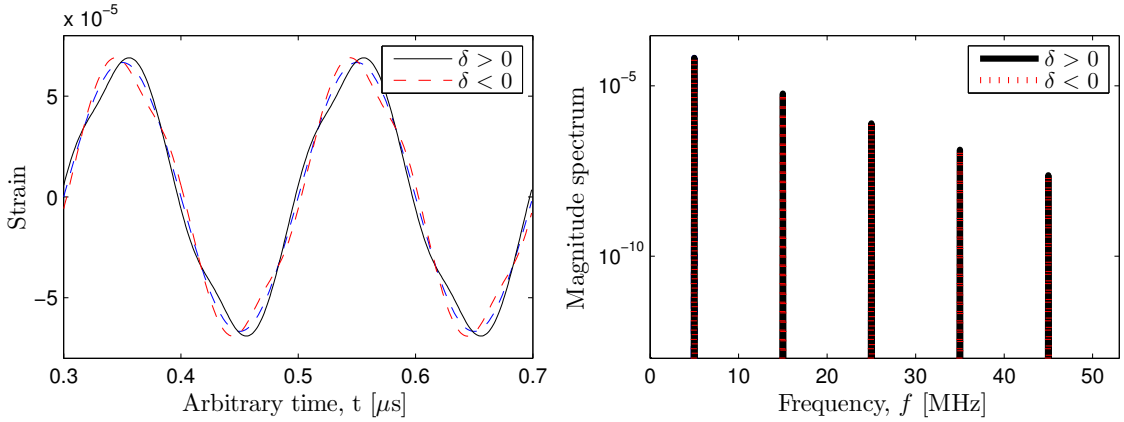

Figure 4.4: *Nonlinear β, δ-model: $\beta = 0$, $\delta = \pm 20000$ (for $4A_0$).*

even and odd harmonics, and for sufficient input energy, the spectrum shows a predilection for odd harmonics (e.g. for $4A_0$).

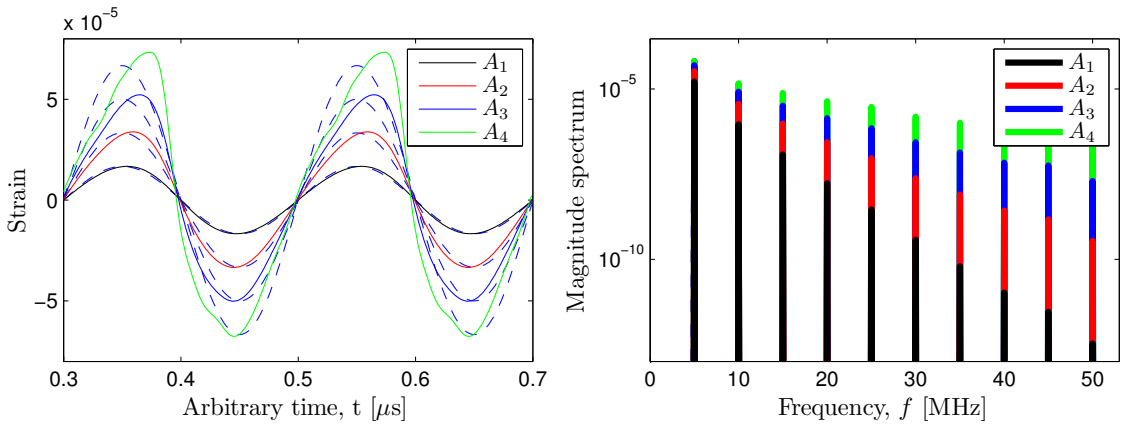

Figure 4.5: *Nonlinear β, δ-model: $\beta = 5$, $\delta = 20000$.*

Finally, Figure 4.6 shows the combination of first- and second-order nonlinearity (β, δ-model for a drive amplitude $4A_0$), for positive and negative δ-values which are much larger than β^2. As can be observed, the distortions of the waveforms significantly change, depending upon the sign and the value of the second-order nonlinear parameter δ. As in the previous case, and for sufficient larger values of δ, the spectrum shows a predilection for odd harmonics (e.g. for δ_2).

4.2 Signal processing and feature extraction

The optimization of the model-based estimation strategy proposed in this dissertation makes an extensive use of signal processing developments. Among these, analysis and parametrization techniques play a fundamental role in our work, so this section is devoted to briefly describe them. The goal of the techniques described here is to provide a suitable representation of ultrasonic signals, appropriate for pathology identification. These can be

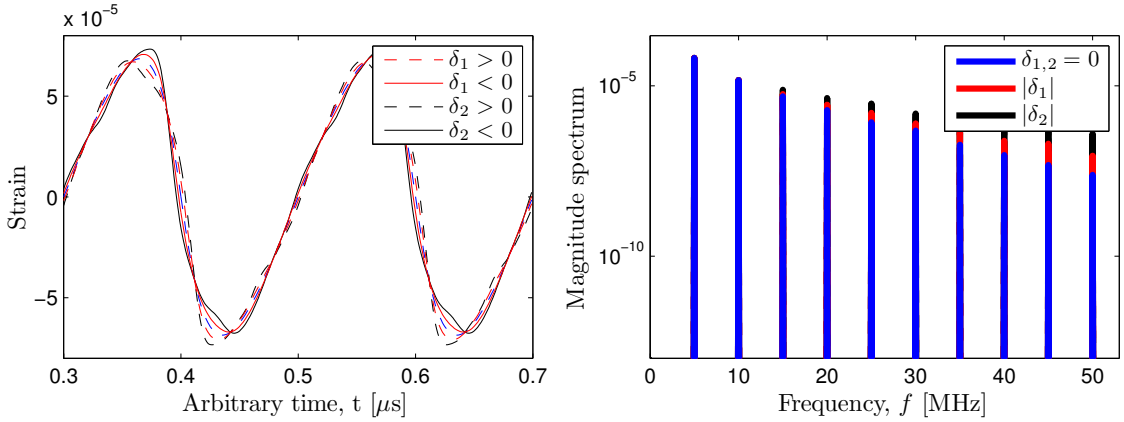

Figure 4.6: *Nonlinear β, δ-model: $\beta = 5$, $\delta_1 = \pm 10000$, $\delta_2 = \pm 20000$ (for $4A_0$).*

classified in three stages. In first place, we find some techniques that can be used to preprocess ultrasonic signals, by means of noise reduction and echo enhancement. Then, different analysis approaches can be applied to the preprocessed signals (e.g. nonparametric and parametric signal models), and the obtained spectral parameters can usually be transformed (e.g. homomorphic transformations), to provide a more uncorrelated and dimensionally reduced representation. It results from the applied analysis that a signal can be represented by a feature vector containing the ultrasonic information of interest. In some cases, this feature vector can be post-processed, leading to a further reduction of its dimensionality.

4.2.1 Preprocessing

Ultrasonic signals are generally contaminated by noise originated from both the measurement system and the material under inspection. Since the specimen-dependent part of the signal remains the same for all measurements, whereas the disturbances are randomly generated in each individual measurement, the SNR can initially be improved by signal averaging. Nevertheless, some artifacts should be eliminated before applying signal averaging. Indeed, at very low SNR (i.e. low signal amplitude or high damage environment), the signals may generally suffer from DC-misalignment effects. One can easily overcome this artifact by applying a baseline correction by subtracting the signal's mean to the signal. In addition, a small random time-shift may be present between two consecutive individual measurements due to imperfections of the measurement system or unstable conditions in the propagation path, causing signal misalignment in the time-domain. Under these conditions, the process of signal averaging results in a signal shape distortion. In order to prevent this distortion, those random shifts can be estimated by the cross-correlation method, so that the signals can be aligned in the time-domain for better averaging. Figure 4.7 depicts the effect of signal averaging on two ultrasonic signals, which results from the measurement of undamaged (high SNR) and damaged (low SNR) area of a layered material. The signals corresponding to an undamaged and damaged area are labeled as $y_{0,i}(n)$ and $y_{1,i}(n)$ $(i = 1, \ldots, N_r)$, respectively,

where N_r denotes the number of measurement repetitions. The resulting average are respectively denoted by $y_0(n)$ and $y_1(n)$. By this simple technique, the SNR can be improved up to $10\log_{10}(N_r)$ dB.

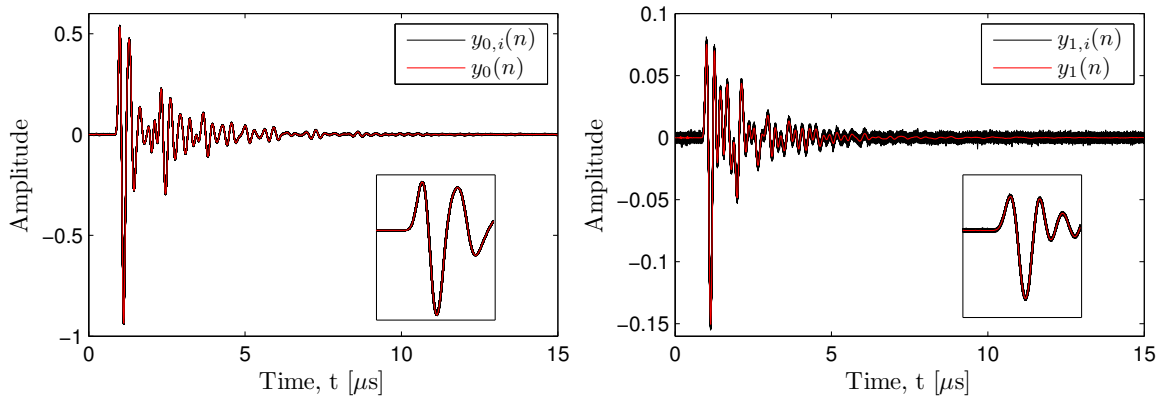

Figure 4.7: *Temporal signal averaging on ultrasonic signals obtained from a layered media: High SNR (left) versus low SNR (right).*

In order to further reduce part of the noise and focus on the frequency band of interest, the signals can be decimated at a sampling frequency $\bar{F}_s = F_s/M$, where F_s and M denote the original sampling frequency and the decimation factor, respectively. Figure 4.8 depicts the effect of M on the time-domain waveform $y_0(n)$ and magnitude spectrum $|Y_0(\omega)|$ of the averaged ultrasonic signal.

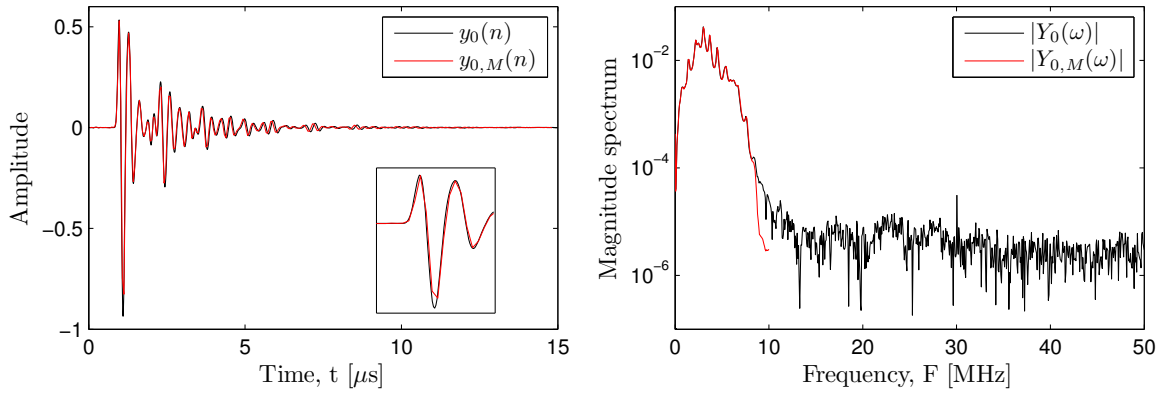

Figure 4.8: *Effect of decimation* ($\mathsf{M} = 5$) *on the time-domain waveform and magnitude spectrum of an ultrasonic signal measured from an undamaged area.*

Secondly, since an NDE system must be insensitive to changes in signal amplitude or energy, ultrasonic signals should be normalized. Typically, the normalization is performed by making use of the *root mean square* (rms) of the signal, so that the signal energy amounts to one. Alternatively, a signal can be normalized with respect to its amplitude, so that its absolute peak value amounts to one. Those operations can be expressed as,

$$y_{pow.}(n) = \frac{y(n)}{y_{rms}(n)} = \frac{y(n)}{\sqrt{\frac{1}{N}\sum_{n=0}^{N-1}\left(y(n)\right)^2}} \quad , \quad y_{peak}(n) = \frac{y(n)}{\max\left(|y(n)|\right)} \tag{4.33}$$

where $y(n)$ and N denote the ultrasonic signal[6] and the number of samples of that signal. Note that $y_{pow.}(n)$ is less sensitive to noise than $y_{peak}(n)$, as the signal's variability is divided by the square root of the number of samples.

Finally, the selection of an appropriate analysis window is considered. The multiplication of a signal by a window in the time-domain corresponds to a convolution in the frequency-domain, which results in two main effects: Spectrum estimation errors (*rippling*), and resolution loss between neighboring frequencies (*leaking*). The degree of *rippling* depends on the relative amplitude between the main lobe and the side lobes of the window spectrum, while the resolution loss is mainly influenced by the main lobe bandwidth [212]. Thus, the choice of the applied window depends on its discriminative characteristics regarding the trade-off between the degree of *leaking* and *rippling* (since both are entangled and the only way to simultaneously avoid both effects is to increase the window size). There are many windows that the literature referrers to (Hanning, Hamming, Blackman, Bartlett, etc. [213]). The default window, that is, when no window is explicitly applied, is the rectangular (Dirichlet) one. For a given length L, this window has the narrowest main lobe, but the highest side lobes among all other windows. Consequently, other window types were designed to reduce the *rippling* but at the cost of increasing the *leaking*, that is, by making a trade-off between main lobe bandwidth and side lobes relative amplitude. Among them, *raised cosine* based windows are frequently used. The mathematical definitions and characteristics of those windows, such as the main lobe bandwidth, side lobe relative amplitude and side lobes decreasing slope, are summarized in Table 4.1.

Window shape	Approximate main lobe bandwidth	Relative peak side lobe amplitude [dB]	Side lobes fall-off [dB/oct.]	Mathematical definition $w(n)$ $(0 \leq n \leq L)$
Rectangular	L/8	-13	-6	1
Hanning	L/4	-31	-18	$\frac{1}{2}\left(1-\cos\left(2\pi\frac{n}{L}\right)\right)$
Hamming	L/4	-41	-6	$0.54-0.46\ \cos\left(2\pi\frac{n}{L}\right)$
Bartlett	L/4	-25	-12	$\frac{2n}{L}\quad(0\leq n\leq L/2)$ $2\left(1-\frac{n}{L}\right)\quad(L/2\leq n\leq L)$
Blackmann	L/2	-57	-18	$0.42-0.5\cos\left(2\pi\frac{n}{L}\right)+0.08\cos\left(4\pi\frac{n}{L}\right)$

Table 4.1: *Windows characteristics reproduced from Oppenheim and Schafer* [212].

[6]From now on, any processing technique described in this section is applied to an undamaged ultrasonic signal, which has been previously averaged and decimated. For sake of notation simplicity, this signal is denoted by $y(n)$.

The *bell-shaped* curves of those windows are depicted in the left plot of Figure 4.9. Additionally, the right plot shows the Fourier transform (FT) of both the rectangular and Hamming windows, in order to illustrate the aforementioned trade-off between main lobe bandwidth and side lobes relative amplitude.

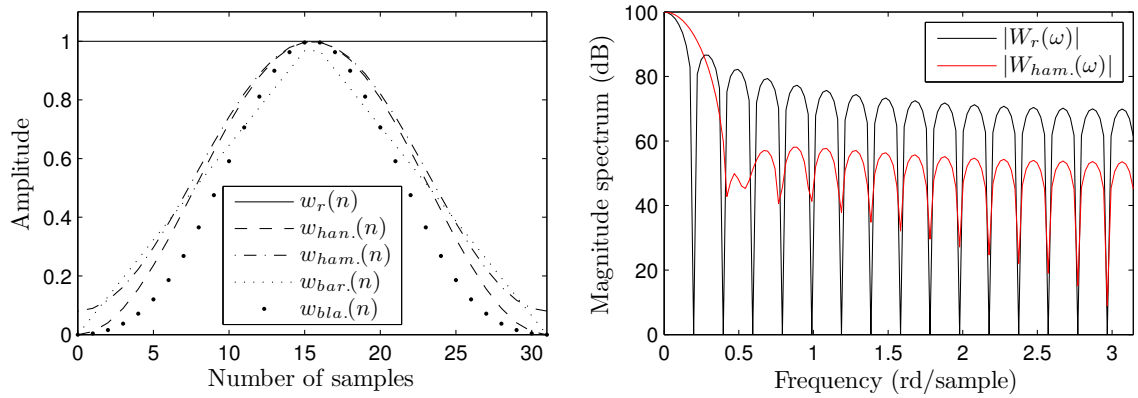

Figure 4.9: Preprocessing analysis windows.

It is worth to point out that signal windowing is generally considered for signals of infinite length. Hence, by increasing the window size, it is possible to avoid the trade-off between *leaking* and *rippling*. In contrast, ultrasonic signals experimentally obtained in pulse-echo or through-transmission modes are finite by nature, i.e. they start and end up with samples whose amplitude approximately amounts to zero. In addition, in that case, the window is also used to weight the signal samples over the time. This can be appreciated in Figure 4.10, where a Hamming window $w_{ham.}(n)$ has been applied over an ultrasonic signal $y_0(n)$. As can be observed, while in the original signal (left) predominates the first wave packet (wave front), the windowed signal (right) exhibits accentuated echoes amplitude, representative of the successive reflections of the transmitted signal between the specimen/transducers interface.

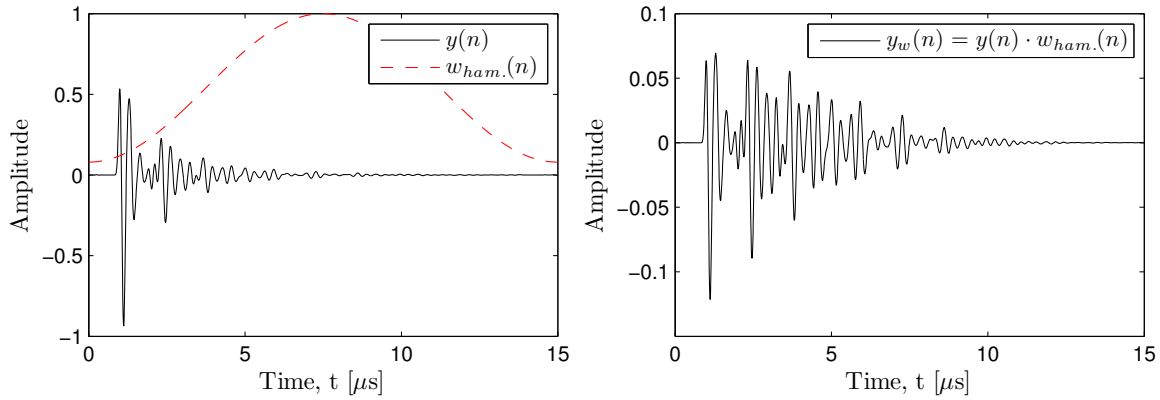

Figure 4.10: *Echoes enhancement of an ultrasonic signal by temporal signal windowing.*

The influence of the signal windowing will be further discussed in next sections, while dealing with other domains of signal representation.

4.2.2 *Spectral estimation*

To perform the feature extraction, we need to obtain the power spectral density (PSD) of the ultrasonic signal. The PSD can be estimated by turning to nonparametric and parametric techniques. For nonparametric techniques, the spectrum estimate is obtained without supposing any underlying model (that is, the spectral features are directly extracted from the signal). In contrast, for parametric techniques, the spectrum estimate is obtained by assuming a model based on the vision of the ultrasonic signal as the result of a discrete-time random process. Stationary (in a wide sense) random processes can be modeled by filtering white noise with a linear time-invariant filter that has a rational system function. In such a case, the ultrasonic signal is viewed as a filter output, where the spectrum shape is given by the filter frequency response and its gain by the white noise power.

A frequently used and simple nonparametric spectrum estimate consists of determining the magnitude spectrum of the signal by applying the DFT. Figure 4.11 depicts the magnitude spectrum of an ultrasonic signal, before and after applying an analysis window. As can be observed, applying an analysis window over the time-domain signal has significant implications on the magnitude spectrum, where the fine spectrum presents an accentuated *peakiness* due to the enhanced echoes.

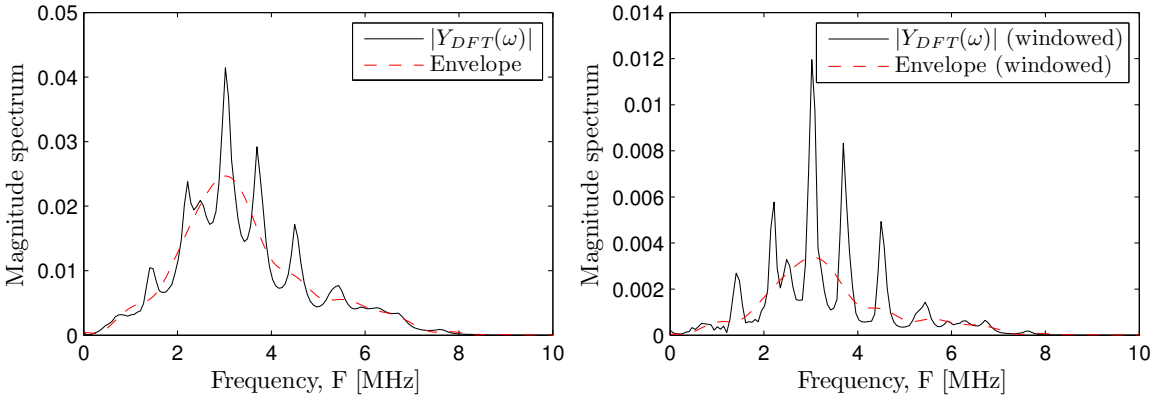

Figure 4.11: *Magnitude spectrum of an ultrasonic signal, before (left) and after (right) applying an analysis window (Hamming).*

Under parametric techniques, we are referring to autoregressive (AR), moving-average (MA) and autoregressive-moving-average (ARMA) models. In particular, AR models are considered here[7], since they have been found to provide a sufficiently accurate representation for many types of signals in many different applications [214], where as in NDE systems, the pursued information is hidden in a random-nature signal. If an AR model is assumed, a linear predictive coding (LPC) spectrum estimate can be computed. In such a case, the ultrasonic signal $y(n)$ is considered as the response of an all-pole filtering to a white noise excitation $x(n)$ [215]. The transfer function $H(z)$ of an all-pole filter is defined as,

$$H(z) = \frac{1}{A(z)} \tag{4.34}$$

[7]Note that the digital model obtained in Chapter 7 for the specimen will be proven to be an AR one.

in which $A(z)$ is a polynomial expression in z^{-1} of the form,

$$A(z) \quad = \quad \sum_{k=0}^{p} a_k z^{-k} \tag{4.35}$$

where the a_k and p denote the filter coefficients and the model-order, respectively. The difference equation corresponding to Equation (4.34) can be written as,

$$x(n) \quad = \quad \sum_{k=0}^{p} a_k y(n-k) \tag{4.36}$$

In addition, for a given a signal $y(n)$, a linear prediction (LP) based on the previous samples of the signal can be defined as,

$$\tilde{y}(n) \quad = \quad \sum_{k=1}^{p} a_k y(n-k) \tag{4.37}$$

When predicted samples are compared to the original ones, the prediction error can be computed as,

$$e(n) \quad = \quad y(n) - \tilde{y}(n) \quad = \quad y(n) - \sum_{k=1}^{p} a_k y(n-k) \tag{4.38}$$

From where Equation (4.36) is recovered when considering $e(n) = Gx(n)$. The LP coefficients a_k can be calculated as the ones that minimizes the error energy, that is,

$$\frac{\partial E}{\partial a_k} \quad \doteq \quad 0 \quad \text{, with} \quad E \quad = \quad \sum_{n=1}^{N} \left(e(n)\right)^2 \tag{4.39}$$

leading to the following classical linear equations system,

$$\sum_{k=1}^{p} a_k \sum_{n} y(n-k)y(n-i) \quad = \quad \sum_{n} y(n)y(n-i) \qquad\qquad (1 \leq i \leq p) \tag{4.40}$$

This system can be solved by the *autocorrelation method*, where the autocorrelation function is defined as,

$$R(i-k) \quad = \quad \sum_{n} y(n-k)y(n-i) \tag{4.41}$$

resulting in,

$$\sum_{k=1}^{p} a_k R(i-k) \quad = \quad R(i) \qquad\qquad (1 \leq i \leq p) \tag{4.42}$$

Note that the autocorrelation matrix that multiplies the vector of coefficients a_k is an Hermian Toeplitz matrix. This Toeplitz structure allows to solve this equations system efficiently by applying the Levinson-Durbin recursion [214].

The corresponding LPC spectrum can be obtained by evaluating $z = e^{j\omega}$ into Equation (4.34). Hence,

$$H(\omega) \quad = \quad H(z)|_{z=e^{j\omega}} \quad = \quad \frac{1}{\sum_{k=0}^{p} a_k e^{-j\omega k}} \tag{4.43}$$

Figure 4.12 depicts the LPC spectrum of an ultrasonic signal for a model-order equal to 18.

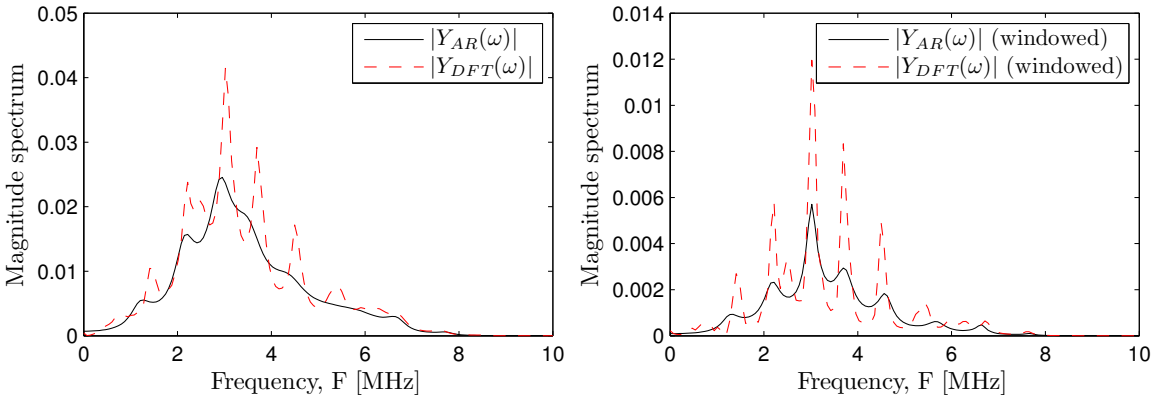

Figure 4.12: *Modeled LPC spectrum of an ultrasonic signal, before (left) and after (right) applying an analysis window (Hamming).*

As can be observed, a relatively low model-order leads to a smoothing of the magnitude spectrum and resonance peaks estimation. Nevertheless, the application of an analysis window enables us to preserve parts of the fine spectrum information, even at such a low model-order. Finally, it must be noted that there are some uncertainties regarding this modeling. Indeed, determining the order p of the LP analysis for ultrasonics seems not to be obvious at first sight, since it does not have an intrinsic meaning as in other applications. This issue will naturally rise up and be further discussed in Chapter 7.

4.2.3 Homomorphic transformations

Systems that satisfy the generalized principle of superposition are called *homomorphic* since they can be represented by algebraically linear mapping between output and input signal spaces [216]. Among the homomorphic transformations, the *cepstrum*[8] is a conventional technique which consists of converting a convolution into a sum [217]. Concretely, the *cepstrum* $\hat{c}(n)$ of a discrete signal $y(n)$ is defined as the inverse Fourier transform (IFT) of the logarithmic spectrum,

$$\hat{c}(n) \quad = \quad \mathfrak{F}^{-1}\left[\log\left(Y(\omega)\right)\right] \quad = \quad \frac{1}{2\pi}\int_{-\pi}^{\pi} \log\left(Y(\omega)\right) e^{j\omega n} d\omega \tag{4.44}$$

where $Y(\omega)$ denotes the spectrum of $y(n)$. Generally, the spectrum $Y(\omega)$ is a complex and even function obtained by applying the FT. Thus, even if $\hat{c}(n)$ represents a real signal (given

[8]The term *cepstrum* has been defined as an anagram of the word spectrum. Playing further on the anagram theme, a filter that operates on a *cepstrum* might be called a *lifter*, and so the *quefrency*, *repiod* and *saphe* respectively stand for the frequency, period, and phase in the cepstral-domain.

that $log(Y(\omega))$ is also an even function), it is usually called *complex cepstrum*, since the term *complex* refers to the use of the complex logarithm, not to the signal itself. Alternatively, a *real cepstrum* can be obtained by considering the magnitude spectrum $|Y(\omega)|$ before applying the logarithmic operation,

$$c(n) = \frac{1}{2\pi}\int_{-\pi}^{\pi} \log\left(|Y(\omega)|\right)e^{j\omega n}d\omega \tag{4.45}$$

By decomposing the spectrum $Y(\omega)$ into its respective magnitude $|Y(\omega)|$ and phase $\angle Y(\omega)$, an expression that relates the *complex* and *real cepstra* can be found as,

$$\hat{c}(n) = c(n) + j\,\mathfrak{F}^{-1}[\angle Y(\omega)] \tag{4.46}$$

As can be observed, the *real cepstrum* is the IFT of the real part of $Y(\omega)$, and is thus equal to the conjugate-symmetric part of $\hat{c}(n)$, denoted by $\hat{c}^*(n)$. Hence, there is a further expression that relates both the *complex* and the *real cepstra*,

$$\hat{c}(n) + \hat{c}^*(n) = 2\,c(n) \;\Leftrightarrow\; c(n) = \frac{\hat{c}(n) + \hat{c}^*(n)}{2} \tag{4.47}$$

In addition, in practice, the *real cepstrum* can be easily obtained by applying the FFT as,

$$c(n) = IFFT\left[\log\left(|FFT(y(n))|\right)\right] \tag{4.48}$$

where IFFT denotes the inverse fast Fourier transform. In such a case, the *real cepstrum* is usually called *cepstrum FFT*. The *cepstrum FFT* of an ultrasonic signal is depicted in Figure 4.13.

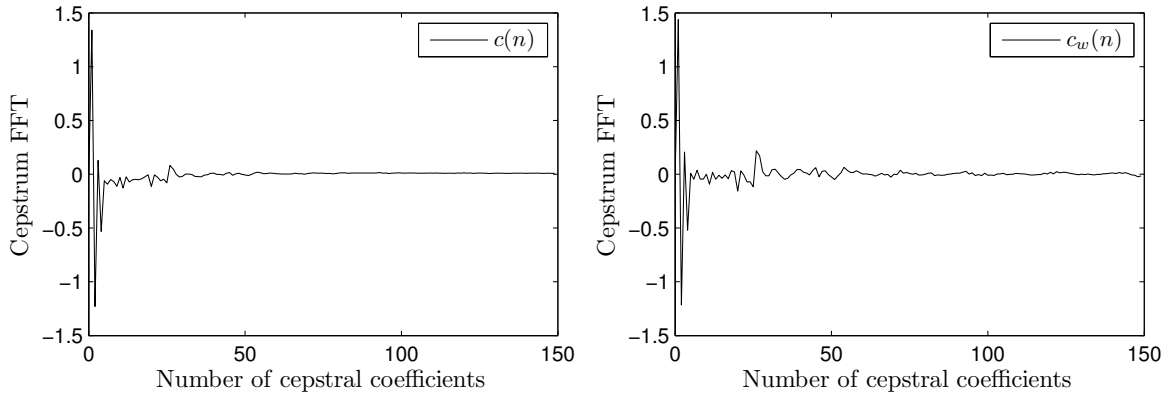

Figure 4.13: *Cesptrum FFT of an ultrasonic signal, before (left) and after (right) applying an analysis window.*

As can be observed, the low-order *cepstral* coefficients are nearly similar for the cases with/without an analysis window. In contrast, there is a significant increase in amplitude for higher-order *cepstral* coefficients for the case where an analysis window has been applied, in particular, around 25, 50, and 75. It is noteworthy that these *quefrencies* corresponds to

time-equivalent sample delays between wave echoes, i.e. the time that needs the wave front to cross two, four and six times the specimen. Thus, due to the harmonic nature of the ultrasonic signals, the wave echoes appear as equidistant peaks at higher *quefrencies*, rightly separated by a *repiod* that corresponds to the fundamental period of the analyzed signal echoes. In addition, the *cepstral* representation enables us to decompose the spectrum in two main characteristics, that are the spectral envelope (i.e. lower *quefrencies*) and the fine spectrum (i.e. higher *quefrencies*).

In an algebraic sense, the associated *complex cepstrum* could also be obtained via FFT. However, computing the *complex cepstrum* is usually cumbersome due to the unwrapping of the digital phase [218]. Indeed, the existence of the *complex cepstrum* is only ensured under the restriction that the complex logarithm could be represented by a convergent power series of the form,

$$\hat{C}(z) \quad = \quad \log\left[Y(z)\right] \quad = \quad \sum_{x=-\infty}^{\infty} \hat{c}(n) z^{-n}, \quad |z| = 1 \tag{4.49}$$

In such a case, $\log\left[Y(z)\right]$ must have the properties of the z-transform for a stable signal [219].

4.2.4 Parameter conversion

By applying a *cepstral* analysis, a more uncorrelated and dimensionally reduced (lower computational cost) signal representation can be obtained. Depending on the used spectral analysis, different types of *cepstra* can be obtained. The most direct way is also often called *cesptrum FFT*, as described in the previous section (i.e. IFFT of the logarithmic magnitude spectrum). However, an LPC-based *cepstrum* can alternatively be obtained by using the logarithmic LPC spectrum (i.e. assuming an AR model),

$$\hat{H}(\omega) \quad = \quad \log\left(H(z)|_{z=e^{j\omega}}\right) \quad = \quad \sum_{n=-\infty}^{\infty} c(n) e^{-j\omega n} \tag{4.50}$$

Additionally, the corresponding *complex cepstrum* can be expressed as,

$$\hat{c}(n) \quad = \quad \log(G)\delta(n) + \hat{c}_a(n) \tag{4.51}$$

where $\delta(n)$ represents a unitary impulse, and $\hat{c}_a(n)$ denotes the *complex cepstrum* of the sequence a_k. Alternatively, Equation (4.51) can also be calculated in a recursive way as,

$$\hat{c}(n) \quad = \quad \begin{cases} 0 & (n < 0) \\ \log(G) & (n = 0) \\ -a_1 & (n = 1) \\ -a_n - \sum_{k=1}^{n-1} \frac{k}{n} \hat{c}(k) a_{n-k} & (n > 1) \end{cases} \tag{4.52}$$

Commonly, this formulation is known as *cepstrum LPC*. Its corresponding *real LPC cesptrum* can be obtained by making use of Equation (4.47) as,

$$c(n) = \begin{cases} \dfrac{\hat{c}(-n)}{2} & (n < 0) \\ \log(G) & (n = 0) \\ \dfrac{\hat{c}(n)}{2} & (n > 0) \end{cases} \tag{4.53}$$

4.2.5 *Dimensionality reduction and deconvolution property*

It can be useful to reduce the number of *cepstral* coefficients, by applying a window to rule out lower and/or higher *quefrencies*. This process is called *liftering* and is defined as,

$$\tilde{c}(n) = c(n)l(n) \qquad (n = 0, \ldots, N-1) \tag{4.54}$$

where $l(n)$ is a windowing function that weight (or even set to zero) the *cepstral* coefficients. Be aware that the *liftering* can be interpreted as a kind of filtering. Indeed, by removing frequency components, one obtains a smoothed time-domain signal. Similarly, removing *cepstral* components leads to a smoothing of the spectrum. The default *liftering*, that is, when no *liftering* is explicitly applied, is the rectangular window. Consequently, an analogy with well-known filters (e.g. low-pass, high-pass and band-pass) used in the frequency-domain can be established, and thus several *liftering* windows can be directly derived from the rectangular one in the cepstral-domain. Let us consider for instance a *short-pass liftering*, which corresponds to a smoothing of the spectrum, preserving its spectral envelope while removing the fine spectrum information. This *liftering* has been usually applied to seismic signals or dereverberation problems, to cancel multiple equidistant echoes [220]. Figure 4.14 depicts such a *liftering* applied on the *cepstrum FFT* obtained from an ultrasonic signal, along with the resulting smoothing of the spectrum.

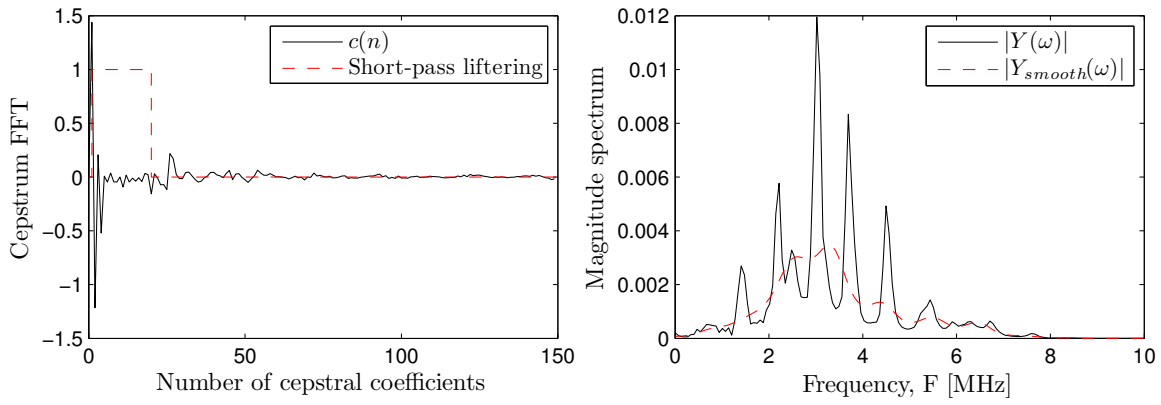

Figure 4.14: *Influence of a rectangular short-pass liftering on the magnitude spectrum of the ultrasonic signal.*

Although it has been less studied, it is interesting to point out that *liftering* the *complex cepstrum* allows to remove echoes on the time-domain waveform. In such a case, the *liftering* can be assimilated to a temporal window (which is not surprising, since we actually are in a quasi-temporal domain). Figure 4.15 shows such effect for an ultrasonic signal.

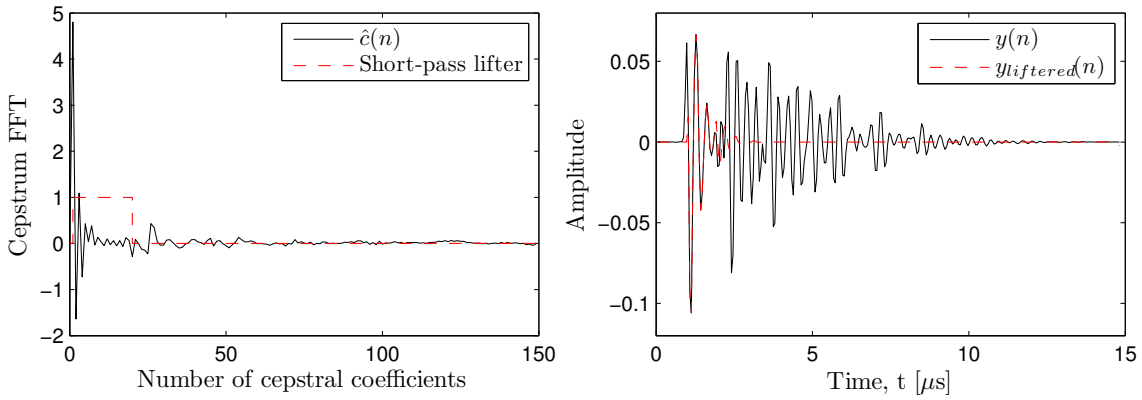

Figure 4.15: *Influence of a rectangular short-pass liftering on the time-domain waveform of an ultrasonic signal.*

On the other hand, windows different from the rectangular one can be applied to weight the *cepstral* coefficients depending on their discriminative performance for pathology detection. Tokhura [221] introduced a window formed by the inverse of the standard deviation of the *cepstral* coefficients $\sigma_c(n)$ (*statistical weighting*), which can be related to the slope of the considered *cepstrum*,

$$l_{sw}(n) = \begin{cases} \dfrac{1}{\sigma_c(n)} & 1 \leq n \leq L \\ 0 & \text{otherwise} \end{cases} \tag{4.55}$$

Other window shapes are proposed by Junqua and Wakita [222]. Among these, a *general exponential lifter* can be used for cases where the *cepstral* distance is too sensitive to the spectral peaks and not sensitive enough to the spectral slope,

$$l_{gel}(n) = \begin{cases} n^s & 1 \leq n \leq L \quad (s \geq 0) \\ 0 & \text{otherwise} \end{cases} \tag{4.56}$$

Alternatively, the *bandpass liftering*, based on a "sine-on-a-pedestal-shaped-function", has also been used in linear predictive analysis,

$$l_{bp}(n) = \begin{cases} 1 + 10.5 \sin\left(\dfrac{\pi n}{L}\right) & 1 \leq n \leq L \\ 0 & \text{otherwise} \end{cases} \tag{4.57}$$

Juang *et al.* [223] reviewed the sources of the LPC spectrum variation for speech signals, and pointed out the following statements, which can intuitively be extrapolated to NDE systems:

(a) Low-order *cepstral* coefficients can be related to the variations of the used transducers that produce the excitation signal transmitted through the specimen.
(b) Middle-order *cepstral* coefficients appear to be related to the material properties.
(c) High-order *cepstral* coefficients mostly contain measurement noise.

Consequently, the *liftering* window should reduce the undesirable variations due to coefficients of lower and higher orders. *Statistical weighting* allows to avoid the variation-type (a), but can strengthen the variation-type (c) in case of large window longitude. In order to remove those two variation types and enhance variation-type (b), a *raised sine* window has been defined as,

$$l_{rs}(n) = \begin{cases} 1 + \frac{1}{2} L \sin\left(\frac{\pi n}{L}\right) & 1 \leq n \leq L \\ 0 & \text{otherwise} \end{cases} \tag{4.58}$$

A further advantage of working in the cepstral-domain is its inherent deconvolutional capability. Indeed, by using a logarithmic domain, a response signal $y(n)$ resulting from the filtering $h(n)$ of an excitation signal $x(n)$ is equivalent to the sum of the corresponding *cepstra* $c_x(n)$ and $c_h(n)$, respectively. Consequently, the *cepstrum* provides an efficient and flexible analysis tool for measuring the likelihood between spectra (e.g. modeled and observed spectra or undamaged and damaged spectra). Indeed, the waveforms recorded from measurements on undamaged and damaged area of a layered material typically differentiate themselves mainly in the wave echoes, whereas the wave front remains almost unchanged. Thus, the deconvolution property of the *cepstrum* enables us to separate the material ($c_h(n)$) from the applied excitation ($c_x(n)$), in order to enhance the damage information when comparing signals obtained from area with distinct damage amount. Hence,

$$\begin{aligned} \Delta c_{(0,1)}(n) &= \left(c_{y_1}(n) - c_{y_0}(n)\right) \\ &= \left(c_{x_1}(n) + c_{h_1}(n)\right) - \left(c_{x_0}(n) + c_{h_0}(n)\right) \\ &= \left(c_{h_1}(n) - c_{h_0}(n)\right) \end{aligned} \tag{4.59}$$

where $c_{y_0}(n)$ and $c_{y_1}(n)$ denote the *cepstra* of signals measured on an undamaged and damaged area, respectively. Finally, the damage information can be evaluated by applying a *liftering* scan, with a given width and displacement, over this *cepstrum* distance $\Delta c_{(0,1)}(n)$ [224]. Indeed, by determining the variation within that dynamic window, it is possible to generate a graph of the *cepstral* distance evolution. This variation is quantified by computing the absolute error within this window as,

$$error\ [\%] = \frac{1}{L} \sum_{n=1}^{L} \left| \Delta c_{(0,1)}(n) \cdot l_r(n) \right| \tag{4.60}$$

As a consequence, this process enables us to detect the *cepstral* coefficients which contain some potential damage information, as depicted in Figure 4.16.

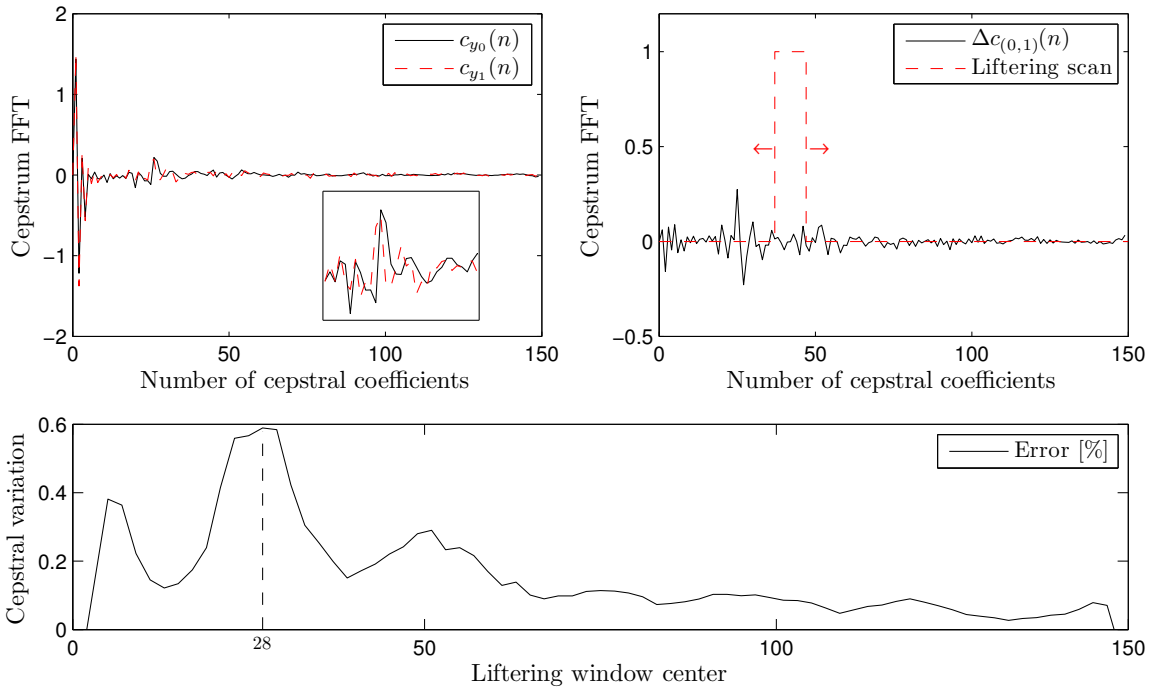

Figure 4.16: *Deconvolution property: (a) Cepstra of undamaged and damaged ultrasonic signals; (b) Rectangular liftering scan (width* $= 10$*, displacement* $= 2$*) applied on the cepstral distance; and (c) Evolution of the cepstral variation.*

As can be observed, the *cesptral* distance (i.e. damage information) shows high values at low-order *cepstral* coefficients, and at high-order *cepstral* coefficients with a common order that approximately amount to 28, which corresponds to the period of the wave echoes in the time-domain (that is, to twice the specimen's thickness in number of samples).

Part II

CONTRIBUTIONS

5

Model-based estimation procedure

The first objective of this dissertation is aimed at providing solutions to several problems that arise in *the model-based estimation procedure* for ultrasonic NDE of layered materials, by making use of digital signal processing and modeling techniques. To this end, this chapter presents a first contribution, which can be understood as a conceptual one. Indeed, on the light of the considerations done over the course of the literature review, we came across a *duality* when looking at the proposals for identifying layered structures, depending whether they stem from the engineering or information theory communities (see Figure 5.1). Therefore, we intent to unify the grounds implied in both area, facing toward the optimization of the performance of such procedure.

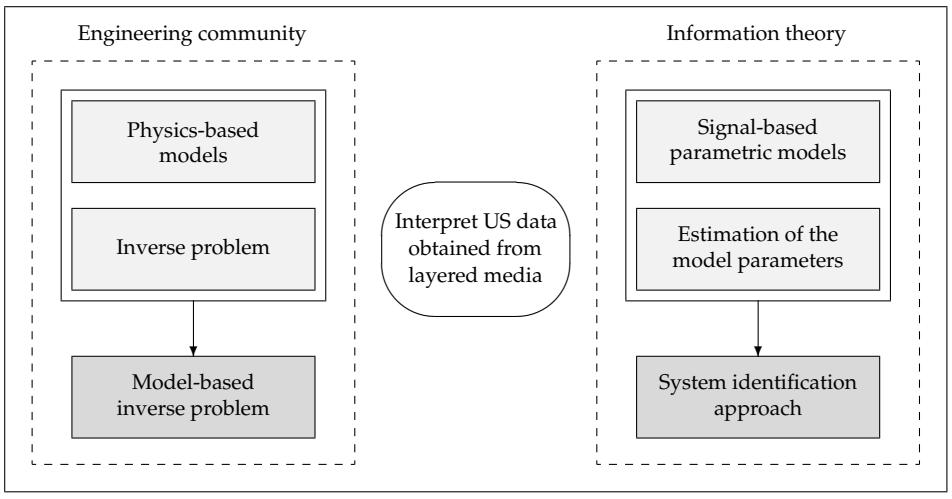

Figure 5.1: *Overview of the duality involved in the model-based estimation procedure.*

Generally, two key aspects of a *model-based estimation procedure* are fundamentals: (1) An appropriate understanding and modeling of the interactions between ultrasonic waves and multilayered media is required; and (2) the model parameters extracted from the measurements should be sensitive enough to the pathologies (that is, damage or consistency changes) that manifest in the specimen under inspection, and minimally sensitive to the measurements noise and model uncertainties. It is noteworthy that point (1) relies on the physics involved in the problem (i.e. its resolution is proper to engineers), whereas point (2) depends upon the signal features (i.e. their extraction is specific to researchers concerned with signal theory).

From an engineering perspective, a conventional *model-based inverse problem* is traditionally solved by minimizing the discrepancy between the experimental observations and the observations predicted by a *physics-based model* by comparing the waveforms in the time-domain, as depicted in Figure 5.2. Despite the potential strength of *model-based inverse problem*, parts of its structure could not be attractive from a practical point of view for inspecting multilayered media: For a fast convergence of the minimization algorithm, this method requires precise and reliable observations. However, due to their structural complexity, multilayered materials require special treatment in ultrasonic signal interpretation. The random nature of the signal generation, the imperfections of the acquisition system, as well as the difficulties in understanding and analyzing multiple and overlapping ultrasonic echoes may have a drastic influence on the performance of the inversion scheme. Additionally, an accurate characterization of pathologies usually require the determination of several model parameters, at the cost of excessive computational resources.

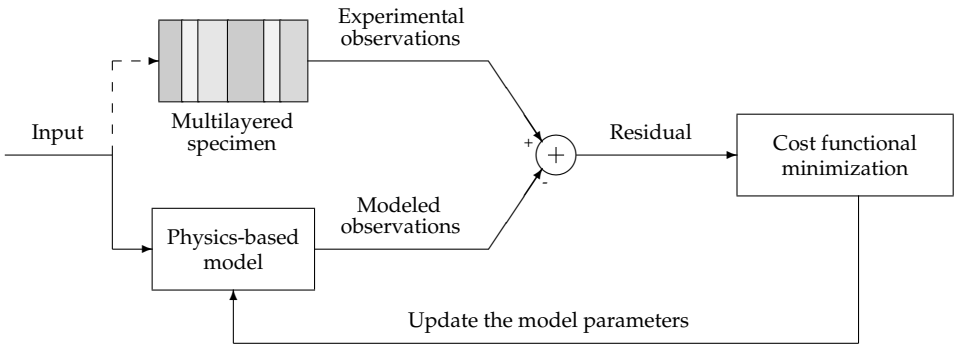

Figure 5.2: *Traditional model-based inverse problem framework.*

From a signal theory perspective, tremendous emphasis has been directed towards *system identification approaches* that enhance both the reliability and the quantitative informational content of signals obtained from conventional NDE systems [11]. Part of this emphasis has focused on the adaptation of advanced signal processing concepts to NDE problems, which had already been successfully applied in other scientific fields such as electrical engineering, speech recognition or geophysics. Among others, those procedures have given raise to the development of inverse problems based on *signal-based parametric models* (trained

over empirical data, in contrast to phenomenological approaches relying on deterministic physical laws[1]). Thus, the ability to reconstruct the ultrasonic signals can be evaluated by estimating the model parameters of the system to identify (which relates the input-output signals) that minimize the modeling error, as depicted in Figure 5.3.

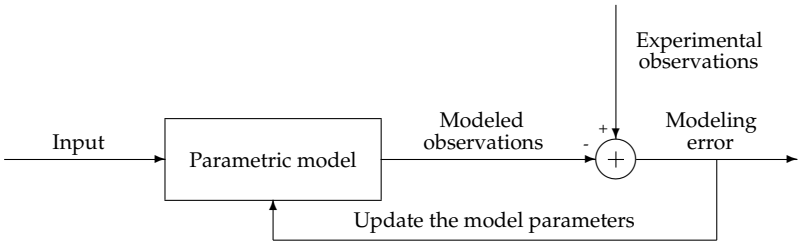

Figure 5.3: *System identification approach.*

From Figure 5.2, one could conclude the difficulty of directly extracting pathology-sensitive features from the ultrasonic signals captured by the transducers. In contrast, Figure 5.3 definitely lacks physical interpretation. In response to those problems, we propose an novel evaluation method based on an analysis-by-synthesis scheme [225, 46], which can be represented by means of the conceptual diagram depicted in Figure 5.4.

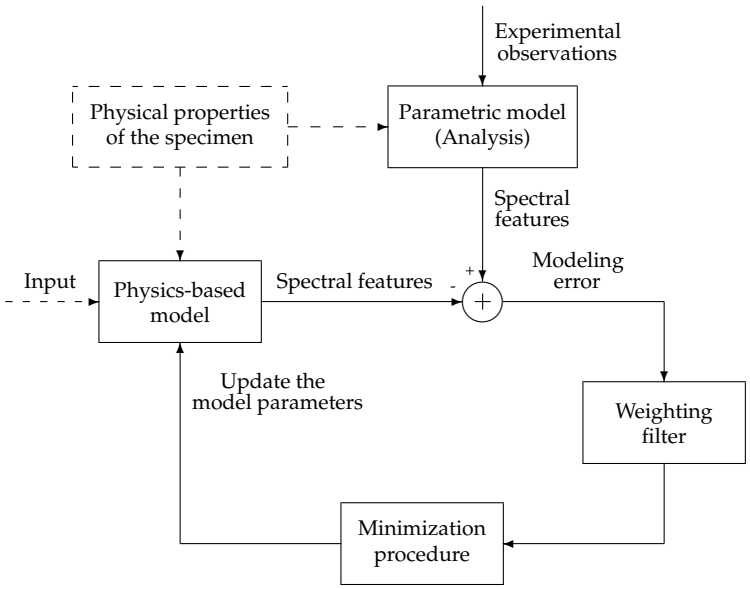

Figure 5.4: *Analysis-by-synthesis scheme.*

[1]From an engineering viewpoint, one usually develops models on the basis of the partial differential equations that describe the physical phenomena of interest (e.g. in our case, the wave equation), in an attempt of reproducing the experimental observation (i.e. the wave response). Alternatively, researchers involved in signal theory use to propose models, whose physical basis is empirical and directly inspired by the appearance of the experimental observation (e.g. in our case, the number, delay and amplitude of echoes contained in the wave response). In particular, the latter approach has a greater flexibility when it comes time to choose the model type and order (e.g. the modeling of ultrasonic signals using low-order autoregressive models [12]), which enables to adjust better the observations. However, it suffers from the absence of a direct link between the signal model parameters and the physical properties of the process.

As a can be observed, the model generates spectral features from the model pathology-sensitive parameters. The analysis-by-synthesis scheme enables us to perform a consistent optimization of the model parameters, in order to minimize the spectral distortion between the experimental observations and the modeled ones. Optionally, one could add a weighting filter that prioritize some spectral components over others. It is noteworthy that this analysis-by-synthesis scheme shows some similarities to those used in today's speech encoders. Consequently, the underlying signal processing and modeling techniques of the analysis-by-synthesis scheme offer several advantages: (1) The noise reduction of the captured signals, (2) a robust parametrization of the signals, to extract pathology-sensitive model parameters, (3) the definition of a distance between the observed and modeled features with a mechanical sense, and (4) an efficient model parameters estimation to identify the pathology.

The remaining chapters of the contributions focus on the different models developed over the course of this dissertation, and their use in the model-based estimation procedure. Despite the valuable efforts required for the development of consistent optimization strategies and the obtaining of relevant experimental observations, those steps of the model-based estimation procedure are moved to Part III, since they are not novel *per se*.

6

Transfer Matrix formalism

In this chapter, we revisit the Transfer Matrix (TM) formalism. The aim of the reconsideration of this classical method is threefold: To (1) review the theoretical grounding for our dissertation, (2) discuss some aspects regarding its implementation, and (3) obtain a formulation that offers us the possibility of extending the TM method to nonlinear media in a natural way. For these purposes, we first expose the theoretical development for a monochromatic linear-elastic wave, and then provide some answers to deal with practical issues such as material damping or discrete-time input signals.

6.1 Theoretical basis

The problem of a normally incident plane longitudinal ultrasonic wave that propagates through a multilayered elastic material is considered. A through-transmission configuration is adopted, representative of the successive reflections that suffer the transmitted signal between layers and specimen/transducers interfaces.

A general harmonic solution to the one-dimensional linear plane wave Equation (4.6) can be stated in the frequency-domain as,

$$u(x,\Omega) \;=\; u^f(x,\Omega) + u^b(x,\Omega) \;=\; Ae^{-j\frac{\Omega}{c}x} + Be^{j\frac{\Omega}{c}x} \tag{6.1}$$

where $u^f(x,\Omega)$ and $u^b(x,\Omega)$ stand for the forward- and backward-propagating parts of the linear displacement $u(x,\Omega)$, respectively. The constants A and B are the wave amplitudes of the forward- and backward-propagating parts, respectively. The ratio between the

continuous-time frequency Ω and the longitudinal wave velocity c is usually referred as the wave number $\gamma = \Omega/c$ [1]. The former is defined as,

$$c = \sqrt{\frac{E(1-\nu)}{\rho(1+\nu)(1-2\nu)}} \tag{6.2}$$

where E, ν and ρ denote the Young modulus, the Poisson ratio and the density of the medium in which the wave propagates, respectively.

The wave interactions within multilayered materials can be approximated by a semi-analytical model based on the TM formalism, which is here derived according to Cretu and Nita [226]. This formalism describes the wave propagation phenomena in finite elastic media, and is here strictly derived for the case of successive homogeneous layers. Let us consider sharp discontinuities between M homogeneous linear-elastic media with the same cross-sections, as depicted in Figure 6.1.

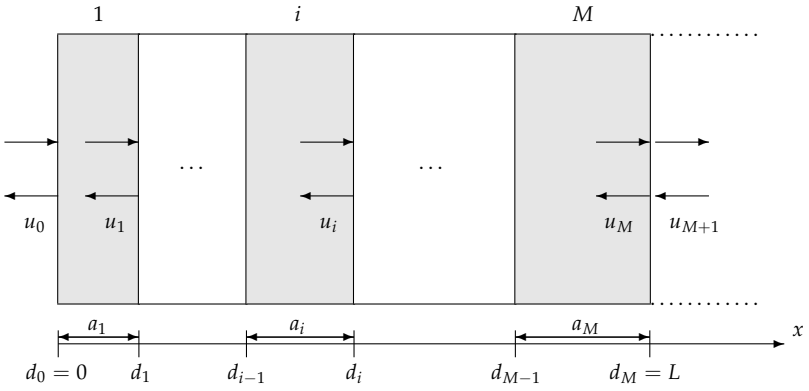

Figure 6.1: *Multilayered structure.*

Hence, the general harmonic solution stated in Equation (6.1) can be particularized for each layer i ($i = 1, \ldots, M$) as,

$$u_i(x, \Omega) = A_i e^{-j\frac{\Omega}{c_i}x} + B_i e^{j\frac{\Omega}{c_i}x} \tag{6.3}$$

In the case of a perfectly bounded interface, the transmission conditions imply the continuity of displacement $u_i(x, \Omega)$ and stress $\sigma_i(x, \Omega)$ across the interface. Making use of these conditions at an arbitrary interface $x = d_i$ ($i = 1, \ldots, M$),

$$\begin{aligned} u_i(d_i, \Omega) &= u_{i+1}(d_i, \Omega) \\ \sigma_i(d_i, \Omega) &= \sigma_{i+1}(d_i, \Omega) \end{aligned} \tag{6.4}$$

a hard transition from layer i to layer $i+1$ can be characterized by the discontinuity matrix $\boldsymbol{\mathcal{D}}_{i,i+1}$,

$$\boldsymbol{\mathcal{U}}_{i+1}(d_i, \Omega) = \boldsymbol{\mathcal{D}}_{i,i+1}\boldsymbol{\mathcal{U}}_i(d_i, \Omega) \qquad (i = 1, \ldots, M) \tag{6.5}$$

[1] Note that in the engineering community, the wave number is commonly denoted by k. Here, we reserve this symbol for the representation of the discrete frequencies, as done by researchers involved in signal theory.

where $\boldsymbol{\mathcal{U}}_j(x,\Omega) = \left[u_j^f(x,\Omega)\; u_j^b(x,\Omega)\right]^T$ and,

$$\boldsymbol{\mathcal{D}}_{i,i+1} = \frac{1}{2}\begin{pmatrix} 1+\dfrac{Z_i}{Z_{i+1}} & 1-\dfrac{Z_i}{Z_{i+1}} \\ 1-\dfrac{Z_i}{Z_{i+1}} & 1+\dfrac{Z_i}{Z_{i+1}} \end{pmatrix} \tag{6.6}$$

The discontinuity matrix depends only on the acoustic impedances $Z_j = \rho_j c_j$ of the two layers being in contact (see Appendix A.1). On the other hand, considering an harmonic wave propagating in the same homogeneous layer i from position $x = d_{i-1}$ to position $x = d_i$, its transformed displacement at the respective locations can be expressed by the propagation matrix $\boldsymbol{\mathcal{P}}_i(\Omega)$,

$$\boldsymbol{\mathcal{U}}_i(d_i,\Omega) = \boldsymbol{\mathcal{P}}_i(\Omega)\boldsymbol{\mathcal{U}}_i(d_{i-1},\Omega) \qquad (i = 1,\ldots,M) \tag{6.7}$$

with

$$\boldsymbol{\mathcal{P}}_i(\Omega) = \begin{pmatrix} e^{-j\frac{\Omega}{c_i}a_i} & 0 \\ 0 & e^{j\frac{\Omega}{c_i}a_i} \end{pmatrix} \tag{6.8}$$

where $a_i = d_i - d_{i-1}$ is the thickness of layer i (see Appendix A.2). Thus, the relation between the input and output state vectors for a layer i can be expressed by $\boldsymbol{\mathcal{U}}_{i+1}(d_i,\Omega) = \boldsymbol{\mathcal{T}}_i(\Omega)\boldsymbol{\mathcal{U}}_i(d_{i-1},\Omega)$, where a transfer matrix $\boldsymbol{\mathcal{T}}_i(\Omega) = \boldsymbol{\mathcal{D}}_{i,i+1}\boldsymbol{\mathcal{P}}_i(\Omega)$ for a single layer is obtained by combining discontinuity and propagation matrices ($i = 1,\ldots,M$),

$$\boldsymbol{\mathcal{T}}_i(\Omega) = \frac{1}{2}\begin{pmatrix} \left(1+\dfrac{Z_i}{Z_{i+1}}\right)e^{-j\frac{\Omega}{c_i}a_i} & \left(1-\dfrac{Z_i}{Z_{i+1}}\right)e^{j\frac{\Omega}{c_i}a_i} \\ \left(1-\dfrac{Z_i}{Z_{i+1}}\right)e^{-j\frac{\Omega}{c_i}a_i} & \left(1+\dfrac{Z_i}{Z_{i+1}}\right)e^{j\frac{\Omega}{c_i}a_i} \end{pmatrix} \tag{6.9}$$

so that the complete transfer matrix, describing the reflection and transmission processes of a multilayered structure, is easily obtained as the product of matrices from successive layers $\boldsymbol{\mathcal{T}}(\Omega) = \prod_{i=0}^{M-1}\boldsymbol{\mathcal{T}}_{M-i}(\Omega)$, leading to a relation between the input and the output state vectors as,

$$\boldsymbol{\mathcal{U}}_{M+1}(L,\Omega) = \boldsymbol{\mathcal{T}}(\Omega)\boldsymbol{\mathcal{U}}_1(0,\Omega) \tag{6.10}$$

where $x = 0$ and $x = L$ correspond to the boundaries of the system.

To solve the resulting system for a through-transmission configuration (the incident wave arises from the left, travels several times through the specimen, and is detected at the right-hand side), the boundary conditions must be specified[2]. First, the incident wave is

[2]Note that the theoretical development done so far may also be valid for other purpose involving the echogenic principle, such as conventional ultrasonic pulse-echo techniques or back-scattering approaches.

modeled by a forward prescribed displacement $u_0^f(0,\Omega)$, whose associated boundary condition involves the continuity of displacement at the left boundary $x = 0$,

$$u_0^f(0,\Omega) \;=\; u_1^f(0,\Omega) + u_1^b(0,\Omega) \tag{6.11}$$

where $u_0^f(0,\Omega)$ is the Fourier transform of the incident monochromatic wave. On the other hand, the wave response is obtained by modeling the receiver as a semi-infinite layer, whose boundary condition is expressed by the radiation energy condition [210] as,

$$u_{M+1}^b(L,\Omega) \;=\; 0 \tag{6.12}$$

Inserting Equations (6.11) and (6.12) into Equation (6.10) leads to,

$$\begin{bmatrix} u_{M+1}^f(L,\Omega) \\ 0 \end{bmatrix} \;=\; \begin{pmatrix} \mathcal{T}_{11}(\Omega) & \mathcal{T}_{12}(\Omega) \\ \mathcal{T}_{21}(\Omega) & \mathcal{T}_{22}(\Omega) \end{pmatrix} \begin{bmatrix} u_1^f(0,\Omega) \\ u_0^f(0,\Omega) - u_1^f(0,\Omega) \end{bmatrix} \tag{6.13}$$

where the $\mathcal{T}_{ij}(\Omega)$ denote the elements of the transfer matrix $\boldsymbol{\mathcal{T}}(\Omega)$. The wave displacement at the receiver position L, in terms of that at the transmitter position 0, is found by solving the former linear equation system,

$$u_{M+1}^f(L,\Omega) \;=\; \frac{\det\left(\boldsymbol{\mathcal{T}}(\Omega)\right)}{\mathcal{T}_{22}(\Omega) - \mathcal{T}_{21}(\Omega)} u_0^f(0,\Omega) \;=\; \mathcal{H}(\Omega) u_0^f(0,\Omega) \tag{6.14}$$

where $\mathcal{H}(\Omega)$ is a complex scalar number, which depends on the frequency of the incident wave.

Finally, it is worth to note that Equation (6.14) is a theoretical result valid for any single continuous-time frequency Ω and any number of layers M. In addition, the derivation of the complete transfer matrix is straightforward and only relies on the principles of the continuum mechanics. Nonetheless, in practice, the input signal is usually a bandpass ultrasonic signal at a relatively low center frequency[3] containing a wide range of frequencies around it, and is commonly represented as a digital time-domain signal. This issue is discussed in the Section 6.3.

6.2 TM formalism extension to absorbing layers

Typically, no substantial changes are required for the TM formalism when dealing with absorbing layers. Indeed, material damping may be introduced in a number of ways. Here, the

[3]That is, a frequency whose wavelength is compatible with the specimen thickness. Therefore, this configuration does not lead to so-called "large-problems" [79], where transfer matrices become ill-conditioned when implementing the TM method. This assumption is reasonable, since it matches the configuration of the subwavelength technique used in the experimental section of this thesis (see Section 9.2).

damping is defined in terms of the dynamic modulus E^* as in [227], and can be expressed for each layer i as,

$$E_i^* = \bar{E}_i + j\tilde{E}_i = \bar{E}_i(1 + j\tan(\delta_i)) \tag{6.15}$$

where $\bar{E}_i$, $\tilde{E}_i$ and $\tan(\delta_i)$ are the storage modulus, the loss modulus and the (dimensionless) loss tangent, respectively. Thus, the complex wave velocity c_i^* can be defined as,

$$c_i^* = \bar{c}_i\sqrt{1 + j\tan(\delta_i)} \tag{6.16}$$

where $\bar{c}_i$ denote the real part of the complex wave velocity. Supposing that the loss is small, a first-order expansion of the square root containing the loss tangent leads to,

$$c_i^* \approx \bar{c}_i\left(1 + j\frac{\tan(\delta_i)}{2}\right) \tag{6.17}$$

Thus, any trivial harmonic solution to the viscoelastic wave equation could be written as,

$$e^{-j\frac{\Omega}{c_i^*}x} = e^{-j\frac{\Omega}{\bar{c}_i}(1-j\frac{\tan(\delta_i)}{2})x} = e^{-j\frac{\Omega}{\bar{c}_i}x}e^{-\frac{\Omega\tan(\delta_i)}{2\bar{c}_i}x} \tag{6.18}$$

As can be observed, the first exponential is complex and represents the harmonic propagation, whereas the second exponential is real and is responsible for the exponential decay of the wave with propagation distance x, known as attenuation. For a small loss, the attenuation may be defined as $\alpha_i = -\Omega\tan(\delta_i)/(2\bar{c}_i)$. Hence,

$$e^{-j\frac{\Omega}{c_i^*}x} = e^{-j\frac{\Omega}{\bar{c}_i}x}e^{\alpha_i x} \tag{6.19}$$

Thus, Equation (6.9) can be easily extended to the case of absorbing layers by substituting the wave velocity c_i by a complex one c_i^*.

6.3 Numerical implementation of the TM formalism

Let us consider that the incident wave $u_0(0, nT)$ at the transmitter position $x = 0$ is represented as a discrete-time signal with N samples ($n = 0, \ldots, N-1$). By applying the Discrete Fourier Transform (DFT), an approximated discrete frequency representation with components $u_0(0, \omega_k)$ ($k = 0, \ldots, N-1$) can be obtained. The TM formalism can then be applied to each frequency bin, in order to obtain the receiver side components $u_{M+1}(L, \omega_k)$. Finally, by applying the inverse Discrete Fourier Transform (IDFT), the wave response $u_{M+1}(L, nT)$ at the receiver position $x = L$ is recovered. The general scheme of this numerical procedure for M layers is depicted in Figure 6.2.

Under this approach, we are employing a discrete-time or normalized frequency $\omega = \Omega/F_s$ ($\omega \in [0, 2\pi]$), where F_s is the sampling frequency. The DFT frequencies ω_k cover the whole frequency range,

$$\omega_k = 2\pi\frac{k}{N} \qquad (k = 0, \ldots, N-1) \tag{6.20}$$

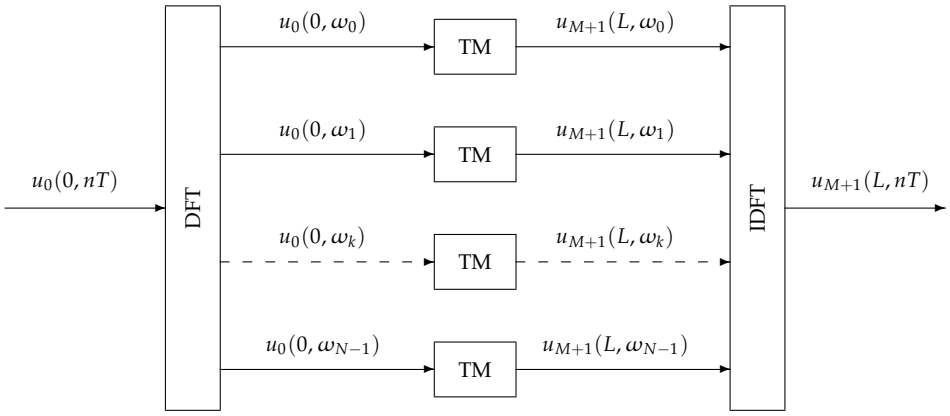

Figure 6.2: *General scheme of the TM formalism numerical procedure.*

According to this scheme, the transfer matrix for a single layer (see Equation (6.9)) can be discretized as well as,

$$\boldsymbol{T}_i^{(k)} \quad = \quad \boldsymbol{\mathcal{T}}_i(\Omega)|_{\Omega=\omega_k F_s} \tag{6.21}$$

leading to the following discrete solution,

$$u_{M+1}^f(L, \omega_k) \quad = \quad \frac{\det\left(\boldsymbol{T}^{(k)}\right)}{T_{22}^{(k)} - T_{21}^{(k)}} u_0^f(0, \omega_k) \quad = \quad H(\omega_k) u_0^f(0, \omega_k) \tag{6.22}$$

where $u_0^f(0, \omega_k)$ is the k^{th}-frequency component of the incident wave obtained by applying the DFT, namely $u_0^f(0, \omega_k) = \sum_{k=0}^{N-1} u_0(0, nT) e^{-jn\omega_k}$, and $\boldsymbol{T}^{(k)}$ denotes the complete transfer matrix corresponding to that frequency, whose elements are labeled as $T_{ij}^{(k)}$. It is worth to point out that each $\boldsymbol{T}_i^{(k)}$ ($i = 0, \ldots, M-1$, $k = 0, \ldots, N-1$) is a 2×2 matrix of complex numbers, allowing a numerical solution for Equation (6.22). Considering the frequency response $H(\omega)$ of the multilayered material for a through-transmission configuration, the proposed formalism implicitly provides a sampled version of it, namely $H(\omega_k) = \mathcal{H}(\Omega)|_{\Omega=\omega_k F_s}$ ($k = 0, \ldots, N-1$). Hence, this formalism does not enable to obtain an analytic representation of the complete frequency response of the material, and in practice its accuracy strongly depends on the number of signal samples N.

7

Signal modeling approach

In this chapter, we propose an alternative model for multilayered materials, which borrows concepts from lattice filter theory and bridge them with the physics involved in the wave-material interactions. In first place, the through-transmission configuration is considered as a discrete-time linear system. Thus, the multilayered material under investigation can be represented by a transfer function, which relates the discrete input and output signals [115]. Then, the ties between the signal model parameters and the physical properties of the layers are carefully inspected. Finally, we show that this model can be represented as a digital filter, and discuss strengths and limitations.

7.1 The two-port model

Multilayered wave-interactions can be described using conventional networks, which consist of discrete layers connected in series [103]. Thus, each layer unit i can be modeled by the two-port network depicted in Figure 7.1. In this figure, the frequency response $H_i(\omega)$ (ω is the normalized frequency defined in the previous chapter) and gains $\{G_{t_i}, G_{r_i}, \hat{G}_{t_i}, \hat{G}_{r_i}\}$ characterize the intra-layer i propagation and the impedance ratios between layers i and $i+1$, respectively. It is worth to mention that the negative signs at the nodes stand for the π-phase shifts ($e^{j\pi}$) that suffer the back-propagating components at the layer discontinuities.

According to Figure 7.1, outputs $Y_i^f(\omega)$ and $Y_i^b(\omega)$ are obtained from inputs $X_i^f(\omega)$ and $X_i^b(\omega)$ as,

$$\begin{aligned} Y_i^f(\omega) &= X_i^f(\omega)H_i(\omega)G_{t_i} - X_i^b(\omega)\hat{G}_{r_i} \\ Y_i^b(\omega) &= X_i^b(\omega)\hat{G}_{t_i}H_i(\omega) - X_i^f(\omega)H_i(\omega)G_{r_i}H_i(\omega) \end{aligned} \tag{7.1}$$

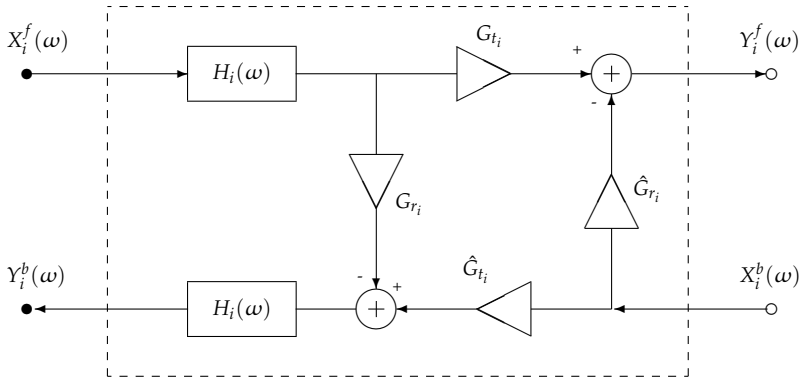

Figure 7.1: *Two-port network for a layer unit i.*

Working through these analytical expressions allows us to write the system in matrix form, with $\boldsymbol{U}_i(\omega) = \left[X_i^f(\omega)\ Y_i^b(\omega)\right]^T$ and $\boldsymbol{U}_{i+1}(\omega) = \left[X_{i+1}^f(\omega)\ Y_{i+1}^b(\omega)\right]^T$,

$$\boldsymbol{U}_{i+1}(\omega) = \begin{pmatrix} \left(G_{t_i} - \dfrac{G_{r_i}\hat{G}_{r_i}}{\hat{G}_{t_i}}\right) H_i(\omega) & -\dfrac{\hat{G}_{r_i}}{\hat{G}_{t_i}}\dfrac{1}{H_i(\omega)} \\ \dfrac{G_{r_i}}{\hat{G}_{t_i}} H_i(\omega) & \dfrac{1}{\hat{G}_{t_i}}\dfrac{1}{H_i(\omega)} \end{pmatrix} \boldsymbol{U}_i(\omega) \tag{7.2}$$

where the output vector of layer i corresponds to the input vector of layer $i+1$, i.e. $\boldsymbol{U}_{i+1}(\omega) = \left[Y_i^f(\omega)\ X_i^b(\omega)\right]^T$. The two-port network of layer i may be written as $\boldsymbol{U}_{i+1}(\omega) = \boldsymbol{T}_i(\omega)\boldsymbol{U}_i(\omega)$, and thus the total frequency response of the material is obtained as $\boldsymbol{T}(\omega) = \prod_{i=0}^{M-1} \boldsymbol{T}_{M-i}(\omega)$. Consequently, the relation between the input and output state vectors of the complete multilayered system $\boldsymbol{U}_{M+1}(\omega) = \boldsymbol{T}(\omega)\boldsymbol{U}_1(\omega)$ can be written as,

$$\begin{bmatrix} X_{M+1}^f(\omega) \\ Y_{M+1}^b(\omega) \end{bmatrix} = \begin{pmatrix} T_{11}(\omega) & T_{12}(\omega) \\ T_{21}(\omega) & T_{22}(\omega) \end{pmatrix} \begin{bmatrix} X_1^f(\omega) \\ Y_1^b(\omega) \end{bmatrix} \tag{7.3}$$

where the $T_{ij}(\omega)$ are the matrix elements of the total frequency response $\boldsymbol{T}(\omega)$. The boundary conditions for a through-transmission configuration (Equations (6.11)-(6.12)) can be represented as well in terms of signal theory concepts, as depicted in Figure 7.2.

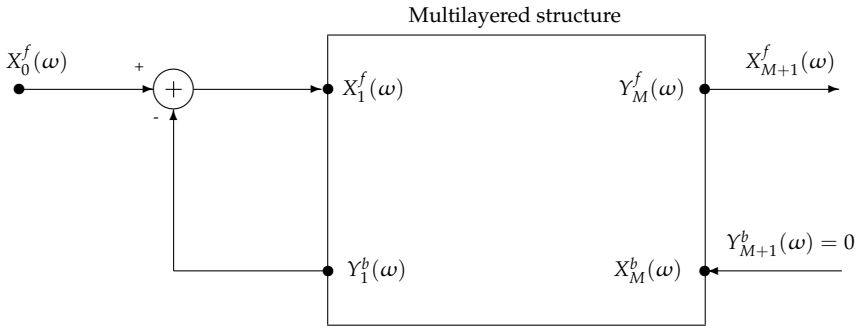

Figure 7.2: *Multilayered structure and boundary conditions in terms of signal modeling principles.*

From this figure, the boundary conditions are set in the two-port connections as,

$$\begin{array}{rcl} X_1^f(\omega) & = & X_0^f(\omega) - Y_1^b(\omega) \\ Y_{M+1}^b(\omega) & = & 0 \end{array} \tag{7.4}$$

Inserting Equation (7.4) into Equation (7.3) allows to find the output of the system as,

$$X_{M+1}^f(\omega) \;=\; \frac{\det\left(\boldsymbol{T}(\omega)\right)}{T_{22}(\omega) - T_{21}(\omega)} X_0^f(\omega) \;=\; H(\omega) X_0^f(\omega) \tag{7.5}$$

It is worth to point out the similarity of this equation with Equation (6.14) and Equation (6.22). This point will be further discussed in the next section.

7.2 Bridging the specimen's signal modeling and the physics

Let us now demonstrate that the TM formalism (see Chapter 6) may be regarded as a particular case of the innovative scheme proposed in the above section. For this purpose, the ties between the signal model parameters (gains and frequency responses) and the mechanical features (impedance ratios and material damping) are carefully inspected.

In the particular case of an incident wave propagating normally through an interface separating two media, the gains $\{G_{t_i}, G_{r_i}, \hat{G}_{t_i}, \hat{G}_{r_i}\}$ depicted in Figure 7.1 are related to the reflection and transmission coefficients associated to the reflected and transmitted wave parts generated by the incident wave. For an incident wave amplitude that amounts to unity, a simple relationship can be established between G_{r_i} and G_{t_i} [228],

$$G_{r_i} + G_{t_i} \;=\; 1 \tag{7.6}$$

When the incident wave travels from medium $i+1$ to medium i, the same relationship can be found for $\hat{G}_{r_i}$ and $\hat{G}_{t_i}$. It is noteworthy that G_{t_i} (resp. $\hat{G}_{t_i}$) may be greater than unity, and that G_{r_i} (resp. $\hat{G}_{r_i}$) may be negative. Indeed, energy is not determined by the wave amplitude alone, but depends upon the medium in which the wave propagates. The energy conservation principle [228] yields,

$$\langle P_{in} \rangle \;=\; \langle P_r \rangle + \langle P_t \rangle \tag{7.7}$$

where $\langle P_{in} \rangle$, $\langle P_t \rangle$ and $\langle P_r \rangle$ are the average power per unit area of the incident, transmitted and reflected wave components, respectively. The former equation can be explicitly written as,

$$\frac{1}{2}\rho_i c_i \omega^2 \;=\; \frac{1}{2}\rho_i c_i \omega^2 G_{r_i}^2 + \frac{1}{2}\rho_{i+1} c_{i+1} \omega^2 G_{t_i}^2 \tag{7.8}$$

From Equations (7.7)-(7.8), we can obtain the following relationships between gains and acoustic impedances,

$$G_{r_i} \;=\; \frac{Z_{i+1} - Z_i}{Z_i + Z_{i+1}} \quad , \quad G_{t_i} \;=\; \frac{2Z_i}{Z_i + Z_{i+1}} \tag{7.9}$$

Similar relationships can be obtained when the incident wave arises from the opposite side,

$$\hat{G}_{r_i} = \frac{Z_i - Z_{i+1}}{Z_i + Z_{i+1}} \quad , \quad \hat{G}_{t_i} = \frac{2Z_{i+1}}{Z_i + Z_{i+1}} \tag{7.10}$$

By inserting Equations (7.9)-(7.10) into the equation system (7.2), the following expression is obtained,

$$\boldsymbol{u}_{i+1}(\omega) = \frac{1}{2} \begin{pmatrix} \left(1 + \frac{Z_i}{Z_{i+1}}\right) H_i(\omega) & \left(1 - \frac{Z_i}{Z_{i+1}}\right) \frac{1}{H_i(\omega)} \\ \left(1 - \frac{Z_i}{Z_{i+1}}\right) H_i(\omega) & \left(1 + \frac{Z_i}{Z_{i+1}}\right) \frac{1}{H_i(\omega)} \end{pmatrix} \boldsymbol{u}_i(\omega) \tag{7.11}$$

which shows a high similarity with Equation (6.9). Let us now assume that the intra-layer frequency response $H_i(\omega)$ of Figure 7.1 has the form,

$$H_i(\omega) = e^{-j\omega m_i} \tag{7.12}$$

where $m_i = \frac{F_s a_i}{c_i}$, that is, the filter response $H_i(\omega)$ consists of an unitary gain and a linear phase with a constant group delay m_i. The latter corresponds to a delay equivalent to the time needed by the wave to cross the thickness of a layer i. By sampling this frequency response, we obtain:

$$H_i(\omega)|_{\omega=\omega_k} = H_i(\omega_k) = e^{-j\omega_k \frac{F_s a_i}{c_i}} \tag{7.13}$$

As can be observed, by inserting Equation (7.13) into the Equation (7.11), Equation (6.21) (i.e. the discrete version of Equation (6.9)) is recovered. Moreover, when dealing with absorbing layers, the definition of the frequency response $H_i(\omega)$ can be extended to,

$$H_i(\omega) = G_{\alpha_i} e^{-j\omega m_i} \tag{7.14}$$

where G_{α_i} denotes the attenuation associated to a layer i. By defining this attenuation as a constant gain $G_{\alpha_i} = e^{\alpha_i a_i}$, we recover a discretized version of the expression obtained in Equation (6.19),

$$H_i(\omega_k) = e^{\alpha_i a_i} e^{-j\omega_k \frac{F_s a_i}{c_i}} = e^{-j\frac{\Omega}{c_i^*} a_i}|_{\Omega=\omega_k F_s} \tag{7.15}$$

Thus, as can be seen, the TM formalism is indeed a particular case of our proposed signal modeling framework, which could be extended by defining the intra-layer response $H_i(\omega)$ in other different or more complex ways.

7.3 Solving the signal modeling approach

The theoretical result presented in Equation (7.5) is unfortunately not straightforwardly implementable, since the derivation of the total frequency response $\boldsymbol{T}(\omega) = \prod_{i=0}^{M-1} \boldsymbol{T}_{M-i}(\omega)$

is, in general, cumbersome. However, in the particular case of the layer frequency response definition made in Equation (7.14), equation system (7.2) can be rewritten as,

$$\boldsymbol{U}_{i+1}(\omega) \;=\; \begin{pmatrix} G_i^{(A)} e^{-j\omega m_i} & G_i^{(B)} e^{j\omega m_i} \\ G_i^{(C)} e^{-j\omega m_i} & G_i^{(D)} e^{j\omega m_i} \end{pmatrix} \boldsymbol{U}_i(\omega) \;=\; \boldsymbol{T}_i(\omega)\boldsymbol{U}_i(\omega) \tag{7.16}$$

where the $G_i^{(j)}$ (with $j = \{A, B, C, D\}$) stand for the resulting gains computed from the layer discontinuities $\{G_{t_i}, G_{r_i}, \hat{G}_{t_i}, \hat{G}_{r_i}\}$ and the absorption ones G_{α_i}. It can be proven that a product of matrices with the previous form can be expressed as a sum of matrices with a similar form (composed of gain-exponential elements). Hence, by making use of the distributive property (see Appendix B.1), the complete matrix product $\boldsymbol{T}(\omega) = \prod_{i=0}^{M-1} \boldsymbol{T}_{M-i}(\omega)$ can be translated into a sum of matrices as,

$$\begin{aligned} \boldsymbol{U}_{M+1}(\omega) \;&=\; \prod_{i=0}^{M-1} \begin{pmatrix} G_{M-i}^{(A)} e^{-j\omega m_{M-i}} & G_{M-i}^{(B)} e^{j\omega m_{M-i}} \\ G_{M-i}^{(C)} e^{-j\omega m_{M-i}} & G_{M-i}^{(D)} e^{j\omega m_{M-i}} \end{pmatrix} \boldsymbol{U}_1(\omega) \\ &=\; \sum_{k=1}^{2^{M-1}} \begin{pmatrix} \bar{G}_k^{(A)} e^{-j\omega \bar{m}_k} & \bar{G}_k^{(B)} e^{j\omega \bar{m}_k} \\ \bar{G}_k^{(C)} e^{-j\omega \bar{m}_k} & \bar{G}_k^{(D)} e^{j\omega \bar{m}_k} \end{pmatrix} \boldsymbol{U}_1(\omega) \end{aligned} \tag{7.17}$$

where the group delays $\bar{m}_k$ are obtained as a linear combination of the group delays m_{M-i}, and the gains labeled with an overscore result from multiplicative combinations of the original gains. It must be noted that subindex k does not correspond to any layer number but to the leaves of the resulting distributive decomposition tree. Unlike the TM formalism, the presented signal-based framework enables to compute analytically the complete frequency response $H(\omega)$ of the material for a through-transmission configuration. Note that the latter does not depend upon the number of signal samples N. However, this approach suffers of a strong lake of efficiency (even worse than the TM formalism) as the complexity burden increases exponentially along the number of layers M.

To avoid this, we take advantage of the mathematical formulation previously developed to define a novel specimen's digital modeling for wave propagation problems. To this end, for each layer i, we introduce a discrete-time transfer function $H_i^D(z) = G_{\alpha_i} z^{-m_i}$ in the z-domain, whose frequency response approximates that proposed in Equation (7.14),

$$H_i(\omega) \;\approx\; H_i^D(z)|_{z=e^{j\omega}} \;=\; G_{\alpha_i} e^{-j\omega m_i} \tag{7.18}$$

where it is must be noted that the delays $m_i \in \mathbb{N}$ are now integer thickness-equivalent sample delays that approximate the delays $m_i = \frac{F_s a_i}{c_i}$ by rounding their values or adjusting the sampling frequency. The transfer function $H_i^D(z)$ stands for a single-coefficient finite impulse response (FIR) filter, with a constant gain G_{α_i} and delay m_i. Substituting Equations (7.9)-(7.10) and $H_i^D(z)$ in the layer matrix of Equation (7.2) yields a z-transformed layer

matrix $\boldsymbol{T}_i^D(z)$ which can be rewritten in terms of z-domain polynomial expressions as,

$$\boldsymbol{U}_{i+1}(z) = \frac{G_{\alpha_i} z^{-m_i}}{1+G_{r_i}} \begin{pmatrix} 1 & G_{r_i} G_{\alpha_i}^{-2} z^{2m_i} \\ G_{r_i} & G_{\alpha_i}^{-2} z^{2m_i} \end{pmatrix} \boldsymbol{U}_i(z) = \boldsymbol{T}_i^D(z) \boldsymbol{U}_i(z) \tag{7.19}$$

It can be proven (see Appendix B.2) that the product of M-layers, $\boldsymbol{T}^D(z) = \prod_{i=0}^{M-1} \boldsymbol{T}_{M-i}^D(z)$, has the following general form,

$$\boldsymbol{T}^D(z) = \left(\prod_{i=1}^{M} \frac{G_{\alpha_i} z^{-m_i}}{1+G_{r_i}} \right) \begin{pmatrix} P_M(G_\alpha, z) & \left(\prod_{i=1}^{M} G_{\alpha_i}^{-2} z^{2m_i} \right) Q_M(G_\alpha^{-1}, z^{-1}) \\ Q_M(G_\alpha, z) & \left(\prod_{i=1}^{M} G_{\alpha_i}^{-2} z^{2m_i} \right) P_M(G_\alpha^{-1}, z^{-1}) \end{pmatrix} \tag{7.20}$$

where the functions $P_M(G_\alpha, z)$ and $Q_M(G_\alpha, z)$ stand for polynomials which are built up following a recursive scheme,

$$\begin{aligned} P_M(G_\alpha, z) &= P_{M-1}(G_\alpha, z) + G_{r_M} G_{\alpha_M}^{-2} z^{2m_M} Q_{M-1}(G_\alpha, z) \\ Q_M(G_\alpha, z) &= G_{r_M} P_{M-1}(G_\alpha, z) + G_{\alpha_M}^{-2} z^{2m_M} Q_{M-1}(G_\alpha, z) \end{aligned} \tag{7.21}$$

with $P_1(G_\alpha, z) = 1$ and $Q_1(G_\alpha, z) = G_{r_1}$. These polynomials incorporate all the multiple transmissions/reflections and attenuation effects of the multilayered structure.

Once the boundary conditions are considered (Equation (7.4)), a discrete-time transfer function of the multilayered structure can be written as,

$$X_{M+1}^f(z) = \left(\prod_{i=1}^{M} \frac{1}{1+G_{r_i}} \right) \left(\frac{P_M(G_\alpha, z) P_M(G_\alpha^{-1}, z^{-1}) - Q_M(G_\alpha, z) Q_M(G_\alpha^{-1}, z^{-1})}{\left(\prod_{i=1}^{M} G_{\alpha_i}^{-1} z^{m_i} \right) P_M(G_\alpha^{-1}, z^{-1}) - \left(\prod_{i=1}^{M} G_{\alpha_i} z^{-m_i} \right) Q_M(G_\alpha, z)} \right) X_0^f(z) \tag{7.22}$$

It must be considered that the polynomials $P_M(G_\alpha, z)$ and $Q_M(G_\alpha, z)$ are not independent, existing a surprising relationship between them (see Appendix B.3), which can be written down as,

$$P_M(G_\alpha, z) P_M(G_\alpha^{-1}, z^{-1}) - Q_M(G_\alpha, z) Q_M(G_\alpha^{-1}, z^{-1}) = \prod_{i=1}^{M} (1 - G_{r_i}^2) \tag{7.23}$$

which leads us to an iterative approach. Inserting Equation (7.23) into Equation (7.22) enables the following simplified filter,

$$X_{M+1}^f(z) = \frac{\prod_{i=1}^{M} G_{t_i} G_{\alpha_i} z^{-m_i}}{P_M(G_\alpha^{-1}, z^{-1}) - \left(\prod_{i=1}^{M} G_{\alpha_i}^2 z^{-2m_i} \right) Q_M(G_\alpha, z)} X_0^f(z) = \frac{N(z)}{D(z)} X_0^f(z) \tag{7.24}$$

This result allows any multilayered material to be modeled as a linear time-invariant (LTI) digital filter (with rational z-transform). The filter coefficients are linked to the physical properties of the material and are obtained from them analytically. In addition, it can be shown that the proposed recursive framework remains valid for any arbitrary discrete-time transfer function $H_i^D(z)$, and could thus be employed in the case of more complex layers' mechanical behavior.

7.4 Discussion

It can be proven that the formalism which delivers the transfer function of Equation (7.20), along with Equation (7.21), extends the recursive formalism proposed by Claerbout [97] for Goupillaud-type structures (i.e. structures which consist of equal wave travel time layers) which, in our proposed form, is now valid for absorbing layers of unequal wave travel time. On the other hand, the iterative expression delivered by Equation (7.24) also extends the energy considerations done by Claerbout [97] to absorbing non-Goupillaud-type structures. Additionally, our approach is straightforward and computationally more efficient than the one proposed by Treitel [228], who suggested that the effect of a multilayered material with arbitrary time delays could be obtained from Goupillaud-type media by lumping several successive layers together by setting the reflection coefficients to zero and the transmission coefficients to unity, at the number of interfaces existing between the constituent iso-time-delay layers.

A bare inspection of Equation (7.24) reveals that the lowest polynomial coefficient of the denominator $D(z)$ is provided by $P_1(G_\alpha^{-1}, z^{-1}) = 1$, ensuring that the filter is causal and realizable. On the other hand, the highest coefficient is 2Λ, with $\Lambda = \sum_{i=1}^{M} m_i$, due to the term $\prod_{i=1}^{M} z^{-2m_i}$ in the denominator. As can be observed, Λ corresponds to a sample delay equivalent to the time needed by the incident wave to cross the total thickness of the multilayered structure. In addition, the numerator $\prod_{i=1}^{M} G_{t_i} G_{\alpha_i} z^{-m_i}$ can be replaced by $b_0 z^{-\Lambda}$, i.e. a gain corresponding to the multiplication of the transmission G_{t_i} and attenuation coefficients G_{α_i} across all layers plus a total thickness sample delay. Finally, Equation (7.24) implies that most of the coefficients a_k are zeros (since $\Lambda \gg M$). Thus, as can be observed, Goupillaud-type structures are a particular case of our formalism, for which the gains $G_{\alpha_i} = 1$ and the unitary sample delays $m_i = 1\ \forall i$, thus leading to the trivial case $\Lambda = M$ (that is, a standard linear prediction form). Hence, the discrete-time transfer function $H^D(z)$ can be alternatively written as a classical delayed all-pole filter with sparse coefficients,

$$H^D(z) = \frac{b_0}{1 + \sum_{k=1}^{2\Lambda} a_k z^{-k}} z^{-\Lambda} \qquad \text{where} \quad ||a_k||_0 \ll 2\Lambda \tag{7.25}$$

where the sparsity is represented as a measure of the cardinality, that would be se so-called l_0-norm. The proposed sparse digital signal model offers several advantages in comparison with previously used physical or signal models. First, this generic model is valid for

an arbitrary number of absorbing layers of unequal-wave travel time, independent of the digital input signal characteristics (e.g. its central frequency and number of samples), and not restricted to any particular boundary conditions. In second place, the model parameters are obtained from a rigorous analysis of the physics involved in the wave-material interactions, and thus the sparsity arises naturally and does not rely on heuristic approaches, as in [7, 41]. Thirdly, this model can be represented as a sparse digital filter, which has thus obvious practical implications. Figure 7.3 summarizes the computational process used to take layered material properties and convert them to a functional digital filter.

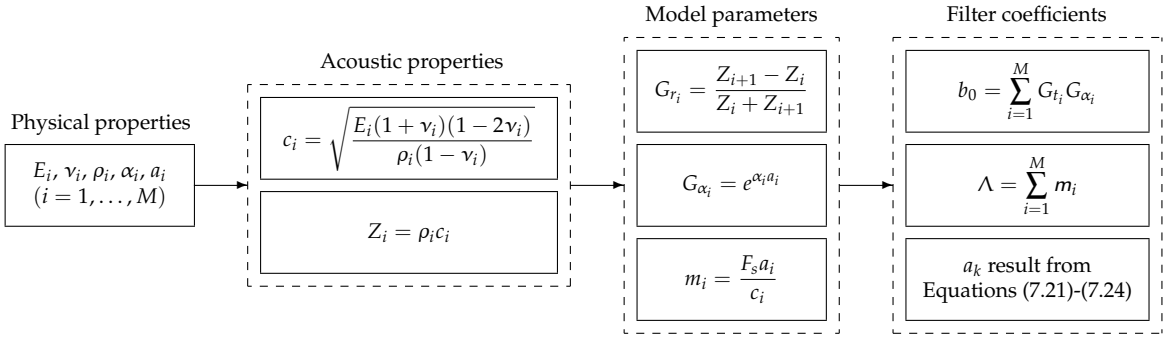

Figure 7.3: *Computational process to take layered material properties and convert them to a functional digital filter.*

It is worth to point out that the proposed recursive formalism to obtain $H^D(z)$ is straightforward and efficient, and also that the frequency response of the structure can easily be obtained by evaluating z in the unitary circle. As a drawback, it should be mentioned that, formally, digital filters require integer delays m_i. Nevertheless, there are well-known ways of overcoming this issue, as increasing the sampling frequency (i.e. using digital interpolation), or by applying fractional delay filter formalisms [229]. Additionally, since the whole formalism is expressed in terms of polynomials in z, one can easily obtain the difference equation, which allows, given a discrete-time input signal $x(n)$, to directly obtain the output signal $y(n)$ by filtering. The sparse structure of the filter, whose maximum number of coefficients is 2Λ but most of them are zeros, is particularly suitable for this task. The latter evidences the simplicity of this proposal, when comparing it to the numerical procedure implied in the TM formalism described in Figure 6.2. Furthermore, in our case, the resulting inverse filter $H^{D^{-1}}(z)$ is a FIR filter, which is inherently stable and can be computed straightforwardly. Thus, ultrasonic output signals obtained from specimens could easily be whitened by inverse filtering. While the inverse filtered response from the undamaged specimen should be similar to the original input signal applied, the opposite is expected for damaged specimens, due to the corresponding model mismatch, resulting in an effective damage detection procedure with a relatively low cost.

8 Nonlinear extensions

In this chapter, we propose two models that extend the ones developed in Chapters 6 and 7, in order to cope with the nonlinear constitutive behavior of multilayered structures. In a first approach, we take advantage of the simple matrix formulation provided by the TM formalism to derive an extended transfer matrix that accounts for constitutive nonlinearity. In a second proposal, we extend the two-port network used during the signal modeling approach to include an additional frequency response for layers with nonlinear constitutive behavior, and thus obtain zero-order and first-order contributions to a discrete-time transfer function for nonlinear multilayered materials.

8.1 Nonlinear extension of the Transfer Matrix formalism

In this section, the TM formalism is extended to the calculation of nonlinear ultrasonic waves up to the first-order nonlinearity (see Chapter 4). To this end, the problem of a linear longitudinal ultrasonic wave that propagates through a nonlinear multilayered elastic material is considered. Instead of directly solving the nonlinear problem, this formalism enables us to decompose the nonlinear problem into two linear subsets which can be solved separately. Concretely, those subsets provide both the zero-order and first-order contributions to the nonlinear wave displacement. In addition, one can prove that the zero-order contribution is equivalent to the solution delivered by the TM formalism (and thus that the latter is a special case of the nonlinear problem).

8.1.1 *Theoretical development*

A general harmonic solution to the one-dimensional nonlinear plane wave Equation (4.8) up to first-order nonlinearity ($\delta = 0$) can be stated in the frequency-domain as in [179][1],

$$\begin{aligned} u(x,\Omega) &= u^{(0),f}(x,\Omega) + u^{(1),f}(x,\Omega) + u^{(0),b}(x,\Omega) + u^{(1),b}(x,\Omega) \\ &= Ae^{-j\frac{\Omega}{c}x} + \frac{1}{2}\beta\left(\frac{\Omega}{c}\right)^2 xA^2e^{-2j\frac{\Omega}{c}x} + Be^{j\frac{\Omega}{c}x} + \frac{1}{2}\beta\left(\frac{\Omega}{c}\right)^2 xB^2e^{2j\frac{\Omega}{c}x} \end{aligned} \tag{8.1}$$

where $u^{(h),f}(x,\Omega)$ and $u^{(h),b}(x,\Omega)$ stand for the forward- and backward-propagating parts of the nonlinear displacement $u(x,\Omega)$, respectively. Note that those parts now consist of both the zero-order (Ω) and first-order (2Ω) perturbation solutions, denoted by the upper index $h \in \{0,1\}$, respectively[2]. Consequently, the fundamental waves (zero-order contribution to the nonlinear displacement) are now labeled with an upper index $h = 0$, whereas the second harmonics (first-order contribution to the nonlinear displacement) are labeled with an upper index $h = 1$.

The wave interactions within nonlinear multilayered materials can be approximated by a semi-analytical model based on an extension of the TM formalism [209], which from now on will be called the Nonlinear Transfer Matrix (NTM) formalism. The latter describes the wave propagation phenomena in finite nonlinear-elastic media, and is here strictly derived for the case of successive homogeneous layers. Note that only the nonlinear effects of second harmonics from fundamental waves in the media are considered (and thus, higher-order harmonics and/or the intrinsic nonlinearity of the interfaces are neglected). To this end, let us consider sharp discontinuities between M homogeneous nonlinear-elastic media with the same cross-sections, as depicted in Figure 8.1.

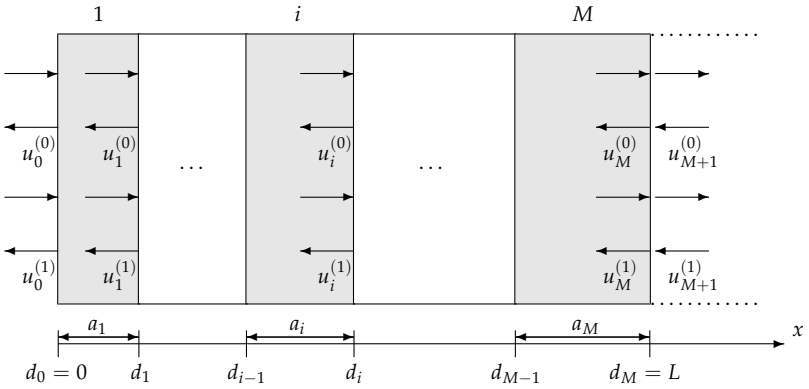

Figure 8.1: *Wave components in a nonlinear multilayered structure.*

[1] In that proposed form, the solution was developed for a nonlinear semi-infinite medium. We adapt it here to a bounded medium, in order to account for forward- and backward propagating components.

[2] Note that for the linear case, we disregarded the upper index (0) to lighten the notation. Now that we consider both fundamental and second harmonics, the upper index (0) is assigned to all variables related to the linear case.

Hence, the general harmonic solution stated in Equation (8.1) can be particularized for each layer i ($i = 1, \ldots, M$) as,

$$\begin{aligned} u_i(x,\Omega) &= A_i e^{-j\frac{\Omega}{c_i}x} + \left(\bar{A}_i + \frac{1}{2}\beta_i \left(\frac{\Omega}{c_i}\right)^2 x A_i^2\right) e^{-2j\frac{\Omega}{c_i}x} \\ &+ B_i e^{j\frac{\Omega}{c_i}x} + \left(\bar{B}_i + \frac{1}{2}\beta_i \left(\frac{\Omega}{c_i}\right)^2 x B_i^2\right) e^{2j\frac{\Omega}{c_i}x} \end{aligned} \tag{8.2}$$

Note that this solution is slightly different to that defined in Equation (8.1). As can be observed, the first-order perturbation solution is now formed of two parts: One, denoted by the quadratic amplitudes of A and B, is generated by the fundamental waves, whose amplitude accumulates with the propagation distance x. The other, denoted by the amplitudes $\bar{A}$ and $\bar{B}$, keeps constant amplitude during the propagation. The latter are introduced in the equation not to represent the intrinsic nonlinearity of the actual layer i, but instead, to be responsible for propagating the nonlinear components from previous layers to next layers[3].

In the case of a perfectly bounded interface, the transmission conditions imply the continuity of displacement $u^{(h)}(x,\Omega)$ and stress $\sigma^{(h)}(x,\Omega)$ across the interface between layers i and $i+1$, for both the zero-order and first-order contributions. Applying those conditions at an arbitrary interface $x = d_i$ ($i = 1, \ldots, M$) leads to,

$$\begin{aligned} u_i^{(h)}(d_i,\Omega) &= u_{i+1}^{(h)}(d_i,\Omega) \\ \sigma_i^{(h)}(d_i,\Omega) &= \sigma_{i+1}^{(h)}(d_i,\Omega) \end{aligned} \qquad (\forall h \in \{0,1\}) \tag{8.3}$$

Note that the zero-order perturbation solution was governed by the equations of the TM formalism. Here, we focus on the first-order perturbation solution to determine the contribution of the second harmonics to the nonlinear displacement. For this purpose, a hard transition from layer i to layer $i+1$ can be described by the first-order discontinuity matrix $\boldsymbol{\mathcal{D}}_{i,i+1}^{(1)}(\Omega)$,

$$\boldsymbol{\mathcal{U}}_{i+1}^{(1)}(d_i,\Omega) = \boldsymbol{\mathcal{D}}_{i,i+1}^{(1)}(\Omega)\boldsymbol{\mathcal{U}}_i^{(1)}(d_i,\Omega) \qquad (i = 1, \ldots, M) \tag{8.4}$$

where the displacement vector for nonlinear acoustic waves must now be extended to,

$$\boldsymbol{\mathcal{U}}_j^{(1)}(x,\Omega) = \left[\left(u_j^{(0),f}(x,\Omega)\right)^2 \;\; \left(u_j^{(0),b}(x,\Omega)\right)^2 \;\; \left(u_j^{(0),f}(x,\Omega)\cdot u_j^{(0),b}(x,\Omega)\right) \;\; \left(u_j^{(1),f}(x,\Omega)\right) \;\; \left(u_j^{(1),b}(x,\Omega)\right)\right]^T \tag{8.5}$$

[3]Let us consider for instance a nonlinear multilayered media which consist of alternating linear and nonlinear layers to underline this concept. If one would omit those parts, the nonlinear components would get stuck into the nonlinear layers and could not be detected at the material boundaries, since they would never propagate through the linear layers.

and the first-order discontinuity matrix $\boldsymbol{\mathcal{D}}_{i,i+1}^{(1)}(\Omega)$ can be expressed as,

$$\boldsymbol{\mathcal{D}}_{i,i+1}^{(1)}(\Omega) = \begin{pmatrix} \mathcal{D}_{i,11}^2 & \mathcal{D}_{i,12}^2 & 2\mathcal{D}_{i,11}\mathcal{D}_{i,12} & 0 & 0 \\ \mathcal{D}_{i,12}^2 & \mathcal{D}_{i,11}^2 & 2\mathcal{D}_{i,11}\mathcal{D}_{i,12} & 0 & 0 \\ \mathcal{D}_{i,11}\mathcal{D}_{i,12} & \mathcal{D}_{i,11}\mathcal{D}_{i,12} & \mathcal{D}_{i,11}^2 + \mathcal{D}_{i,12}^2 & 0 & 0 \\ \mathcal{D}_{i,41}(\Omega) & \mathcal{D}_{i,41}(\Omega) & -\mathcal{D}_{i,43}(\Omega) & \mathcal{D}_{i,11} & \mathcal{D}_{i,12} \\ -\mathcal{D}_{i,41}(\Omega) & -\mathcal{D}_{i,41}(\Omega) & \mathcal{D}_{i,43}(\Omega) & \mathcal{D}_{i,12} & \mathcal{D}_{i,11} \end{pmatrix} \tag{8.6}$$

where the $\mathcal{D}_{i,jk}$ and $\mathcal{D}_{i,jk}(\Omega)$ denote linear and nonlinear frequency-dependent elements of the first-order discontinuity matrix $\boldsymbol{\mathcal{D}}_{i,i+1}^{(1)}(\Omega)$ for a layer i, respectively. As demonstrated in Appendix C.1, linear elements $\mathcal{D}_{i,11}$ and $\mathcal{D}_{i,12}$ correspond to,

$$\mathcal{D}_{i,11} = \frac{1}{2}\left(1 + \frac{Z_i}{Z_{i+1}}\right) \quad , \quad \mathcal{D}_{i,12} = \frac{1}{2}\left(1 - \frac{Z_i}{Z_{i+1}}\right) \tag{8.7}$$

whereas nonlinear frequency-dependent elements $\mathcal{D}_{i,41}(\Omega)$ and $\mathcal{D}_{i,43}(\Omega)$ can be written down as,

$$\begin{aligned} \mathcal{D}_{i,41}(\Omega) &= -\frac{j}{4}\left(\beta_i \frac{\Omega}{c_i}\frac{Z_i}{Z_{i+1}} + \frac{1}{2}\beta_{i+1}\frac{\Omega}{c_{i+1}}\left(1 - 3\left(\frac{Z_i}{Z_{i+1}}\right)^2\right)\right) \\ \mathcal{D}_{i,43}(\Omega) &= -j\left(\beta_i \frac{\Omega}{c_i}\frac{Z_i}{Z_{i+1}} - \frac{1}{4}\beta_{i+1}\frac{\Omega}{c_{i+1}}\left(1 + 3\left(\frac{Z_i}{Z_{i+1}}\right)^2\right)\right) \end{aligned} \tag{8.8}$$

As can be observed, this matrix does not only depend on the acoustic impedances Z_j of the two layers being in contact (in contrast to the linear case), but also on the continuous-time frequency Ω and the first-order nonlinear elastic properties β_j of those layers. On the other hand, considering a harmonic wave propagating in the same nonlinear homogeneous layer i from position $x = d_{i-1}$ to position $x = d_i$, its transformed displacement at the respective locations can be expressed by the first-order propagation matrix $\boldsymbol{\mathcal{P}}_i^{(1)}(\Omega)$,

$$\boldsymbol{\mathcal{U}}_i^{(1)}(d_i, \Omega) = \boldsymbol{\mathcal{P}}_i^{(1)}(\Omega)\boldsymbol{\mathcal{U}}_i^{(1)}(d_{i-1}, \Omega) \qquad (i = 1, \ldots, M) \tag{8.9}$$

with

$$\boldsymbol{\mathcal{P}}_i^{(1)}(\Omega) = \begin{pmatrix} e^{-2j\frac{\Omega}{c_i}a_i} & 0 & 0 & 0 & 0 \\ 0 & e^{2j\frac{\Omega}{c_i}a_i} & 0 & 0 & 0 \\ 0 & 0 & 1 & 0 & 0 \\ \eta_i(\Omega)e^{-2j\frac{\Omega}{c_i}a_i} & 0 & 0 & e^{-2j\frac{\Omega}{c_i}a_i} & 0 \\ 0 & \eta_i(\Omega)e^{2j\frac{\Omega}{c_i}a_i} & 0 & 0 & e^{2j\frac{\Omega}{c_i}a_i} \end{pmatrix} \tag{8.10}$$

where $\eta_i(\Omega) = \frac{1}{2}\beta_i \left(\Omega/c_i\right)^2 a_i$ (see Appendix C.2)[4]. Thus, the relation between the input and output state vectors for a nonlinear layer i can be expressed by $\boldsymbol{\mathcal{U}}_{i+1}^{(1)}(d_i,\Omega) = \boldsymbol{\mathcal{T}}_i^{(1)}(\Omega)\boldsymbol{\mathcal{U}}_i^{(1)}(d_{i-1},\Omega)$, where a first-order transfer matrix $\boldsymbol{\mathcal{T}}_i^{(1)}(\Omega) = \boldsymbol{\mathcal{D}}_{i,i+1}^{(1)}(\Omega)\boldsymbol{\mathcal{P}}_i^{(1)}(\Omega)$ for a single layer is obtained by combining first-order discontinuity and propagation matrices ($i = 1,\ldots,M$),

$$\boldsymbol{\mathcal{T}}_i^{(1)}(\Omega) = \begin{pmatrix} \mathcal{D}_{i,11}^2 e^{-2j\frac{\Omega}{c_i}a_i} & \mathcal{D}_{i,12}^2 e^{2j\frac{\Omega}{c_i}a_i} & 2\mathcal{D}_{i,11}\mathcal{D}_{i,12} & 0 & 0 \\ \mathcal{D}_{i,12}^2 e^{-2j\frac{\Omega}{c_i}a_i} & \mathcal{D}_{i,11}^2 e^{2j\frac{\Omega}{c_i}a_i} & 2\mathcal{D}_{i,11}\mathcal{D}_{12} & 0 & 0 \\ \mathcal{D}_{i,11}\mathcal{D}_{i,12} e^{-2j\frac{\Omega}{c_i}a_i} & \mathcal{D}_{i,11}\mathcal{D}_{i,12} e^{2j\frac{\Omega}{c_i}a_i} & \mathcal{D}_{i,11}^2 + \mathcal{D}_{i,12}^2 & 0 & 0 \\ \left(\mathcal{D}_{i,41}(\Omega) + \eta_i(\Omega)\mathcal{D}_{i,11}\right) e^{-2j\frac{\Omega}{c_i}a_i} & \left(\mathcal{D}_{i,41}(\Omega) + \eta_i(\Omega)\mathcal{D}_{i,12}\right) e^{2j\frac{\Omega}{c_i}a_i} & -\mathcal{D}_{i,43}(\Omega) & \mathcal{D}_{i,11} e^{-2j\frac{\Omega}{c_i}a_i} & \mathcal{D}_{i,12} e^{2j\frac{\Omega}{c_i}a_i} \\ \left(-\mathcal{D}_{i,41}(\Omega) + \eta_i(\Omega)\mathcal{D}_{i,12}\right) e^{-2j\frac{\Omega}{c_i}a_i} & \left(-\mathcal{D}_{i,41}(\Omega) + \eta_i(\Omega)\mathcal{D}_{i,11}\right) e^{2j\frac{\Omega}{c_i}a_i} & \mathcal{D}_{i,43}(\Omega) & \mathcal{D}_{i,12} e^{-2j\frac{\Omega}{c_i}a_i} & \mathcal{D}_{i,11} e^{2j\frac{\Omega}{c_i}a_i} \end{pmatrix} \tag{8.11}$$

so that the complete first-order transfer matrix, describing the reflection and transmission processes of a nonlinear multilayered structure, is easily obtained as the product of matrices from successive layers $\boldsymbol{\mathcal{T}}^{(1)}(\Omega) = \prod_{i=0}^{M-1} \boldsymbol{\mathcal{T}}_{M-i}^{(1)}(\Omega)$, leading to a relation between the input and the output state vectors as,

$$\boldsymbol{\mathcal{U}}_{M+1}^{(1)}(L,\Omega) = \boldsymbol{\mathcal{T}}^{(1)}(\Omega)\boldsymbol{\mathcal{U}}_1^{(1)}(0,\Omega) \tag{8.12}$$

where $x = 0$ and $x = L$ correspond to the transmitter and receiver positions, respectively.

As in the linear case, the resulting system for a through-transmission configuration can be solved by specifying the boundary conditions. First, the incident wave is modeled by a purely linear forward prescribed displacement, whose associated boundary condition involves the continuity of displacement at the left boundary $x = 0$,

$$\begin{aligned} u_0^{(0),f}(0,\Omega) &= u_1^{(0),f}(0,\Omega) + u_1^{(0),b}(0,\Omega) \\ 0 &= u_1^{(1),f}(0,\Omega) + u_1^{(1),b}(0,\Omega) \end{aligned} \tag{8.13}$$

where $u_0^{(0),f}(0,\Omega)$ is the Fourier transform of the incident monochromatic wave. On the other hand, the first-order contribution to the nonlinear wave response is obtained by modeling the receiver as a semi-infinite layer, whose boundary condition is expressed by the radiation energy condition [210] as,

$$\begin{aligned} u_{M+1}^{(0),b}(L,\Omega) &= 0 \\ u_{M+1}^{(1),b}(L,\Omega) &= 0 \end{aligned} \tag{8.14}$$

[4]Note that the result provided by Yun *et al.* [209] in Equations (24)-(25) seems to be erroneous. It is indeed intuitively obvious that the nonlinear properties β_i will not explicitly appear in the lower-right terms of the first-order propagation matrix.

Inserting Equations (8.13) and (8.14) into Equation (8.12) leads to,

$$\begin{bmatrix} \left(u_{M+1}^{(0),f}(L,\Omega)\right)^2 \\ 0 \\ 0 \\ u_{M+1}^{(1),f}(L,\Omega) \\ 0 \end{bmatrix} = \boldsymbol{\mathcal{T}}^{(1)}(\Omega) \begin{bmatrix} \left(u_1^{(0),f}(0,\Omega)\right)^2 \\ \left(u_0^{(0),f}(0,\Omega) - u_1^{(0),f}(0,\Omega)\right)^2 \\ u_1^{(0),f}(0,\Omega) \cdot \left(u_0^{(0),f}(0,\Omega) - u_1^{(0),f}(0,\Omega)\right) \\ u_1^{(1),f}(0,\Omega) \\ -u_1^{(1),f}(0,\Omega) \end{bmatrix} \tag{8.15}$$

with,

$$\boldsymbol{\mathcal{T}}^{(1)}(\Omega) = \begin{pmatrix} \mathcal{T}_{11}^{(1)}(\Omega) & \mathcal{T}_{12}^{(1)}(\Omega) & \mathcal{T}_{13}^{(1)}(\Omega) & 0 & 0 \\ \mathcal{T}_{21}^{(1)}(\Omega) & \mathcal{T}_{22}^{(1)}(\Omega) & \mathcal{T}_{23}^{(1)}(\Omega) & 0 & 0 \\ \mathcal{T}_{31}^{(1)}(\Omega) & \mathcal{T}_{32}^{(1)}(\Omega) & \mathcal{T}_{33}^{(1)}(\Omega) & 0 & 0 \\ \mathcal{T}_{41}^{(1)}(\Omega) & \mathcal{T}_{42}^{(1)}(\Omega) & \mathcal{T}_{43}^{(1)}(\Omega) & \mathcal{T}_{44}^{(1)}(\Omega) & \mathcal{T}_{45}^{(1)}(\Omega) \\ \mathcal{T}_{51}^{(1)}(\Omega) & \mathcal{T}_{52}^{(1)}(\Omega) & \mathcal{T}_{53}^{(1)}(\Omega) & \mathcal{T}_{54}^{(1)}(\Omega) & \mathcal{T}_{55}^{(1)}(\Omega) \end{pmatrix} \tag{8.16}$$

where the $\mathcal{T}_{ij}^{(1)}(\Omega)$ denote the elements of the first-order transfer matrix $\boldsymbol{\mathcal{T}}^{(1)}(\Omega)$. A careful inspection of this matrix enables us to relate its 19 non-zero elements to only 5 independent elements, namely $\mathcal{T}_{11}^{(1)}(\Omega)$, $\mathcal{T}_{12}^{(1)}(\Omega)$, $\mathcal{T}_{41}^{(1)}(\Omega)$, $\mathcal{T}_{42}^{(1)}(\Omega)$, and $\mathcal{T}_{43}^{(1)}(\Omega)$. A thorough derivation of those identities is provided in Appendix C.3. As a result, the first-order transfer matrix $\boldsymbol{\mathcal{T}}^{(1)}(\Omega)$ can be rewritten as,

$$\boldsymbol{\mathcal{T}}^{(1)}(\Omega) = \begin{pmatrix} \mathcal{T}_{11}^{(1)}(\Omega) & \mathcal{T}_{12}^{(1)}(\Omega) & 2\sqrt{\mathcal{T}_{11}^{(1)}(\Omega)\mathcal{T}_{12}^{(1)}(\Omega)} & 0 & 0 \\ \mathcal{T}_{12}^{(1)}(-\Omega) & \mathcal{T}_{11}^{(1)}(-\Omega) & 2\sqrt{\mathcal{T}_{11}^{(1)}(-\Omega)\mathcal{T}_{12}^{(1)}(-\Omega)} & 0 & 0 \\ \sqrt{\mathcal{T}_{11}^{(1)}(\Omega)\mathcal{T}_{12}^{(1)}(-\Omega)} & \sqrt{\mathcal{T}_{11}^{(1)}(-\Omega)\mathcal{T}_{12}^{(1)}(\Omega)} & \sqrt{\mathcal{T}_{11}^{(1)}(\Omega)\mathcal{T}_{11}^{(1)}(-\Omega)} + \sqrt{\mathcal{T}_{12}^{(1)}(\Omega)\mathcal{T}_{12}^{(1)}(-\Omega)} & 0 & 0 \\ \mathcal{T}_{41}^{(1)}(\Omega) & \mathcal{T}_{42}^{(1)}(\Omega) & \mathcal{T}_{43}^{(1)}(\Omega) & \sqrt{\mathcal{T}_{11}^{(1)}(2\Omega)} & \sqrt{\mathcal{T}_{12}^{(1)}(2\Omega)} \\ \mathcal{T}_{42}^{(1)}(-\Omega) & \mathcal{T}_{41}^{(1)}(-\Omega) & \mathcal{T}_{43}^{(1)}(-\Omega) & \sqrt{\mathcal{T}_{12}^{(1)}(-2\Omega)} & \sqrt{\mathcal{T}_{11}^{(1)}(-2\Omega)} \end{pmatrix} \tag{8.17}$$

Hence, the first-order contribution to the nonlinear wave displacement at the receiver position L, in terms of that at the transmitter position, is found by solving Equation (8.15) as,

$$\begin{aligned} u_{M+1}^{(1),f}(L,\Omega) = & \left(\frac{\mathcal{T}_{11}^{(1)}(-\Omega)\left(\mathcal{T}_{41}^{(1)}(\Omega)\left(\sqrt{\mathcal{T}_{11}^{(1)}(-2\Omega)} - \sqrt{\mathcal{T}_{12}^{(1)}(-2\Omega)}\right) + \mathcal{T}_{42}^{(1)}(-\Omega)\left(\sqrt{\mathcal{T}_{11}^{(1)}(2\Omega)} - \sqrt{\mathcal{T}_{12}^{(1)}(2\Omega)}\right)\right)}{\left(\sqrt{\mathcal{T}_{11}^{(1)}(-\Omega)} - \sqrt{\mathcal{T}_{12}^{(1)}(-\Omega)}\right)^2 \left(\sqrt{\mathcal{T}_{11}^{(1)}(-2\Omega)} - \sqrt{\mathcal{T}_{12}^{(1)}(-2\Omega)}\right)} \right. \\ & + \frac{\mathcal{T}_{12}^{(1)}(-\Omega)\left(\mathcal{T}_{42}^{(1)}(\Omega)\left(\sqrt{\mathcal{T}_{11}^{(1)}(-2\Omega)} - \sqrt{\mathcal{T}_{12}^{(1)}(-2\Omega)}\right) + \mathcal{T}_{41}^{(1)}(-\Omega)\left(\sqrt{\mathcal{T}_{11}^{(1)}(2\Omega)} - \sqrt{\mathcal{T}_{12}^{(1)}(2\Omega)}\right)\right)}{\left(\sqrt{\mathcal{T}_{11}^{(1)}(-\Omega)} - \sqrt{\mathcal{T}_{12}^{(1)}(-\Omega)}\right)^2 \left(\sqrt{\mathcal{T}_{11}^{(1)}(-2\Omega)} - \sqrt{\mathcal{T}_{12}^{(1)}(-2\Omega)}\right)} \\ & \left. - \frac{\sqrt{\mathcal{T}_{11}^{(1)}(-\Omega)\mathcal{T}_{12}^{(1)}(-\Omega)}\left(\mathcal{T}_{43}^{(1)}(\Omega)\left(\sqrt{\mathcal{T}_{11}^{(1)}(-2\Omega)} - \sqrt{\mathcal{T}_{12}^{(1)}(-2\Omega)}\right) + \mathcal{T}_{43}^{(1)}(-\Omega)\left(\sqrt{\mathcal{T}_{11}^{(1)}(2\Omega)} - \sqrt{\mathcal{T}_{12}^{(1)}(2\Omega)}\right)\right)}{\left(\sqrt{\mathcal{T}_{11}^{(1)}(-\Omega)} - \sqrt{\mathcal{T}_{12}^{(1)}(-\Omega)}\right)^2 \left(\sqrt{\mathcal{T}_{11}^{(1)}(-2\Omega)} - \sqrt{\mathcal{T}_{12}^{(1)}(-2\Omega)}\right)} \right) \left(u_0^{(0),f}(0,\Omega)\right)^2 \\ = & \mathcal{H}^{(1)}(\Omega)\left(u_0^{(0),f}(0,\Omega)\right)^2 \end{aligned} \tag{8.18}$$

where, in the end, $\mathcal{H}^{(1)}(\Omega)$ is simply a complex scalar number, which depends both on the frequency and twice the frequency of the incident wave. As expected, this first-order contribution depends upon the square of the linear displacement at the transmitter position. Finally, the nonlinear wave displacement can be obtained as the sum of the zero-order contribution plus the first-order contribution,

$$\begin{aligned} u^f_{M+1}(L,\Omega) &= u^{(0),f}_{M+1}(L,\Omega) + u^{(1),f}_{M+1}(L,\Omega) \\ &= \mathcal{H}^{(0)}(\Omega) u^{(0),f}_0(0,\Omega) + \mathcal{H}^{(1)}(\Omega)\left(u^{(0),f}_0(0,\Omega)\right)^2 \end{aligned} \tag{8.19}$$

where $\mathcal{H}^{(0)}(\Omega)$ is the complex scalar number obtained in Equation (6.14) using the TM formalism. Although the NTM formalism relies on physical principles described by a nonlinear partial differential equation, one of its strength is that it provides a solution by solving only linear equations. As can observed, the nonlinear problem has been solved by calculating the first-order contribution to the nonlinear wave displacement and adding it to the zero-order contribution found with the TM formalism (see Equation (8.19)). In addition, it is noteworthy that this formalism could be extended in the same fashion to account for the contributions of third and higher-order harmonics, and/or to second-order nonlinearity ($\delta \neq 0$). However, in those cases, the dimension of the complete higher-order transfer matrix would significantly increase due to the frequency-mixing effects involved in the higher-order harmonics generation (e.g. when fundamental (Ω) and second-order harmonics (2Ω) mixed up, they generate both fundamental $(2\Omega - \Omega)$ and third-order $(\Omega + 2\Omega)$ harmonics).

As for the linear case, the NTM formalism could also be extended to account for material attenuation. Since the mathematics involved in this task is nearly identical to that of the linear case, we do not report it here. Again, this theoretical result is valid for any single continuous-time frequency Ω and any number of layers M. Practical issues are discussed in next section.

8.1.2 Numerical implementation of the NTM formalism

Equation (8.19) suggests that one has to solve both the TM and NTM formalisms to obtain the nonlinear wave displacement. However, one could intuitively expect that the linear TM formalism is a special case of NTM one, and that the first-order transfer matrix $\boldsymbol{\mathcal{T}}^{(1)}(\Omega)$ somehow encompasses the zero-order one $\boldsymbol{\mathcal{T}}^{(0)}(\Omega)$. Indeed, by setting the nonlinear parameters to zero ($\beta_i = 0$, $\forall i$), we can obtain a simplified version of the first-order transfer matrix $\boldsymbol{\mathcal{T}}^{(1)}(\Omega)$ as,

$$\boldsymbol{\mathcal{T}}^{(1)}_{\beta\to 0}(\Omega) = \begin{pmatrix} \mathcal{T}^{(1)}_{11}(\Omega) & \mathcal{T}^{(1)}_{12}(\Omega) & 2\sqrt{\mathcal{T}^{(1)}_{11}(\Omega)\mathcal{T}^{(1)}_{12}(\Omega)} \\ \mathcal{T}^{(1)}_{12}(-\Omega) & \mathcal{T}^{(1)}_{11}(-\Omega) & 2\sqrt{\mathcal{T}^{(1)}_{11}(-\Omega)\mathcal{T}^{(1)}_{12}(-\Omega)} \\ \sqrt{\mathcal{T}^{(1)}_{11}(\Omega)\mathcal{T}^{(1)}_{12}(-\Omega)} & \sqrt{\mathcal{T}^{(1)}_{11}(-\Omega)\mathcal{T}^{(1)}_{12}(\Omega)} & \sqrt{\mathcal{T}^{(1)}_{11}(\Omega)\mathcal{T}^{(1)}_{11}(-\Omega)} + \sqrt{\mathcal{T}^{(1)}_{12}(\Omega)\mathcal{T}^{(1)}_{12}(-\Omega)} \end{pmatrix} \tag{8.20}$$

Solving the two first rows of the simplified underlying system leads to,

$$\left(u_{M+1}^{(0),f}(L,\Omega)\right)^2 = \left(\frac{\det\left(\sqrt{\boldsymbol{\mathcal{T}}_{2\times2}^{(1)}(\Omega)}\right)}{\sqrt{\mathcal{T}_{11}^{(1)}(-\Omega)}-\sqrt{\mathcal{T}_{12}^{(1)}(-\Omega)}}\right)^2 \left(u_0^{(0),f}(0,\Omega)\right)^2 = \left(\mathcal{H}^{(0)}(\Omega)\right)^2\left(u_0^{(0),f}(0,\Omega)\right)^2 \tag{8.21}$$

where $\boldsymbol{\mathcal{T}}_{2\times2}^{(1)}(\Omega)$ denotes the 2×2 sub-matrix encompassed by $\boldsymbol{\mathcal{T}}_{\beta\to0}^{(1)}(\Omega)$ or $\boldsymbol{\mathcal{T}}^{(1)}(\Omega)$. As can be observed, this equation delivers the square of the zero-order contribution to the nonlinear wave displacement at the receiver position L, in terms of that at the transmitter position. In other words, this equation represents a quadratic form of the solution obtained with the TM formalism in Equation (6.14), when considering the following identities (details can be found in Appendix C.4):

$$\sqrt{\mathcal{T}_{11}^{(1)}(\Omega)} = \mathcal{T}_{11}^{(0)}(\Omega) = \mathcal{T}_{22}^{(0)}(-\Omega) \quad , \quad \sqrt{\mathcal{T}_{12}^{(1)}(\Omega)} = \mathcal{T}_{12}^{(0)}(\Omega) = \mathcal{T}_{21}^{(0)}(-\Omega) \tag{8.22}$$

Consequently, one could obtain both the zero-order and first-order contributions to the nonlinear wave displacement from Equation (8.15). Therefore, in practice, the solution to the NTM formalism expressed in Equation (8.19) can be solved straightforwardly without implementing previously the TM formalism. In addition, the latter can be simultaneously recovered by setting the nonlinear parameters to zero. Despite the fact that the TM formalism is a special case of the NTM one is somehow trivial, it is nevertheless interesting to mention how the first-order transfer matrix encompass the zero-order one,

$$\boldsymbol{\mathcal{T}}^{(1)}(\Omega) = \begin{pmatrix} \left\{\boldsymbol{\mathcal{T}}^{(0)}(\Omega)\right\}^2 & \mathbf{0} \\ \boldsymbol{\mathcal{T}}_{NL}^{(1)}(\Omega) & \boldsymbol{\mathcal{T}}^{(0)}(2\Omega) \end{pmatrix} \tag{8.23}$$

where $\left\{\boldsymbol{\mathcal{T}}^{(0)}(\Omega)\right\}^2$ and $\boldsymbol{\mathcal{T}}_{NL}^{(1)}(\Omega)$ denote the quadratic form of the zero-order transfer matrix $\boldsymbol{\mathcal{T}}^{(0)}(\Omega)$ and the sub-matrix of $\boldsymbol{\mathcal{T}}^{(1)}(\Omega)$ that explicitly contains the nonlinear terms, respectively. Although this representation has no practical implication (since we showed that it is not necessary to first solve the linear problem), it may have conceptual implication at the time of understanding how transfer matrices of higher-orders will grow up. Hence, it is to expect that a second-order transfer matrix will contain (1) a cubic form of the zero-order transfer matrix, (2) a mixed matrix made of a quadratic form of the zero-order transfer matrix combined with the nonlinear terms of first-order β, (3) a zero-order transfer matrix evaluated at thrice the frequency, and finally (4) a matrix that explicitly contains the nonlinear terms of second-order β^2 (and eventually δ if one considers nonlinearity of second-order).

As discussed in Section 6.3, in practice, the input signal is usually a purely linear band-pass ultrasonic signal at a relatively low center frequency containing a wide range of frequencies around it, and is commonly represented as a digital time-domain signal. Thus, the incident wave $u_0^{(0)}(0, nT)$ at the transmitter position $x = 0$ can be represented as a discrete-time signal with N samples ($n = 0, \ldots, N-1$). By applying the DFT, a discrete frequency representation with components $u_0^{(0)}(0, \omega_k)$ ($k = 0, \ldots, N-1$) can be obtained. The NTM formalism can then be applied to each frequency bin, in order to obtain the zero-order and first-order contributions for the receiver side components, denoted by $u_{M+1}^{(0)}(L, \omega_k)$ and $u_{M+1}^{(1)}(L, \omega_k)$, respectively. Finally, by applying the IDFT to both contributions, one can recover the zero-order $u_{M+1}^{(0)}(L, nT)$ and first-order contributions $u_{M+1}^{(1)}(L, nT)$ to the nonlinear wave response $u_{M+1}(L, nT)$ at the receiver position $x = L$. The general scheme of this numerical procedure for M layers is depicted in Figure 8.2.

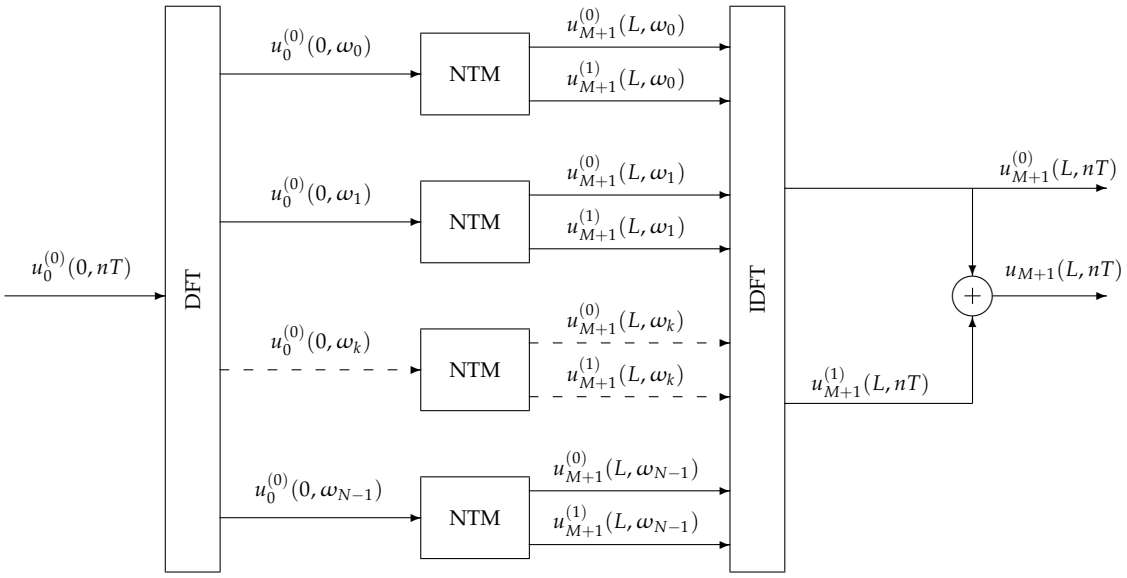

Figure 8.2: *General scheme of the NTM formalism numerical procedure.*

Under this approach, some considerations must be made regarding the Shannon-Nyquist theorem while dealing with nonlinear systems, since a sampling frequency of $F_s/2$ is no more valid. As can be observed in the proposed framework, second harmonics appear at the frequency 2Ω and thus require the consideration of a sampling frequency of at least $F_s = 4F_{max}$ (that is, the input signal must now be a band-limited signal oversampled with a sampling rate of 2)[5].

According to this scheme, the first-order transfer matrix for a single layer (see Equation (8.11)) can be discretized as well as,

$$\boldsymbol{T}_i^{(1)}(\omega_k) \quad = \quad \boldsymbol{\mathcal{T}}_i^{(1)}(\Omega)|_{\Omega=\omega_k F_s} \tag{8.24}$$

[5]In practice, the sampling frequency is usually selected as $F_s \gg 4F_{max}$, so that, even in the nonlinear regime, the proposed framework will not fail.

leading to the following discrete solution,

$$u^{f}_{M+1}(L,\omega_k) \;=\; H^{(0)}(\omega_k)u_0^{(0),f}(0,\omega_k) + H^{(1)}(\omega_k)\left[u_0^{(0),f}(0,\omega_k)\right]^2 \tag{8.25}$$

where $H^{(0)}(\omega_k)$ and $H^{(1)}(\omega_k)$ implicitly contain the zero-order and first-order contributions to the complete first-order transfer matrix $\boldsymbol{T}^{(1)}(\omega_k)$ corresponding to the k^{th}-frequency component. It is worth to point out that each $\boldsymbol{T}_i^{(1)}(\omega_k)$ ($i = 0,\ldots,M-1$, $k = 0,\ldots,N-1$) is a 5×5 matrix of complex numbers, allowing a numerical solution for Equation (8.25). The computational cost of that solution is significantly higher than for the linear case, due to the larger dimension of $\boldsymbol{T}_i^{(1)}(\omega_k)$ and particularly due to the k^{th}-frequency component dependency of the first-order discontinuity matrix $\boldsymbol{D}_{i,i+1}^{(1)}(\omega_k)$. Even though, the NTM formalism allows to handle nonlinear problems in a relatively straightforward and efficient way, especially since only five elements ($\mathcal{T}_{11}^{(1)}(\omega_k)$, $\mathcal{T}_{12}^{(1)}(\omega_k)$, $\mathcal{T}_{41}^{(1)}(\omega_k)$, $\mathcal{T}_{42}^{(1)}(\omega_k)$, and $\mathcal{T}_{43}^{(1)}(\omega_k)$) of the 5×5 complete first-order transfer matrix are really needed to be computed.

8.2 Nonlinear signal modeling approach

In this section, we propose to extend the signal modeling approach described in Chapter 7 to account for constitutive nonlinearity. To this end, the problem of a linear longitudinal ultrasonic wave that propagates through a nonlinear multilayered elastic material is considered. Representing a nonlinear system in terms of signal modeling concepts is generally cumbersome as most of them have been developed for linear systems. Thus, instead of directly solving the nonlinear problem, we propose to compute the first-order contribution to the nonlinear wave displacement separately. Doing so, the through-transmission configuration for the isolated first-order component can be considered as well as a discrete-time linear system. Consequently, the nonlinear multilayered material under investigation can be represented by a pair of transfer functions, which relate the discrete input and output signals, and account for both the zero-order and first-order contributions to the nonlinear wave displacement. As for the NTM formalism, be aware that, under this approach, the input signal must now be a band-limited signal up to $F_s/4$ instead of $F_s/2$ (that is, the input signal must be oversampled with a sampling rate of 2).

8.2.1 Theoretical foundations

Let us consider the four-port network depicted in Figure 8.3. In this figure, the frequency responses $H_i^{(0)}(\omega)$ and $H_i^{(1)}(\omega)$ stand for the intra-layer i propagation of fundamental waves and second harmonics, respectively[6]. Note that $\omega \in [0, 2\pi]$ is the normalized frequency defined in the previous section. The gains $\{G_{t_i}, G_{r_i}, \hat{G}_{t_i}, \hat{G}_{r_i}\}$ characterize the impedance ratios between layers i and $i+1$, according to those defined for the linear case. Additionally, we introduce a further frequency response $H_i^{NL}(\omega)$, which characterizes the contribution of the

[6] As done above for the NTM formalism, the upper index (0) is now assigned to all variables related to the linear signal model, due to the presence of both fundamental waves and second harmonics. For sake of clarity, let us rename those frequency responses as the zero-order and first-order frequency responses.

linear wave component to the second harmonics when accumulating over the propagation path of a layer i. From now on, this frequency response will be called the nonlinear frequency response of a layer i. The negative signs at the nodes stand for the π-phase shifts ($e^{j\pi}$) that suffer the back-propagating components at the layer discontinuities. Be aware that the symbol $*$ denotes a convolution of time-domain signals, which is equivalent to a spectral multiplication. Also note that $X_i^{f,0}(\omega)$ and $X_i^{b,0}(\omega)$ are always $F_s/4$ band-limited signals, that is, $X_i^{j,0}(\omega) = 0$ for $\pi/2 < |\omega| < 3\pi/2, \forall j = f, b$.

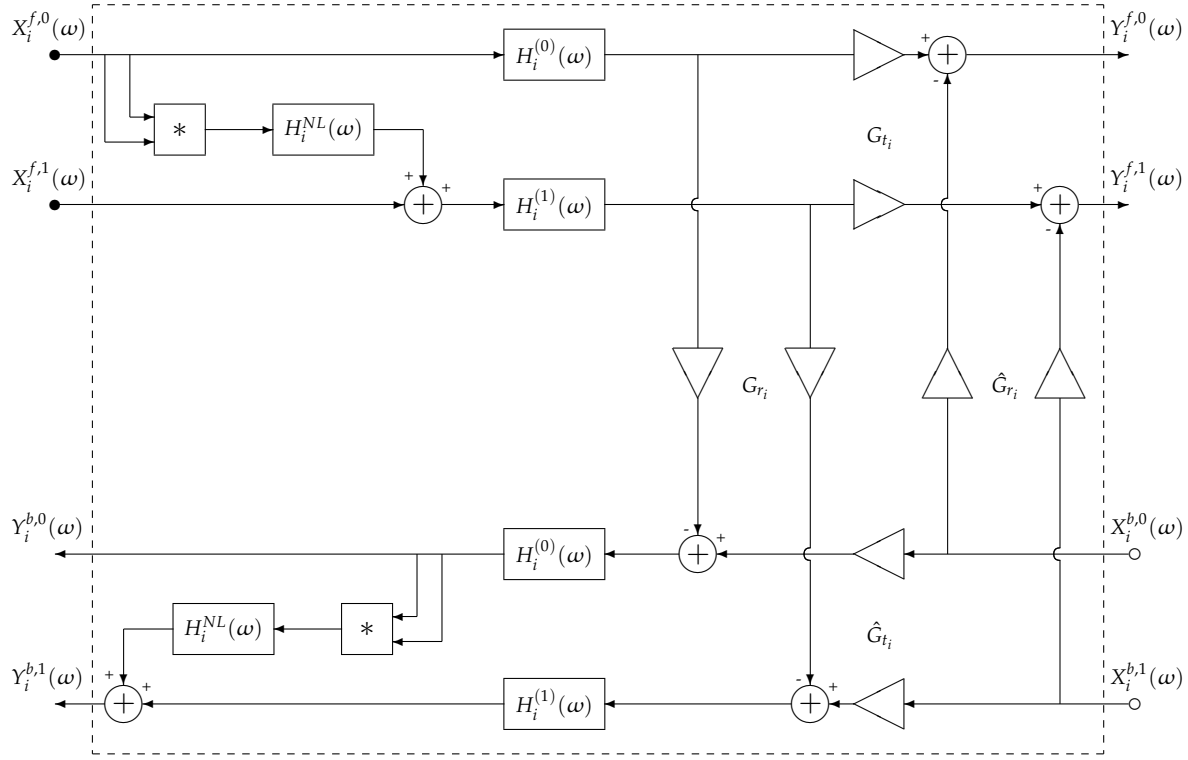

Figure 8.3: *Four-port network for a nonlinear layer unit i.*

According to Figure 8.3, outputs $Y_i^{f,0}(\omega)$, $Y_i^{b,0}(\omega)$, $Y_i^{f,1}(\omega)$, and $Y_i^{b,1}(\omega)$ are obtained from inputs $X_i^{f,0}(\omega)$, $X_i^{b,0}(\omega)$, $X_i^{f,1}(\omega)$, and $X_i^{b,1}(\omega)$ as,

$$\begin{aligned}
Y_i^{f,0}(\omega) &= X_i^{f,0}(\omega)H_i^{(0)}(\omega)G_{t_i} - X_i^{b,0}(\omega)\hat{G}_{r_i} \\
Y_i^{b,0}(\omega) &= X_i^{b,0}(\omega)\hat{G}_{t_i}H_i^{(0)}(\omega) - X_i^{f,0}(\omega)H_i^{(0)}(\omega)G_{r_i}H_i^{(0)}(\omega) \\
Y_i^{f,1}(\omega) &= \left[X_i^{f,1}(\omega) + H_i^{NL}(\omega)\left(X_i^{f,0}(\omega)\right)^2\right]H_i^{(1)}(\omega)G_{t_i} - X_i^{b,1}(\omega)\hat{G}_{r_i} \\
Y_i^{b,1}(\omega) &= X_i^{b,1}(\omega)H_i^{(1)}(\omega)\hat{G}_{t_i} - \left[X_i^{f,1}(\omega) + H_i^{NL}(\omega)\left(X_i^{f,0}(\omega)\right)^2\right]H_i^{(1)}(\omega)G_{r_i}H_i^{(1)}(\omega) \\
&- \left(Y_i^{b,0}(\omega)\right)^2 H_i^{NL}(\omega)
\end{aligned} \tag{8.26}$$

Working through these analytical expressions allows us to write the system in matrix form, with $\boldsymbol{u}_i^{(1)}(\omega) = \left[\left(X_i^{f,0}(\omega)\right)^2 \;\; \left(Y_i^{b,0}(\omega)\right)^2 \;\; X_i^{f,0}(\omega)\cdot Y_i^{b,0}(\omega) \;\; X_i^{f,1}(\omega) \;\; Y_i^{b,1}(\omega)\right]^T$ and

$$\boldsymbol{U}_{i+1}^{(1)}(\omega) = \left[\left(X_{i+1}^{f,0}(\omega) \right)^2 \quad \left(Y_{i+1}^{b,0}(\omega) \right)^2 \quad X_{i+1}^{f,0}(\omega) \cdot Y_{i+1}^{b,0}(\omega) \quad X_{i+1}^{f,1}(\omega) \quad Y_{i+1}^{b,1}(\omega) \right]^T,$$

$$\boldsymbol{U}_{i+1}^{(1)}(\omega) = \begin{pmatrix} \left[\left(G_{t_i} - \frac{G_{r_i}\hat{G}_{r_i}}{\hat{G}_{t_i}} \right) H_i^{(0)}(\omega) \right]^2 & \left[-\frac{\hat{G}_{r_i}}{\hat{G}_{t_i}} \frac{1}{H_i^{(0)}(\omega)} \right]^2 & -2\left(G_{t_i} - \frac{G_{r_i}\hat{G}_{r_i}}{\hat{G}_{t_i}} \right) \frac{\hat{G}_{r_i}}{\hat{G}_{t_i}} & 0 & 0 \\ \left[\frac{G_{r_i}}{\hat{G}_{t_i}} H_i^{(0)}(\omega) \right]^2 & \left[\frac{1}{\hat{G}_{t_i}} \frac{1}{H_i^{(0)}(\omega)} \right]^2 & 2\frac{G_{r_i}}{\hat{G}_{t_i}^2} & 0 & 0 \\ \left(G_{t_i} - \frac{G_{r_i}\hat{G}_{r_i}}{\hat{G}_{t_i}} \right) \frac{G_{r_i}}{\hat{G}_{t_i}} \left(H_i^{(0)}(\omega) \right)^2 & -\frac{\hat{G}_{r_i}}{\hat{G}_{t_i}^2} \frac{1}{\left(H_i^{(0)}(\omega) \right)^2} & \frac{1}{\hat{G}_{t_i}} \left(G_{t_i} - 2\frac{G_{r_i}\hat{G}_{r_i}}{\hat{G}_{t_i}} \right) & 0 & 0 \\ H_i^{NL}(\omega) \left(G_{t_i} - \frac{G_{r_i}\hat{G}_{r_i}}{\hat{G}_{t_i}} \right) H_i^{(1)}(\omega) & -H_i^{NL}(\omega) \frac{\hat{G}_{r_i}}{\hat{G}_{t_i}} \frac{1}{H_i^{(1)}(\omega)} & 0 & \left(G_{t_i} - \frac{G_{r_i}\hat{G}_{r_i}}{\hat{G}_{t_i}} \right) H_i^{(1)}(\omega) & -\frac{\hat{G}_{r_i}}{\hat{G}_{t_i}} \frac{1}{H_i^{(1)}(\omega)} \\ H_i^{NL}(\omega) \frac{G_{r_i}}{\hat{G}_{t_i}} H_i^{(1)}(\omega) & H_i^{NL}(\omega) \frac{1}{\hat{G}_{t_i}} \frac{1}{H_i^{(1)}(\omega)} & 0 & \frac{G_{r_i}}{\hat{G}_{t_i}} H_i^{(1)}(\omega) & \frac{1}{\hat{G}_{t_i}} \frac{1}{H_i^{(1)}(\omega)} \end{pmatrix} \boldsymbol{U}_i^{(1)}(\omega) \tag{8.27}$$

where the output vector of layer i corresponds to the input vector of layer $i+1$, i.e. $\boldsymbol{U}_{i+1}^{(1)}(\omega) = \left[\left(Y_i^{f,0}(\omega) \right)^2 \quad \left(X_i^{b,0}(\omega) \right)^2 \quad Y_i^{f,0}(\omega) \cdot X_i^{b,0}(\omega) \quad Y_i^{f,1}(\omega) \quad X_i^{b,1}(\omega) \right]^T$. The four-port network of layer i may be written as $\boldsymbol{U}_{i+1}^{(1)}(\omega) = \boldsymbol{T}_i^{(1)}(\omega)\boldsymbol{U}_i^{(1)}(\omega)$, and thus the total frequency response of the nonlinear material is obtained as $\boldsymbol{T}^{(1)}(\omega) = \prod_{i=0}^{M-1} \boldsymbol{T}_{M-i}^{(1)}(\omega)$. Consequently, the relation between the input and output state vectors of the complete nonlinear multilayered system $\boldsymbol{U}_{M+1}^{(1)}(\omega) = \boldsymbol{T}^{(1)}(\omega)\boldsymbol{U}_1^{(1)}(\omega)$ can be written as,

$$\begin{bmatrix} \left(X_{M+1}^{f,0}(\omega) \right)^2 \\ \left(Y_{M+1}^{b,0}(\omega) \right)^2 \\ X_{M+1}^{f,0}(\omega) \cdot Y_{M+1}^{b,0}(\omega) \\ X_{M+1}^{f,1}(\omega) \\ Y_{M+1}^{b,0}(\omega) \end{bmatrix} = \begin{pmatrix} T_{11}^{(1)}(\omega) & T_{12}^{(1)}(\omega) & T_{13}^{(1)}(\omega) & 0 & 0 \\ T_{21}^{(1)}(\omega) & T_{22}^{(1)}(\omega) & T_{23}^{(1)}(\omega) & 0 & 0 \\ T_{31}^{(1)}(\omega) & T_{32}^{(1)}(\omega) & T_{33}^{(1)}(\omega) & 0 & 0 \\ T_{41}^{(1)}(\omega) & T_{42}^{(1)}(\omega) & T_{43}^{(1)}(\omega) & T_{44}^{(1)}(\omega) & T_{45}^{(1)}(\omega) \\ T_{51}^{(1)}(\omega) & T_{52}^{(1)}(\omega) & T_{53}^{(1)}(\omega) & T_{54}^{(1)}(\omega) & T_{55}^{(1)}(\omega) \end{pmatrix} \begin{bmatrix} \left(X_1^{f,0}(\omega) \right)^2 \\ \left(Y_1^{b,0}(\omega) \right)^2 \\ X_1^{f,0}(\omega) \cdot Y_1^{b,0}(\omega) \\ X_1^{f,1}(\omega) \\ Y_1^{b,0}(\omega) \end{bmatrix} \tag{8.28}$$

where the $T_{ij}^{(1)}(\omega)$ are the matrix elements of the total frequency response of first-order $\boldsymbol{T}^{(1)}(\omega)$. The boundary conditions for that through-transmission configuration (Equations (8.13)-(8.14)) can be represented as well in terms of signal theory concepts, as depicted in Figure 8.4.

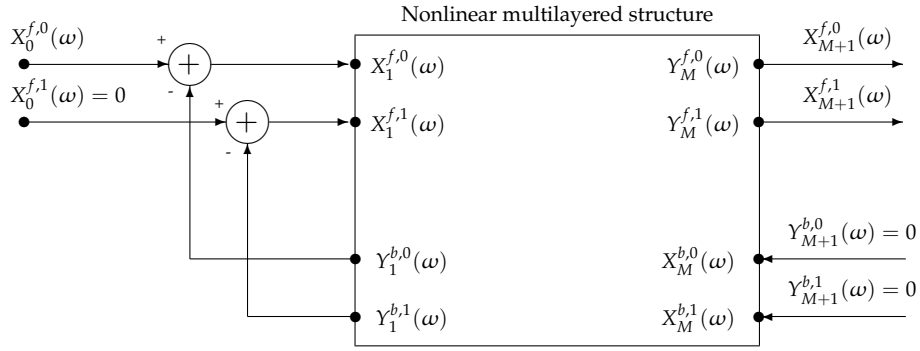

Figure 8.4: *Nonlinear multilayered structure and boundary conditions in terms of signal modeling principles.*

From this figure, the boundary conditions are set in the four-port connections as,

$$\begin{array}{rcl} X_1^{f,0}(\omega) & = & X_0^{f,0}(\omega) - Y_1^{b,0}(\omega) \\ X_1^{f,1}(\omega) & = & -Y_1^{b,1}(\omega) \\ Y_{M+1}^{b,0}(\omega) & = & 0 \\ Y_{M+1}^{b,1}(\omega) & = & 0 \end{array} \tag{8.29}$$

Inserting Equations (8.29) into Equation (8.28) leads to,

$$\begin{bmatrix} \left(X_{M+1}^{f,0}(\omega)\right)^2 \\ 0 \\ 0 \\ X_{M+1}^{f,1}(\omega) \\ 0 \end{bmatrix} = \boldsymbol{T}^{(1)}(\omega) \begin{bmatrix} \left(X_1^{f,0}(\omega)\right)^2 \\ \left(X_0^{f,0}(\omega) - X_1^{f,0}(\omega)\right)^2 \\ X_1^{f,0}(\omega) \cdot \left(X_0^{f,0}(\omega) - X_1^{f,0}(\omega)\right) \\ X_1^{f,1}(\omega) \\ -X_1^{f,1}(\omega) \end{bmatrix} \tag{8.30}$$

It is worth to point out the similarity of this equation with Equation (8.15). This point will be further discussed in the next section.

8.2.2 Bridging the nonlinear signal modeling and the physics

In section 7.2, we already examined the ties between the signal model parameters (gains and frequency responses) and the mechanical features (impedance ratios and material damping). Here, we can also link the nonlinear signal model parameters (nonlinear and first-order frequency responses) to the nonlinear mechanical features (constitutive nonlinearity of the material). For this purpose, let us first replace the gains and zero-order frequency responses from Equations (7.9), (7.10), and (7.14) into Equation (8.27). Hence,

$$\boldsymbol{T}_i^{(1)}(\omega) = \begin{pmatrix} D_{i,11}^2 G_{\alpha_i}^2 e^{-2j\omega m_i} & D_{i,12}^2 G_{\alpha_i}^{-2} e^{2j\omega m_i} & 2D_{i,11}D_{i,12} & 0 & 0 \\ D_{i,12}^2 G_{\alpha_i}^2 e^{-2j\omega m_i} & D_{i,11}^2 G_{\alpha_i}^{-2} e^{2j\omega m_i} & 2D_{i,11}D_{i,12} & 0 & 0 \\ D_{i,11}D_{i,12} G_{\alpha_i}^2 e^{-2j\omega m_i} & D_{i,11}D_{i,12} G_{\alpha_i}^{-2} e^{2j\omega m_i} & D_{i,11}^2 + D_{i,12}^2 & 0 & 0 \\ D_{i,11} H_i^{NL}(\omega) H_i^{(1)}(\omega) & D_{i,12} H_i^{NL}(\omega) \dfrac{1}{H_i^{(1)}(\omega)} & 0 & D_{i,11} H_i^{(1)}(\omega) & D_{i,12} \dfrac{1}{H_i^{(1)}(\omega)} \\ D_{i,12} H_i^{NL}(\omega) H_i^{(1)}(\omega) & D_{i,11} H_i^{NL}(\omega) \dfrac{1}{H_i^{(1)}(\omega)} & 0 & D_{i,12} H_i^{(1)}(\omega) & D_{i,11} \dfrac{1}{H_i^{(1)}(\omega)} \end{pmatrix} \tag{8.31}$$

with

$$D_{i,11} = \frac{1}{2}\left(1 + \frac{Z_i}{Z_{i+1}}\right) \quad , \quad D_{i,12} = \frac{1}{2}\left(1 - \frac{Z_i}{Z_{i+1}}\right) \tag{8.32}$$

Again, this matrix shows a high similarity with that of Equation (8.11). Let us now assume that the first-order frequency response $H_i^{(1)}(\omega)$ of Figure 8.3 has the form,

$$H_i^{(1)}(\omega) = \left(H_i^{(0)}(\omega)\right)^2 = G_{\alpha_i}^2 e^{-2j\omega m_i} = G_{\alpha_i} H_i^{(0)}(2\omega) \tag{8.33}$$

From this equation, it results that the output of a signal passing through $H_i^{(1)}(\omega)$ is equivalent to that of a signal passing twice through $H_i^{(0)}(\omega)$. In other words, the second harmonics attenuate and suffer a delay that is twice that of the fundamental waves. Alternatively, we can view $H_i^{(1)}(\omega)$ as a spectral expansion of $H_i^{(0)}(\omega)$ (in the same way as in a digital sampling frequency interpolation) by a factor of 2, which once again supports the fact that $X_i^{j,0}(\omega)$ must be band-limited to $F_s/4$, $\forall j = f, b$. By sampling this frequency response, we obtain:

$$H_i^{(1)}(\omega) \;=\; e^{2\alpha_i a_i} e^{-2j\omega \frac{F_s a_i}{c_i}} \;=\; e^{-2j\frac{\Omega}{c_i^*} a_i}\Big|_{\Omega=\omega F_s} \tag{8.34}$$

On the other hand, let us consider that a sampled version of the nonlinear frequency response $H_i^{NL}(\omega)$ of Figure 8.3 may have the form,

$$H_i^{NL}(\omega) \;=\; \frac{1}{2}\beta_i \left(\frac{F_s \omega}{c_i}\right)^2 a_i \;=\; \eta_i(\Omega)\big|_{\Omega=\omega F_s} \tag{8.35}$$

that is, the nonlinear filter response $H_i^{NL}(\omega)$ has a quadratic response, which accounts for the nonlinear accumulation over a distance a_i corresponding to the thickness of a layer i, and corresponds to a discrete-time version of the nonlinear term in Equation (8.10). As expected, this response cannot be represented by means of a LTI filter. Nevertheless, one could intent to approximate it by using such a filter for the frequency region of interest. Inserting Equations (8.34)-(8.35) into Equation (8.31) leads to,

$$\boldsymbol{T}_i^{(1)}(\omega) \;=\; \begin{pmatrix} D_{i,11}^2 e^{-2j\omega\frac{F_s a_i}{c_i^*}} & D_{i,12}^2 e^{2j\omega\frac{F_s a_i}{c_i^*}} & 2D_{i,11}D_{i,12} & 0 & 0 \\ D_{i,12}^2 e^{-2j\omega\frac{F_s a_i}{c_i^*}} & D_{i,11}^2 e^{2j\omega\frac{F_s a_i}{c_i^*}} & 2D_{i,11}D_{12} & 0 & 0 \\ D_{i,11}D_{i,12} e^{-2j\omega\frac{F_s a_i}{c_i^*}} & D_{i,11}D_{i,12} e^{2j\omega\frac{F_s a_i}{c_i^*}} & D_{i,11}^2 + D_{i,12}^2 & 0 & 0 \\ \eta_i(\omega F_s) D_{i,11} e^{-2j\omega\frac{F_s a_i}{c_i^*}} & \eta_i(\omega F_s) D_{i,12} e^{2j\omega\frac{F_s a_i}{c_i^*}} & 0 & D_{i,11} e^{-2j\omega\frac{F_s a_i}{c_i^*}} & D_{i,12} e^{2j\omega\frac{F_s a_i}{c_i^*}} \\ \eta_i(\omega F_s) D_{i,12} e^{-2j\omega\frac{F_s a_i}{c_i^*}} & \eta_i(\omega F_s) D_{i,11} e^{2j\omega\frac{F_s a_i}{c_i^*}} & 0 & D_{i,12} e^{-2j\omega\frac{F_s a_i}{c_i^*}} & D_{i,11} e^{2j\omega\frac{F_s a_i}{c_i^*}} \end{pmatrix} \tag{8.36}$$

and, as can be observed, Equation (8.24) (i.e. a discrete version of Equation (8.11)) is approximately recovered. However, a few elements of the discrete transfer matrix of first-order $\boldsymbol{T}_i^{(1)}(\omega_k)$ for a nonlinear layer i, namely $\mathcal{D}_{i,41}(\omega_k)$ and $\mathcal{D}_{i,43}(\omega_k)$, do not explicitly arise in the nonlinear signal modeling approach. This issue, along with the solution to Equation (8.30), are discussed in next section.

8.2.3 Discussion

Let us first explain why some elements present in the NTM formalism are difficult to integrate in the nonlinear signal model. A careful inspection of Equations (C.1)-(C.4) shows that the nonlinear frequency-dependent elements $\mathcal{D}_{i,41}(\Omega)$ and $\mathcal{D}_{i,43}(\Omega)$ of the first-order discontinuity matrix naturally arise from the transmission conditions at a nonlinear interface, and more concretely from the formulation of the stress continuity. Indeed, the latter

depends upon the derivative of the displacement for the first-order perturbation solution and the square of the derivative for the zero-order solution. Both of them contribute to elements involving the square of the linear displacement, and thus to $\mathcal{D}_{i,41}(\Omega)$. In addition, the square of the derivative for the zero-order solution contributes to elements involving cross-terms, and thus to $\mathcal{D}_{i,43}(\Omega)$. Unfortunately, such concepts as derivatives of propagating distance-dependent amplitudes are hardly expressible in terms of a network-like model[7].

Nevertheless, we could argue that those nonlinear terms arising from the first-order discontinuity matrix might be negligible in comparison to the ones arising from the first-order propagation matrix (which are both phenomenologically and from a signal perspective well-defined), and could thus further solve the nonlinear contribution to this system. To this end, making use of the physical interpretations done in the previous section enables us to rewrite the total frequency response of first-order $\boldsymbol{T}^{(1)}(\omega)$ as,

$$\boldsymbol{T}^{(1)}(\omega) = \begin{pmatrix} T_{11}^{(1)}(\omega) & T_{12}^{(1)}(\omega) & 2\sqrt{T_{11}^{(1)}(\omega)T_{12}^{(1)}(\omega)} & 0 & 0 \\ T_{12}^{(1)}(-\omega) & T_{11}^{(1)}(-\omega) & 2\sqrt{T_{11}^{(1)}(-\omega)T_{11}^{(1)}(-\omega)} & 0 & 0 \\ \sqrt{T_{11}^{(1)}(\omega)T_{12}^{(1)}(-\omega)} & \sqrt{T_{11}^{(1)}(-\omega)T_{12}^{(1)}(\omega)} & \sqrt{T_{11}^{(1)}(\omega)T_{11}^{(1)}(-\omega)} + \sqrt{T_{12}^{(1)}(\omega)T_{12}^{(1)}(-\omega)} & 0 & 0 \\ T_{41}^{(1)}(\omega) & T_{42}^{(1)}(\omega) & T_{43}^{(1)}(\omega) & \sqrt{T_{11}^{(1)}(2\omega)} & \sqrt{T_{12}^{(1)}(2\omega)} \\ T_{42}^{(1)}(-\omega) & T_{41}^{(1)}(-\omega) & T_{43}^{(1)}(-\omega) & \sqrt{T_{12}^{(1)}(-2\omega)} & \sqrt{T_{11}^{(1)}(-2\omega)} \end{pmatrix} \tag{8.37}$$

Again, this matrix shows a high similarity with that of Equation (8.17). Details on the relations between the elements of that matrix can be found in Appendix D. Thus, the first-order contribution to the nonlinear system can be found by solving Equation (8.30) as,

$$\begin{aligned} X_{M+1}^{(1),f}(\omega) &= \left(\frac{T_{11}^{(1)}(-\omega)\left(T_{41}^{(1)}(\omega)\left(\sqrt{T_{11}^{(1)}(-2\omega)} - \sqrt{T_{12}^{(1)}(-2\omega)}\right) + T_{42}^{(1)}(-\omega)\left(\sqrt{T_{11}^{(1)}(2\omega)} - \sqrt{T_{12}^{(1)}(2\omega)}\right)\right)}{\left(\sqrt{T_{11}^{(1)}(-\omega)} - \sqrt{T_{12}^{(1)}(-\omega)}\right)^2 \left(\sqrt{T_{11}^{(1)}(-2\omega)} - \sqrt{T_{12}^{(1)}(-2\omega)}\right)} \right. \\ &+ \frac{T_{12}^{(1)}(-\omega)\left(T_{42}^{(1)}(\omega)\left(\sqrt{T_{11}^{(1)}(-2\omega)} - \sqrt{T_{12}^{(1)}(-2\omega)}\right) + T_{41}^{(1)}(-\omega)\left(\sqrt{T_{11}^{(1)}(2\omega)} - \sqrt{T_{12}^{(1)}(2\omega)}\right)\right)}{\left(\sqrt{T_{11}^{(1)}(-\omega)} - \sqrt{T_{12}^{(1)}(-\omega)}\right)^2 \left(\sqrt{T_{11}^{(1)}(-2\omega)} - \sqrt{T_{12}^{(1)}(-2\omega)}\right)} \\ &- \left. \frac{\sqrt{T_{11}^{(1)}(-\omega)T_{12}^{(1)}(-\omega)}\left(T_{43}^{(1)}(\omega)\left(\sqrt{T_{11}^{(1)}(-2\omega)} - \sqrt{T_{12}^{(1)}(-2\omega)}\right) + T_{43}^{(1)}(-\omega)\left(\sqrt{T_{11}^{(1)}(2\omega)} - \sqrt{T_{12}^{(1)}(2\omega)}\right)\right)}{\left(\sqrt{T_{11}^{(1)}(-\omega)} - \sqrt{T_{12}^{(1)}(-\omega)}\right)^2 \left(\sqrt{T_{11}^{(1)}(-2\omega)} - \sqrt{T_{12}^{(1)}(-2\omega)}\right)} \right) \left(X_0^{(0),f}(\omega)\right)^2 \\ &= H^{(1)}(\omega)\left(X_0^{(0),f}(\omega)\right)^2 \end{aligned} \tag{8.38}$$

As for the zero-order contribution, the obtained theoretical result is unfortunately not straightforwardly implementable, since the derivation of the total frequency response of first-order $\boldsymbol{T}^{(1)}(\omega) = \prod_{i=0}^{M-1} \boldsymbol{T}_{M-i}^{(1)}(\omega)$ is cumbersome.

To get around it, we could, on the one hand, apply the formulation proposed in Equation (7.17). However, it is far from obvious that a product of matrices with the form of the

[7]Let us consider for instance a simple function $f(x) = A(x)e^{-jx}$ to highlight this fact. By deriving this function with respect to x, on could obtain $f'(x) = -jA(x)e^{-jx} + A'(x)e^{-jx} = -jf(x) + A'(x)e^{-jx}$. In analogy to our case, we see that the derivative can be expressed by means of the function itself multiplied by some constant plus an additional term. The first term can easily be represented in a circuit model, whereas the second one is relatively complex to predict, foremost depending on the form that takes $A(x)$.

frequency response of first-order $\boldsymbol{T}_i^{(1)}(\omega)$ could be expressed as a sum of matrices that retains the same form, especially due to the asymmetry of the exponential elements, which prohibits the use of the distributive property (in any case, such an approach would suffer of a drastic lake of efficiency, worse than the NTM formalism). On the other hand, we can take advantage of the digital modeling of the specimen proposed in Section 7.3 to address the solution to the first-order contribution. Indeed, part of the elements of the total frequency response of first-order $\boldsymbol{T}^{(1)}(\omega)$ can be expressed in terms of the z-domain polynomial expressions $P_M(G_\alpha, z)$ and $Q_M(G_\alpha, z)$ obtained in Equation (7.21). Nonetheless, we encounter a further problem in our intent to express the nonlinear frequency response $H_i^{NL}(\omega)$ as a discrete-time transfer function in the z-domain. Thus, we provide here a possible *procedure to follow*, rather than a straightforward and rigorous solution. This solution is subjected to find a discrete-time transfer function $H_i^{NL}(z)$ in the z-domain, whose frequency response approximates sufficiently well that proposed in Equation (8.35) for the frequency range of interest. Indeed, a frequency response with a quadratic response could be approximated (e.g by a Taylor series expansion), but it is not clear how to determine the type and order of the approximation. Substituting Equations (7.9)-(7.10), $H_i^{(0),D}(z)$, $H_i^{(1),D}(z)$ and $H_i^{NL}(z)$ in the first-order layer matrix of Equation (8.27) yields a z-transformed layer matrix of first-order $\boldsymbol{T}_i^{(1)}(z)$ which can be rewritten in terms of z-domain polynomial expressions as,

$$\boldsymbol{T}_i^{(1)}(z) = \left(\frac{G_{\alpha_i} z^{-m_i}}{1+G_{r_i}}\right)^2 \begin{pmatrix} 1 & G_{r_i}^2 G_{\alpha_i}^{-4} z^{4m_i} & 2G_{r_i} G_{\alpha_i}^{-2} z^{2m_i} & 0 & 0 \\ G_{r_i}^2 & G_{\alpha_i}^{-4} z^{4m_i} & 2G_{r_i} G_{\alpha_i}^{-2} z^{2m_i} & 0 & 0 \\ G_{r_i} & G_{r_i} G_{\alpha_i}^{-4} z^{4m_i} & \left(1+G_{r_i}^2\right) G_{\alpha_i}^{-2} z^{2m_i} & 0 & 0 \\ (1+G_{r_i})\, H_i^{NL}(z) & G_{r_i}(1+G_{r_i})\, H_i^{NL}(z) G_{\alpha_i}^{-4} z^{4m_i} & 0 & 1+G_{r_i} & G_{r_i}(1+G_{r_i})\, G_{\alpha_i}^{-4} z^{4m_i} \\ G_{r_i}(1+G_{r_i})\, H_i^{NL}(z) & (1+G_{r_i})\, H_i^{NL}(z) G_{\alpha_i}^{-4} z^{4m_i} & 0 & G_{r_i}(1+G_{r_i}) & (1+G_{r_i})\, G_{\alpha_i}^{-4} z^{4m_i} \end{pmatrix} \tag{8.39}$$

It can be proven that the product of M-layers, $\boldsymbol{T}^{(1)}(z) = \prod_{i=0}^{M-1} \boldsymbol{T}_{M-i}^{(1)}(z)$, has the following general form,

$$\boldsymbol{T}^{(1)}(z) = \left(\prod_{i=1}^{M} \frac{G_{\alpha_i} z^{-m_i}}{1+G_{r_i}}\right)^2 \begin{pmatrix} P_M^2(G_\alpha, z) & \left(\prod_{i=1}^{M} G_{\alpha_i}^{-4} z^{4m_i}\right) Q_M^2(G_\alpha^{-1}, z^{-1}) & 2\left(\prod_{i=1}^{M} G_{\alpha_i}^{-2} z^{2m_i}\right) P_M(G_\alpha, z) Q_M(G_\alpha^{-1}, z^{-1}) & 0 & 0 \\ Q_M^2(G_\alpha, z) & \left(\prod_{i=1}^{M} G_{\alpha_i}^{-4} z^{4m_i}\right) P_M^2(G_\alpha^{-1}, z^{-1}) & 2\left(\prod_{i=1}^{M} G_{\alpha_i}^{-2} z^{2m_i}\right) P_M(G_\alpha^{-1}, z^{-1}) Q_M(G_\alpha, z) & 0 & 0 \\ P_M(G_\alpha, z) Q_M(G_\alpha, z) & \left(\prod_{i=1}^{M} G_{\alpha_i}^{-4} z^{4m_i}\right) P_M(G_\alpha^{-1}, z^{-1}) Q_M(G_\alpha^{-1}, z^{-1}) & \left(\prod_{i=1}^{M} G_{\alpha_i}^{-2} z^{2m_i}\right) \left(P_M(G_\alpha, z) P_M(G_\alpha^{-1}, z^{-1}) + Q_M(G_\alpha, z) Q_M(G_\alpha^{-1}, z^{-1})\right) & 0 & 0 \\ R_M(G_\alpha, z) & \left(\prod_{i=1}^{M} G_{\alpha_i}^{-4} z^{4m_i}\right) S_M(G_\alpha^{-1}, z^{-1}) & 2\left(\prod_{i=1}^{M} G_{\alpha_i}^{-2} z^{2m_i}\right) V_M(G_\alpha, z) & \left(\prod_{i=1}^{M} (1+G_{r_i})\right) P_M(G_\alpha^2, z^2) & \left(\prod_{i=1}^{M} (1+G_{r_i}) G_{\alpha_i}^{-4} z^{4m_i}\right) Q_M(G_\alpha^{-2}, z^{-2}) \\ S_M(G_\alpha, z) & \left(\prod_{i=1}^{M} G_{\alpha_i}^{-4} z^{4m_i}\right) R_M(G_\alpha^{-1}, z^{-1}) & 2\left(\prod_{i=1}^{M} G_{\alpha_i}^{-2} z^{2m_i}\right) V_M(G_\alpha^{-1}, z^{-1}) & \left(\prod_{i=1}^{M} (1+G_{r_i})\right) Q_M(G_\alpha^2, z^2) & \left(\prod_{i=1}^{M} (1+G_{r_i}) G_{\alpha_i}^{-4} z^{4m_i}\right) P_M(G_\alpha^{-2}, z^{-2}) \end{pmatrix} \tag{8.40}$$

where the functions $R_M(G_\alpha, z)$, $S_M(G_\alpha, z)$ and $V_M(G_\alpha, z)$ stand for polynomials which are built up following a recursive scheme,

$$\begin{aligned}
R_M(G_\alpha, z) &= (1+G_{r_M})H_M^{NL}(z)\left(P_{M-1}^2(G_\alpha, z) + G_{r_M}G_{\alpha_M}^{-4}z^{4m_M}Q_{M-1}^2(G_\alpha, z)\right) \\
&+ (1+G_{r_M})\left(R_{M-1}(G_\alpha, z) + G_{r_M}G_{\alpha_M}^{-4}z^{4m_M}S_{M-1}(G_\alpha, z)\right) \\
S_M(G_\alpha, z) &= (1+G_{r_M})H_M^{NL}(z)\left(G_{r_M}P_{M-1}^2(G_\alpha, z) + G_{\alpha_M}^{-4}z^{4m_M}Q_{M-1}^2(G_\alpha, z)\right) \\
&+ (1+G_{r_M})\left(G_{r_M}R_{M-1}(G_\alpha, z) + G_{\alpha_M}^{-4}z^{4m_M}S_{M-1}(G_\alpha, z)\right) \\
V_M(G_\alpha, z) &= 2(1+G_{r_M})H_M^{NL}(z)\left(G_{\alpha_M}^2 z^{-2m_M}P_{M-1}(G_\alpha, z)Q_{M-1}(G_\alpha^{-1}, z^{-1})\right. \\
&+ \left. G_{r_M}G_{\alpha_M}^{-2}z^{2m_M}P_{M-1}(G_\alpha^{-1}, z^{-1})Q_{M-1}(G_\alpha, z)\right)
\end{aligned} \tag{8.41}$$

with $R_1(G_\alpha, z) = (1+G_{r_1})H_1^{NL}(z)$, $S_1(G_\alpha, z) = G_{r_1}(1+G_{r_1})H_1^{NL}(z)$ and $V_1(G_\alpha, z) = 0$. Note that these polynomials incorporate all the nonlinear effects of the multilayered structure. Once the boundary conditions are considered (Equation (8.29)), the first-order contribution to the nonlinear displacement leads to,

$$\begin{aligned}
X_{M+1}^{f_r,(1)}(z) &= \frac{1}{D^{(1)}(z)}\left(\prod_{i=1}^{M}\frac{G_{\alpha_i}^2 z^{-2m_i}}{1+G_{r_i}}\right)\left(\left(\left(\prod_{i=1}^{M}G_{\alpha_i}^{-4}z^{4m_i}\right)P_M(G_\alpha^{-2}, z^{-2}) - Q_M(G_\alpha^2, z^2)\right)\right. \\
&\cdot \left(R_M(G_\alpha, z)P_M^2(G_\alpha^{-1}, z^{-1}) + S_M(G_\alpha^{-1}, z^{-1})Q_M^2(G_\alpha, z) - 2V_M(G_\alpha, z)P_M(G_\alpha, z)Q_M(G_\alpha^{-1}, z^{-1})\right) \\
&+ \left(P_M(G_\alpha^2, z^2) - \left(\prod_{i=1}^{M}G_{\alpha_i}^{-4}z^{4m_i}\right)Q_M(G_\alpha^{-2}, z^{-2})\right) \\
&\cdot \left.\left(S_M(G_\alpha, z)P_M^2(G_\alpha^{-1}, z^{-1}) + R_M(G_\alpha^{-1}, z^{-1})Q_M^2(G_\alpha, z) - 2V_M(G_\alpha^{-1}, z^{-1})P_M(G_\alpha, z)Q_M(G_\alpha^{-1}, z^{-1})\right)\right)\left(X_0^{f_r,(0)}(z)\right)^2
\end{aligned} \tag{8.42}$$

where the denominator of first-order $D^{(1)}(z)$ can be written as,

$$D^{(1)}(z) = \left(P_M(G_\alpha^{-1}, z^{-1}) - \left(\prod_{i=1}^{M}G_{\alpha_i}^2 z^{-2m_i}\right)Q_M(G_\alpha, z)\right)^2\left(P_M(G_\alpha^{-2}, z^{-2}) - \left(\prod_{i=1}^{M}G_{\alpha_i}^2 z^{-2m_i}\right)Q_M(G_\alpha^2, z^2)\right) \tag{8.43}$$

Note that the form that takes Equation (8.42) complicates drastically a possible simplification. Nonetheless, the underlying structure of the polynomial expressions suggests that the discrete-time transfer function of first-order $H^{(1)}(z)$ could be alternatively written as,

$$H^{(1)}(z) = \frac{\prod_{i=1}^{M}G_{t_i}H_i^{NL}(z)G_{\alpha_i}^2 z^{-2m_i}\Delta_M(G_\alpha, z)}{\left(P_M(G_\alpha^{-1}, z^{-1}) - \left(\prod_{i=1}^{M}G_{\alpha_i}^2 z^{-2m_i}\right)Q_M(G_\alpha, z)\right)^2\left(P_M(G_\alpha^{-2}, z^{-2}) - \left(\prod_{i=1}^{M}G_{\alpha_i}^2 z^{-2m_i}\right)Q_M(G_\alpha^2, z^2)\right)} \tag{8.44}$$

where $\Delta_M(G_\alpha, z)$ is a polynomial which accounts for the complex interactions between $P_M(G_\alpha, z)$, $Q_M(G_\alpha, z)$, $R_M(G_\alpha, z)$, $S_M(G_\alpha, z)$, and $V_M(G_\alpha, z)$. In that case, $H^{(1)}(z)$ seems to be a delayed pole-zero filter with sparse coefficients. As intuitively expected, the numerator now consists of a delay and attenuation that are twice that of the linear case, and the first-order denominator incorporates a quadratic form of the zero-order one. Finally, it is worth to point out that the nonlinear terms ($H_i^{NL}(z)$ and $\Delta_M(G_\alpha, z)$) only arise in the numerator.

If one could compute such a filter, the nonlinear wave displacement could be written as the sum of the zero-order and first-order contributions,

$$X_{M+1}^{f,(1)}(z) \quad = \quad H^{(0)}(z)X_0^{f,(0)}(z) + H^{(1)}(z)\left(X_0^{f,(0)}(z)\right)^2 \tag{8.45}$$

In addition, such a filter would preserve all the advantages of the zero-order one discussed in Section 7.4. As for the NTM formalism, be aware that the zero-order contribution $H^{(0)}(z)$ could be directly obtained by solving the two first rows of the underlying system to Equation (8.40), without previously solving the linear digital signal model described in Equation (7.25).

Although the nonlinear signal model, in its proposed form, lacks of practical applicability, future research in that vein should be conducted, especially on the feasibility of expressing the nonlinear frequency response as a discrete-time transfer function, along with the possibility of representing some missing physical components into the network diagram. Finding a discrete-time transfer function $H^{NL}(z)$ that approximates the nonlinear frequency response $H^{NL}(\omega)$ for the frequency range of interest in a suitable way is particularly challenging, since the resulting filter of first-order $H^{(1)}(z)$ might have a huge number of coefficients.

Part III

METHODOLOGY

9 Materials and methods

This chapter describes the materials and methods used over the course of this dissertation. In Section 9.1, we introduce the context and motivation of the employed materials, describing their potential and the challenge that they offer from a structural viewpoint, and focusing on the requirement of efficient ultrasonic NDE techniques to identify their damage mechanisms. Section 9.2 presents the specimens tested and the experimental configuration used to analyze them. Finally, Section 9.3 provides the theoretical background for the inverse problem and system identification approaches used for characterizing the pathologies of the introduced specimens.

9.1 Context and motivation

The aim of this section is twofold: First, we describe the potential of the chosen *multilayered*[1] materials, focusing on the challenge that they offer from both a structural and socio-economical point of view. Secondly, we emphasize the structural complexity of those materials, and thus the need of reliable ultrasonic NDE techniques to (i) characterize their mechanical properties, and (ii) monitor their structural health for damage assessment or quality control purposes.

9.1.1 Carbon fiber-reinforced polymers

Fiber-reinforced polymers (FRP), such as carbon and and glass fiber-reinforced polymers (CFRP and GFRP) and the promising self-reinforced polymers (e.g. isotactic polypropylene),

[1]Note that the chosen materials are not necessarily layered by nature. Under layered materials, we understand that the presence of the material in the experimental environment (e.g. water, embedded system) will produce bounded interfaces, so that the overall system could be considered as layered.

are high performance and competitive advanced materials with a growing applicability due to their extreme strength-to-weight and rigidity-to-weight efficiency ratios. Continued improvements in the development of cost-effective manufacturing methods and development of low-cost fibers and resin materials have increased the use of composites for aerospace and automotive products. More recently, those materials originally developed for aeronautical purposes, have presented themselves as a feasible alternative to design civil engineer structures (e.g. buildings and bridges) [230, 231, 232], for which lightweight, high strength, and construction time exigences are converted into critical design aspects (see Figure 9.1). Nonetheless, the ever expanding structural applications of composites expose them to various environmental and loading conditions, causing higher probability of induced (micro-) damage in the material. Depending upon the material and laminate stacking sequence, the induced damage generally consists of a complex and interacting global ensemble of discrete damage modes, which may finally lead to failure [233].

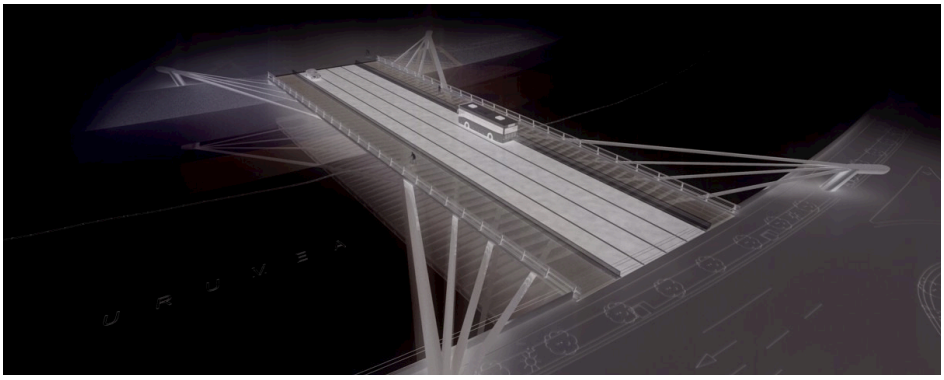

Figure 9.1: *Example of a novel infrastructural application involving an all-composite bridge made of carbon and glass fiber-reinforced polymers.*[2]

Hence, despite their outstanding characteristics, the application of FRP has been limited by the problem of damage tolerance [234]. Indeed, one of the major drawbacks associated with composite materials is their vulnerability to impact damage (e.g. hail, bird strike, tool drop, or runway stones during taxiing), which usually occurs in the phase of manufacturing, service or maintenance. Composite laminates do not allow significant energy dissipation by plastic deformation, and this leads to weaker through-the-thickness than in-plane mechanical properties for the structure [235]. As a consequence, during an impact the fibers absorb part of the energy and distribute some of the load through the laminate thickness, leading to a quite complex three-dimensional damage pattern consisting of delamination, sub-surface matrix cracking, fiber-matrix debonding and fiber fracture [236]. During the structure's life cycle, the occurrence of two kinds of impact loading has to be regarded: Low and high-velocity impacts. The latter are easy to detect, since high-speed impactors interact with the material for a short time period, and thus lead to evident external and visible damage. In

[2]Courtesy from colleagues of the Nondestructive Evaluation Laboratory, which were awarded with the Silver Medal at the 1^{st} Structural Engineering Design International Contest for their *all-composite* bridge proposal (2008).

contrast, the former can cause significant internal degradation that remains invisible from the front surface, with inner damage spreading over a wider area than that starting from the contact point of the impactor. Generally[3], three phases of impact damages can be roughly identified: Initially, matrix cracks are generated by shear or tensile stresses mainly in the intermediate or back-wall layers. Then, delaminations grow from the crack tips between layers of different orientation (the higher the orientation mismatch, the larger the delaminations). They typically appear in regular patterns producing altogether a three-dimensional spiral staircase. Finally, as the impact energy further increases, fiber breakage initially appear on the surface of the sample and may propagate into intermediate layers, leading in some cases to total perforation of the laminate [237] (see Figure 9.2). All these complex failure mechanisms can in turn induce severe degradation to the residual macro-scale mechanical properties of the material, while remaining invisible from the surface [238].

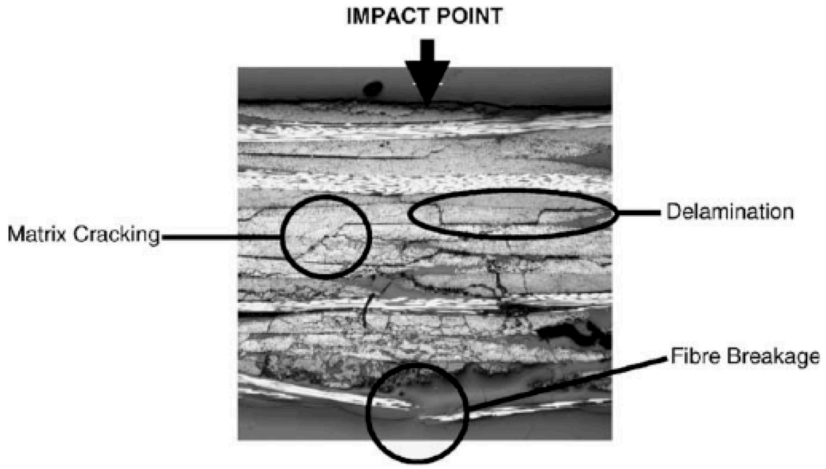

Figure 9.2: *Impact damage mechanisms (identified in micrographs*[4]).

Due to their excellent properties for light-weight structures, FRP's are employed in many types of industry (e.g. aircraft, wind turbine, rotor-machinery, automobile) which, however, implies cyclic loading in operation. Cyclic mechanical loading usually induces many matrix cracks, fibre-matrix debonding, delamination, and fibre fracture, accompanied by stiffness degradation of the composite before ultimate failure [240]. Investigations on CFRP under fatigue loads have shown an occurrence of several consecutive damage mechanisms, and strong correlations have been found between stiffness reduction and development of defects, thus allowing grouping of different damage mechanisms into three characteristic phases during fatigue life. Under dynamic tension, phase I is characterized by the appearance of matrix cracks and fibre-matrix interfacial cracking forms parallel to the fibre orientation mainly in the off-axis layers which encounter the highest stress non-parallel to the reinforcement direction. These intralaminar cracks through the whole thickness of the

[3]That is, for cross-ply and quasi-isotropic laminates, since this family of stacking sequence is the most used in the industry (the damage propagation pattern could be slightly different for angle-ply and asymmetric laminates.)

[4]Reproduced from Mitrevski *et al.* [239].

layers reduce the stiffness of the affected plies. After saturation of these transverse cracks, phase II is marked by the formation of longitudinal cracks in the vicinity of the areas where transverse cracks predominate. As a consequence, delimitation formation can be observed at the intersections of transverse and longitudinal cracks. Phase III initiates the final damage mode, longitudinal splitting, where entire parts of the 0°-plies are detached from the remaining laminate due to longitudinal cracks and delamination growth. In addition, both transverse and longitudinal cracks lead to fibre fracture due to stress concentrations at the crack tips or induced shear stress due to kinking at crack bridging zones, leading to a steep decline in stiffness until final failure [241, 242]. Compressive fatigue loading involves a slightly different damage formation (e.g. initial stiffness loss is smaller) which cannot be classified in these three phases. Due to the combination of damage mechanisms induced by tension and compression, reversed loads result in faster material degradation and earlier ultimate failure at comparable stresses [243].

Alternatively, industrial concern has tended to focus on the problem of *fatigue after impact damage* (also known as post-impact fatigue damage), which has led to the development of the 'no-growth' concept [244]. As a consequence, the fatigue behavior of composites after impact damage has been investigated extensively. However, the effect of damage growth mechanisms on post-impact fatigue response is not fully understood and an effective damage-tolerance methodology of post-impact composites has not been established yet [245]. Experimental investigations have given raise to the following observations: Impact damage leads to shorter life, especially in the compressive loading regime where buckling in the vicinity of delaminations occurs [246]. Under compressive fatigue loading, impact damage leads to growth of the delaminations opposite to the impact site in loading direction and transverse to it as well as to buckling of strips around the damage zone [247]. Larger accumulated damage in the impact zone leads to a stronger decrease of lifetime and rapid delamination growth is usually an indication of imminent failure [248]. Many damage and life prediction models based on the observation of crack densities and stiffness degradation have been developed. However, industrial applications usually preclude simple (destructive) determination of these parameters in operation. Therefore, early and proactive detection of the embedded damages are important from both the mechanical performance and the safety perspectives, and thus justifies the requirement of NDE techniques to measure the material stiffness properties and discriminate between the different failure mechanisms.

Over the past decades, several inspection techniques for monitoring mechanically induced damage in composites have been proposed, such as cracks counting, structural health monitoring (SHM) via embedded piezo-actuators, acoustic emission (AE), liquid penetrants, X-ray radiography, thermography, and fiber-optic and fiber Bragg gratings (FBG's). Nonetheless, most of these techniques undergo several restrictions. The application of crack counting is limited to transparent and unpainted materials [249]. SHM uses variations in electric sensitivity, and thus requires conductive materials [241]. On the other hand, AE involves the detection of energy released by the material under stress during cracking events.

This method is very efficient for monitoring structures under in-service conditions, but does not provide a precise identification of the size, shape and location of flaws, especially in anisotropic materials such as composites. In addition, environmental noise can easily mask the measurements [250]. Liquid penetrants are used to infiltrate flaws and damaged components, but can usually only resolve damage connected to the surface. Alternatively, X-ray radiography can be adopted for the through-thickness detection of defects. However, the resulting image is usually difficult to interpret, particularly in the presence of numerous superimposed damage planes that hinder the locating of different delaminated and cracked layers. Thermographic inspection is based on the analysis of thermal patterns induced either by heating the specimen or by applying a mechanical oscillatory load. This technique is sensitive to delaminations, but is not able to provide information on the through-thickness location of the flaw [237].

Ultrasound is currently one of the most frequently used and accepted NDE techniques that are proven to provide effective and reliable results at relatively low cost [15]. The usually adopted normal incidence technique [251, 252] is most sensitive to flaws that lie parallel to the surface (delaminations). In contrast, matrix cracks, lying perpendicularly to the surface, and fiber fracture paths are difficult to detect because they do not offer a wide enough reflecting surface. By orienting the transducer at an angle to the tested surface, in order to acquire the energy backscattered from damage, transverse cracks running parallel to the fiber direction can be detected [253, 254]. Thus, for a complete non-destructive evaluation of the induced damage, more that one measurement technique is usually required. As a drawback, it is worth to mention that standard ultrasound techniques usually imply the use of an immersion bath and often double-sided access which hampers *in-situ* applications. However, recent improvements could tend to overcome this limitation. For instance, Chen *et al.* [247] proposed an emerging ultrasonic imaging technology based on acoustography, which resulted in a new measurement system that could be used for *in-situ* imaging of impact damage in composite specimens during long-term fatigue tests. In another related proposal, Matikas [150] proposed the use of advanced nondestructive evaluation techniques such as ultrasonic microscopy (i.e the propagation of surface acoustic waves (SAW)) and nonlinear acoustics to characterize the damage and monitor in real-time aging structural components used in aerospace applications. More recently, Rheinfurth *et al.* [241] experimentally explored the applicability of air-coupled Lamb waves to monitoring mechanically induced fatigue damage in composites. This non-contact technique enabled them to perform measurements without unclamping of the specimens out of the servo-hydraulic testing machine used for cyclic loading. These encouraging results motivated us to further explore classical and emerging ultrasound laboratory techniques to monitor the mechanical properties of damaged composites, in order to enhance our understanding of this complex material and to think up possible improvements for in-service conditions assessment.

9.1.2 Tissue-equivalent materials

Tissue engineering is a continuously growing field that aims at developing biological substitutes that restore, maintain, or improve tissue function [255]. Tissue engineering is therefore of crucial importance to study aspects of cell physiology and pathology, and is also geared toward the realization of implantable tissues. The majority of tissue-engineered materials are grown by culturing cells from a patient or donor, then seeding them onto an appropriate scaffold, and finally stimulating them to form specific tissues that mimic the complex 3D structures and biological functions of natural tissues [256]. This approach has successfully been applied to deliver tissue-engineered materials for treating cartilage, skin, cornea, and bone defects. Currently, most of the research focuses almost exclusively on the biological aspects of tissue culture at the detriment of manufacturing and product realization issues. Thus, there is still a lack of commercial and clinical viability for many tissue-engineered materials, mainly due to poor process control and monitoring in tissue production [257].

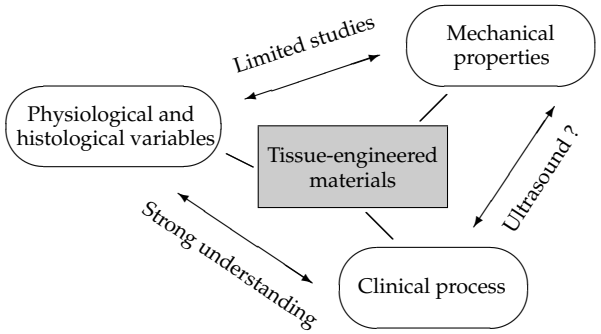

Figure 9.3: *Overview of the ties between engineering and biology at the time of studying tissue culture.*

Typically, the process of tissue engineering involves several stages including cell culture, scaffold production, bioreactor system, and final product preservation, whereas the main monitoring requirement is to assess the culture's progress during production, and to relate it to such factors as cells number and structure. Current available analysis methods for evaluating tissue formation are histology and direct mechanical measurements. Although these methods provide valuable information for cell phenotype and proliferation, as well as mechanical characterization such as compressive moduli of scaffolds, they are not suitable for continuous monitoring of the sample *in vivo* as they destroy cells and scaffolds (i.e. extracellular matrix). In addition, these methods require large sample numbers for statistical analysis, since the different samples are prepared and measured at varying times, and the tissue growth usually undergoes high deviation between specimens [258]. Thus, tissue engineers need a real-time system that could non-invasively monitor tissue growth and consequent scaffold degradation in the same specimen over time. Nevertheless, only a few attempts to develop such methods have been reported.

Among the process monitoring techniques that have been applied to move tissue engineering forward, it is worth to mention well-established nonlinear optical techniques, such as the multi-photon excitation microscopy or second harmonic imaging. The former ones have been used for noninvasive *in vivo* characterization and imaging of sub-cellular properties [259, 260]. However, the potential of these techniques greatly depends on practical factors, such as the engineering of high-quality probes (in terms of reproducibility) and strategies to incorporate the monitoring tools in the cell-culture environment. Alternatively, other imaging methods, such as magnetic resonance imaging and computed tomography, provide scaffold structural information, but are limited to deliver only morphological information, and the imaging reconstruction procedures are quite extensive [261].

In tissue engineering, biodegradable polymer scaffolds are used to deliver cells and regenerate tissue as well as provide temporary mechanical support. In principle, the degradation rate of the scaffold should match the rate of tissue formation, hence the degradation behavior of a scaffold has a critical impact on the long-term performance of a tissue-engineered construct *in vivo*. Among them, hydrogels (e.g. agarose, fibrin, collagen) have been extensively used as scaffold materials because of their viscoelastic characteristics, biocompatibility, the simplicity of their fabrication and their high water content, providing a highly hydrated environment to the embedded cells, which is permeable for oxygen, nutrients and cellular wastes [262, 263]. However, a major limitation of hydrogel-based scaffolds is that their mechanical properties are usually significantly weaker than those of natural tissues [264].

Recently, a novel spherical indentation method for characterizing the viscoelastic properties of hydrogel-based constructs under cell culture conditions has been proposed [265]. A sensitive long working distance microscope was used for measuring the time-dependent deformation of thin circular hydrogel membranes under a constant load. Then, the elastic modulus as a function of time could be determined by making use of a theory of viscoelasticity for large deformation. It is noteworthy that this kind of measurements can be performed for specimens that are fully immersed in solution and at elevated temperatures with no risk of damaging the instrumentation. However, the method is only applicable to relatively thin and large membranes and has to evoke specially designed sample holders to minimize any clamping stress applied on the hydrogel membranes. Hence, Yang *et al.* [266] developed an alternative indentation system, ideally sample holder-free, combined with a high-resolution imaging technique (optical coherence tomography) for *in situ* characterization of thick specimens in a nondestructive fashion and under sterile conditions.

Alternatively, ultrasound may have potential to provide real-time assessment of the macroscopic construct properties, since the intrinsic ultrasonic properties are directly related to the structure and composition of the tissue under investigation. The use of ultrasound for monitoring properties of tissue-engineered products has received only little attention until recently. Among this few works, Hattori *et al.* [267] developed a new evaluation system for articular cartilage, which revealed that ultrasound analysis is able to quantitatively evaluate

cartilage degeneration and cartilage repair. In a similar work, their ultrasonic evaluation system was capable of judging the success or failure of cartilage regeneration procedures, and therefore suggested that ultrasound is a valuable tool for diagnosis of cartilage regeneration [268]. In another related work, Rice *et al.* [269] performed high-frequency ultrasound measurements in pulse-echo mode to determine the propagation and backscatter properties of cartilage specimens. Then, they compare the ultrasonic properties (velocity and attenuation) obtained at different time steps during the process evolution with mechanical tests and biochemical properties of the matrix. More recently, Kreitz *et al.* [270] demonstrated the potential of ultrasound for quantitative *in vitro* evaluation of tissue development in fibrin-based tissue-engineered structures. These encouraging results motivated us to further develop ultrasound-based system under culturing environment to monitor the alteration of the mechanical properties of the constructs over time, in order to enhance our understanding of the bioprocess of tissue-engineered products.

9.2 Experimental work description

This section exposes several aspects of the experimental work carried out over the course of this dissertation, focusing on the samples preparation description and the experimental configuration used to evaluate those samples. The proposed methodology is organized in four parts: Firstly, Section 9.2.1 describes a conventional through-transmission method for measuring the properties of traditional materials with known acoustic properties. This experiment serves us as a calibration for our system and provides us fundamental experimental data for validating our models. Secondly, Section 9.2.2 presents some conventional through-transmission measurement methods applied for damage assessment in carbon fiber-reinforced polymers. Both the impact and post-impact fatigue damage mechanisms are investigated. In addition, we also investigate the feasibility of measuring the acoustic nonlinearity of carbon fiber-reinforced polymers using a finite-amplitude through-transmission method, based on the second harmonic generation technique. In Section 9.2.3, we finally introduce a novel embedded system for ultrasonic monitoring of tissue-engineered products. This system is calibrated on a tissue-equivalent material, and then applied for monitoring the generation of an artificial tissue culture.

9.2.1 System calibration framework

In this section, we analyze several traditional materials (i.e. metals and plastics) with the aim of evaluating the performance of the theoretical models described in Part II. The materials were chosen so that they cover a relatively wide range of mechanical (e.g. wave velocity, density, etc.) and geometrical (e.g. thickness) properties. The properties reported in the literature for those materials are summarized in Table 9.1.

Material	Wave velocity c_p $[m/s]$	Density ρ $[kg/m^3]$	Attenuation α $[Np/m]$	Thickness a $[mm]$
Aluminium	[6320-6420][5,6]	2700[7]	3 @ 5 MHz / 20 @ 10 MHz[7]	3.79 / 9.90
Brass	[4369-4700][7,8]	[8480-8600][7,10]	-	2.90
PMMA	[2673-2750][9]	[1180-1200][11]	[50-72] @ [4-7] MHz[11]	2.61 / 9.98

Table 9.1: *Mechanical and geometrical properties of traditional materials.*

For this experiment, we assemble the aforementioned single layers together to obtain a set of multilayered materials (ranging from 2 to 4 layers). This operation has been carefully carried out in immersion with degassed water as coupling medium to avoid voids or bubbles getting stuck between the layers. To evaluate the reproducibility of the experiment, each layered configuration has also been tested in its reverse side (assuming that we are working in the linear regime), and the layered specimens were completely dismounted and assembled again between each experiment. The resulting combinations are summarized in Table 9.2.

Type of multilayer	Specimen	Materials
Single layer	$S_{1,1}$	Aluminium^a
	$S_{1,2}$	Aluminium^b
	$S_{1,3}$	Brass
	$S_{1,4}$	PMMA^a
	$S_{1,5}$	PMMA^b
Two layers	$S_{2,1}$	Aluminium^b - PMMA^a
	$S_{2,2}$	PMMA^a - Aluminium^b
	$S_{2,3}$	Aluminium^b - PMMA^b
	$S_{2,4}$	PMMA^b - Aluminium^b
Three layers	$S_{3,1}$	PMMA^a - Aluminium^b - PMMA^b
	$S_{3,2}$	PMMA^b - Aluminium^b - PMMA^a
Four layers	$S_{4,1}$	Aluminium^a - PMMA^a - Aluminium^b - PMMA^b
	$S_{4,2}$	PMMA^b - Aluminium^b - PMMA^a - Aluminium^a
	$S_{4,3}$	Brass - PMMA^a - Aluminium^b - PMMA^b
	$S_{4,4}$	PMMA^b - Aluminium^b - PMMA^a - Brass

Table 9.2: *Overview of the obtained one-layer and multilayered specimens.*

[5] http://www.ondacorp.com/images/Solids.pdf
[6] http://www.olympus-ims.com/en/ndt-tutorials/thickness-gage/appendices-velocities/
[7] http://www.astm.org/BOOKSTORE/DS68/pg41.pdf
[8] http://www.ndtsystems.com/Reference/Velocity_Table/velocity_table.html
[9] Reported by Carlson *et al.* [271]. The attenuation has a nearly linear behavior for the given frequency range.

Note that the one-layer specimens consisting of the same material involved layers of different thicknesses, which are denoted with increasing indexes from the thinest to the largest layer[10].

In this first experiment, the specimens were excited by a low-frequency ultrasonic sine-burst at two different frequencies (5.5 and 6 MHz), consisting of one cycle of 8 Vpp amplitude. This excitation signal was generated by an arbitrary wave generator (Agilent 33220). The water path between the unfocused transducers was fixed to 124 mm, that is a large enough distance so that the echoes from the transducers-material interactions does not interfer with echoes from the layers of the material. The specimens were approximately located in the middle of the distance between the transducers, and scanned over a two-dimensional plane parallel to the transducer areas (C-scan mode). The scan was carried out in an immersion tank with degassed water at room temperature equipped with three-dimensional motion controllers. The response signals were registered during 20 μs. The response signals were sampled with a high resolution A/D converter after 40 dB pre-amplification stage, applying a sampling frequency of $F_s = 100$ MHz, providing $N = 2000$ samples, which were uniformly quantized with 12 bits. Figure 9.4 depicts the experimental setup used to register the ultrasonic signals.

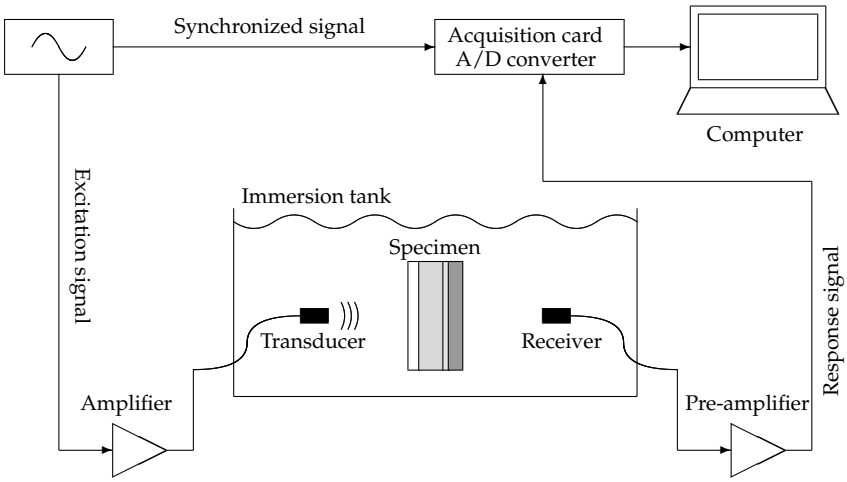

Figure 9.4: *Experimental configuration for the system calibration (immersion measurements).*

The measurement procedure was repeated for each frequency over an area of 2×2 mm^2 with a step of 1 mm close to the center of the specimens, providing 2×9 measurements for each specimen. Each of these measurements corresponds to the resulting average of 500 captures of the signal, providing an effective reduction of noise for the detected response signal, increasing the signal-to-noise ratio around 27 dB. Only compressional waves were generated by the transducers and no mode conversion waves were measured in the present case, although the methodology could be extended to other measurements configuration[11]. Figure 9.5 illustrates the experimental configuration for a layered specimen.

[10]Those layers were not necessarily cut off from the same sample, and thus may have slightly different mechanical properties.

[11]Be aware that this will be the case for all the considered experiments.

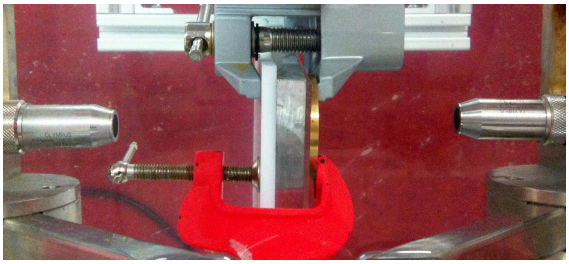

Figure 9.5: *Experimental configuration for measuring a layered specimen.*

9.2.2 Ultrasonic through-transmission measurements

In this section, several CFRP plates with distinct structural complexity and exposed to different damaging mechanisms have been evaluated. To obtain the ultrasonic measurements, linear and nonlinear normal incidence techniques were adopted, either in contact or in immersion. To this end, a through-transmission sub-wavelength technique has been proposed, where longitudinal waves are transmitted through layers, whose size is much smaller than the wavelength of the transmitter.

Measures for impact damage assessment

Typically, the properties of laminates are provided by the manufacturer. In our case, several mechanical and geometrical properties of the analyzed specimens (labeled as specimen (A) and (B)) were unknown after manufacture, and were therefore characterized at our laboratory. The fiber properties can be extracted by burning off the resin of a specimen's sample in an oven at 500°C during approximately sixteen hours. In first place, we introduced images of the burned samples in an AutoCAD software to count the number of layers of each sample, to measure the thickness of each layer by digital media, and to determine the orientation of the fibers with respect to the longitudinal axis of the specimen. Secondly, we weighted the fibers of each layer, and this enabled us to calculate their density and elastic constants. Finally, the elastic constants of the polymer matrix can be deduced from those of the fibers by making use of well-known mixing rules. From those measurements, it results that specimen (A) and (B) are symmetric CFRP plates consisting of five and four layers, respectively. Their mechanical and geometrical properties are summarized in Table 9.3.

Specimen	Layer (n°)	Y. Modulus $E\ [GPa]$	P. Ratio $\nu\ [-]$	Density $\rho\ [kg/m^3]$	Attenuation $\alpha\ [Np/m]$	Thickness $a\ [mm]$
(A)	I, V	12.0427	0.2937	1874.7	395.4729	0.255
	II, IV	8.9068	0.3148	1456.4	393.0409	0.185
	III	7.0132	0.3308	1140.1	381.3457	0.770
(B)	I, IV	6.5675	0.3158	2054.3	469.5061	0.345
	II, III	6.8586	0.3136	2065.4	464.7600	0.305

Table 9.3: *Mechanical and geometrical properties of the layers $I - V$ and $I - IV$ that compose the multilayered specimens (A) and (B), respectively.*

Damages were generated by applying several free-fall impact energies (0.388, 0.674, 1.313, 2.280, and 5.385 Joules), varying the mass and height of each impactor to obtain five relevant damage locations (labeled from 0 to 5, where 0 indicates no-damage). The impact damage generation procedure is depicted in Figure 9.6.

Figure 9.6: *Impact damage generation procedure: (1) CFRP plates; (2) drop weight tower; and (3) impacted area of the specimen.*

In this first experiment, both plates were measured with a slightly different configuration. For sake of brevity, the values indicated hereafter are related to specimen (A), and those related to specimen (B) are indicated in gray between brackets. Specimen (A) (Specimen (B)) was excited by a low-frequency ultrasonic sine-burst at a central frequency of 5 MHz, consisting of one cycle of 0.2 μs and 5 Vpp amplitude. This excitation signal was generated by an arbitrary wave generator (Agilent 33220). The response signals were registered during 10 μs (15 μs), that is, up to the time for which there were no more reflections from the specimen/transducers interfaces. The response signals were sampled with a high resolution A/D converter after 40 dB pre-amplification stage, applying a sampling frequency of $F_s = 200$ MHz ($F_s = 100$ MHz), providing $N = 2000$ ($N = 1500$) samples, which were uniformly quantized with 12 bits. Figure 9.7 depicts the experimental setup used to register the ultrasonic signals.

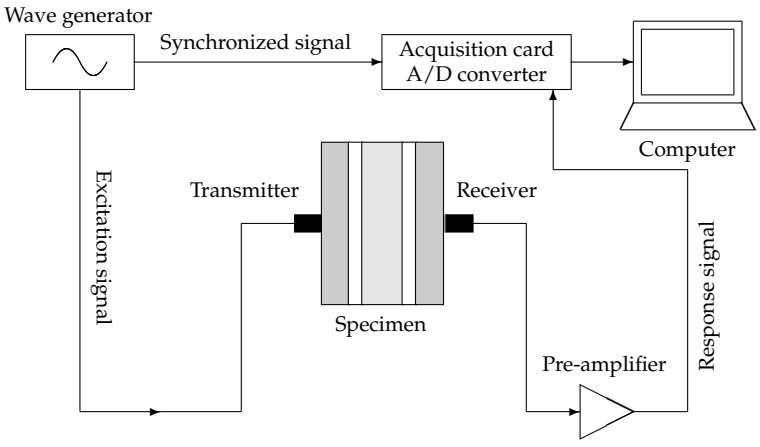

Figure 9.7: *Experimental configuration of the excitation-propagation-measurement system (contact measurements).*

Initially, the response signal was measured at the undamaged location for calibration. Then, the measurement procedure was repeated ten (forty) times on each location, to generate a relevant data set that account for the uncertainties due to the variability of the transducers alignment with respect to the impact location. Each of these measurements corresponds to the resulting average of 300 captures of the signal, providing an effective reduction of noise for the detected response signal, increasing the signal-to-noise ratio around 25 dB. Due to the high impedance of the interface air/solid, the transducers were adhered to the specimen with a coupling gel, to favor the transmission of the ultrasonic waves.

Measures for 'fatigue after impact damage' assessment

In this case, the properties of laminates were completely provided by the manufacturer. The specimen (labeled as specimen (C)) was manufactured from a Cycom 977-2-35-12k HTS prepreg with a stacking sequence which corresponds to a $[0/90]_{4s}$ lay-up[12]. During lay-up, the laminates were compacted every four layers in the stacking sequence by applying vacuum for 15 minutes. Curing was realized in an autoclave at 177°C for three hours with a pressure of 7 bar. From the manufactured plates, the specimen (C) with the dimensions $250 \times 35 \times 2$ mm^3 was machined. The mechanical and geometrical properties are given in Table 9.4.

Layer	Y. Modulus $E\ [GPa]$	P. Ratio $\nu\ [-]$	Density $\rho\ [kg/m^3]$	Attenuation $\alpha\ [Np/m]$	Thickness $a\ [mm]$
0°-orientation	11.1616	0.3007	1589.5	293.023	0.1215
90°-orientation	11.1616	0.3007	1589.5	293.023	0.1215

Table 9.4: *Mechanical and geometrical properties of the layers that compose the multilayered specimen (C).*

In first place, impact damage was introduced with a drop weight tower. A photo sensor activating a clamp ensured anti-rebound after the first impact, and the contact force was measured with a strain gauge full bridge included in the semi-spherical striker. The impact damaged specimen was subjected with 3.8 Joule impact energy. Then, fatigue testing was conducted with a servo-hydraulic Instron/Schenk 100 kN fatigue testing machine with hydraulic clamps at a stress ratio of $R = -1$. The clamping pressure was set according to loading forces. The fatigue damage was generated by applying fatigue load in tension-compression (up to 100000 cycles). The specimens and the *fatigue after impact damage* generation procedure are depicted in Figure 9.8.

As in the previous experiment, the specimen was excited by a low-frequency ultrasonic sine-burst at a central frequency of 5 MHz, consisting of one cycle of 0.2 μs and 5 Vpp amplitude. This excitation signal was generated by an arbitrary wave generator (Agilent 33220). In this second experiment, the specimen was located at the focal distance ($d_f = 30$ mm) of the focused transducers, and scanned over a two-dimensional plane parallel to the transducer areas (C-scan mode) in an immersion tank with degassed water at room temperature equipped with three-dimensional motion controllers. The response signals were

[12]Courtesy from the Institute of Polymers and Composites, TU Hamburg-Harburg, Germany

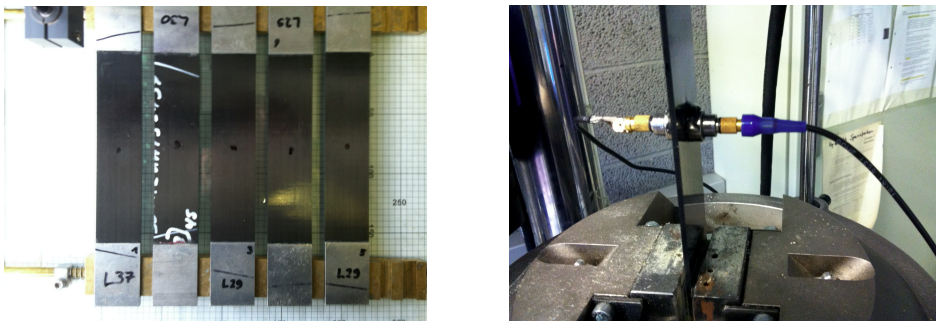

Figure 9.8: *'Fatigue after impact damage' generation procedue: (1) CFRP plates with marked impacted area; and (2) CFRP plate mounted on the servo-hydraulic fatigue testing machine.*

registered during 10 μs, that is, up to the time for which there were no more reflections from the specimen/transducers interfaces. The response signals were sampled with a high resolution A/D converter after 40 dB pre-amplification stage, applying a sampling frequency of $F_s = 200$ MHz, providing $N = 2000$ samples, which were uniformly quantized with 12 bits. Figure 9.9 depicts the experimental setup used to register the ultrasonic signals.

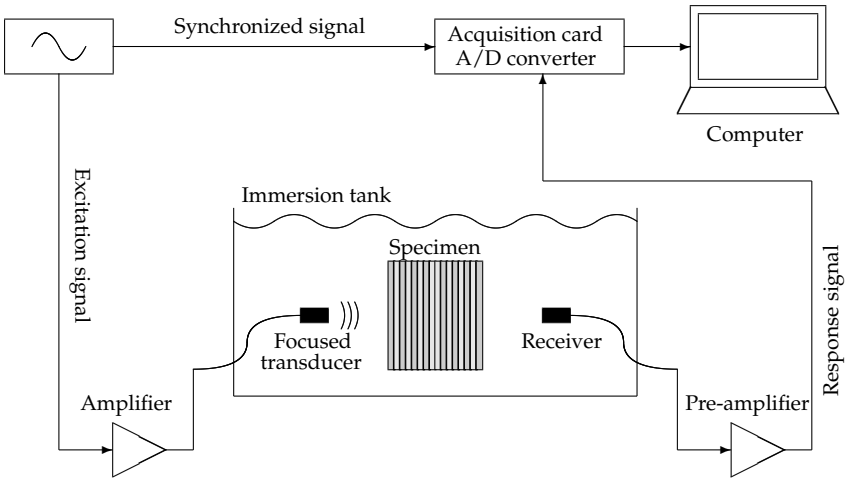

Figure 9.9: *Experimental configuration of the excitation-propagation-measurement system (immersion measurements).*

Initially, the response signal was measured at an undamaged location (far from the impacted area) for calibration. Then, the measurement procedure was repeated over an area of 40×20 mm^2 with a step of 1 mm around the impacted area, providing a data set of 860 measurements (plus one taken in water only, after removing the specimen). Each of these measurements corresponds to the resulting average of 500 captures of the signal, providing an effective reduction of noise for the detected response signal, increasing the signal-to-noise ratio around 27 dB.

Nonlinear ultrasound measurements

In this case, we propose a through-transmission finite-amplitude nonlinear ultrasound method to quantify the nonlinearity of carbon fiber-reinforced polymers, namely the specimen (C) described in Table 9.4. The presence of non-linear distortions from the electronic equipment represents the major practical difficulty of this technique when analyzing the response signals, since it may mask the intrinsic nonlinear response of the material under investigation. Hence, to evaluate the sensitivity of the proposed methodology, the experiment has first been carried out on water and serves us as a calibration of the instrumentation, now that several references in the literature provide tabulated values for the nonlinear parameter of first-order for water.

In this experiment, the specimen was excited by 10 low-frequency ultrasonic sine-bursts at a central frequency of $F_c = 5$ MHz at five different energies corresponding to $2^{(j-1)} \cdot 200$ mV, with $j = 0, \ldots, 4$. Those excitation signals were generated by an arbitrary wave generator (Agilent 33220), using a focused transducer. The specimens were located at the focal distance ($d_f = 30$ mm), and scanned over a two-dimensional plane parallel to the transducer areas in an immersion tank with degassed water at room temperature equipped with three-dimensional motion controllers. The response signals were registered during 10 μs using a needle hydrophone with a linear response up to 20 MHz, which is located few millimeters behind the specimen. As in the previous experiments, the response signals were sampled with a high resolution A/D converter after 40 dB pre-amplification stage, applying a sampling frequency of $F_s = 200$ MHz, providing $N = 2000$ samples, which were uniformly quantized with 12 bits. Each of the measurements corresponds to the resulting average of 500 captures of the signal, providing an effective reduction of noise for the detected response signal, increasing the signal-to-noise ratio around 27 dB. Figure 9.10 depicts the experimental setup used to record the ultrasonic signals.

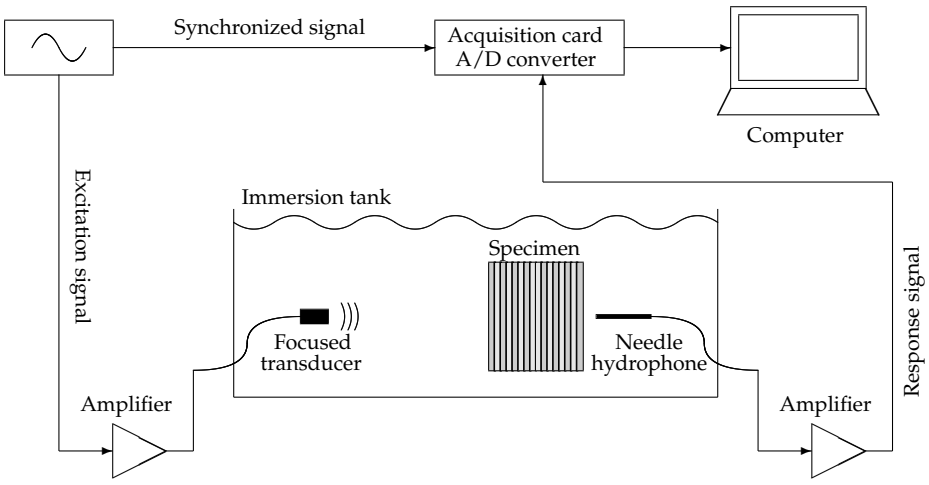

Figure 9.10: *Experimental configuration of the nonlinear excitation-propagation-measurement system.*

9.2.3 Embedded systems for ultrasonic monitoring of biomaterials

In this section, an ultrasound-monitoring Petri dish has been designed to monitor in real-time the evolution of relevant mechanical properties during engineered tissue formation processes. This system has several advantages: (i) the entire sample holding equipment can be autoclaved and measurements can be taken under sterile conditions; and (ii) the system is capable of working under cell culture conditions (37°C, 5% CO_2) and testing of the tissue-engineered material can be done while submerged in culture media. It is noteworthy that these environmental properties are of extreme importance when measuring mechanical properties of tissue culture, since changes in environment can significantly affect them [272].

The Petri dish with a specifically designed high-frequency ultrasonic transmitter and receiver in angle position was manufactured for real-time measurement of mechanical properties of thin layers of tissue culture, whose thickness is of the order of 100 μm. The bottom part of the Petri dish that holds the tissue culture is circular and made of a biocompatible material, in order to mimic a conventional culture flask. A thin cover is carefully deposed above the tissue culture to ensure that the thickness of the tissue layer remains constant at the measurement location. In addition, this cover is made of a material with a much higher impedance than that of the tissue layer to provide a high reflection coefficient (i.e. a nearly perfect reflector). This cover is narrow enough (few millimeters) to guarantee that it won't hamper the culture medium (e.g. nutrients) to reach the tissue layer. The monitored Petri dish is connected to the electronic setup detailed in Figure 9.11.

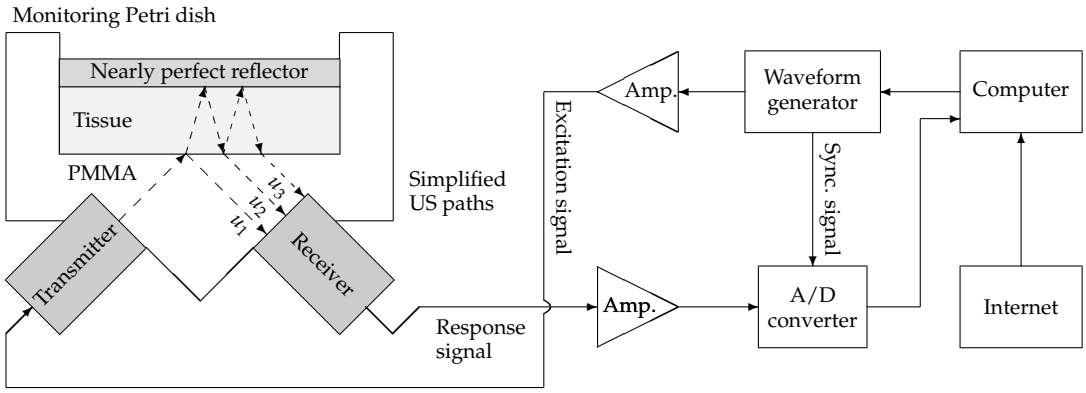

Figure 9.11: *Schematic experimental and electronic setup for the ultrasonic embedded system.*

The transmitting and receiving transducers are designed to be in angle position (45°) in order to avoid reverberation echoes inside the petri dish plate parts. The transmitted signal is generated as a one-cycle burst composed by a 20 MHz sine of amplitude that amounts to 5 Vpp with a repetition rate of 1000 pulses/second, using an arbitrary wave generator (Agilent 33220). The recorded signals are digitized with a high resolution A/D converter after 40 dB preamplification, during a period of 5 μs and a sampling rate of 400 MHz. Each measurement corresponds to the average of 300 captures of the signal, providing an effective reduction of noise according to the signal-to-noise ratio (25 dB). The recorded signals are

mainly composed of three different waveforms (simplified paths of Figure 9.11), namely (1) the wave front that propagates only through the Petri dish layer (labeled as u_1), (2) a wave that crosses both the Petri dish layer and the specimen (labeled as u_2), and (3) a wave echo produced by the former wave after crossing twice the specimen (labeled as u_3).

Any new diagnostic technique for monitoring tissue culture needs an evaluation stage in terms of its potential, limitations and sensitivity prior to employ it for biological process. In this context, tissue-equivalent materials play an important role in evaluating novel diagnostic methods for monitoring tissue-engineered products [273]. In our case, a tissue-equivalent phantom is important for quality control of the developed ultrasound diagnostic system. In addition, synthetic materials used in tissue-equivalent phantoms must be manufactured in a controlled way to be acoustically equivalent to human tissues [274]. One of the most used materials, due to its manageability and capacity to mimic speed of sound in soft tissue, is a mixture based on a polysaccharide gel (agar), distilled water, glycerol and graphite. The glycerol concentration determines the speed of sound in the medium, whereas the graphite concentration determines the attenuation [275].

In first place, the sensitivity and reproducibility of the system has been verified by monitoring a gelation process. The materials and the concentration for the gel culture (labeled as specimen (D)) were chosen according to Ortega *et al.* [275]: 92.5% of water, 5% of glycerol and 2.5% of agar. In order to obtain an homogeneous solution, water has been first heated and then the remaining components have been added. The final mixture was carefully deposed on the dish, resulting in a gel layer of about 300 μm thickness, and a diameter of 2 cm. The gelation process has been monitored during half an hour at 5 s intervals, resulting in a database of 350 measurements. At the initial time of the process, the wave velocity in the gel layer is unknown. Nonetheless, it is well-known that its value amounts approximately to 1500 [m/s], and thus the resulting wavelength (75 μm) is compatible with the gel layer thickness. The material properties of the Petri dish material (PMMA, polymetylmetacrilate) and the gel culture are summarized in Table 9.5.

Material	Modulus [GPa]	Poisson ν	Density ρ [kg/m^3]	Velocity c_p [m/s]
PMMA	$E = 2.96$	0.43	1180	2672
Gel (initial)	unknown	0.5	1000	unknown

Table 9.5: *Mechanical and geometrical properties of the layers that compose the multilayered embedded specimen (D).*

In second place, this diagnostic technique has been applied for monitoring the generation of artificial human oral mucosa[13]. The isolation and culture of human gingival fibroblasts has been achieved according to Ximenes Oliveira [276]: First, oral mucosa samples were obtained from patients submitted to different procedures of minor oral surgery. Secondly, the samples were washed with phosphate buffered saline (PBS) to eliminate adhered

[13]Courtesy from the Tissular Engineering Group, Department of Histology, University of Granada

materials. Thirdly, an enzymatic method was carried out to digest the extracellular matrix of the oral mucosa chorion and to separate the stromal fibroblasts, by using the type I collagenase sterile solution of Clostridum hystoliticum at 2% in Dulbecco's modified Eagle's medium (DMEM), during 10-12 hours at 37°C. To obtain primary cell cultures, the enzymatic solution with stromal cells was then centrifuged at 1000 rpm, during 10 minutes, and the achieved cell pellet was cultured in culture flasks of 25 cm^2 surface area, using DMEM as culture medium, complemented with 10% fetal bovine serum (FBS) and 1% antibiotic. Finally, the cells were incubated at 37°C with 5% carbon dioxide, and the culture medium was changed every three days. On the other hand, a fibrin-agarose stromal substitute has been elaborated: First, the fibrin was obtained from frozen plasma of human blood donors. To produce a fibrin-agarose gel, 15.2 ml of human plasma were then added to 150000 cultured fibroblasts resuspended in 1.5 ml of DMEM with 10% FBS. To prevent degradation of the scaffold by fibrinolysis, the mixture was supplemented with 300 μl of tranexamic acid. Finally, 2ml of 1% CaCl2 were added to the solution to precipitate fibrin polymerization. At the same time, type VII agarose was melted and solved in PBS, and added to the fibrin mixture at a final concentration of 2%.

In this experiment, the cells-seeded construct (labeled as specimen (E)) was carefully deposed on the dish, resulting in a tissue layer of about 100 μm thickness, and a diameter of 1 cm. Before the construct starts hardening, the cover was meticulously deposed above it, then the culture media was added, and the embedded system was finally placed in chamber under cell culture conditions (37°C, 5% CO_2). The biological process has been monitored during seven days at 2 min intervals, resulting in a database of 5016 measurements. As for the gel, the wave velocity in the tissue layer is unknown at the initial time of the process. Figure 9.12 provides an overview of the embedded ultrasonic system and samples preparation.

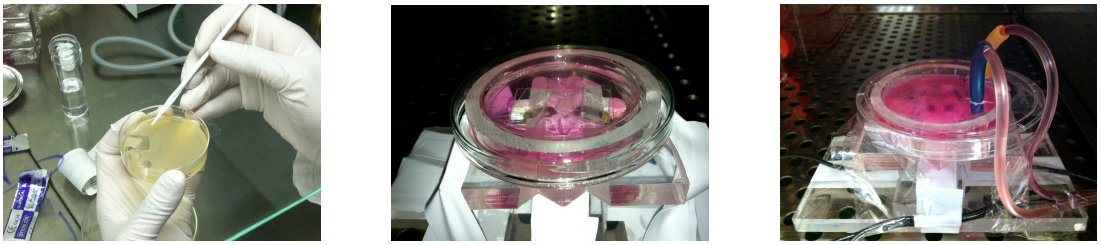

Figure 9.12: *Embedded ultrasonic system: (1) Elaboration of the fibrin-agarose stromal substitute; (2) monitoring Petri dish with ultrasonic transducers in angle position; and (3) tissue culture submerged in culture media under physiological conditions.*

9.3 Inverse problem and system identification

An inverse problem (IP) can be defined in opposition to the forward problem (FP). A FP consists of finding the response of a system given a known model. In contrast, an IP consists of retrieving unknown information of the model given the response of a system. Recently, some authors have applied IP's to identify damages or characterize material properties [118,

277, 278, 279], defining a corpus of knowledge for reconstructing an unknown part of a system model. The theoretical background on the IP theory described here is provided by Tarantola *et al.* [9], and grounds today's most powerful reconstruction method for finding an optimal solution. The aim of this section is to provide the mathematical basis to the qualitative schemes introduced in Chapter 5.

9.3.1 Deterministic approach

The fundamental idea of the IP consists of the use of an iterative strategy based on the minimization of the discrepancy between the experimental and numerically predicted response signals, denoted by $y(n)$ and $y^{(\theta)}(n)$, respectively, where $\boldsymbol{\theta}$ denotes a finite set of parameters used to describe the damage state of the system. The discrepancy is represented by a residual feature vector $\boldsymbol{r}^{(\theta)}$ defined as,

$$\boldsymbol{r}^{(\theta)} \quad = \quad \boldsymbol{y} - \boldsymbol{y}^{(\theta)} \tag{9.1}$$

where $\boldsymbol{y}$ and $\boldsymbol{y}^{(\theta)}$ denote the feature vectors representing the signals $y(n)$ and $y^{(\theta)}(n)$, respectively. This feature vectors can be obtained through the parametrization and analysis techniques presented in Section 4.2. Note that under certain circumstances, the residual vector may be directly computed in the time-domain. In such a case, it is necessary to previously perform a cross-correlation between the observed $y(n)$ and modeled signals $y^{(\theta)}(n)$, in order to prevent the signal misalignment due to random time-shifts from possible imperfections of the measurement system (see Section 4.2.1). Since two vectors cannot be compared directly, a scalar number called cost functional $f^{(\theta)}$ is derived from the residual vector defined in Equation (9.1). Typically, the IP approach consists of three steps, that are the parametrization (how to choose the parameters $\boldsymbol{\theta}$), the cost functional definition (how to define $f^{(\theta)}$), and the optimization (how to choose the algorithm to minimize $f^{(\theta)}$).

Parametrization

The issue of the pathology parametrization is cumbersome when dealing with a large set of parameters $\boldsymbol{\theta}$, describing the properties of the material under inspection. Thus, many IP's are ill-posed: Solutions may not exist, they could be unstable and non-converging, or there may exist multiple solutions. From the conceptual point of view, parametrization can be understood as a powerful regularization tool for IP's, since it provides prior information in the form of hypothesis on the possible form of the sought solutions. Therefore, the choice of parameters has crucial implications in the convergence, the sensitivity and uniqueness of the results. This ill-conditioning is rooted in the physical meaning of the problem, and cannot be completely avoided by purely mathematical manipulations. Instead, regularization techniques have been developed to stabilize the minimization process by adding some prior knowledge on the searched model parameters to the cost functional. These regularization techniques were formally introduced by Tikhonov and Arsenin [280], and extended by Menke [281] and Aster *et al.* [282]. In fact, defining a parametrization with a reduced set of

parameters is in itself already a kind of regularization, since it restricts the solutions' field [283]. The latter approach will be adopted over the course of this dissertation.

Cost functional

There are many ways to design a cost functional. The necessary conditions are (a) that a full coincidence of prediction and measurement (zero discrepancy) should coincide with the absolute minimum of the cost functional, and (b) this minimum must be unique. The cost functional $f^{(\boldsymbol{\theta})}$ is usually defined by means of a least-square estimation of the residual energy as,

$$f^{(\boldsymbol{\theta})} = ||\boldsymbol{r}^{(\boldsymbol{\theta})}||_2^2 \tag{9.2}$$

in the case of a L_2-norm definition, or alternatively as,

$$f^{(\boldsymbol{\theta})} = ||\boldsymbol{r}^{(\boldsymbol{\theta})}||_1^2 \tag{9.3}$$

in the case of a L_1-norm definition, being less sensitive to outliers. In contrast to gradient-based algorithms, for which the cost functional is defined as $f^{(\boldsymbol{\theta})}$, the latter is usually defined in an alternative way as $\hat{f}^{(\boldsymbol{\theta})}$ when the minimization is carried out by global search algorithms (e.g. GA's),

$$\hat{f}^{(\boldsymbol{\theta})} = \log\left(f^{(\boldsymbol{\theta})} + \varepsilon\right) \tag{9.4}$$

where ε is a small non-dimensional value (here adopted as $\varepsilon = 10^{-16}$) that ensures the existence of $\hat{f}^{(\boldsymbol{\theta})}$ when $f^{(\boldsymbol{\theta})}$ tends to zero, and speeds up the convergence of the selected optimization algorithm [284, 285].

Optimization

According to Lee and Wooh [286], the parameters $\boldsymbol{\theta}$ that characterize the pathology are found by a search algorithm that minimizes the cost functional by means of a least-square estimation of the residual energy,

$$\hat{\boldsymbol{\theta}} = \arg\min_{\boldsymbol{\theta}} \hat{f}^{(\boldsymbol{\theta})} \tag{9.5}$$

The cost functional minimization can be performed by two alternative families of methods. The former consists of conventional gradient-based methods, such as the Gauss-Newton algorithms, the Broyden-Fletcher-Goldfarb-Shanno (BFGS) algorithm, or simulated annealing, just to name some of the most popular ones. The other family involves random search algorithms, for instance genetic algorithms (GA's) [287] or particle sworm algorithms. In this thesis, BFGS algorithm is typically used as a local search algorithm based on Hessian update [121], and assisted by finite differentiation and line search, for calibrating the model at the initial time of the monitoring process. GA's are then applied to minimize Equation (9.5), since the cost functional $\hat{f}^{(\boldsymbol{\theta})}$ is non-convex, implying that the cost functional may have more than one local minimum. This algorithm performs a stochastic search through the space of possible solutions and yields a higher probability of finding the global optimum compared

to standard iterative gradient-based optimization algorithms [288]. As a further drawback, note that the convergence of gradient-based algorithms strongly relies on the initial guess. A deeper insight on GA is provided in next section.

Genetic algorithms

The GA's are an heuristic optimization technique based on the rules of natural selection and genetics, which simulates the mechanism of survival competitions. First, a population of individuals (called chromosomes) is randomly generated. The population comprises a group of chromosomes that represent possible solutions $\boldsymbol{\theta}_i$ ($i = 1, \ldots, N_p$) in a (multidimensional) problem domain. Each solution $\boldsymbol{\theta}_i$ is evaluated by computing its cost functional $\hat{f}^{(\boldsymbol{\theta}_i)}$, for which one forward problem is solved independently. A new (child) population is formed by stochastically modifying the survivors, applying genetic operators such as tournament, crossover, and mutation to inject genetic diversity in the population (i.e to ensure that the solution does not fall in local minima). Then, the child chromosomes with higher fitness replace some of their parent chromosomes. The process runs until a stopping criterion (for instance a number of generations N_g) is reached. The choice of N_g , as well as the probabilities of the genetic operators, are set so, that the convergence to a global optimum is guaranteed, while establishing a trade-off between the system identification error and the computational cost. The termination criterion can of course be modified, for instance by creating some convergence criterion and then ending the iterations when this criterion is met. In this work, we simply applied the algorithm to a group of *representative* signals and examined the evolution of the currently best solution for these. After a certain number of iterations, we could no longer see any further improvement of the solutions and N_g was fixed to this number when applying the algorithm to the remaining signals [111].

A number of parameters have to be adjusted to optimize the computational efficiency of the GA's and guarantee its good convergence. The population size and number of generations, as well as several probabilities, are set so, that the convergence is guaranteed, while establishing a trade-off between the modeling error and the computational cost. Table 9.6 summarizes the selected configuration parameters used over the course of this dissertation (the population size and number of generations will be specified in each model-based estimation procedure described in Part IV).

Parameters	Values
Population size	-
Number of generations	-
Probability of crossover	0.8
Probability of mutation	0.3
Probability of tournament	0.7

Table 9.6: *Configuration parameters of the search algorithm.*

The flowchart of the system identification approach by applying genetic algorithms is depicted in Figure 9.13.

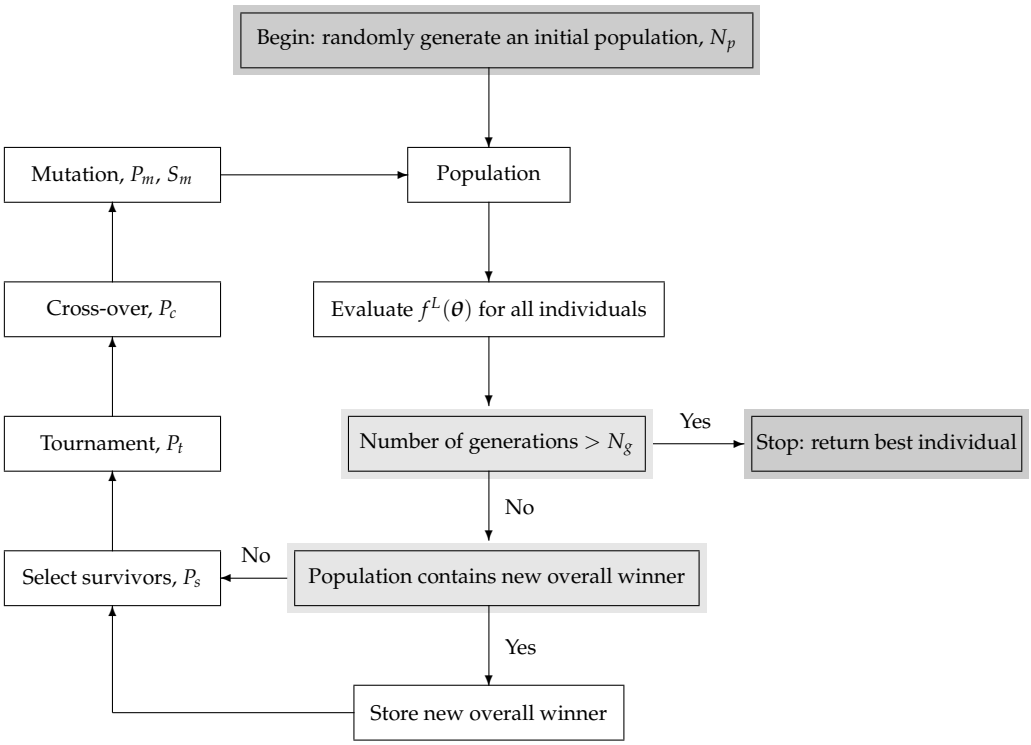

Figure 9.13: *Flowchart of the system identification approach by applying genetic algorithms. User-dependent variables: N_p: Number of individuals in population; N_g: Number of generations; P_s: Fraction of surviving individuals; P_t: Probability of tournament; P_c: Probability of crossover; P_m: Probability of mutation; and S_m: Scale of mutation.*

9.3.2 Probabilistic inverse problem

Reconstructing the values of the model parameters (moduli, attenuation parameters, etc.) has a limited meaning if one considers the existence of intrinsic noise in the measurements, heterogeneity of properties within the specimen, and even the fact that the model used to idealize its behavior is just an approximation of reality. To provide a suitable answer instead of deterministic values, probabilistic ones should be provided, which carry information about the degree of uncertainty and the nature of their scattering. This can be solved by treating the input and known data as uncertain up to some degree, and consequently obtaining the solution model in terms of a set of probability density functions (PDF) over each model parameter.

Following the probabilistic formulation of the model-based IP established by Tarantola *et al.* [9], the solution is not a single-valued set of model parameters $\mathcal{M}$. On the contrary, the solution is provided by a PDF $p(\mathcal{M})$ of the values of the model parameters $\mathcal{M}$ within the manifold $\mathfrak{M}$ of possible values. Here, this formulation is generalized to the case where several model classes $\mathcal{C}$ are candidates to idealize the real input-output system. Including this

variable into the IP formulation will allow to derive the model-class selection formulation as a particular case of inverse problem [289].

Since an absolute probability cannot be computed, statistical inference theory is used to incorporate the following information to the prior information about the measured observations $\mathcal{O}$: (1) the model parameters $\mathcal{M}$, (2) the model class $\mathcal{C}$, and (3) the information of the idealized relationship between them $\mathcal{O} = \mathcal{O}(\mathcal{M})$ computed by a model pertaining to a model class $\mathcal{C}$. The former are defined by the probability densities to prior data, labeled as $p^0(\mathcal{O})$, $p^0(\mathcal{M})$ and $p^0(\mathcal{C})$, respectively, whereas the additional information provided by the model class $\mathcal{C}$ about the relationship between observations and model is given by the PDF $p^m(\mathcal{O}, \mathcal{M}|\mathcal{C})$. The posterior probability $p(\mathcal{O}, \mathcal{M}, \mathcal{C})$ of the hypothetical model $\mathcal{M}$ is obtained jointly with the observations $\mathcal{O}$ and class $\mathcal{C}$ as,

$$p(\mathcal{O}, \mathcal{M}, \mathcal{C}) \quad = \quad k_1 \frac{p^0(\mathcal{O}, \mathcal{M}, \mathcal{C}) p^m(\mathcal{O}, \mathcal{M}, \mathcal{C})}{\mu(\mathcal{O}, \mathcal{M}, \mathcal{C})} \tag{9.6}$$

where $\mu(\mathcal{O}, \mathcal{M}, \mathcal{C})$ is the noninformative density function and k_1 is a normalization constant. Some assumptions will be made at this point:

1. Assuming that $\mathcal{O}$, $\mathcal{M}$ and $\mathcal{C}$ are independent *a priori* allows to split the joint prior information $p^0(\mathcal{O}, \mathcal{M}, \mathcal{C}) = p^0(\mathcal{O}) p^0(\mathcal{M}) p^0(\mathcal{C})$ and the uniform distribution $\mu(\mathcal{O}, \mathcal{M}, \mathcal{C}) = \mu(\mathcal{O})\mu(\mathcal{M})\mu(\mathcal{C})$.
2. The probabilistic model can be represented by a computation of $\mathcal{O}$ depending on $\mathcal{M}$, which yields $p^m(\mathcal{O}, \mathcal{M}, \mathcal{C}) = p^m(\mathcal{O}|\mathcal{M}, \mathcal{C}) p^m(\mathcal{M}|\mathcal{C}) p^m(\mathcal{C})$.
3. The model is not assumed to provide conditional information between model and class, i.e. $p^m(\mathcal{M}|\mathcal{C}) = \mu(\mathcal{M})$ and $p^m(\mathcal{C}) = \mu(\mathcal{C})$ are noninformative. This simplifies the expression to,

$$p(\mathcal{O}, \mathcal{M}, \mathcal{C}) \quad = \quad k_1 \frac{p^0(\mathcal{O}) p^0(\mathcal{M}) p^0(\mathcal{C}) p^m(\mathcal{O}|\mathcal{M}, \mathcal{C})}{\mu(\mathcal{O})} \tag{9.7}$$

   The posterior probability of the model $\mathcal{M}$ is then obtained from the joint probability $p(\mathcal{O}, \mathcal{M}, \mathcal{C})$ by extracting the marginal probability $p(\mathcal{M})\big|_{\mathcal{C}=\mathcal{C}_i}$ for all possible observations $\mathcal{O} \in \mathfrak{O} \Rightarrow p^0(\mathcal{C} = \mathcal{C}_i) = 1$, given that the model class $\mathcal{C}_i \in \mathfrak{C}$ is assumed to be true,

$$p(\mathcal{M})\big|_{\mathcal{C}=\mathcal{C}_i} \quad = \quad \int_{\mathcal{C}=\mathcal{C}_i} \int_{\mathfrak{O}} p(\mathcal{O}, \mathcal{M}, \mathcal{C}) d\mathcal{O} d\mathcal{C} \quad = \quad k_2 \int_{\mathfrak{O}} \frac{p^0(\mathcal{O}) p^0(\mathcal{M}) p^m(\mathcal{O}|\mathcal{M}, \mathcal{C})}{\mu(\mathcal{O})} d\mathcal{O} \tag{9.8}$$

   where k_2 is a normalization constant that replaces the dropped distributions.
4. We assume to have no prior information about the model $p^0(\mathcal{M})$, which is therefore represented by the noninformative distribution $p^0(\mathcal{M}) = \mu(\mathcal{M})$, which can in turn be dropped in the case that Jeffreys parameters [290] are adopted,

$$p(\mathcal{M})\big|_{\mathcal{C}=\mathcal{C}_i} \quad = \quad k_3 \int_{\mathfrak{O}} p^0(\mathcal{O}) p^m(\mathcal{O}|\mathcal{M}, \mathcal{C}) d\mathcal{O} \tag{9.9}$$

where k_3 is a normalization constant that replaces the dropped uniform distributions, and is needed for $p(\mathcal{M})\big|_{\mathcal{C}=\mathcal{C}_i}$ to fulfill the theorem of total probability, that is:

$$\int_{\mathfrak{M}} p(\mathcal{M})\big|_{\mathcal{C}=\mathcal{C}_i} d\mathcal{M} \quad = \quad 1 \tag{9.10}$$

5. The observations are assumed to follow a Gaussian distribution $\mathcal{O} \sim \mathcal{N}(E[\mathcal{O}^{\text{exp}}], C^{\text{exp}})$ whose mean is that of the experimental observations $\mathcal{O}^{\text{exp}}$, and whose covariance matrix C^{exp} stands for the measurement noise.
6. The observations are assumed to be a Gaussian process $\mathcal{O} \sim \mathcal{N}(\mathcal{O}(\mathcal{M}), C^{\text{num}})$ centered at the numerically computed ones $E[\mathcal{O}^{\text{num}}] = \mathcal{O}(\mathcal{M})$ with covariance matrix C^{num}.

The probabilistic observations $\mathcal{O}$ are in our case a vector of functions of time $\mathcal{O} = o_i(t)$ at every measuring time $t \in [0, T]$ and repetition $i \in [1...N_i]$, and the assumptions made above are valid for every instant t and sensor i. Considering that the compound probability of the information from all sensors and time instants is the product of that of each one individually, and that this product is equivalent to a summation within the exponentiation (since an integration along the continuous time can be seen as a summation over every infinitesimal dt), the Gaussian distribution allows an explicit expression of the probability densities,

$$J(\mathcal{M}) \quad = \quad \frac{1}{2} \sum_{i,j=1}^{N_i} \int_{t=0}^{t=T} \left(o_i(t,\mathcal{M}) - o_i^{\text{exp}}(t)\right) \left(c_{ij}^{\text{exp}} + c_{ij}^{\text{num}}\right)^{-1} \left(o_j(t,\mathcal{M}) - o_j^{\text{exp}}(t)\right) dt \tag{9.11}$$

where the term $J(\mathcal{M})$ corresponds to a misfit function between model and observations,

$$p(\mathcal{M})\big|_{\mathcal{C}=\mathcal{C}_i} \quad = \quad k_4 e^{-J(\mathcal{M})} \tag{9.12}$$

where the constant k_4 is derived from the theorem of total probability applied over all possible models $\mathfrak{M}$, which is integrated by Quasi Montecarlo using a Sobol sequence with 2^{18} points. The best-fitting model is found by minimizing $J(\mathcal{M})$ instead of maximizing $p(\mathcal{M})$ since,

$$\hat{\mathcal{M}} \quad = \quad \underset{\mathcal{M}}{\text{argmax}} \left\{ p(\mathcal{M})\big|_{\mathcal{C}=\mathcal{C}_i} = k_4 e^{-J(\mathcal{M})} \right\} \quad = \quad \underset{\mathcal{M}}{\text{argmin}} \left\{ J(\mathcal{M}) \right\} \tag{9.13}$$

The probabilistic nature of the reconstruction is partly motivated by the fact that the model is just an approximation of the experimental setup. If several models are candidates based on different hypothesis about the system, the former probabilistic formulation of the IP will be shown to be able to provide information to rank them. The bottom idea is the following: if the model-class (based on the candidate hypothesis) is considered as an uncertain discrete variable, its probability can eventually be extracted as a marginal probability from Equation (9.7). The probability of each model-class will therefore have the sense of degree

of certainty of being true in the sense that the probabilistic conjunction of certainty provided by the experimental measurements and model are coherent.

Let the model class $\mathcal{C} \in \mathfrak{C}$ denotes an idealized mathematical model of the experimental system, whereas $\mathcal{M}$ denotes the set of model parameters that the model-class depends on. Different model classes can be formulated and hypothesized to idealize the experimental system, and each of them can be used to solve the probabilistic IP, yielding different values of model parameters. To select among the infinitely many possible model classes that can be defined, a probabilistic criteria can be defined based on their compatibility between prior information about the observations $\mathcal{O}$, the model parameters $\mathcal{M}$ and the model class $\mathcal{C}$ [149].

The goal is to find the probability $p(\mathcal{C})$, understood as a measure of plausibility of a model class $\mathcal{C}$ [291]. It can be derived as the marginal probability of the posterior probability $p(\mathcal{O}, \mathcal{M}, \mathcal{C})$ defined in Equation (9.7),

$$p(\mathcal{C}) \quad = \quad \int_{\mathfrak{O}} \int_{\mathfrak{M}} p(\mathcal{O}, \mathcal{M}, \mathcal{C}) d\mathcal{M} d\mathcal{O} \quad = \quad k_1 p^0(\mathcal{C}) \int_{\mathfrak{O}} \int_{\mathfrak{M}} \frac{p^0(\mathcal{O}) p^0(\mathcal{M}) p^m(\mathcal{O}|\mathcal{M}, \mathcal{C})}{\mu(\mathcal{O})} d\mathcal{M} d\mathcal{O} \tag{9.14}$$

Once $p(\mathcal{C})$ is computed for every class, its value allows to rank the models according to how compatible they are with the observations. This also enables us to find a correct trade-off between model simplicity (i.e. low number of model parameters) and fitting to observations (i.e. reasonably low modeling error).

In the case that the model parameters m are Jeffrey's constants, they can be replaced by unitary logarithmic parameters $\overline{m}$,

$$m_m \quad = \quad m_m^0 e^{\overline{m} \ln \left(m_m^1 / m_m^0 \right)} \tag{9.15}$$

which maps the dimensional parameters m_m from the preferential range $m_m \in [m_m^0, m_m^1]$ to a non-dimensional Jeffrey's parameter range $\overline{m} \in [0, 1]$. This furthermore stabilizes the search algorithms and, in this case, the noninformative distribution $\mu(\mathcal{M})$ can just be replaced by a constant.

9.3.3 Assessment of the performance

This section aims at defining an evaluation framework for assessing the performance of the system identification methods defined in the following chapters. The system identification generally consumes a huge amount of experimental data and requires an expensive training process. Thus, for an optimal use of the available data set, the training/test is performed using the *leaving-one-out* technique [292]. Therefore, $N_r - 1$ signals are used to train a reference *cepstral* vector corresponding to a certain damage level, while the remaining signal is used for the test (N_r denotes the number of measurement repetitions on the same damage level). Rotating the measurements enables us to train the system always with N_r signals, while testing it with $N_d \times N_r$ signals (N_d is the number of dame area). The performance of the system is evaluated by defining a weighted error rate [293, 294, 295]. Let the results of

the test be a confusion table $R(i,j)$, with $i = 1, \ldots, N_d$, where $R(i,j)$ represents the measurements number at damage level i that have been classified as a damage level j. The weighted error rate is then defined as,

$$w_{err}[\%] \quad = \quad 100 \times \frac{\sum_{i=1}^{N_d} \sum_{j=1}^{N_d} R(i,j) \cdot \frac{|i-j|}{3}}{N_r \cdot N_d} \tag{9.16}$$

Thus, when the erroneously recognized class corresponds to a damage close to that of the correct class, the error has less influence on the error rate.

Part IV

RESULTS

10

Evaluation of the specimen's digital modeling

In this chapter, we evaluate the performance of our digital model for describing multi-layered specimens. In Section 10.1, we propose a synthetic comparison between the TM formalism and our novel model. Section 10.2 presents an experimental validation where the signals predicted by our model are contrasted against signals obtained experimentally.

10.1 Synthetic comparison between the TM formalism and the specimen's digital model

In this section, a numerical study is carried out to compare our novel digital modeling of the specimen with the TM formalism. With the aim of simulating real experimental conditions, the numerical characteristics (e.g. material, frequency, etc.) of that synthetic experiment are chosen according to the experimental framework described in Section 9.2.2. That is, we evaluate ultrasonic signals that mimic the measurements used to characterize a CFRP composite plate obtained using a through-transmission configuration with a low-frequency ultrasonic signal containing a wide range of frequencies. Considering the transmitter as a damped mechanical system with a single degree-of-freedom, the Fourier transform of the input signal $X(F)$, with $F = \Omega/2\pi$, is often assumed to be Gaussian [296] with the center frequency F_c of the transducer as mean and half bandwidth B as standard deviation. Hence,

$$X(F) = \frac{1}{\sqrt{2\pi}B} e^{-\frac{(F-F_c)^2}{2B^2}} \tag{10.1}$$

where the frequencies F, F_c and B are expressed in Hertz. The characteristics of the transmitted wave are set to $F_c = 5$ MHz and $B = 2.5$ MHz, respectively. A high resolution is chosen for signal sampling with a frequency $F_s = 200$ MHz, while a signal period of 10 μs is considered in order to ensure the capture of several wave echoes, providing $N = 2000$ samples. The resulting discrete-time input signal $x(n)$ and its magnitude spectrum $|X(\omega)|$ are shown in Figure 10.1.

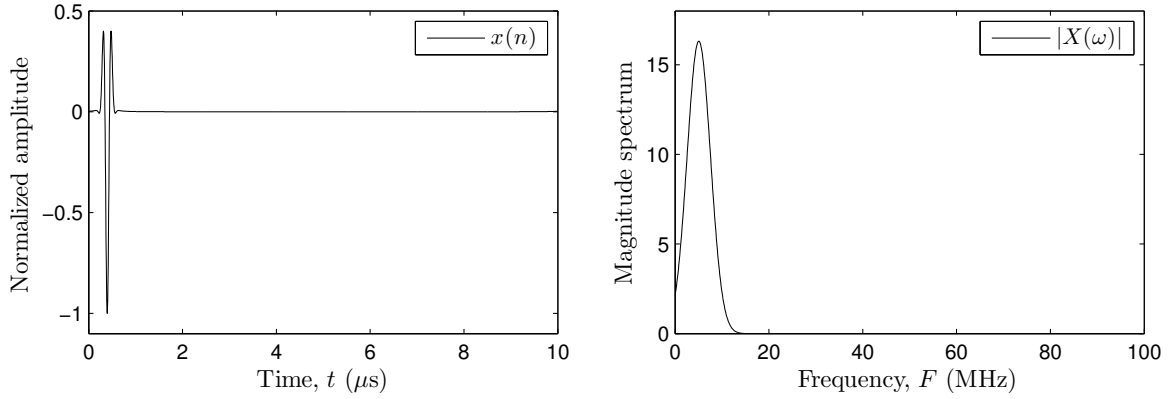

Figure 10.1: *Discrete-time input signal $x(n)$ (left) and its magnitude spectrum $|X(\omega)|$ (right). Note that the abscissas have been scaled according to a sampling frequency $F_s = 200$ MHz.*

The specimen considered is a layered CFRP symmetric plate which consists of five layers. Since a major damage mode in composites is delamination, an interface layer of much smaller thickness than both plies and wavelength of the central frequency is assumed between every two consecutive layers in the material. Thus, the resulting multilayered specimen consists of $M = 9$ layers, whose mechanical and geometrical properties are summarized in Table 10.1. These properties are chosen according to the experimental values provided in Table 9.3 (specimen (A)).

Layer (n°)	Young Modulus $E\ [GPa]$	Poisson Ratio $\nu\ [-]$	Density $\rho\ [kg/m^3]$	Attenuation $\alpha\ [Np/m]$	Thickness $a\ [mm]$
I, V	12.0427	0.2937	1874.7	395.4729	0.255
II, IV	8.9068	0.3148	1456.4	393.0409	0.185
III	7.0132	0.3308	1140.1	381.3457	0.770
$\mathcal{I}$	5.1321	0.3500	1002.0	402.1311	0.010

Table 10.1: *Mechanical and geometrical properties of the layers $I - V$ and interfaces $\mathcal{I}$ that compose the multilayered specimen used for the experimental comparison.*

From these properties, a discrete-time transfer function $H^D(z)$ can be obtained through Equation (7.25). Figure 10.2 shows the numerator $N(z)$ and denominator $D(z)$ coefficients of this function for the considered specimen. As can be observed, and in accordance with the discussion in Section 7.4, the numerator consists of a single coefficient $b_0 = 0.86$ at a sample-equivalent delay equal to the total thickness of the plate $\Lambda = 114$, while the denominator is mostly composed of zeros (as predicted from Equations (7.24)-(7.25)).

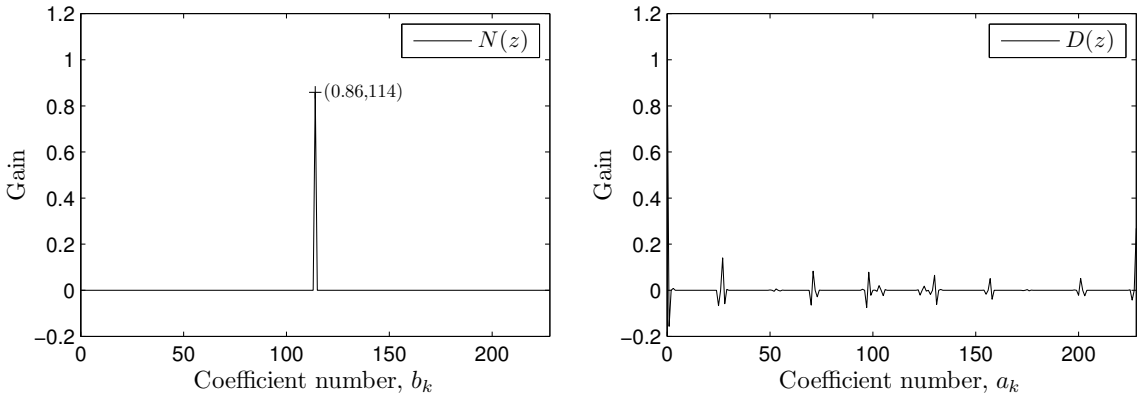

Figure 10.2: *Representation of the numerator $N(z)$ (left) and denominator $D(z)$ (right) coefficients from the discrete-time transfer function $H^D(z)$ for an undamaged specimen.*

Similarly, a transfer function can also be obtained for a damaged specimen. We briefly recall that, in CFRP plates, three phases of impact damages can be roughly identified, namely (1) matrix cracks in intermediate or back-wall layers, (2) delaminations between layers of different orientation, and (3) fiber breakage [237]. To illustrate the influence of impact damages on the filter coefficients, we impose matrix cracks (stiffness reduction of 5 %) to the back-wall layer (V) and a delamination between layers IV and V, modeled as a stiffness reduction (75 %) of the interface layer $\mathcal{I}$ in-between.

Figure 10.3 shows the transfer function coefficients for this damaged synthetic specimen. The shift ($\Lambda = 115$) and gain loss of the coefficient $b_0 = 0.64$ indicate a wave velocity and amplitude reductions, which are strongly correlated with a stiffness reduction and attenuation increase of the material, respectively. Furthermore, the damage tends to affect almost all the denominator coefficients a_k in amplitude, whereas additional coefficients appear at new positions (due to the symmetry break of the plate structure), thus reducing the sparsity ($||a_k||_0$). Unfortunately, a deeper physical interpretation from the a_k-domain is not easily assessable.

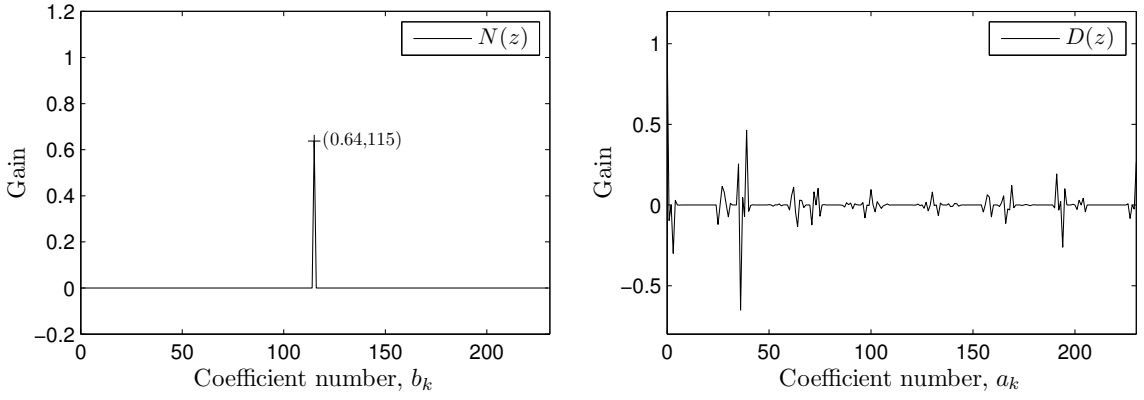

Figure 10.3: *Representation of the numerator $N(z)$ (left) and denominator $D(z)$ (right) coefficients from the discrete-time transfer function $H^D(z)$ for a damaged synthetic specimen.*

As commented in Section 7.4, our specimen's digital model enables to obtain the output signal $y(n)$ directly by filtering. Thus, Figure 10.4 compares the discrete time-domain signals obtained with the digital modeling of the specimen (labeled as $y_{DMS}(n)$) and the TM formalism (labeled as $y_{TM}(n)$). The undamaged case is represented in the left figure (a), whereas the damaged one is depicted in the right figure (b). Note that the digital model provides results nearly identical to those obtained with the TM formalism, but in a simpler way.

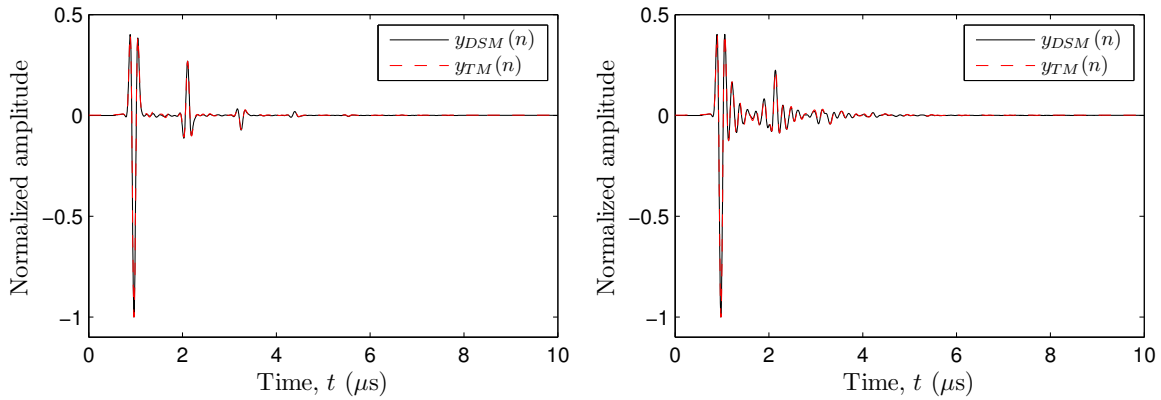

(a) Undamaged

(b) Damaged

Figure 10.4: *(a) Time-domain signals $y_{DMS}(n)$ and $y_{TM}(n)$ obtained for the undamaged specimen through the specimen's digital model and the TM formalism, respectively. (b) Same comparison for the damaged synthetic specimen.*

Since a bare visual inspection of the time-domain signals does not enable us to detect discrepancies between both formalisms, a further comparison is performed in the frequency-domain. The spectrum of the output signal provided by the specimen's digital model can easily be obtained by evaluating z in the unitary circle, namely $Y(\omega) = H(\omega)X(\omega)$ with $H(\omega) = H^D(z)|_{z=e^{j\omega}}$. In contrast, the spectrum of the output signal obtained with the TM formalism is directly derived from Equation (6.22) in a sampled form $Y(\omega_k)$. The magnitude and phase spectra for the undamaged specimen are depicted in Figure 10.5, while Figure 10.6 shows them for the damaged synthetic specimen.

Those figures show that the TM formalism and the digital model provide again nearly identical results. However, the latter has the advantage that the computation of the frequency response is analytical, while the former only provides values for individual frequencies (and its complexity thus depends upon the number of such frequencies). Finally, the scarce discrepancies between both formalisms can be explained as follows: Actually, both methods deliver approximations of the underlying ideal spectrum of the output signal $Y_{ideal}(\omega)$. On the one hand, the sampled spectrum obtained with the TM formalism differs from the ideal one due to the inherent resolution loss of the DFT. The latter effect may be reduced by increasing the number of samples of the input signal (by zero-padding), at the cost of a higher computational resources (increased number of $\boldsymbol{P}^{(k)}$- and $\boldsymbol{T}^{(k)}$-matrices). On the other hand, the frequency response obtained with the specimen's digital model deviates

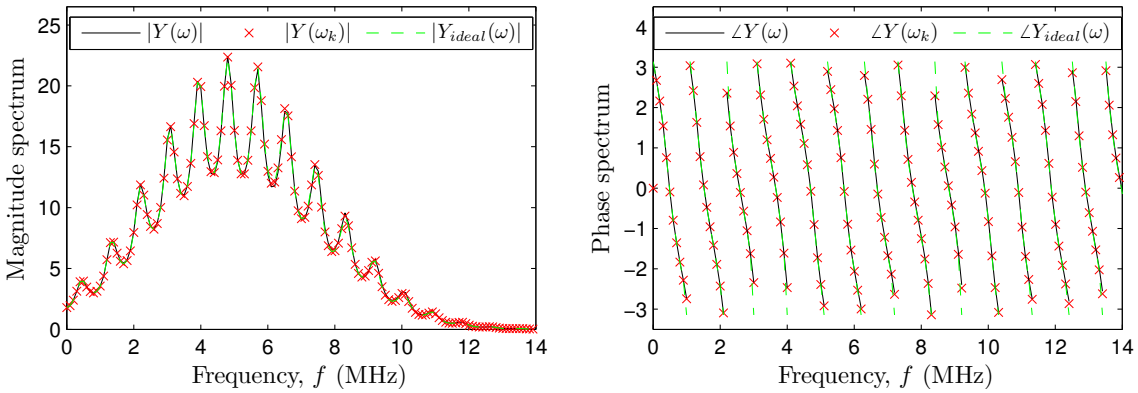

Figure 10.5: *Analytical magnitude ($|Y(\omega)|$) and phase ($\angle Y(\omega)$) spectra obtained through the proposed specimen's digital model (continuous line) for the undamaged specimen, together with the sampled versions obtained by the TM formalism (discrete crosses).*

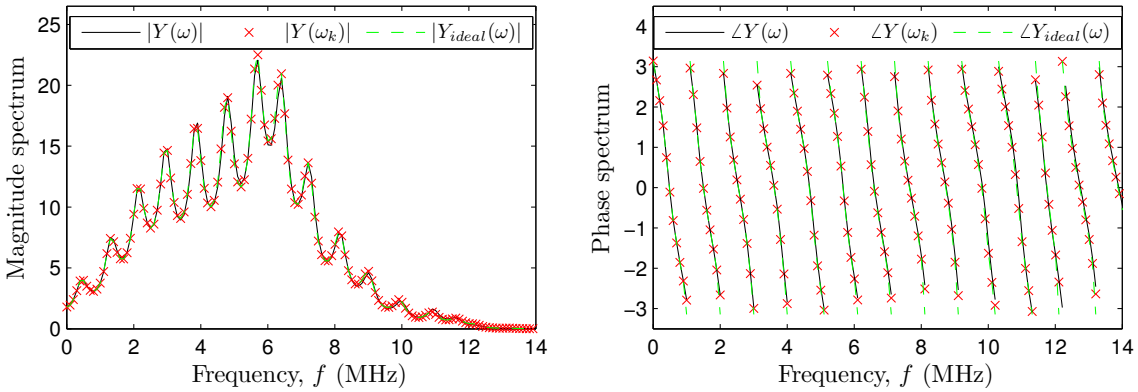

Figure 10.6: *Analytical magnitude ($|Y(\omega)|$) and phase ($\angle Y(\omega)$) spectra obtained through the proposed specimen's digital model (continuous line) for the damaged synthetic specimen, together with the sampled versions obtained by the TM formalism (discrete crosses).*

also from the ideal one since the delays m_i are restricted to integer values. As mentioned in Section 7.4, increasing the sampling frequency or applying a fractional filter formalism helps to mitigate this problem. This also increases the computational cost but to a lesser extend than zero-padding in the TM formalism (only the input signals are longer, but the number of non-zero coefficients a_k remains constant).

10.2 Experimental validation

The present section aims at demonstrating the capability of that digital model to predict the measurements obtained from several multilayered specimens (see Section 9.2.1). To evaluate the performance of our model, the key concept is to examine if the model can reproduce complex situations where numerous echoes overlap. To this end, we propose the following steps: Firstly, we need to determine the density of the single layers by measuring their volume and weight. The second tackled problem is the calibration of the model with the

signals experimentally obtained from the single layers. Then, the density and the values delivered by the calibration are used as input in the model to simulate the propagation through layered specimens. The matching between the resulting modeled signals and those experimentally obtained from the layered specimens is evaluated by observing if the residuals contain components other than measurement noise [297]. Finally, some aspects related to the coefficients of the obtained digital filters are discussed.

The calibration is achieved by the matching procedure described in Section 9.3.1, in which two model parameters (the wave velocity and the attenuation coefficient) are adjusted with GA's to find the optimal characterization of single layers (i.e. aluminum, brass, and PMMA). In this case, the minimization is a carried out in the time-domain as follows. From the mechanical and geometrical properties, a digital model of the specimen (i.e. a discrete-time transfer function $H^D(z)$) can be obtained through Equation (7.25) for each single layer. Consequently, given a discrete-time input signal $x(n)$, this model enables us to obtain the output signal $\tilde{y}(n)$ directly by digital filtering. Then, the latter is compared to the corresponding output signal $y(n)$ obtained experimentally. It is worth to mention that the input signal used here is not the synthetic one described in Figure 10.1, but a realistic ahead-shifted version of the output signal measured in water (obtained by removing the specimen) depicted in Figure 10.7. Indeed, such a strategy allows us to take into account the effect of the transducers within the wave propagation simulation.

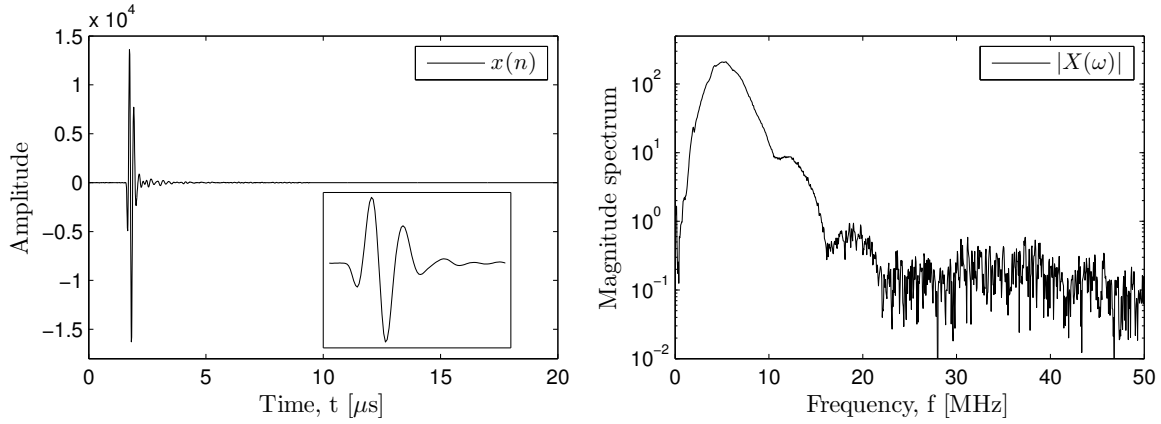

Figure 10.7: *Discrete-time input signal $x(n)$ (left) and its magnitude spectrum $|X(\omega)|$ (right) used as excitation for the synthetic layered specimens ($F_c = 5.5$ MHz). Note that the abscissas have been scaled according to a sampling frequency $F_s = 100$ MHz.*

The aforementioned calibration step has been applied to each measurement area and each frequency, and thus enables us to obtain statistically relevant range values for the mechanical properties of those single layers. The mean and standard deviation derived from those values, along with the density values, are summarized in Table 10.2. As can be observed, these values are in good agreement with those reported in Table 9.1. The values for specimens $S_{1,2}$, $S_{1,3}$ and $S_{1,5}$ are particularly close to those tabulated in the literature, whereas the values for specimens $S_{1,1}$ and $S_{1,4}$ slightly differ from them. Nonetheless, one

could have anticipated such discrepancy, since the density values for those specimens already indicated some divergence with respect to the expected values[1].

Specimen	Material	Density ρ [kg/m^3]	Wave velocity c_p [m/s]		Attenuation α [Np/m]	
			5.5 [MHz]	6 [MHz]	5.5 [MHz]	6 [MHz]
$S_{1,1}$	Aluminium^a	2876	6198 ± 8	6200 ± 9	49.0 ± 1.7	49.7 ± 1.4
$S_{1,2}$	Aluminium^b	2663	6382 ± 14	6377 ± 13	24.6 ± 0.2	24.3 ± 1.0
$S_{1,3}$	Brass	8626	4207 ± 12	4206 ± 14	23.0 ± 2.0	23.2 ± 2.0
$S_{1,4}$	PMMA^a	1168	2613 ± 3	2614 ± 2	105.8 ± 7.2	98.1 ± 5.0
$S_{1,5}$	PMMA^b	1195	2681 ± 4	2682 ± 2	69.4 ± 1.2	71.7 ± 1.1

Table 10.2: *Mechanical properties of the materials obtained from the calibration procedure (in this case, the configuration parameters of the GA's were set to $N_g = 200$ and $N_p = 50$).*

Figure 10.8 depicts the resulting matching (for the optimal model parameters) between a measurement $y_{S_{1,j}}(n)$ and the numerically predicted model $\tilde{y}_{S_{1,j}}(n)$ for the single layers, $\forall j = 1, \ldots, 4$. As can be seen, a fairly good matching is obtained.

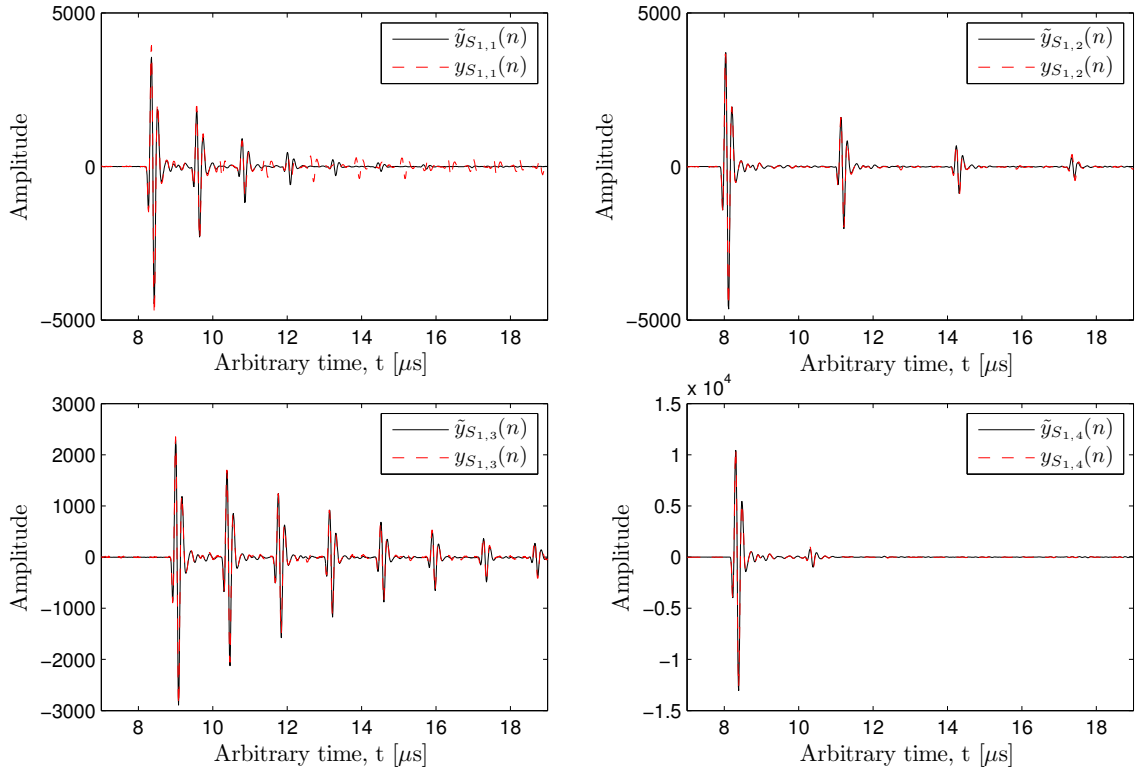

Figure 10.8: *Comparison between experimental measurements and signals predicted by the specimen's digital model for the single layers $S_{1,j}$, $j = 1, \ldots, 4$.*

[1]Consequently, those results suggest that specimen $S_{1,1}$ probably is an alloy made of aluminum and some other metal. In the same vein, specimen $S_{1,4}$ might be a plastic material with nearly similar properties to PMMA (e.g. PEEK, etc.). Those differences are definitely not surprising, since the samples were obtained from spare laboratory materials, and in no case they discredit the results.

The residuals $e_{S_{1,j}}(n)$ are plotted in Figure 10.9 to highlight which parts of the wave responses the model could not reproduce. As can be observed, there are two main sources of modeling error. The first one is common to all materials and is highly correlated to the signal echoes. This *approximation* error approximately amounts to 10% of the signal's amplitude, and can thus be considered as acceptable. It arises foremost from two factors: (1) the modeled signal can diverge from the experimental one since the delays m_i are restricted to integer values, and (2) the layers are idealized as homogeneous material (however, microheterogeneities might be present in the material, which are not contemplated in the model). The second error is common to all metals and can be considered as a *phenomenological* error. Indeed, some echoes with nearly constant amplitudes (noticeable in the upper left plot of Figure 10.8) are definitely not present in the model. Those echoes are hypothesized to be transversal waves (S-waves) originated by longitudinal waves (P-waves) due to some superficial or contact effects (e.g. mode conversion due to a nonplanar water-specimen interface). It is therefore not surprising that the model does not reproduce them, since it has been developed to cope only with longitudinal waves. In any case, this *phenomenological* error has an even lower amplitude than the *approximation* one.

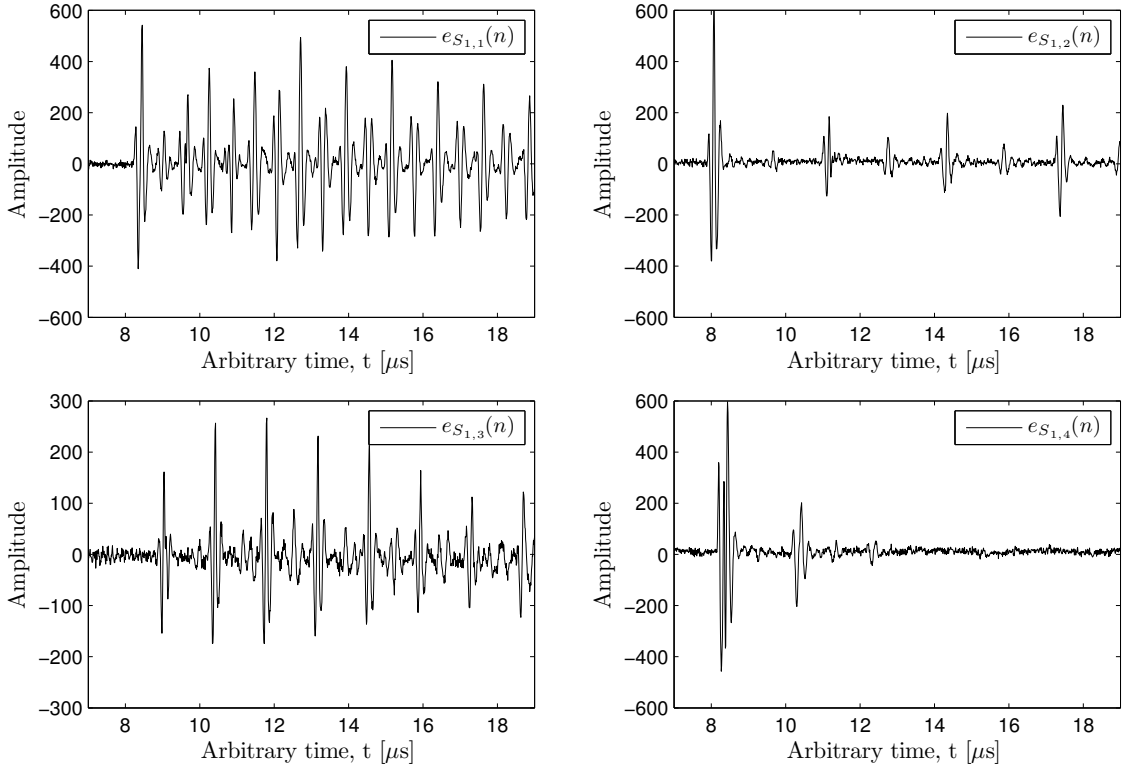

Figure 10.9: *Error between experimental measurements and signals predicted by the specimen's digital model for the single layers* $S_{1,j}$, $j = 1, \ldots, 4$.

Using the properties obtained in Table 10.2, a digital model (i.e. transfer function $H^D(z)$) can straight-forwardly be computed for each multilayered configuration enumerated in Table 9.2. The resulting matching between a measurement $y_{S_{2,j}}(n)$ and the numerically pre-

dicted model $\tilde{y}_{S_{2,j}}(n)$ for the bi-layered specimens, $\forall j = 1, \ldots, 4$, is depicted in Figure 10.10. Note that the right plots represent the same specimens as in the left plots, but measured in their reverse side. Again, a fairly good matching is obtained between the experimental and modeled signals. In addition, left and right plots are nearly similar and further support both the reproducibility of the experiment and the capability of the model to predict the measurements[2]. Finally, it is noteworthy that the transversal waves were almost completely filtered out by the plastic layer.

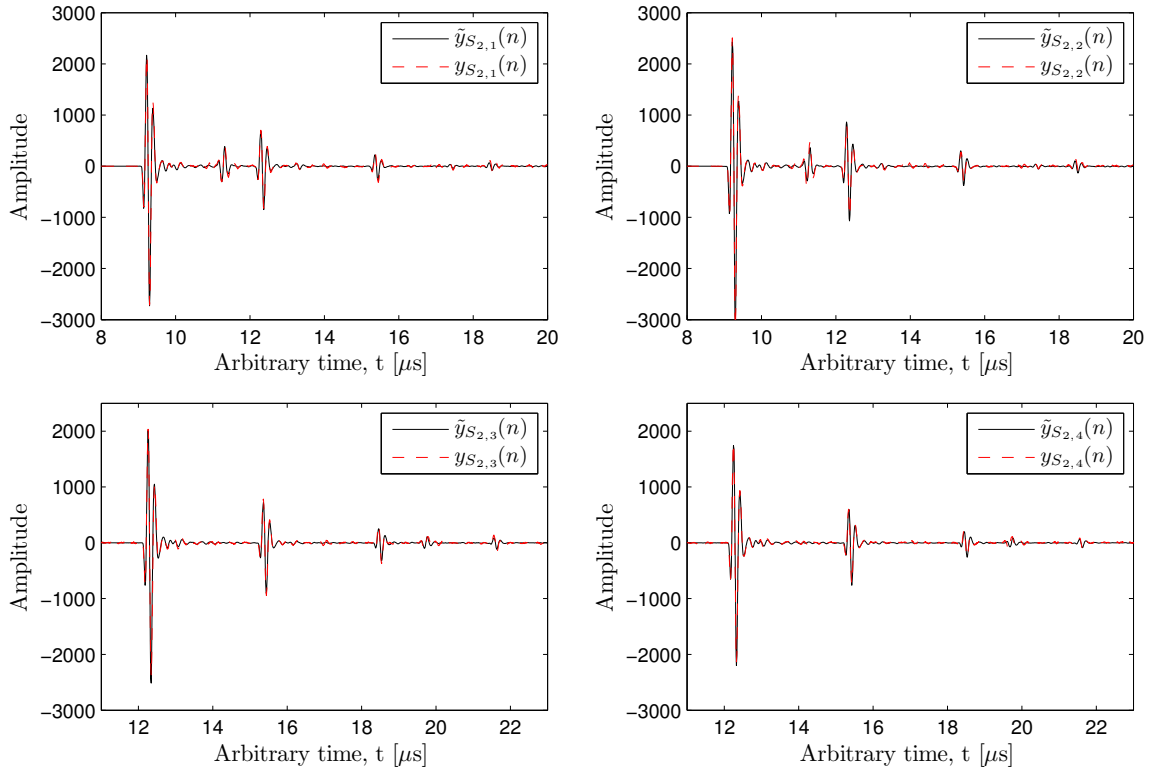

Figure 10.10: *Comparison between experimental measurements and signals predicted by the specimen's digital model for the bi-layered specimens* $S_{2,j}$, $j = 1, \ldots, 4$.

Figure 10.11 depicts the resulting matching between a measurement $y_{S_{3,j}}(n)$ and the numerically predicted model $\tilde{y}_{S_{3,j}}(n)$ for the three-layered specimens, $\forall j = 1, 2$. The obtained matching between the experimental and modeled signals is reasonably good again. As for the bi-layered case, the right plot is again nearly identical to the left one, except for the slight amplitude difference. In such a configuration, the transversal waves are now totally absorbed by both plastic layers.

[2]The slight discrepancy in amplitude can be explained as follows: The layered specimens were disassembled and mounted again between each specific measurement, and this task possibly leads to slight changes in the contact pressure between the single layers, which in turn leads to a small alteration of the wave front amplitude.

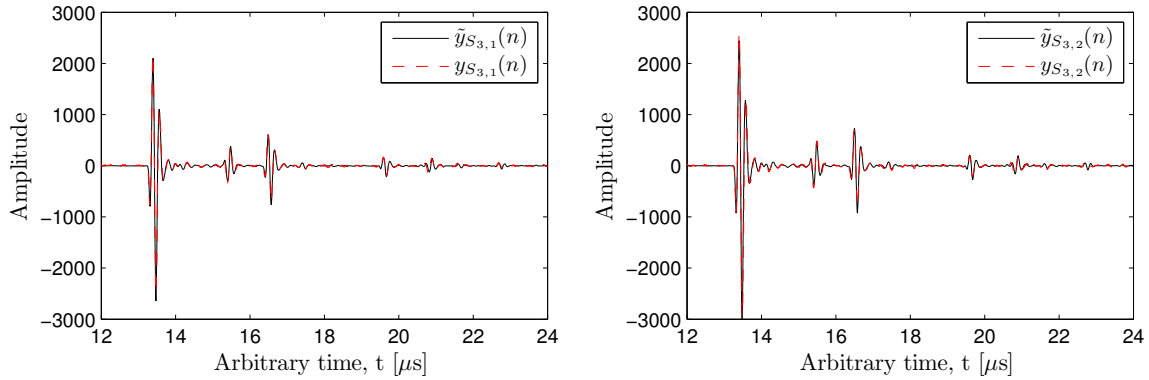

Figure 10.11: *Comparison between experimental measurements and signals predicted by the specimen's digital model for the three-layered specimens* $S_{3,j}$, $j = 1, \ldots, 2$.

Finally, the resulting matching between a measurement $y_{S_{4,j}}(n)$ and the numerically predicted model $\tilde{y}_{S_{4,j}}(n)$ for the four-layered specimens, $\forall j = 1, \ldots, 4$, is depicted in Figure 10.12. In this case, the obtained matching between the experimental and modeled signals is remarkable, especially because in this situation, numerous and overlapped echoes are observable. This configuration definitely supports the potential of our digital model to face up complex wave responses originated from multilayered specimens.

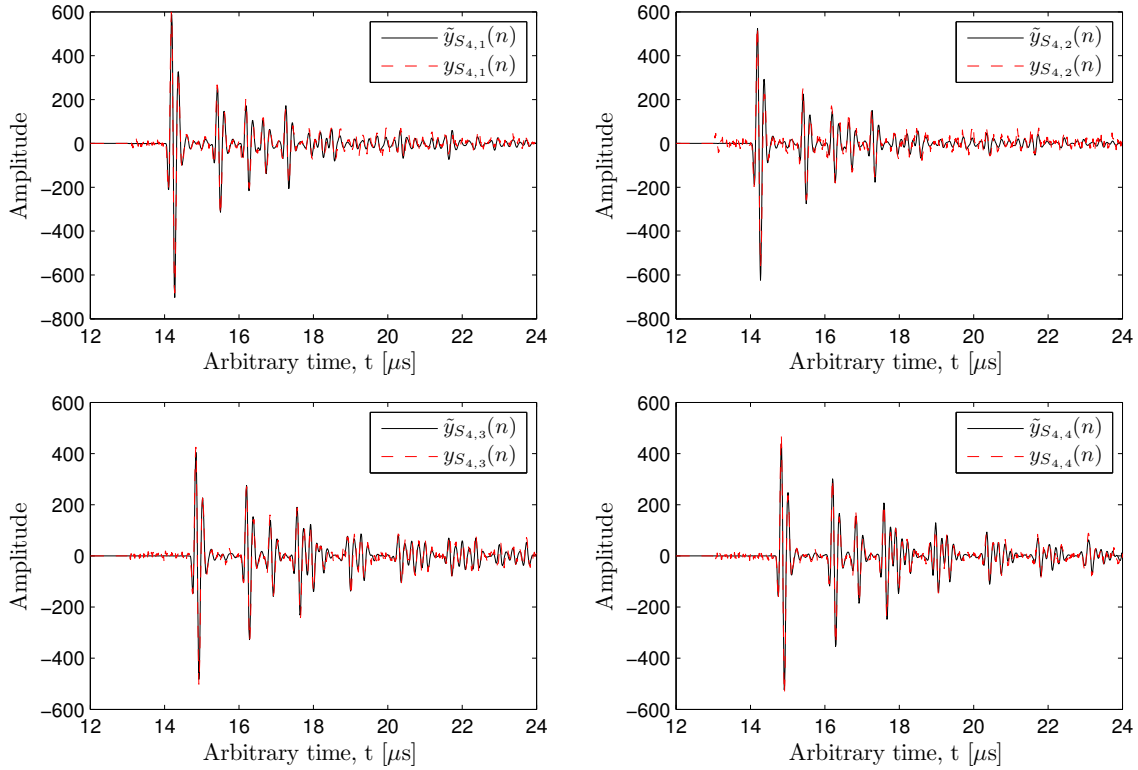

Figure 10.12: *Comparison between experimental measurements and signals predicted by the specimen's digital model for the four-layered specimens* $S_{4,j}$, $j = 1, \ldots, 4$.

A further inspection of the modeling error shows that the residuals $e_{S_{4,j}}(n)$ $(j = 1, 4)$ now only contain few components other than measurement noise, i.e. the *phenomenological*

error has entirely disappeared and the *approximation* error has a more random distribution. One can thus conclude that this model can satisfactorily be used to describe multilayers.

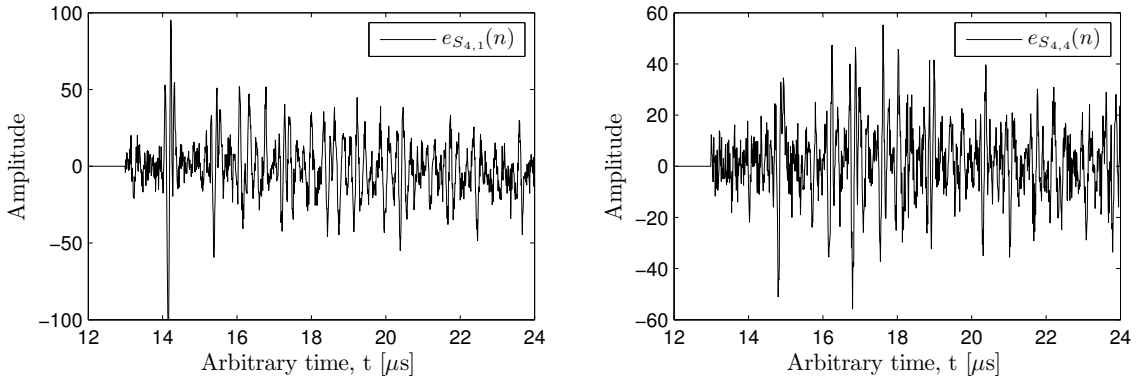

Figure 10.13: *Error between experimental measurements and signals predicted by the specimen's digital model for the four-layered specimens* $S_{4,j}$, $j = 1, \ldots, 4$.

Finally, as an example, the numerator $N(z)$ and denominator $D(z)$ coefficients of the discrete-time transfer function for the specimen $S_{4,4}$ is shown in Figure 10.14. As expected, the numerator consists of a single coefficient $b_0 = 0.0291$ at a sample-equivalent delay equal to the total thickness of the plate $\Lambda = 1315$, and the denominator is mostly composed of zeros (only 32 non-zero coefficients from 2631).

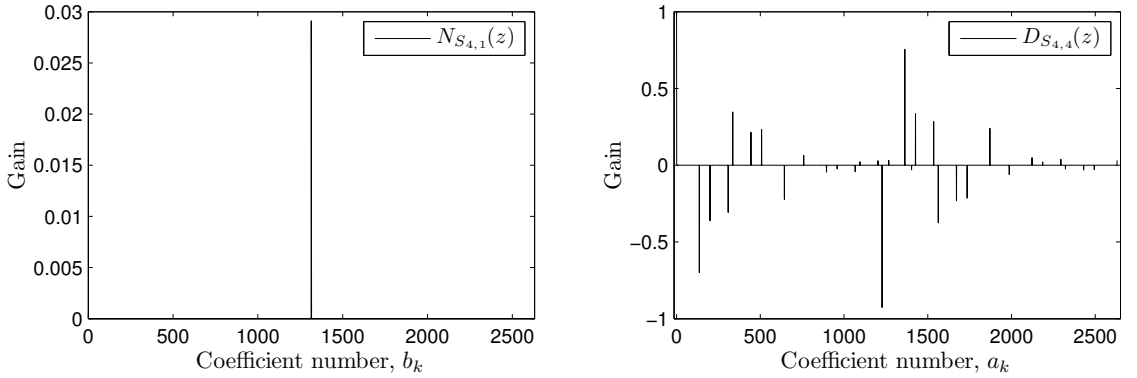

Figure 10.14: *Representation of the numerator* $N(z)$ *(left) and denominator* $D(z)$ *(right) coefficients from the discrete-time transfer function* $H^D(z)$ *for a four-layered specimen.*

Although a rigorous physical interpretation from the a_k-domain is not easily assessable, it is noteworthy that (1) the number of non-zero coefficients a_k is not directly related to the number of observable echoes in the wave response; and that (2) the a_k follow a repetitive pattern where higher-order coefficients are somehow sign-changed and amplitude-reduced versions of lower-order ones. Consequently, this model based on the physical properties of the layers seems to be more precise than the proposals based on Bernoulli-Gaussian models, which assume that the output signal is made of superimposed Gaussian echoes that are time-shifted, amplitude-scaled, and noise-corrupted version of the input signal [112, 131].

10.3 Discussion

As it has been shown, our proposed digital modeling of the specimen fairly good approximates the responses of the real specimens. Initially, the TM formalism could also be applicable to such approximations in principle, but its direct implementation has been found to suffer from numerical instabilities, particularly when considering layers of large thickness and high-frequency ultrasound (i.e. the large *frequency-thickness* products that arise in this formalism are usually referred to as the large "fd-problem" [79]). Indeed, the layered configurations presented here deal with relatively large layers, whereas the used frequencies are also relatively large (that is, the wave lengths corresponding to those frequencies are particularly small compared to the size of the layers). To evaluate the applicability of the TM formalism in this case, let us consider the specimens $S_{1,1}$ and $S_{4,3}$, in order to cover a broad range of specimen's thicknesses. Figure 10.15 depicts the output signals $\hat{y}_{S_{1,1}}(n)$ and $\hat{y}_{S_{4,3}}(n)$ predicted by the TM formalism for a single layer and a four-layered specimen. As can be observed, both cases suffer from numerical instabilities, even when considering a single layer that is relatively thin. These anomalies are due to the poor conditioning of the transfer matrices when performing multiplications that combine both decaying and growing terms. In the first case (left plot), we represent the waveform obtained while considering only the stable frequencies (approximately up to 15 MHz). As can be seen, the resulting signal covers a coherent amplitude range, but the waveform is completely altered. In the second case (right plot), we represent again the waveform obtained while considering only the stable frequencies (approximately up to 10 MHz). In such a case, the signal is a sine-wave at a low-frequency, but with a huge amplitude.

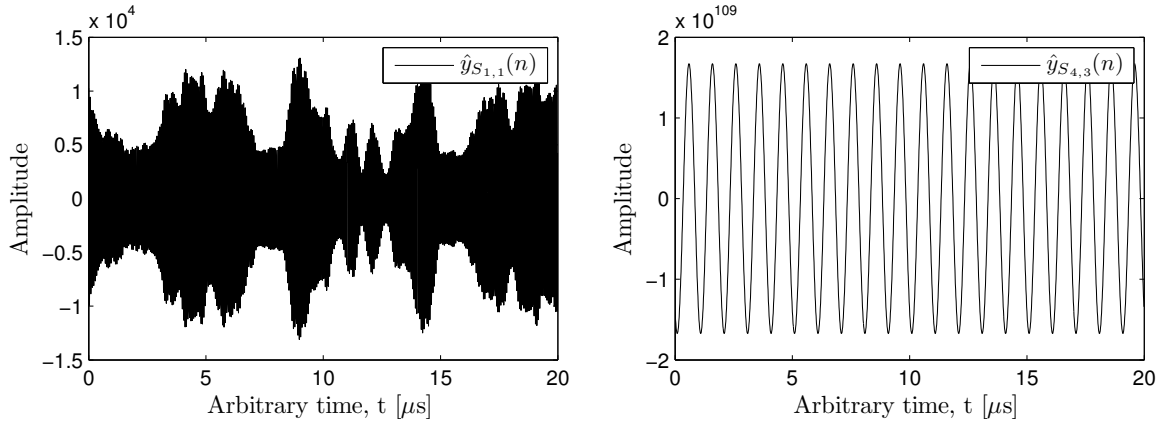

Figure 10.15: *Examples of numerical instabilities that may arise in the TM formalism in the case of large "fd-problems".*

As commented in Section 3.3.1, many modifications of the original TM approach and other slightly alternative methods have been proposed to palliate this precision problem. However, none of them is really efficient when dealing with complex problems (i.e. some

suffer from high computational resources, whereas others are limited to multilayered materials that consist of a reduced number of layers). To conclude, Table 10.3 summarizes the strengths and limitations of our digital model with respect to the original TM approach.

Models	Specimen's digital model	TM approach
Strengths	◦ Very-low complexity ◦ Valid for any number of layers ◦ Valid for absorbing layers ◦ Valid for layers of unequal wave-travel time ◦ Suitable for large "fd-problems" ◦ Enables to compute the underlying sparse transfer function	◦ Low complexity ◦ Valid for any number of layers ◦ Valid for absorbing layers ◦ Valid for layers of unequal wave-travel time
Limitations	◦ Limited to integer delays	◦ Depends on the input signal's appearance ◦ Depends on the number of samples of the input signal ◦ Unstable for large "fd-problems"

Table 10.3: *Strengths and limitations of the novel digital modeling of the specimen.*

11

Robust parametrization for impact damage detection in CFRP plates

In this chapter, we propose different approaches for modeling ultrasonic signals and evaluate their discriminative capability for impact damage identification in CFRP plates. Section 11.1 proposes an initial approximation to find a robust parametrization of such signals by applying a signal processing and features extraction procedure. In Section 11.2, we propose the use of sparse and physics-based models for some practical NDE applications and show that these models improve the results provided by common spectrum estimation techniques.

11.1 Identification results through classical spectral estimation methods

This section aims at enhancing the interpretation of ultrasonic signals obtained from an impacted CFRP plate by applying classical parametrization techniques to extract relevant features from these signals. To this end, a cepstral-based feature extractor is firstly designed and optimized by using a classification system based on *cepstral* distances. Then, this feature extractor is applied in a model-based estimation procedure which, by using a numerical model of the specimen, infers the values of the damage parameters [293].

11.1.1 Ultrasonic NDE framework

The specimen tested here is the layered CFRP symmetric plate described as specimen (B) in Table 9.3 that consists of four layers. After acquisition, the captured signals have been preprocessed in order to provide a suitable representation of the ultrasonic signal. In a first

step, the signals have been decimated at a sample frequency F_s of 20 MHz (i.e the decimation factor is $M = 5$ and the number of samples is $N = 300$), in order to reduce part of the noise and focus on the frequency band of interest.

On the other hand, in order to finally provide consistent damage information that characterize the specimen health state, the model-based estimation strategy described in Section 9.3 is applied to find the values of the damage parameters θ that best fit the experimental measurements. In this experiment, the model used to idealize the experimental system describing the ultrasonic wave propagation in multilayered composites consists of the TM formalism described in Chapter 6. The identification of the damage parameters is performed according to Fahim *et al.* [298], assuming that the damage in each layer, respectively in each interface, is strongly correlated with a reduction of the Young modulus. GA's are applied to minimize Equation (9.5), and provide the inverse problem optimal solution.

11.1.2 Cepstral-based feature extractor design and optimization

First, the selection of a suitable analysis window is considered. In this case, a classical Hamming window has been applied to the ultrasonic signals. In our case, the window is foremost used to weight the signal samples over the time (see Section 4.2.1). As illustrated in Figure 11.1, while in the original signal (left) the first peak (wave front) predominates, the windowed signal (right) exhibits accentuated echoes amplitude, representative of the successive reflections of the transmitted wave between the interface specimen/transducers.

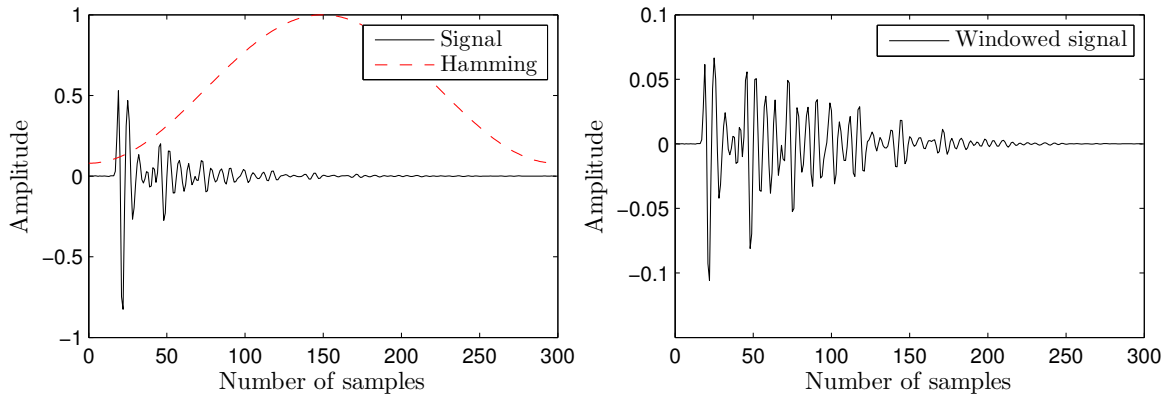

Figure 11.1: *Use of a temporal window to show off the echoes of the ultrasonic signal.*

Windowed signals are then transformed to the cepstral-domain. This experiment focuses on the *real cepstrum* $c(n)$, which is defined according to Equation (4.48). Preliminar experiments showed that the *complex cepstrum* $\hat{c}(n)$ does not provide any improvement, while its computation is cumbersome due to the unwrapping of the digital phase. Consequently, only the *real cepstrum* is considered.

In order to evaluate the effect of the analysis window and the cepstral-domain on the discriminative capability for impact damage assessment, a classification system based on the *leaving-one-out* technique has been developed as in Section 9.3.3: On the one hand, the captured signals are directly evaluated in the time-domain using an Euclidean distance

(SIGNAL). On the other hand, *cepstra* obtained from those signals are evaluated with an Euclidean (*cepstral*) distance (RC). For both domains, several analysis windows of variable length are selected, namely a rectangular window of 300 samples (R-300) and Hamming windows of decreasing length (H-300, H-200, H-150 and H-100) to successively weight slightly different wave echoes. The performance of the system is evaluated by making use of the weighted error rate defined in Equation (9.16). Table 11.1 shows that the use of the cesptral-domain drastically reduces the weighted error rate in comparison with the use of the time-domain. In addition, it can be observed that the use of Hamming windows improves the classification in comparison with the rectangular one, except for the window that amounts to 100 samples. Thus, it can be concluded that the echoes are as important as the wave front for discriminating between the different damage levels. Therefore, the echoes may be enhanced with a Hamming window, whose optimal longitude amounts to a range of $150 - 300$ samples.

	R-300	H-300	H-200	H-150	H-100
SIGNAL	32.50	26.25	26.11	26.94	30.55
RC	12.08	10.41	9.72	8.88	16.25

Table 11.1: *Weighted error rate (in %) obtained for several analysis windows and domains.*

In order to further improve the classification, it is common to restrict the Euclidean distance to L *cepstral* coefficients. This process is called *liftering* and not only allows to reduce the number of *cepstral* components in computations but also corresponds to a smoothing of the spectrum, preserving its spectral envelope while removing the fine detail information (see Section 4.2.5). In addition, applying windows different from the rectangular also allows to weight the *cepstral* coefficients depending on their discriminative performance. Among them, it has been shown that a *raised-sine* window could be successfully applied for damage classification using ultrasonic signals [299]. Alternatively, we can also consider an AR modeling approach to estimate the spectrum (see Section 4.2.2). The expected effect of using a signal model is to reduce the variance when the spectrum is estimated. In addition, spectrum smoothing also represents a further advantage of using a signal modeling approach.

In a second experiment, we have evaluated the effects of smoothing over the discriminative capability of the *cepstrum* for damage identification. Both approaches, AR modeling and *liftering*, have been jointly tested. In order to do this, weighted error rates for different LPC orders and *liftering* window lengths have been computed. This experiment will allow us to design an optimal LPC modeling and *liftering* of the ultrasonic signals. The corresponding (bidimensional) results are shown in Figure 11.2. As can be observed, the obtained results show a clear minimum (weighted error rate less than 2%) for a *raised-sine liftering* window, whose length amounts to $28 - 29$ *cepstral* coefficients. Moreover, this minimum appears to be independent of the AR model order, as long as it is high enough ($p > 20$). Consequently, the damage parameters reconstruction performed in the next section to validate the feature

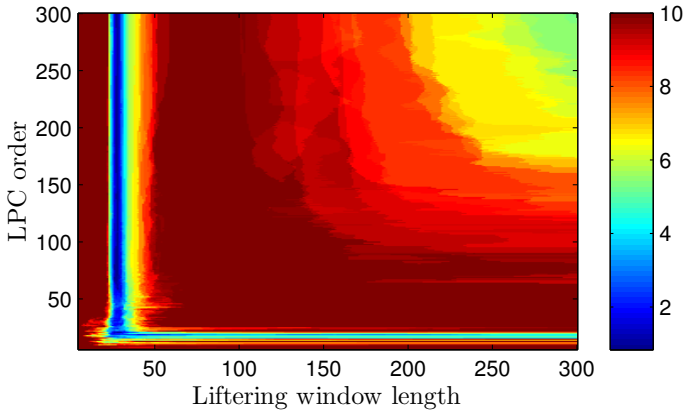

Figure 11.2: *Weighted error (in %) with respect to different prediction orders and liftering window lengths.*

extractor will be performed with a *raised-sine liftering* window of 28 samples and a prediction order of 28. It is worth to note that this number coincides with the echo time in number of samples (that is the time needed by the wave to cross twice the specimen). This could suggest that the *cepstrum* is, in some way, able to test the layer symmetry in the specimen (i.e. the undamaged composite considered here has a symmetric layer distribution). When the specimen is damaged, symmetry is usually broken, and a *liftering* window of echo length applied over the *cepstrum* is able to measure it.

11.1.3 Feature extractor validation

This section aims to validate the previous signal processing and feature extraction procedure. The identification of the damage distribution is assessed by defining a finite set of parameters, as described in Section 9.3.1. The configuration pattern for those parameters is selected with respect to the following assumptions:

- The damage parameters evolution is monotonically dependent on the damage level.
- Damage, such as delamination, concentrates mostly in the last interface, and then propagates internally and nearly symmetrically.

Consequently, the set of parameters is restricted to 3 parameters: θ_1 denotes the Young modulus of the extremity layers, θ_2 the Young modulus of the extremity interface, and θ_3 the Young modulus of the middle interface. Each parameter is defined in a dimensionless and logarithmic scale, with respect to the undamaged state.

The robustness of the model-based estimation procedure is illustrated in Figure 11.3. This figure compares the results obtained by performing the optimization directly in the time-domain with the ones obtained when the optimized *cepstral* parametrization described in the previous section is applied. The damage correlation parameters are plotted against the impact energy values. Each box has lines at the median value (red), at the lower and upper quartile values, and whiskers at the minimum and maximum values (black). Outliers are represented by a red cross. In these plots, a consistent decrease of the elastic modulus is

expected as the damage energy increases. As can be observed, the optimization performed

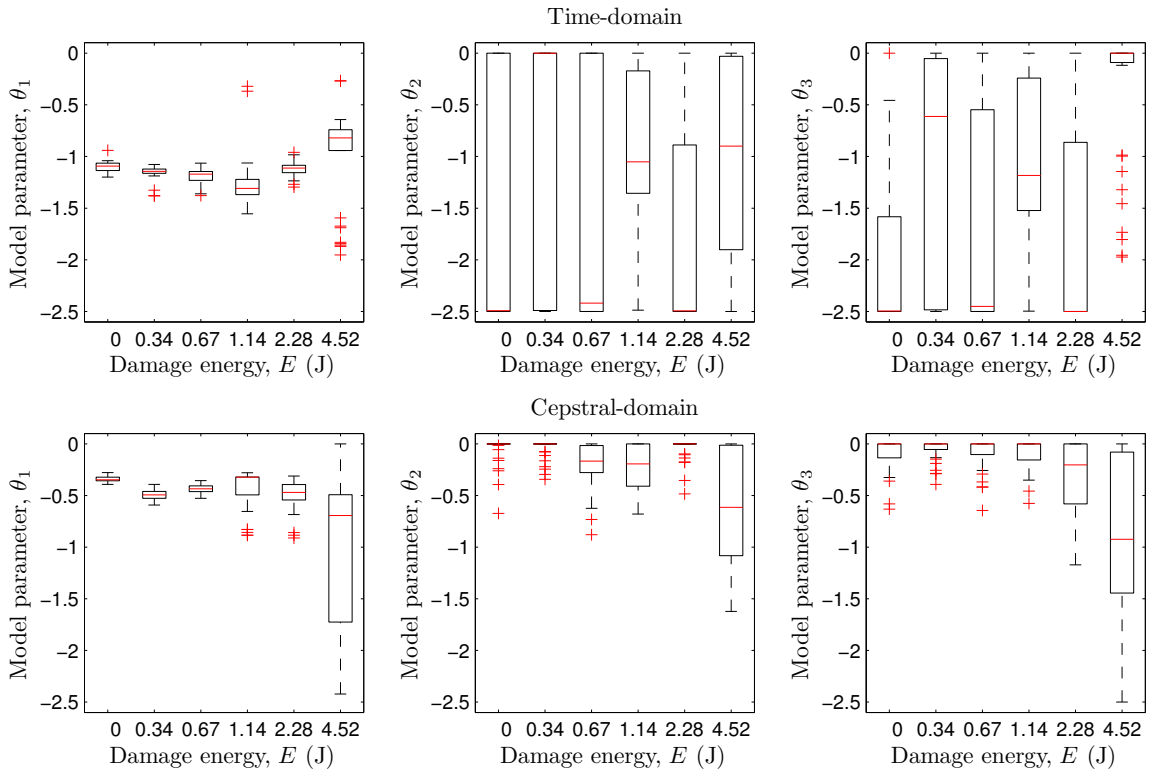

Figure 11.3: *Representation of the damage parameters evolution for simulations performed in the* time-domain *(first row), and* cepstral-domain *(second row) (in this case, the configuration parameters of the GA's have been set to* $N_g = 200$ *and* $N_p = 50$*).*

in the cepstral-domain leads to a more consistent damage evolution than the one delivered by the time-domain solution. In addition, the reduced set of *cepstral* features improves the statistical distribution of the damage parameters: (1) The variability of the damage parameters at each damage level is drastically reduced; and (2) the median values of the damage parameters consistently decrease while increasing the damage level. A careful interpretation allows us to conclude that matrix cracks θ_1 initially appear on the extremity layers and increase with the damage level. Those are closely followed by delaminations θ_2, which occur at early stage of the impact energy and increase with the damage level. Finally, delaminations θ_3 occur at some later stage of the impact energy for the inner interface, and those observations thus validate the aforementioned hypothesis (i.e. monotonic evolution and damage propagation).

11.1.4 Discussion

This experiment shows the capability of the real LPC *cepstrum* to discriminate the damage level of a CFRP plate subjected to different impact energies. The discriminative performance of the proposed parametrization has been evaluated by a system based on *cepstral* distances with a AR model that identified the concrete damage level corresponding to a given test

signal, leading to the following conclusions: (1) It has been shown that it is recommended to include the wave echoes to perform the analysis, and they may thus be enhanced using a suitable analysis window. (2) The *cepstrum* is an appropriated domain to perform a feature extraction. Concretely, this experiment has presented a *cepstral* coefficients selection based on the use of a simple *liftering* window with the appropriate size (that is twice the specimen's thickness in samples number).

Finally, the optimal *cepstral* parametrization has been inserted in a model-based estimation procedure, and enabled us to consistently reconstruct the damage parameters corresponding to different impact energies.

11.2 Identification results through sparse and physics-based models

In a first part, we take full advantage of the digital modeling of the specimen obtained in Chapter 7, exploiting its sparse structure for some practical NDE applications. To palliate some aspects of this modeling, a purely heuristic sparse signal model is considered in a second part.

11.2.1 Physics-based digital signal model

To evaluate the capability of our specimen's digital model for damage discrimination, a set of experiments are carried out. In the first experiment, a damage detection framework takes advance of the convenient filter form provided by the specimen's digital model. In the second experiment, a damage identification system based on *cepstral* distances with an underlying model as in the previous is developed.

Damage detection evaluation

The nature of the proposed digital model, namely its all-pole structure, allows a simple and efficient use for industrial NDE applications. Ultrasonic response signals obtained from specimens can be whitened by inverse filtering, where the filter is computed from the material's properties provided by the manufacturer. While the inverse filtered response from the undamaged specimen is expected to be similar to the original excitation signal applied, the opposite is awaited for damaged specimens, due to the corresponding model mismatch, resulting in an effective damage detection procedure with a relatively low cost.

In this first experiment, we evaluate this approach on the 10×6 signals obtained from the symmetric CFRP plate consisting of five layers, named as specimen (A) in Table 9.3. Given the transfer function $H^D(z)$, which represents the undamaged multilayered composite material in a through-transmission configuration, the experimental response signal $y(n)$ can be whitened by inverse filtering, resulting in an approximation $\tilde{x}(n)$ of the original excitation signal $x(n)$ applied to the specimen. In general, it is not guaranteed that an inverse filter ${H^D}^{-1}(z)$ fulfill stability conditions. In our case, $H^D(z)$ is an all-pole filter, and thus the resulting inverse one is a FIR filter, which is inherently stable and can be computed straightforwardly. The specimen's state can then be classified by defining a modeling error in terms

of the squared error between the actual excitation signal $x(n)$ and the inverse filter response $\tilde{x}(n)$,

$$\varepsilon_w \;=\; \sum_{n=0}^{N-1} e_w(n)^2 \;=\; \sum_{n=0}^{N-1} \left(\tilde{x}(n) - x(n)\right)^2 \tag{11.1}$$

where $e_w(n)$ denotes the whitening error. Figure 11.4 shows a diagram of the proposed scheme. It is expected that the experimental response signal obtained from an undamaged specimen $y_0(n)$ is well-approximated by the model, so it should be well-whitened, resulting in a low modeling error value ε_w. In contrast, the experimental response signal obtained from a damaged location $y_i(n) \in \{y_1(n), \ldots, y_5(n)\}$ is expected not to be well-whitened, leading to larger modeling error values.

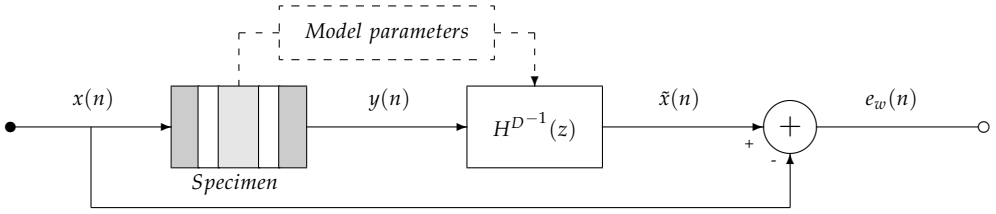

Figure 11.4: *Diagram of the inverse filtering scheme proposed to compute the whitening error.*

Nevertheless, the former damage detection framework still exhibits several drawbacks. First, the response signal energy decreases significantly as the impact energy increases. Thus, the modeling error ε_w alone is not as discriminative as initially expected. We get through this difficulty by introducing a relative modeling error $E_r = \varepsilon_w/\varepsilon_{nw}$, where ε_{nw} denotes the original response signal energy (non-whitened), that is $\varepsilon_{nw} = \sum_{n=0}^{N-1} y(n)^2$. Secondly, as commented in the previous section, the damage information is mostly concentrated in the wave echoes (which represent successive wave transitions across the specimen), whereas the wave front remains almost unsensitive to damage. To account for this fact, temporal windowing $w(n)$ can be applied to the signals being compared, or more easily over the whitening error signal $e_w(n)$.

To evaluate the aforementioned damage detection framework, a model fitness measure is introduced as $\rho = 1/E_r$. Figure 11.5 shows the ρ-values obtained for the experimental data set, using five different temporal windows. The length of these windows was chosen so that the analysis focuses on the signal echoes. The first window is a rectangular one of full signal length (RECT$^{(0)}$), whereas the other applied rectangular windows (RECT$^{(i)}$) depend on the specimen thickness Λ expressed in number of samples. To focus on the later echoes, 2Λ samples are successively removed from the analysis, that is, RECT$^{(1)}$ considers all the signal samples except the ones corresponding to the wave front, RECT$^{(2)}$ all the signal samples except the ones corresponding to the wave front and the first echo (a wave that crossed thrice the specimen), and so on. The last applied window is a Hamming window of signal length, used to enhance the echoes as in Section 11.1.2. As can be observed, moderate and severe damage levels $(2-5)$ are correctly discriminated by the proposed measure

independently of the window used. The influence of the temporal windowing can be appreciated better for no and mild damage levels (0 and 1), which are, as expected, the most difficult cases to discriminate. By considering the complete signal (RECT$^{(0)}$), it is difficult to establish a clear threshold to discriminate between these levels. In contrast, removing the wave front (RECT$^{(1)}$) or enhancing the echoes (HAMM) by windowing provides significant improvements. Shifting the rectangular window on the later echoes (RECT$^{(2)}$) improves further the discrimination. Indeed, the proposed analysis provides the best results for the latter window, and a fitness threshold around 1.05 (see Figure 11.5), leading to 10% of type I errors and 0% of type II errors. Removing further echoes (RECT$^{(3)}$) makes the results worse. This could be explained because only a few samples, which suffer from severe quantization effects, are considered.

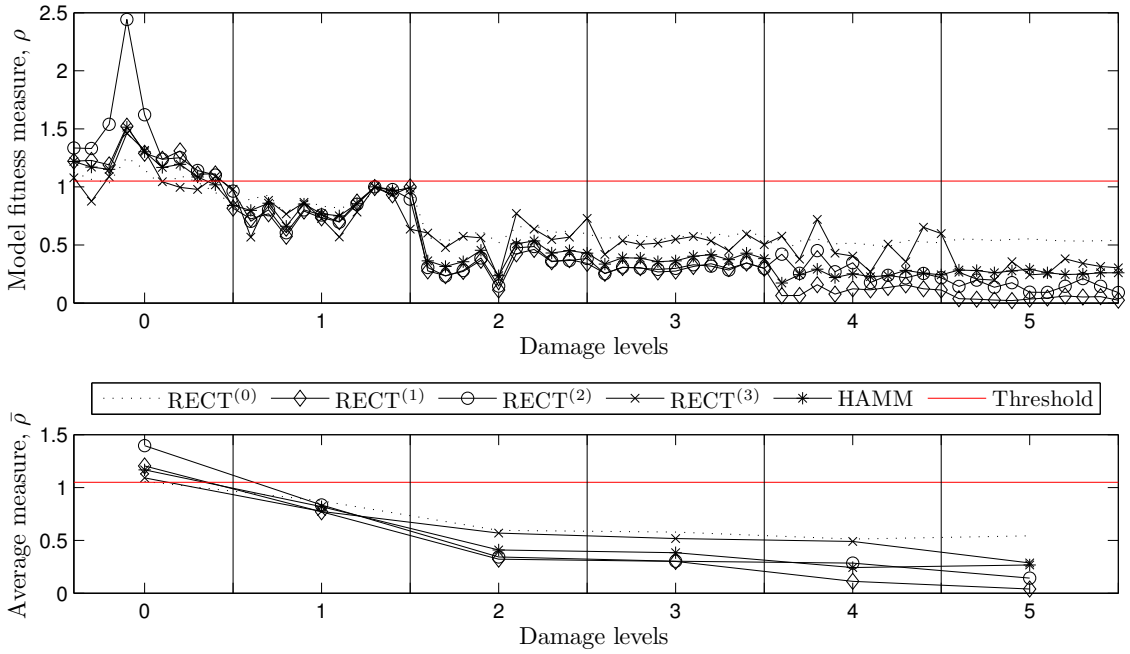

Figure 11.5: *Model fitness measure ρ for each signal and average measure ρ̄ obtained by considering rectangular windows of* 2000, 1680, 1520, *and* 1360 *samples and a Hamming window.*

As can be seen, this experimental case study illustrates the potential of the proposed formalism, which achieves a very low complexity method (i.e the raw signal is basically filtered by a FIR filter) for binary classification between damaged and undamaged area of a specimen, using a sparse physics-based transfer function, analytically derived from the mechanical and geometrical properties of the material.

Damage identification evaluation

In this second experiment, the proposed model is evaluated as underlying model in a damage recognition system based on *cepstral* distances as in Section 11.1.2. First, the same signals than those used in the previous damage detection experiment are preprocessed in order to reduce part of the noise and focus on the frequency band of interest. Thus, the sampling

frequency is reduced to $F_s = 25$ MHz ($N = 250$ samples) by decimation ($M = 8$), and temporal windowing is applied over the resulting signals. In particular, rectangular (R) and Hamming (H) windows are used here, where the rectangular window corresponds to a decimated version of the most performant window obtained from the previous experiment (RECT$^{(2)}$). Damage classification is performed from Euclidean distances in the real cepstral-domain, where the spectrum estimate of the specimen under investigation is defined according to Equation (4.50). Non-parametric and parametric methods can be used to this end (see Section 4.2.2). In this experiment, the periodogram is employed as non-parametric technique, serving us as baseline (*FFT* technique). As a first parametric technique, we consider a short-term linear prediction model (LPC) consisting of a standard all-pole filter with order $p = 14$ (*LPC* technique). This order p, and so the number of coefficients, is chosen to correspond to the thickness-equivalent sample delay of the plate $\Lambda = 14$.

A simplified analysis of the complex wave propagation pattern within a CFRP plate showed that a standard all-pole model could be improved for a damaged specimen by including a few coefficients which extends the specimen's transfer function with a middle and long-term predictors [294]. Thus, a second model is defined as an all-pole model of order $p = 28$, that is, twice the specimen's thickness expressed in samples, where the coefficients from positions 15 to 27 are forced to be zeros (*Simplified model 1*). The rest of coefficients (original LPC and 28^{th} ones) are obtained from the input/output signals by means of the Prony's method [215]. Additionally, we can define a third extended model, which also includes a middle-term coefficient placed at position 25 (*Simplified model 2*). The goal of this middle-term coefficient is to account for the damage by placing a fixed virtual interface in the plate [294]. However, it must be considered that the structural complexity of the material suggests that flaws may occur at different locations, and that a single virtual interface cannot account for all possible failure mechanisms. Therefore, in practice, the position of this interface must be determined empirically.

Instead of using a model based on a simplified analysis of the material, we can apply our proposed digital modeling of the specimen to analytically derive the position and extent of the coefficients from the properties of the CFRP plate. The delays m_i of these sparse coefficients are fixed according to the positions obtained from the model for an undamaged specimen, and the gains are estimated by means of the Prony's method, that is, it is assumed that damage affects mostly the gains of the sparse prediction coefficients a_k provided by the transfer function. The latter assumption implies that the changes caused in the signals due to damage should be absorbed by the gains at the fixed positions. Finally, a full LPC model with order $p = 28$ (maximum delay obtained in any previous model) is proposed for a fair comparison (*Full LPC*).

As in Section 11.1, the *leaving-one-out* technique (see Section 9.3.3) is used to perform the training/test and the accuracy of the system is evaluated by the weighted error rate defined in Equation (9.16). To evaluate the capability of the proposed classification system, *cepstra* are extracted from the aforementioned models. Table 11.2 shows the results obtained

for these different cepstrum-based techniques, namely *FFT*, *LPC*, *Simplified model 1 (SM 1)*, *Simplified model 2 (SM 2)*, *Specimen's digital model (SDM)*, and *Full LPC*, and summarizes the position of the prediction coefficients corresponding to these models.

Cepstrum-based techniques	a_k-coefficient positions 1 2 3 4 5 6 7 8 9 10 11 12 13 14 15 16 17 18 19 20 21 22 23 24 25 26 27 28	NZ	($N = 250$)	
			$w(n)$	w_{err} [%]
FFT		-	R	7.33
			H	8.33
LPC		14	R	9.33
			H	9.33
SM 1		15	R	8.00
			H	3.00
SM 2		16	R	7.67
			H	2.67
SDM		15	R	6.67
			H	**1.67**
Full LPC		28	R	6.67
			H	2.00

Table 11.2: *Classification errors (in %) for different cepstrum-based techniques, along with the order and extend of the non-zero coefficients a_k (indicated by grey cells).*

First, these results confirm that the modeling order p is tightly linked to twice the thickness-equivalent sample delay of the plate. Indeed, all the cesptra extracted from all-pole models with $p = 28$ reduce drastically the weighted error compared to classical spectrum estimation methods (*LPC* and *FFT*). Adding a single middle and long-term prediction coefficients to a standard all-pole model (*Simplified models*) enables us to obtain cepstra that improve significantly the damage discrimination compared to the short-term *LPC* cepstrum. It is noteworthy that modeling the multilayered specimen with a short-term LPC model is equivalent to consider our material as a Goupillaud-type structure with $\Lambda = M = 14$. As can be observed, a sparse signal modeling whose coefficient positions are analytically obtained from the material's properties provides even better discrimination than those simplified sparse-like models. Even more remarkable is the fact that this sparse model with a reduced number of parameters yields better results than a LPC-model with the same order (*Full LPC*). Concretely, minimal weighted error (1.67%) is obtained with the specimen's digital model for signals that have been previously preprocessed with a Hamming window. As can be observed, rectangular windowing follows the same tendency albeit provides worse results, i.e. the resulting weighted errors are typically around $2-4$ times higher than the ones obtained with Hamming windowing (except for the *FFT* and *LPC* cepstra). Indeed, in contrast to the previous experiment where signals were only processed in the time-domain, the current evaluation involves spectrum estimates, where the rectangular windowing is usually avoided due to its poor performance (as predicted by the results provided in Section 11.1).

11.2.2 Heuristic sparse signal model

In the previous damage identification experiment, the delays of the sparse coefficients were fixed according to the positions obtained from the digital model for an undamaged specimen. Implicitly, this means that damage affects mostly the gains of the sparse prediction

coefficients a_k provided by the transfer function. However, fixed delay positions do not respond to the phenomena associated with damage propagation due to increasing impact energies. In addition, the results exposed in Section 10.1 suggest that damage affects both the gains and positions of the sparse prediction coefficients a_k. Consequently, one can expect that a sparse digital model, whose parameters behave dynamically depending upon the damage state of the material, will have a better discriminative capability for damage identification than the digital model for an undamaged specimen used above. Thus, in this third experiment, we propose an initial *blind* approximation that relies on a model-based estimation procedure (see the analysis-by-synthesis scheme in Chapter 5) which, by assuming an underlying sparse digital model of the specimen, infers the order and extent of the model parameters corresponding to a certain damage level.

Material and methods

The proposed methodology consists of three elements: The (1) signal acquisition of the ultrasonic signals obtained from the wave interactions with a CFRP plate, a (2) sparse signal model that idealizes the ultrasound-composite interactions, and is solved by the Prony's method, and a (3) model-based estimation procedure, which is used to predict the optimal coefficient positions corresponding to a certain damage level.

The proposed approach is evaluated on the same signals than those used in the two previous experiments (see Section 11.2.1), and the preprocessing applied to those signals is identical to that used in the previous damage identification experiment. As commented above, we propose to use a purely heuristic digital modeling of the specimen, where the relation between the material's properties and the model parameters is *a priori* unknown. Hence,

$$H(z) \quad = \quad \frac{b_0}{1 + \sum_{k=1}^{p} a_k z^{-k}} z^{-\Lambda} \tag{11.2}$$

where most of the coefficients a_k are assumed to be zeros ($||a_k||_0 \ll p$). The only *prior* underlying mechanical concepts used here are provided by the formal analysis done in Chapter 7, namely that the model is a delayed all-pole model, whose denominator has a polynomial order p fixed to 2Λ, where Λ corresponds to a sample delay equivalent to the time needed by the incident wave to cross the total thickness of the multilayered structure. In addition, the numerator is defined so that it only consists of a gain b_0 plus a total thickness-equivalent sample delay Λ.

Hence, provided the coefficient position vector $\boldsymbol{k}$, Prony's method enables us to obtain the optimal amplitudes for a filter with a given input/output signals. Unfortunately, there is no method that provides both optimal sparse positions and amplitudes. Thus, we apply a model-based estimation procedure to find the values of the coefficient position vector $\boldsymbol{k}$ that best fit the experimental response signals $y^{(C)}(n)$, as depicted in Figure 11.6. Given the transfer function $H^{(C)}(z)$ corresponding to a certain damage class $C \in [0-5]$, the excitation signal $x(n)$ applied to the specimen can be filtered, resulting in an approximation $y_H^{(C)}(n)$ of

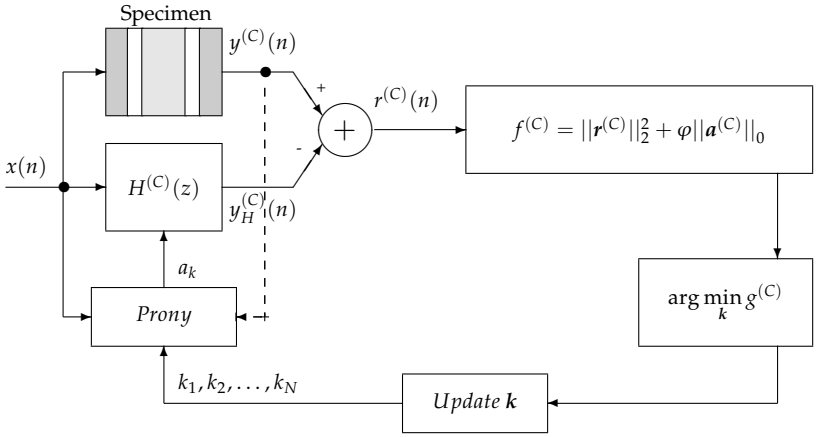

Figure 11.6: *Model-based estimation procedure for a damage class C.*

the experimental response signal $y^{(C)}(n)$ measured from the specimen, and corresponding to the same damage class C. Generally, the model coefficients are found such that the 2-norm of the residual $r(n)$ (the difference between the observed signal and the predicted one) is minimized. In this case, since $H^{(C)}(z)$ is an all-pole filter with sparse coefficients, we can reasonably assume that the optimal predictor is not the one that only minimizes the 2-norm but the one that also leaves the fewest non-zero prediction coefficients, i.e. the sparsest one. Sparsity is often measured as the cardinality, that is the so-called 0-norm [300, 301]. Thus, the specimen can be analyzed by defining a modeling error (or energy) in terms of the mean squared error between the actual response signal $y^{(C)}(n)$ and the modeled response $y_H^{(C)}(n)$, plus a sparsity term that accounts for the number of non-zeros coefficients in the transfer function,

$$f^{(C)} = ||\boldsymbol{r}^{(C)}||_2^2 + \varphi||\boldsymbol{a}^{(C)}||_0 \tag{11.3}$$

where φ is an empirical regularization term, defined so that the modeling error due to the sparsity term corresponds to a certain amount of the least squared error (setting $\varphi = 0$ leads to a standard linear prediction form). To account for all the N_r measurement repetitions within a damage class C, a mean cost functional $g^{(C)}$ is introduced as,

$$g^{(C)} = \frac{1}{N_r}\sum_{i=1}^{N_r} f_i^{(C)} \tag{11.4}$$

Then, the parameters $\boldsymbol{k}$ that characterize the coefficient positions are found by a search algorithm that minimizes the cost functional $g^{(C)}$,

$$\hat{\boldsymbol{k}} = \arg\min_{\boldsymbol{k}} g^{(C)} \tag{11.5}$$

Binary genetic algorithms are applied to minimize this function, and provide the optimal solution to the model-based estimation.

Experimental results

To evaluate the discriminative capability of the proposed method, a set of experiments have been carried out. Again, a damage recognition system based on *cepstral* distances is developed according to Section 9.3.3. As in the damage detection experiment of Section 11.2.1, each signal has been previously preprocessed with a Hamming window of 250 samples in the time-domain. The tested techniques employ the *real cepstrum* $c(n)$, where the spectrum estimate of the specimen under investigation is defined according to Equation (4.50).

As in the previous sections, the *leaving-one-out* technique (see Section 9.3.3) is used to perform the training/test and the accuracy of the system is evaluated by the weighted error rate defined in Equation (9.16). Table 11.3 shows the results obtained for the proposed method. Concretely, the approach called *Real cepstrum* consists of using the periodogram and corresponds to our baseline (i.e. non-parametric technique). The technique labeled as *LPC cepstrum* is based on the use of a standard all-pole model with order $p = 28$, and corresponds to the *Full LPC* used in Section 11.2.1. Then, the technique designated as *SDM cepstrum* relies on our specimen's digital modeling, whose sparse coefficient positions were provided in Table 11.2. Finally, the method named *Dynamic cesptrum* is based on the sparse signal model described by Equation (11.2), and whose coefficient positions $\boldsymbol{k}$ were determined according to the optimal results obtained with the model-based estimation procedure. As can be observed, minimal weighted and absolute errors (1.67% and 3%, respectively) are obtained with the dynamic approach. It is also worth to note that a sparse modeling, with a lower number of parameters, has a better discriminative capability than classical spectrum estimation approaches. However, this heuristic model does not improve the classification results obtained with the specimen's digital model for an undamaged specimen, and requires much larger computational resources.

Cepstrum-based techniques	Number of non-zero a_k	w_{err} [%]	*err* [%]
Real cepstrum	–	8.33	23.33
LPC cepstrum	28	2.00	6.67
SDM cepstrum	15	**1.67**	-
Dynamic cepstrum	$13 - 19$	**1.67**	3

Table 11.3: *Classification errors for different cepstrum-based techniques.*

Finally, Table 11.4 presents the optimal position $\boldsymbol{k}$ obtained from the model-based estimation procedure for the prediction coefficients corresponding to each damage class C. The resulting thickness equivalent sample delay is $\Lambda = 14$ for the specimen tested. The simulations have been performed for a wide range of regularization terms $\varphi \in [3 - 8] \cdot 10^{-5}$. As can be observed, the coefficient position vector $\boldsymbol{k}$ changes slightly from one damage level to the next one. Some coefficients vanish and/or appear at new positions, due to the symmetry break of the plate structure. It is worth to point out that diagonal patterns which appear along increasing damage levels (e.g. from positions 13 to 18 and from 16 to 21) may

Damage level	a_k-coefficient positions																											NZ
	1	2	3	4	5	6	7	8	9	10	11	12	13	14	15	16	17	18	19	20	21	22	23	24	25	26	27	28	
Damage 0	■	■	■	■	■	■	■	■	■	■	■		■			■												■	15
Damage 1	■	■	■	■	■	■	■	■	■		■			■			■						■					■	15
Damage 2	■	■	■	■			■		■	■	■				■			■							■				14
Damage 3	■	■	■	■			■		■	■				■	■	■					■								13
Damage 4	■	■					■			■	■	■	■	■	■	■		■				■	■						14
Damage 5	■	■		■	■		■	■	■				■	■	■	■	■	■			■			■	■	■		■	19

Table 11.4: *Optimal solution of the model-based estimation for the positions of the non-zero coefficients a_k (indicated by grey cells), along with the number of non-zero (NZ) coefficients ($\varphi = 6e - 5$).*

be related to wave velocity reductions (i.e. to stiffness reduction of the specimen layers). Unfortunately, a direct physical interpretation from the a_k-domain is not easily assessable.

By way of conclusion, Figure 11.7 shows the transfer function coefficients for damage class $C = 4$, and compares the discrete time-domain signal obtained with the heuristic digital modeling of the specimen with an individual measurement of that class.

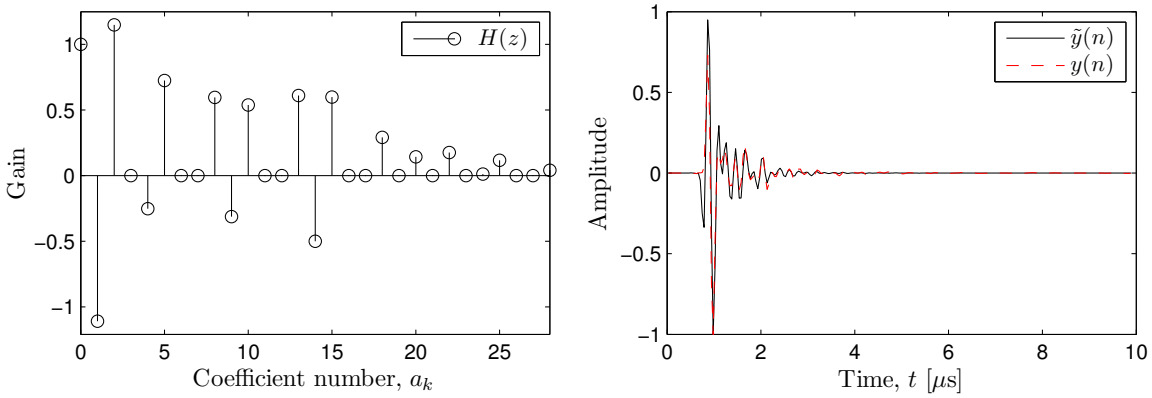

Figure 11.7: *Denominator coefficients from the discrete-time transfer function $H(z)$ for the damage class $C = 4$ (left) and comparison between an experimental measurement and a signal predicted by the heuristic digital signal model (right).*

11.3 Conclusions

In an initial approximation, the signal processing and features extraction procedure applied to the ultrasonic signals provided us some preliminary results to select a robust parametrization for such signals in order to identify impact damage in CFRP plates. Concretely, the classification error could be reduced by (1) enhancing the wave echoes with a suitable analysis window (Hamming), (2) selecting *cepstral* coefficients based on the use of a simple *liftering* window with the appropriate size (related to twice the specimen's thickness expressed in number of samples), and (3) by performing a recognition experiment based on *cepstral* distances with an underlying AR model.

In a second part, we showed the capability of our digital modeling of the specimen to identify damage in composite materials, particularly in a CFRP plate subjected to different impact energies. A set of experimental case studies has been proposed to evaluate the potential of the developed specimen's digital model in some practical NDE applications. In

a first experiment, a damage detection evaluation has been carried out, showing that the digital filter represents an extremely fast and promising tool to discriminate damaged from undamaged specimens by inverse filtering. Indeed, this inverse filter is a sparse FIR filter, whose coefficients were directly obtained from the material's properties, without requiring any experimental calibration. In a second experiment, the discriminative performance of the proposed model has been evaluated by a system based on *cepstral* distances that recognizes the specific damage level corresponding to a given test signal. The damage levels have been identified with an accuracy of 98.37 % with a model that consists of 15 parameters, that is, half the amount of a full LPC model. It has been demonstrated that a sparse signal modeling with a reduced number of coefficients provides better results than other common spectrum estimation techniques. In contrast to standard or empirical models, the coefficients position and extent of our model are inherently linked to the material's properties (i.e. stiffness, geometry, etc.), and thus to its health state. Nonetheless, the coefficient positions were fixed according to the digital modeling of an undamaged specimen.

To face this unrealistic modeling, a purely heuristic sparse signal model was considered. First, a model-based estimation procedure has been proposed, to infer the order and extent of the model parameters corresponding to a certain impact damage level. Then, the performance of the proposed parametrization has been evaluated by a system based on *cepstral* distances that recognizes the specific damage level corresponding to a given test signal and it has been confirmed that modeling the complex wave propagation pattern using a sparse transfer function provides better results than other classical spectrum estimation techniques. Additionally, it has been observed that the prediction coefficients behave dynamically, depending upon the damage state of the material. Nevertheless, its was shown that the classification results obtained with this heuristic model do not improve the ones obtained with our modeling of the undamaged specimen. This characteristic promotes the use of our specimen's digital model, since an heuristic approach suffers from a prohibitive computational costs that makes it almost unviable.

12

Model-based estimation procedure for 3D damage reconstruction in CFRP plates

This chapter investigates the use of the model-based estimation procedure described in Chapter 5 for damage identification in CFRP plates. Section 12.1 focuses on impact and fatigue damage assessment using an immersion setup, whereas Section 12.2 briefly highlights the potential of nonlinear ultrasound evaluation for damage assessment in CFRP plates.

12.1 Impact damage assessment using linear immersion measurements

This section is directed toward the use of our proposed digital modeling of the specimen within a model-based estimation procedure in order to provide consistent damage information for characterizing the specimen's health state. Indeed, this model has been so far demonstrated to be useful to mimic ultrasonic signals obtained from conventional undamaged layered materials (see Section 10.2). In addition, we also have shown the capability of this model to identify damage in composite materials, particularly in a CFRP plate subjected to different impact energies (see Section 11.2). However, in the later case, the damage identification relies on fixed coefficient positions obtained from the undamaged material's properties (that is, the damage was essentially modeled as changes in the gains of those coefficients). Thus, the objective of this section is to evaluate our model with variable amplitudes and also positions, with the aim of adjusting signals obtained from complexly damaged areas, in order to reconstruct the altered mechanical properties due to such damage.

Here, this approach is evaluated on the CFRP plate described as specimen (C) in Table 9.4 with a stacking sequence which corresponds to a $[0/90]_{4s}$ lay-up. The model-based estimation procedure applied to find the values of the damage parameters $\boldsymbol{\theta}$ that best fit the experimental measurements is depicted in Figure 12.1.

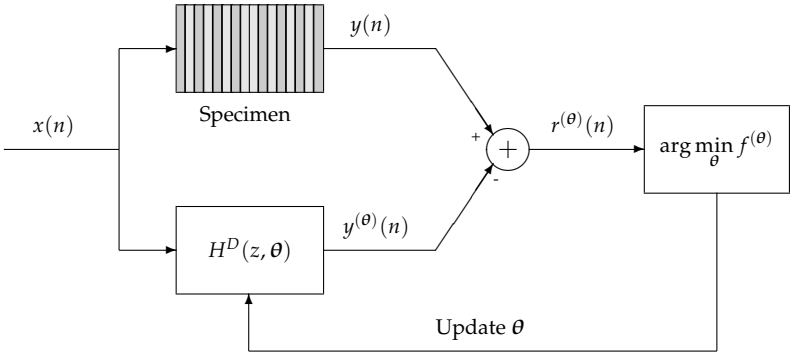

Figure 12.1: *Diagram of the model-based estimation procedure used to reconstruct linear mechanical properties of the specimen.*

Given the transfer function $H^D(z,\boldsymbol{\theta})$ corresponding to a certain damage state $\boldsymbol{\theta}$, the excitation signal $x(n)$ applied to the specimen can be filtered, resulting in an approximation $y^{(\boldsymbol{\theta})}(n)$ of an individual response signal $y(n)$ measured from the specimen. The damage parameters $\boldsymbol{\theta}$ are updated until the 2-norm of the residual $r^{(\boldsymbol{\theta})}(n)$ (the difference between the observed signal and the predicted one) is minimized. The parameters $\hat{\boldsymbol{\theta}}$ that characterize the damage are found by a search algorithm that minimizes the cost functional $f^{(\boldsymbol{\theta})}$,

$$\hat{\boldsymbol{\theta}} \quad = \quad \arg\min_{\boldsymbol{\theta}} f^{(\boldsymbol{\theta})} \tag{12.1}$$

GA's are applied to minimize Equation (12.1), and provide the optimal solution to the model-based estimation. As in Section 10.2, the input signal used here is the realistic ahead-shifted version of the output signal measured in water (obtained by removing the specimen) depicted in Figure 12.2.

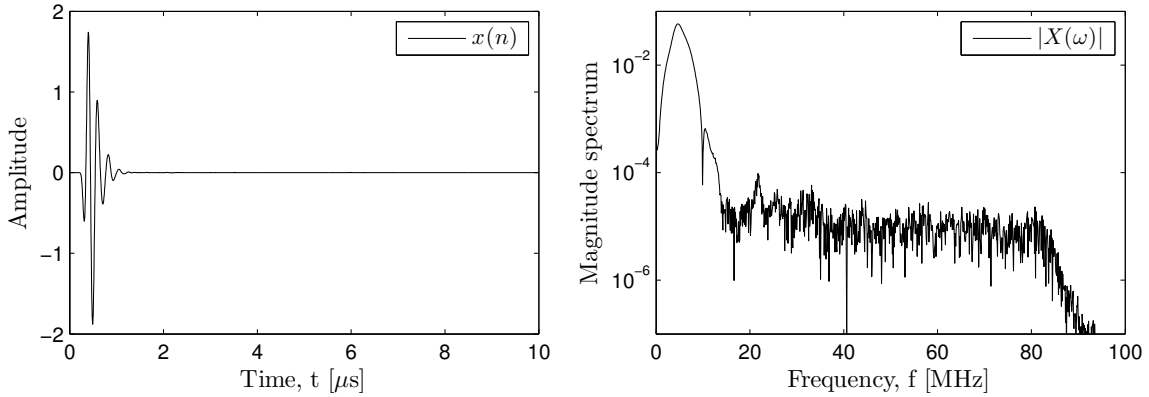

Figure 12.2: *Discrete-time input signal $x(n)$ (left) and its magnitude spectrum $|X(\omega)|$ (right) used as excitation for the CFRP plate ($F_c = 5$ MHz). Note that the abscissas have been scaled according to a sampling frequency $F_s = 200$ MHz.*

Unfortunately, neither the spectral nor the *cepstral* domains result adequate for this experimental case, from there the minimization is now directly performed on the raw signals in the time-domain. This is due to the selected sampling frequency F_s, the frequency response of the available transducers, and the fact that a large frequency-band of the spectrum of the input signal $X(\omega)$ mostly consists of noise. The latter inconvenience particularly distorts the distance measures in those domains. This will be discussed in detail in Section 12.3.

Finally, since a major damage mode in composites is delamination, an interface layer of much smaller thickness than both plies and wavelength of the central frequency is assumed between every two consecutive layers in the digital modeling of the specimen. Thus, the resulting model consists of $M = 32$ layers (that are the 16 layers of the real specimen, plus 14 interfaces in-between, plus 2 water layers ahead of and behind the specimen). The mechanical and geometrical properties of those interfaces are summarized in Table 12.1. Those were partially provided by the manufacturer (e.g. ρ), whereas the remaining ones were obtained according to the properties of the polymer matrix (e.g E, ν, and α), since the joining between the individual pre-preg lamina was obtained by autoclave, which applies pressure and temperature over a thickness of approximately 10 μm to finally constitute the final layered structure.

Properties	Y. Modulus $E\ [GPa]$	P. Ratio $\nu\ [-]$	Density $\rho\ [kg/m^3]$	Attenuation $\alpha\ [Np/m]$	Thickness $a\ [mm]$
Interface	5.2728	0.3500	1310	361.1595	0.01

Table 12.1: *Mechanical and geometrical properties of the layers and interfaces that compose the multilayered composite material.*

12.1.1 System calibration

The first tackled problem is the calibration of the digital modeling of the specimen that solves the forward problem, since the properties provided by the manufacturer may slightly differ from the real ones. Consequently, the calibration is achieved by the matching procedure described in Section 9.3.1, in which two parameters (the Young modulus E_m and the damping coefficient α_m of the polymer matrix) are adjusted with GA's to find the optimal characterization of measurements obtained from an undamaged area of the specimen. In this case, the minimization is a carried out in the time-domain according to the scheme depicted in Figure 12.1. In particular, we randomly select 12 measurement points far from the impacted area to perform the calibration, and the final calibrated values are obtained as the mean of those individual values. Figure 12.3 depicts the resulting matching (for the optimal parameters $\boldsymbol{\theta}_{cal.}$) between a measurement $y_0(n)$ and the numerically predicted model $\tilde{y}_0(n)$ for un undamaged area. As can be seen, a fairly good matching is obtained.

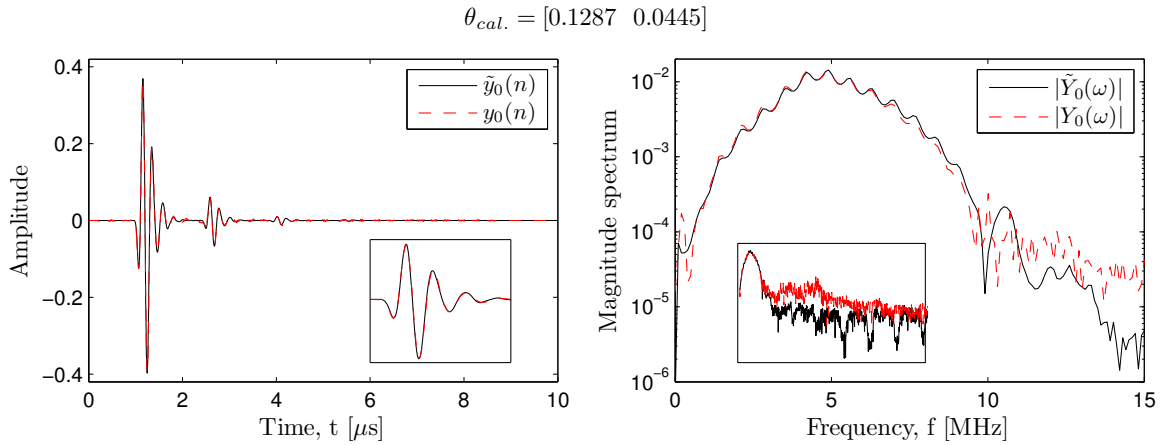

Figure 12.3: *Calibration of the signal predicted by the specimen's digital model $\tilde{y}_0(n)$ with a measurement $y_0(n)$ obtained from a undamaged area.*

The modified properties of the layers/interfaces obtained from the calibration step are summarized in Table 12.2.

Layers	Y. Modulus $E\ [GPa]$	P. Ratio $\nu\ [-]$	Density $\rho\ [kg/m^3]$	Attenuation $\alpha\ [Np/m]$	Thickness $a\ [mm]$
0°-orientation	11.0346	0.3007	1589.5	291.8043	0.1215
90°-orientation	11.0356	0.3007	1589.5	291.8043	0.1215
Interface	5.1921	0.3500	1310	354.0515	0.01

Table 12.2: *Mechanical and geometrical properties of the layers and interfaces obtained from the calibration step.*

12.1.2 Hypothesis on the damage distribution

The issue of the damage parametrization is cumbersome when dealing with such a large set of damage parameters $\boldsymbol{\theta} \in \{E_i, \nu_i, \rho_i, \alpha_i, a_i\}$, with $i = 1, \ldots, M$, describing the mechanical and geometrical properties of the material's layers and interfaces. In order to restrict the solution field, we perform the parametrization step with a reduced set of variables. This kind of regularization is based on the *prior* knowledge on the damage propagation pattern described in Section 9.1.1. Indeed, in CFRP plates, three phases of impact damages can be roughly identified; initially matrix cracks are generated by shear or tensile stresses mainly in the intermediate or back-wall layers; then delaminations grow from the crack tips between layers of different orientation; and finally fiber breakage appear initially on the surface of the sample and may propagate into intermediate layers [15, 237]. Then, fatigue damage usually generate further matrix cracks in the layers whose orientation is perpendicular to the applied cycled loading. Consequently, we assume that damage is strongly correlated with a global stiffness reduction of the material. Thus, nine damage model parameters $\boldsymbol{\theta} = \{\theta_{int}, \theta_{90}, \theta^*_{int}\}$ are chosen as a trade-off between algorithm's convergence and computational cost. The damage parameter θ_{int} accounts for a stiffness reduction of the layers' interfaces E_{int} due to delaminations between layers of different orientation (except the

interface between the two back-wall layers), θ^*_{int} accounts for a stiffness reduction of the layers' interface E^*_{int} due to delaminations between the two back-wall layers (i.e delimitation due to impact concentrates mostly in the interface opposite to the impacted side), and $\boldsymbol{\theta}_{90}$ accounts for a stiffness reduction of 7 layers $\boldsymbol{E}_{90}$ by means of matrix cracking in the layers with 90°-orientation (actually, there are 8 layers with such an orientation, but it is reasonable to assume that both in the middle behave jointly). Each damage model parameter θ_i, with $i = 1, \ldots, 9$, is defined in a dimensionless and logarithmic scale as,

$$E_{opt,i} \quad = \quad E_i e^{-\theta_i} \qquad\qquad (i = 1, \ldots, 9) \tag{12.2}$$

where $\theta_i \in [0, 3]$, that is the optimized stiffness value $E_{opt,i}$ remains the same as the original undamaged one $E_i \in [E_{int}, \boldsymbol{E}_{90}, E^*_{int}]$ for the lower bond, whereas the upper bond corresponds to the maximal induced damage (95% stiffness loss).

12.1.3 Damage parameter estimation

Using the calibrated properties obtained from the calibration step in Section 12.1.1, a digital model (i.e. transfer function $H^D(z)$) can be updated for each of the 41×21 measurements using the model-based estimation procedure depicted at the beginning of this chapter. Figure 12.4 depicts two examples of the resulting matching (for the nine optimal damage model parameters $\boldsymbol{\theta}_{opt.}$ mentioned above) between measurements $y_j(n)$ and the numerically predicted model $\tilde{y}_j(n)$ for low-damaged areas of the specimen, $j = 1, 2$. Left plot represents a signal from a nearly undamaged location outside from the impacted area (i.e. the damage parameter θ_6 reveals a slight stiffness reduction due to matrix cracks in some of the layers with 90°-orientation), whereas right plot represents a signal from a location around the impacted area that suffer a stronger reduction of the stiffness of the back-wall layer with 90°-orientation (i.e. matrix cracks, revealed by θ_8) and the interface between that layer and the adjacent layer with 0°-orientation (i.e. delamination, revealed by θ_9). Again, a fairly good matching is obtained between the experimental and modeled signals.

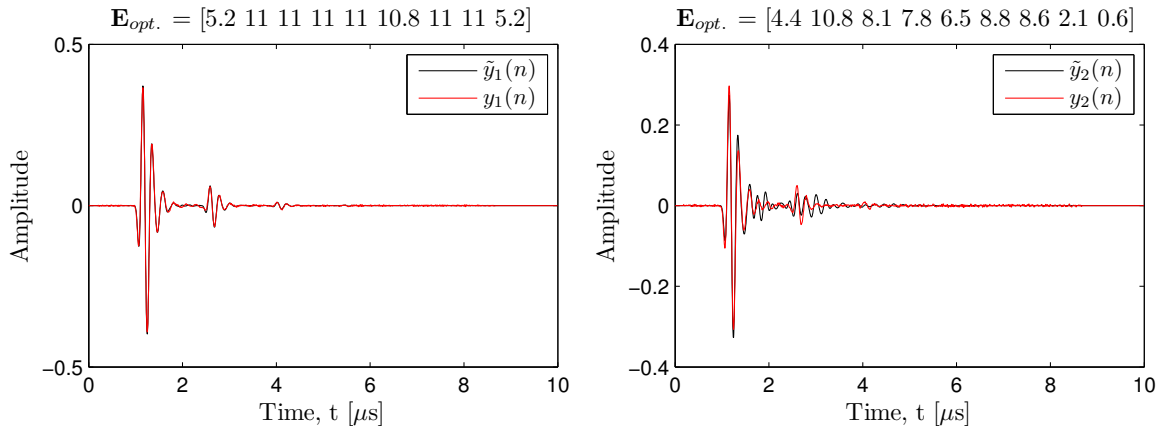

Figure 12.4: *Comparison between experimental measurements and signals predicted by the specimen's digital model for low-damage areas.*

Figure 12.5 depicts two examples of the resulting matching between a measurement $y_j(n)$ and the numerically predicted model $\tilde{y}_j(n)$ for moderately damaged areas of the specimen, $j = 3, 4$. Left plot represents a signal from a location that suffers nearly the same impact than that of the right plot in Figure 12.4. In addition, the material endures also a considerable stiffness reduction of the inner layers with 90°-orientation (i.e. matrix cracks, revealed by θ_4, θ_7 and θ_8). In contrast, right plot represents a signal from a location within the impacted area that suffer a drastic stiffness reduction of almost all layers with 90°-orientation (i.e. θ_j, with $j = 3, \ldots, 8$). The obtained matching between the experimental and modeled signals is reasonably good again.

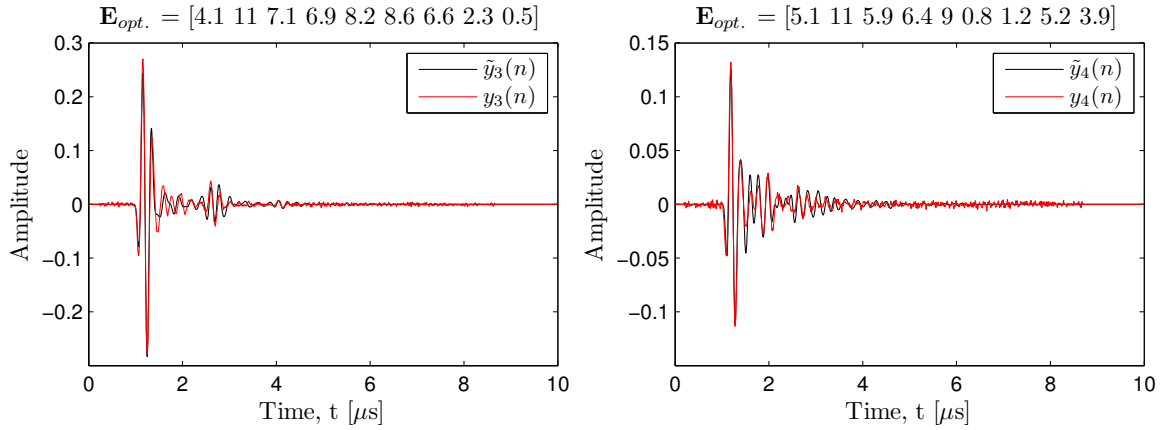

Figure 12.5: *Comparison between experimental measurements and signals predicted by the specimen's digital model for moderately damaged areas.*

Two examples of the resulting matching between a measurement $y_j(n)$ and the numerically predicted model $\tilde{y}_j(n)$ for severe damaged areas of the specimen, $j = 5, 6$, can be found in Figure 12.6.

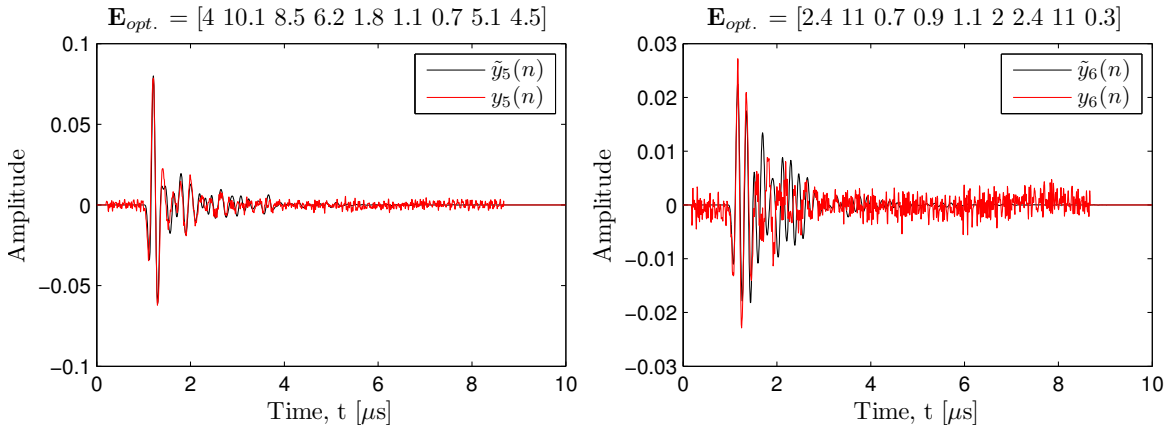

Figure 12.6: *Comparison between experimental measurements and signals predicted by the specimen's digital model for severely damaged areas.*

Left plot represents a signal from a location that suffers an impact nearly identical to that of the right plot in Figure 12.5. In addition, the material endures an even larger stiffness reduction of the inner layers with 90°-orientation (i.e. matrix cracks, revealed by θ_j ($j = 4, \ldots, 8$)). In contrast, right plot represents a signal from a location within the impacted area that suffer a drastic stiffness reduction of almost all layers with 90°-orientation and all interfaces (i.e. matrix cracks and delaminations, revealed by every θ_j). This signal with a very low SNR may correspond to a location that has endured both the effects of impact and fatigue. Even though, the damage parameter estimation is far from inconsistent. Despite the overlapping echoes and low signal amplitude, the obtained matching between the experimental and modeled signals is particularly remarkable.

Additionally, a further inspection of the modeling error shows that the residuals $e_j(n)$ ($j = 1, 5$) only contain few components other than measurement noise, i.e. the *approximation* error (see Section 10.2) nearly amounts to 10% of the signal's amplitude, and can thus be considered as acceptable. These results definitely support the potential of our specimen's digital model to face up wave responses originated from multilayered specimens affected by complex damage mechanisms.

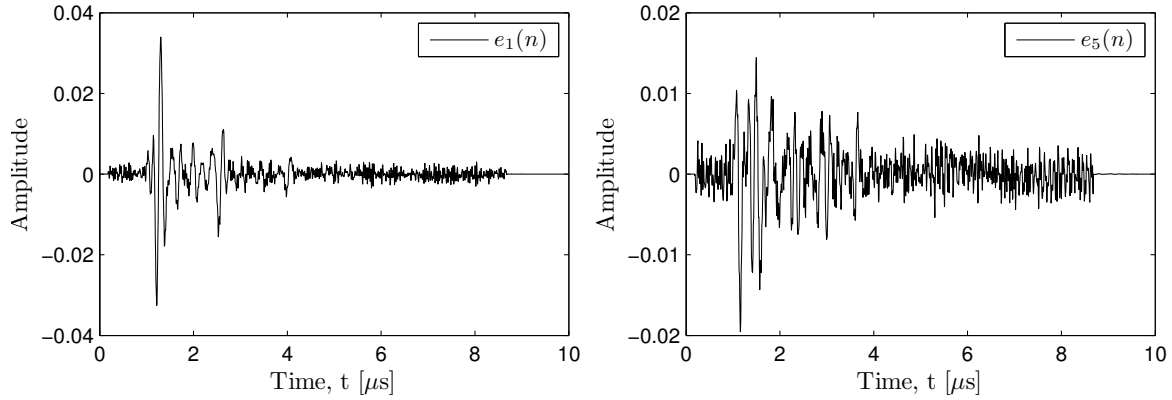

Figure 12.7: *Error between experimental measurements and signals predicted by the specimen's digital model for a low and severe damage area.*

Finally, as an example, the numerator $N(z)$ and denominator $D(z)$ coefficients of the discrete-time transfer functions for a low and severe damage areas are shown in Figure 12.8. For the low damage case (upper figures), the numerator consists of a single coefficient $b_0 = 0.1158$ at a sample-equivalent delay equal to the total thickness of the plate $\Lambda = 287$, and the denominator is mostly composed of zeros (only 193 non-zero coefficients from 574). For the severe damage case (lower figures), the numerator consists of a single coefficient $b_0 = 0.06$ at a sample-equivalent delay equal to the total thickness of the plate $\Lambda = 435$, and the denominator is mostly composed of non-zero coefficients (only 17 zeros).

From those plots, one can draw the following conclusions. As expected, damage affects the single coefficient b_0 of the numerator which moves right (i.e. damage reduces the material stiffness, which in turn reduces the wave velocity). In addition, the sparsity of the

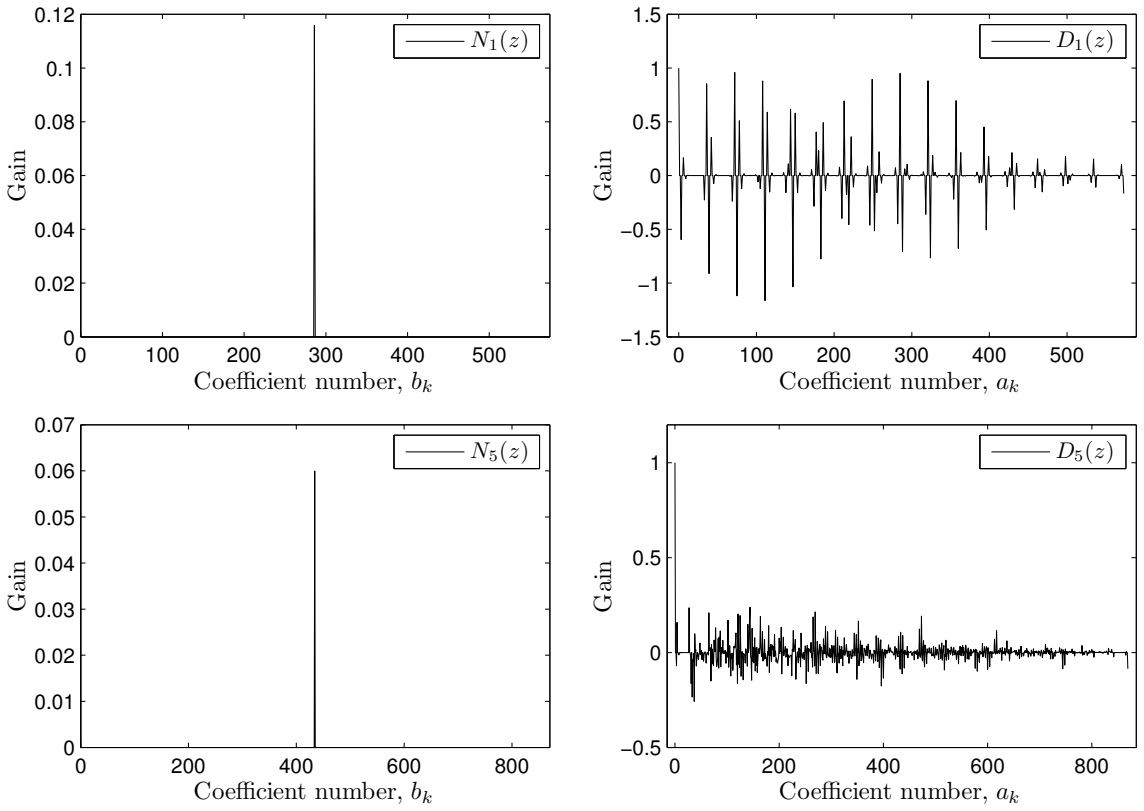

Figure 12.8: *Representation of the numerator $N(z)$ (left) and denominator $D(z)$ (right) coefficients from the discrete-time transfer functions $H^D(z)$ for a low and severe damage areas*

denominator considerably decreases as the damage increases (as predicted by Figures 10.2-10.3 and as suggested by Table 11.4). This fact confirms that the sparsity is not only related to the sample-equivalent layer's thickness, but also somehow connected to the symmetry of the material. Furthermore, it is noteworthy that damage leads to a significant increase of the transfer function length, since the thickness-equivalent sample delay Λ growths. Be aware that this does not mean that the thickness of the material's layers increase, but only that the wave velocity c_i of the layers decreases (i.e. $\Lambda = \sum_{i=1}^{M} m_i$, with $m_i = \left[\frac{F_s a_i}{c_i}\right]$). Those observations make the use of *blind* sparse signal models as in [41, 43] unrealistic. Indeed, one can approximately design an heuristic model-based procedure which estimates the gains and positions of the coefficients (see Section 11.2.2), but including also a variable filter's length definitely makes such an approach difficult.

12.1.4 Sensitivity study

Some uncertainties can arise during the estimation of the damage parameters due to a combination of successive errors that could stem from the model-based estimation procedure: (1) Uncertainties from the inversion algorithm (e.g. convergence burden due to the large number of damage parameters, noisy measurements, etc.), (2) uncertainties from the damage parameters (i.e. erroneous selection, missing parameters, correlated parameters, etc.), and (3)

uncertainties in the specimen's digital model (i.e. neglecting of dispersion or nonlinear phenomena, erroneous boundary conditions, unknown material properties, etc). Consequently, this section aims at evaluating the robustness of the search algorithm and the correctness of the hypothesis done on the damage distribution regarding the optimized damaged parameters $\boldsymbol{\theta}_{opt.}$ obtained by our proposal.

Sensitivity to algorithm convergence

The uncertainty from the inversion algorithm can be faced up by observing the capacity of the GA's to reach a local optimum, and verifying its deviation from the *true value*. For this purpose, the cost functional is plotted against the number of generations, highlighting the convergence slope of the optimization process. Figure 12.9 shows the evolution of the cost functional along each generation of the best individual of the population for a low and severe damage case. As can be observed, in both cases, the cost functional converges to its optimal value many generations before attaining the end of the optimization process. Consequently, the algorithm convergence may not have a drastic influence on the estimation of the damage parameters, and one can reasonably expect that the algorithm has not been get trapped in a local minimum.

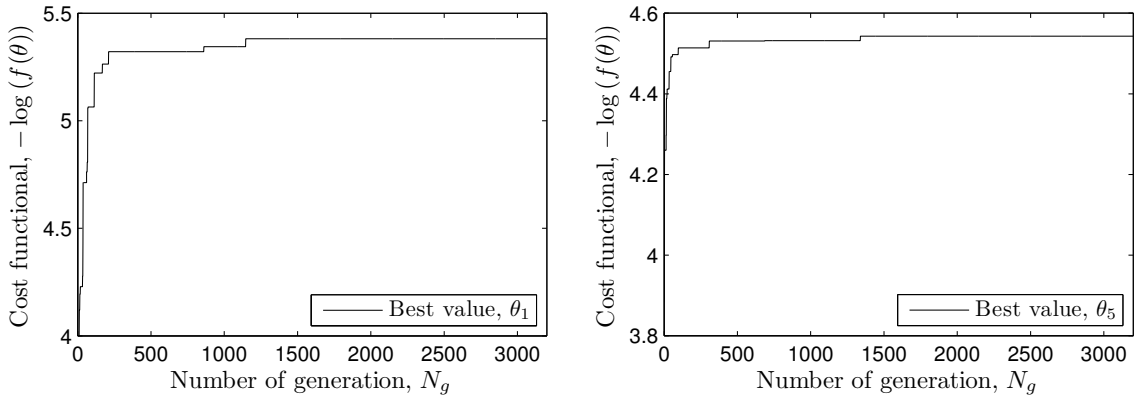

Figure 12.9: *Evolution of the cost functional with respect to the number of generations ($N_g = 3200$ and $N_p = 800$) for a low and severe damage area.*

Sensitivity to the damage distribution

In Figure 12.10, the complete stiffness maps obtained of each damage parameter θ_i ($i = 1, \ldots, 9$) are plotted in the xz-plane. The correctness of those maps can be evaluated by observing the consistency of the damage distribution (i.e. realistic distribution, connectivity of the damaged *pixels*, etc.) according to each damage parameter θ_i.

As can be observed, the impact damage is clearly visible in the center of each map. In addition, the impact damage appear to increase with depth in the layers with 90°-orientation, that is, the damage initially affect the back-wall layer and then propagates within the structure, drawing a complex *tree roots-like* structure (the matrix cacks of layers close to the impacted area appear in the center, whereas the matrix cracks of layers close to the opposite side of the impacted area appear around the center). As expected, the interface between

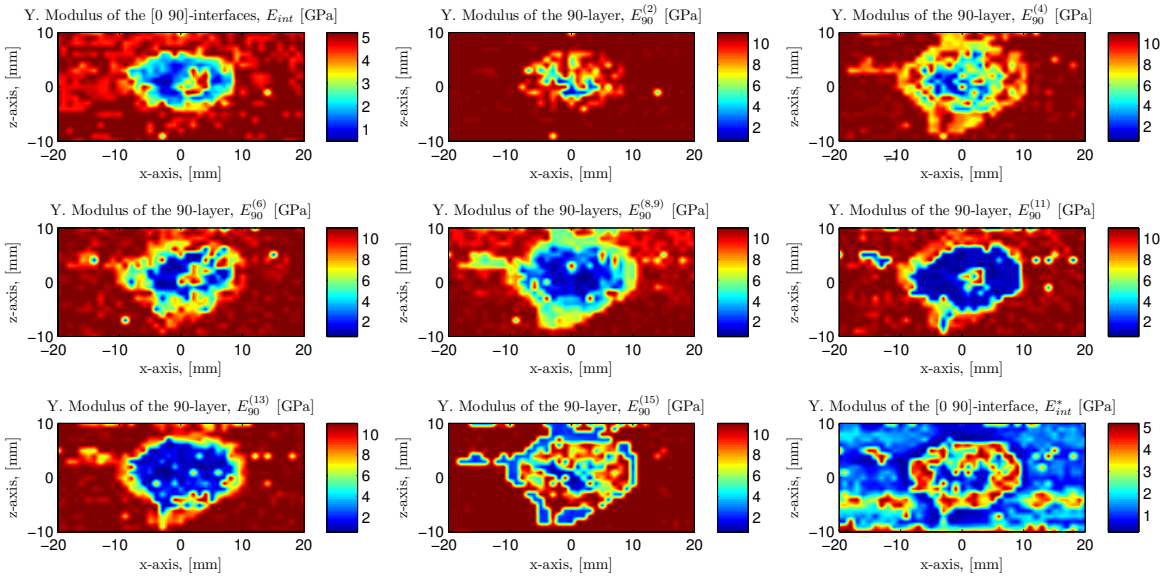

Figure 12.10: *Complete stiffness maps obtained of each damage parameter θ_i ($i = 1, \ldots, 9$). The upper index j, with $j = 1, \ldots, 15$, associated to the stiffness of the layers with 90°-orientation, corresponds to the position of those layers in the stacked sequence.*

the two back-wall layers with different orientations suffer from strong delaminations. The more isolated damaged area located on the horizontal lines around $z = -5$, $z = 5$ and $z = 10$ mm could be due the fatigue damage, which usually generates longitudinal cracks. Consequently, the damage distribution seems to be reasonable, but it remains open if other hypothesis on the damage parameters would have provided similar results (i.e. increase of the attenuation coefficient, etc.). Finally, replacing the damage parameters θ_i at their corresponding locations within the layered structure enables us to obtain a *tridimensional* stacked representation of the damage distribution over the thickness of the CFRP plate. Figure 12.11 depicts such a representation for some of the layers/interfaces (only 5 of these are plotted to ensure a good visibility).

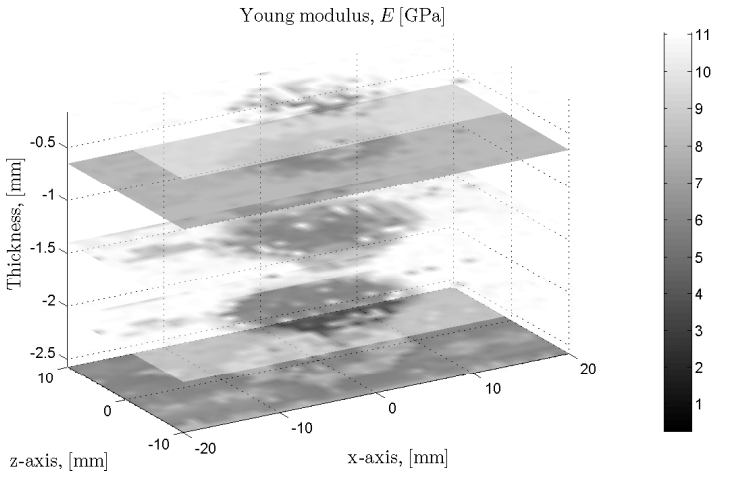

Figure 12.11: *Tridimensional stacked representation of the damage distribution expressed in terms of stiffness reduction (in GPa) over the thickness (the latter has been magnified to a factor 10).*

It is noteworthy that in contrast to conventional C-scan imaging, the proposed methodology enables us both to identify (i.e. damage type and location) and quantify complex damage mechanisms in the structure. Figure 12.12 depicts the wave velocity map of such a conventional C-scan, which is easily obtained by cross-correlating the signals measured with the specimen in-place with that measured in water. As can be observed, this figure provides a global information of the stiffness reduction in the xz-plane, but does not deliver any interpretation of the trough-thickness damage distribution. Nonetheless, this figure further supports the results obtained with the model-based estimation procedure, since both the impacted area and the more isolated damaged area have a similar shape than those encountered above.

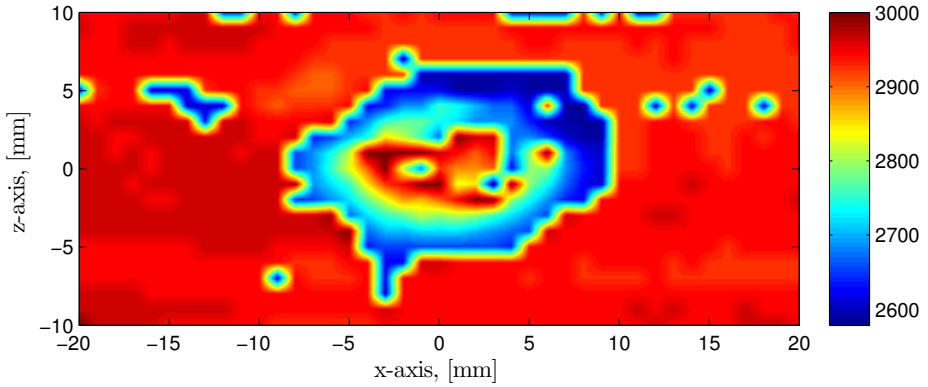

Figure 12.12: *Wave velocity (in m/s) map obtained with a conventional C-scan approach.*

Comparison with other techniques

Finally, our results are compared to those obtained with other techniques, such as radiograph and micrograph imaging[1], as depicted in Figure 12.13. Radiography was conducted with a HP cabinet x-ray system from the Faxitron Series. Zinc iodide-based x-ray penetrant was applied on cracks in the vicinity of the impact damage on the specimen for 30 minutes before exposure to x-rays, in order to reach the delaminations [242]. Left figure shows the radiography obtained from that specimen, which reveals an impacted area which is consistent with that obtained with our method. However, the radiography also reveals matrix cracks that were not detectable with our approach. Nevertheless, it must be considered that a through-transmission configuration under normal incidence cannot detect longitudinal cracks perpendicular to the plane wave propagation. Right figure shows a schematic of the micrograph of a cross-section (in the yz-plane) for that specimen. The grey and white layers are the plies with 0°-orientation and 90°-orientation, respectively. As can be observed, the matrix cracks affect only the layers with 90°-orientation, and their in-depth propagation profile remind that *tree roots-like* structure observed in Figure 12.10. In addition, it can be seen that the delamination mostly affects the interface between the two back-wall layers.

[1]Courtesy from the Institute of Polymers and Composites, TU Hamburg-Harburg, Germany

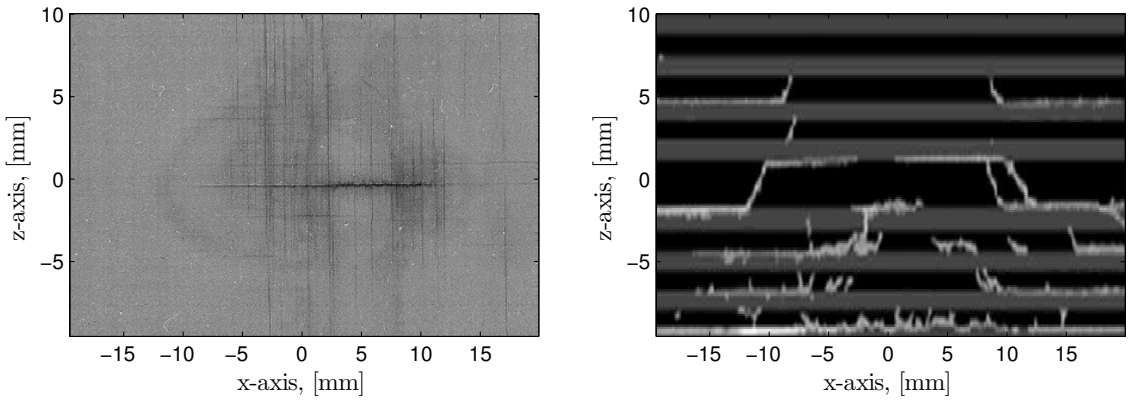

Figure 12.13: *Radiograph and schematic of a micrograph of a cross-section for an impacted specimen removed after 100000 cycles of loading.*

12.2 Prospective results using nonlinear immersion measurements

In this section, we evaluate the performance of the NTM formalism described in Chapter 8 for describing multilayered specimens with classical nonlinear constitutive behavior. To this end, we first propose a synthetic comparison between the NTM formalism and its linear counterpart. Then, this nonlinear model is inserted in a model-based estimation procedure to reconstruct the linear and nonlinear mechanical properties of a CFRP plate subjected to impact and fatigue damage.

12.2.1 Preliminary evaluation of the NTM formalism

In this section, a numerical study is carried out to evaluate the NTM formalism. With the aim of simulating real experimental conditions, the numerical characteristics (e.g. material, frequency, etc.) of that synthetic experiment are chosen according to the experimental framework described in Section 9.2.2. That is, we evaluate ultrasonic signals that mimic the measurements used to characterize a CFRP composite plate obtained using a finite-amplitude nonlinear through-transmission configuration with a low-frequency ultrasonic signal containing a wide range of frequencies. Note that, in a such a case, the NTM formalism does not suffer from numerical instabilities due to the resulting *frequency-thickness* product[2]. As in Section 10.1, the transmitter is considered as a damped mechanical system with a single degree-of-freedom, so that the Fourier transform of the input signal $X(F)$, with $F = \Omega/2\pi$, is assumed to be Gaussian with the center frequency $F_c = 5$ MHz of the transducer as mean and the bandwidth $B = F_c/10 = 0.5$ MHz as standard deviation. Note that the bandwidth is much smaller than in the linear case. Indeed, in the nonlinear regime, a burst of (nearly) pure tone at high-energy level is used as input signal, such that the second-harmonic amplitude can be well distinguished from the fundamental one. A high resolution is chosen for signal sampling with a frequency $F_s = 200$ MHz, while a signal period of 10 μs is considered

[2]As the TM formalism, the NTM formalism can neither be validated on the traditional layered materials described in Section 10.2. Ideally, one could employ the nonlinear digital modeling of the specimen presented in Section 8.2, but we showed that it was not applicable so far.

in order to ensure the capture of several wave echoes, providing $N = 2000$ samples. The resulting discrete-time input signal $x(n)$ and its magnitude spectrum $|X(\omega)|$ are shown in Figure 12.14.

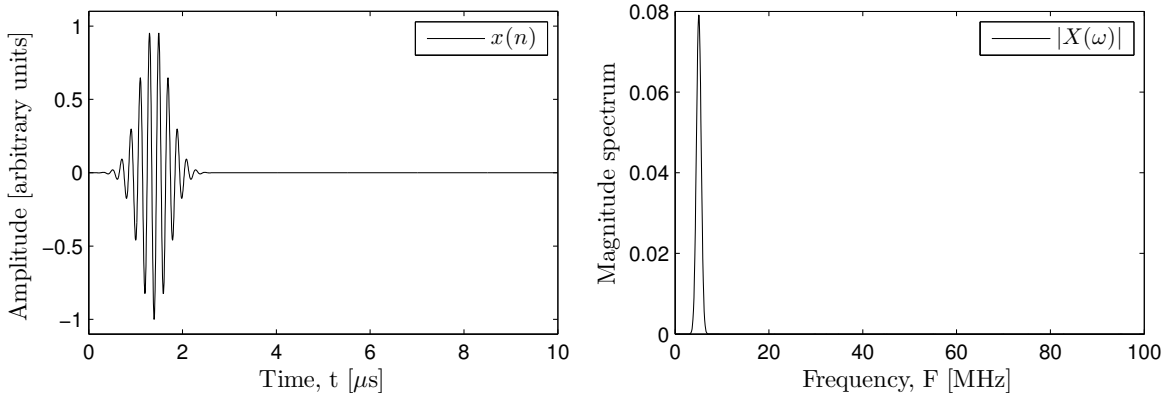

Figure 12.14: *Discrete-time input signal $x(n)$ (left) and its magnitude spectrum $|X(\omega)|$ (right). Note that the abscissas have been scaled according to a sampling frequency $F_s = 200$ MHz.*

The specimen considered is a layered CFRP symmetric plate which consists of 16 layers. Since a major damage mode in composites is delamination, an interface layer of much smaller thickness than both plies and wavelength of the central frequency is assumed between every two consecutive layers in the material. Thus, the resulting multilayered specimen consists of $M = 32$ layers, whose mechanical and geometrical properties are summarized in Table 12.3. These properties are chosen according to the experimental values provided in Table 9.4.

Layer	Y. Modulus $E\ [GPa]$	P. Ratio $\nu\ [-]$	Density $\rho\ [kg/m^3]$	Attenuation $\alpha\ [Np/m]$	Thickness $a\ [mm]$	Nonlinearity β [-]
0°-orient.	11.1616	0.3007	1589.5	293.0230	0.1215	unknown
90°-orient.	11.1616	0.3007	1589.5	293.0230	0.1215	unknown
Interface	5.2728	0.3500	1310	361.1595	0.01	unknown

Table 12.3: *Mechanical and geometrical properties of the layers and interfaces that compose the multilayered composite material.*

From these properties and the above excitation signal, the nonlinear response signal can be obtained through the scheme depicted in Figure 8.2. Firstly, the nonlinear properties β_j, $\forall j = 1, \ldots, 32$ are set to zero. Figure 12.15 compares the response signals obtained with the NTM and TM formalisms. As expected, both formalisms provide the same response signals, since the TM formalism is a sub-case of the NTM formalism (see Section 8.1.2).

Then, the nonlinear properties of the layers/interfaces are set to $\beta_j = 100$, $\forall j = 2, \ldots, 31$ (that of water is set to $\beta_j = 5$, $\forall j = 1, 32$), and the resulting signals are depicted in Figure 12.16. As can be observed, this model predicts the acoustical manifestations of the nonlinear constitutive behavior, i.e. the distortion of the waveform in the time-domain and the

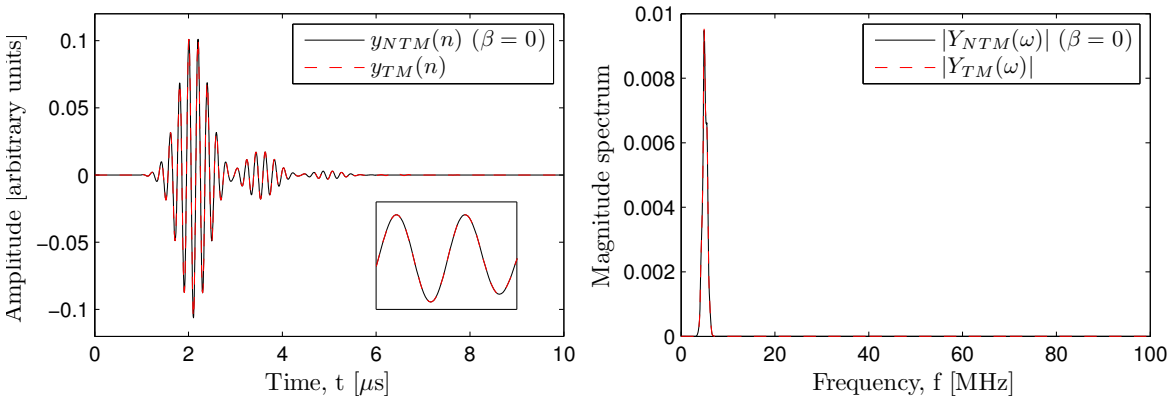

Figure 12.15: *Time-domain signals $y_{NTM}(n)$ and $y_{TM}(n)$ and magnitude spectra $|Y_{NTM}(\omega)|$ and $|Y_{TM}(\omega)|$ obtained through the NTM ($\beta = 0$) and TM formalisms, respectively.*

observation of a second harmonic peak as local maximum in the frequency-domain, in a consistent way (see Section 4.1.2).

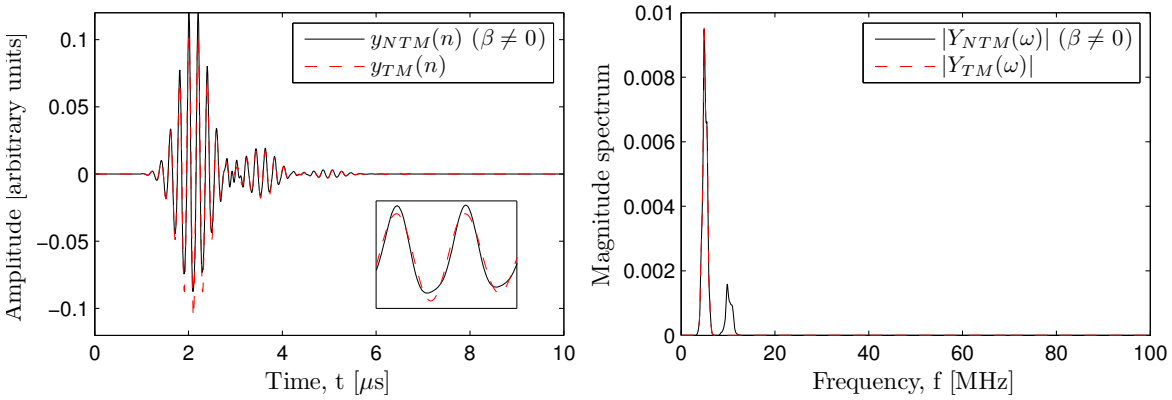

Figure 12.16: *Time-domain signals $y_{NTM}(n)$ and $y_{TM}(n)$ and magnitude spectra $|Y_{NTM}(\omega)|$ and $|Y_{TM}(\omega)|$ obtained through the NTM ($\beta \neq 0$) and TM formalisms, respectively.*

12.2.2 Experimental results

The present section aims at demonstrating the capability of the NTM formalism to predict the nonlinear measurements obtained from a multilayered specimen. Here, this approach is evaluated on the CFRP plate described as specimen (C) in Table 9.4 with a stacking sequence which corresponds to a $[0/90]_{4s}$ lay-up. The model-based estimation procedure applied to find the values of the damage parameters $\boldsymbol{\theta}$ that best fit the experimental measurements is depicted in Figure 12.17. Note that the unique difference between this scheme and that presented in the previous section is that the digital modeling of the specimen $H^D(z, \boldsymbol{\theta})$ has been replaced by the NTM formalism.

Given the nonlinear model corresponding to a certain damage state $\boldsymbol{\theta}$ and the excitation signal $x(n)$ applied to the specimen enables us to compute an approximation $y^{(\boldsymbol{\theta})}(n)$ of an

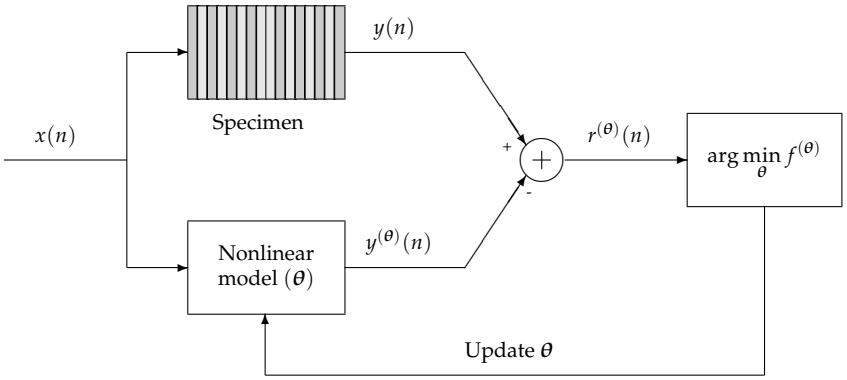

Figure 12.17: *Diagram of the model-based estimation procedure used to reconstruct linear and nonlinear mechanical properties of the specimen.*

individual response signal $y(n)$ measured from the specimen, according to the scheme depicted in Figure 8.2. The remaining of the optimization process is identical to that described in the previous section.

It must be noted that the measurements now exhibit a nonlinear constitutive behavior, which is achieved by the finite-amplitude method (see Section 9.2.2) through an input signal at high energy. This also implies that the signal measured in water at such an high energy and also used as excitation is also nonlinear. Thus, the purely linear input signal $x(n)$ used here is a realistic *linearized* and ahead-shifted version of the output signal measured in water (obtained by removing the specimen) depicted in Figure 12.18. Under linearization, we consider a low-pass filtered version of that signal to remove the nonlinear components.

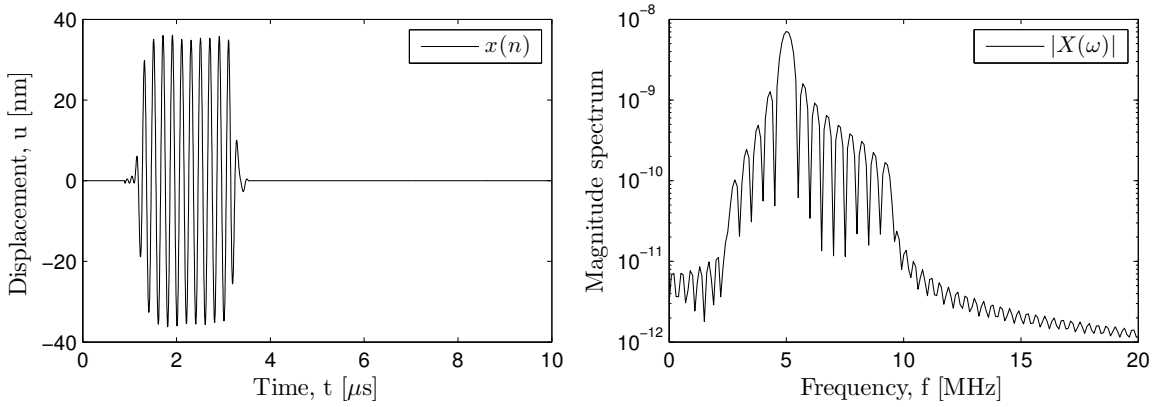

Figure 12.18: *Discrete-time input signal $x(n)$ (left) and its magnitude spectrum $|X(\omega)|$ (right) used as excitation for the CFRP plate ($F_c = 5$ MHz). Note that the abscissas have been scaled according to a sampling frequency $F_s = 200$ MHz.*

System calibration

As for the linear case, the first tackled problem is the calibration of the NTM formalism that solves the forward problem, since the properties provided by the manufacturer may slightly differ from the real ones. In addition, the nonlinear properties of the layers/interfaces

are virtually nonexistent in the literature. Consequently, the calibration is achieved by the matching procedure described in Section 9.3.1, in which four parameters (the Young modulus E_m and the damping coefficient α_m of the polymer matrix, and the nonlinear properties β_L and β_I of the layers and interfaces, respectively) are adjusted with GA's to find the optimal characterization of measurements obtained from undamaged area of the specimen. Figure 12.19 depicts the resulting matching (for the optimal parameters $\theta_{cal.}$) between a nonlinear measurement $y_0(n)$ and the numerically predicted model $\tilde{y}_0(n)$ for un undamaged area.

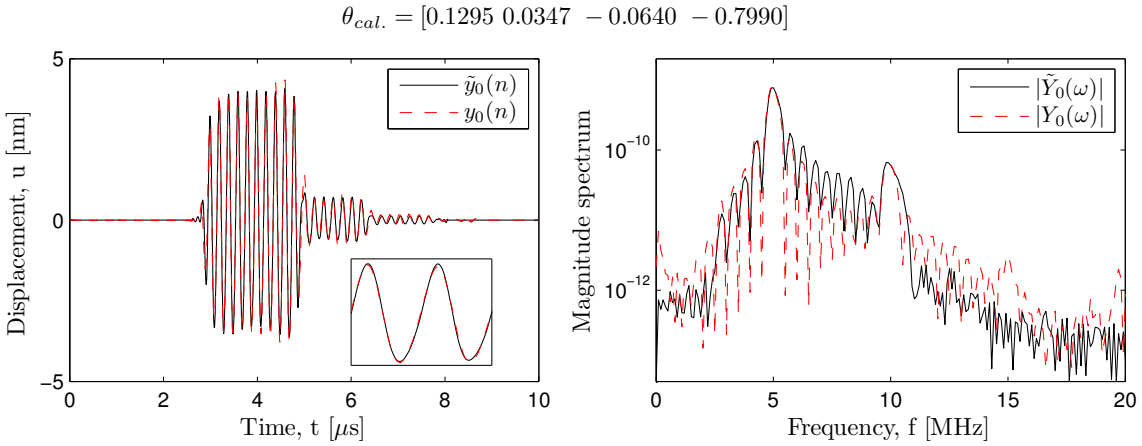

Figure 12.19: *Calibration of the signal predicted by the nonlinear model $\tilde{y}_0(n)$ with a nonlinear measurement $y_0(n)$ obtained from an undamaged area.*

As can be seen, a fairly good matching is obtained. The slight discrepancy between the modeled and observed signals, particularly visible in the frequency-domain, are mainly due to the fact that the modeled nonlinear characteristics are restricted to the second harmonic and the nonlinearity of first-order (see Section 8.2). In contrast, the nonlinear measurement seems to contain also higher-harmonic components. The modified properties of the layers/interfaces obtained from the calibration step are summarized in Table 12.4.

Layer	Y. Modulus $E\ [GPa]$	P. Ratio $\nu\ [-]$	Density $\rho\ [kg/m^3]$	Attenuation $\alpha\ [Np/m]$	Thickness $a\ [mm]$	Nonlinearity β [-]
0°-orient.	11.0416	0.3007	1589.5	288.864	0.1215	308.469
90°-orient.	11.0416	0.3007	1589.5	288.864	0.1215	308.469
Interface	5.1965	0.3500	1310	350.446	0.01	173.244

Table 12.4: *Mechanical and geometrical properties of the layers and interfaces that compose the multilayered composite material.*

Hypothesis on the damage distribution

In the nonlinear regime, the issue of the parametrization is even more troublesome, since an additional property has to be taken into account to describe the linear and nonlinear mechanical and geometrical properties of the material's layers and interfaces, i.e. $\theta \in$

$\{E_i, \nu_i, \rho_i, \alpha_i, a_i, \beta_i\}$, with $i = 1, \ldots, M$. We again perform a regularization to restrict the solution field, based on the *prior* knowledge on the damage propagation pattern described in Section 9.1.1. To deal with all possible damage mechanisms, one could suggest the addition of the nonlinear properties to the finite set of damage parameters defined in Section 12.1.2. However, such a set would be particularly large and may probably affect the convergence capability of the proposed search algorithm drastically. It is usually speculated that nonlinear properties may deliver valuable information on the material degradation, particularly sensitive to early damage manifestation (i.e. far more sensitive than the linear acoustic properties). Consequently, to undergo the limitation of the size of the finite set, we focus on measurements from low and moderate damaged areas from the specimen. In such a case, it is reasonable to assume that the early damage propagates nearly symmetrically through the specimen's thickness, such that the set of linear properties can be slightly reduced and extended with nonlinear properties. As in the previous section, nine damage parameters $\boldsymbol{\theta} = \{\theta_{int}, \boldsymbol{\theta}_{90}, \theta^*_{int}, \theta^{NL}_{90}, \theta^{NL}_{int}, \theta^{NL}_{int^*}\}$ are chosen as a trade-off between algorithm's convergence and computational cost. The damage parameters θ_{int} and θ^*_{int} are defined in an identical way as in Section 12.1.2. The four-component vector $\boldsymbol{\theta}_{90}$ accounts for a stiffness reduction $\boldsymbol{E}_{90}$ of 7 layers by means of matrix cracking in the layers with 90°-orientation (assuming now a symmetric damage distribution). The damage parameter θ^{NL}_{90} accounts for an increase of the nonlinear parameter β_{90} in the layers with 90°-orientation (i.e. increasing density of micro-cracks due to impact and fatigue), whereas θ^{NL}_{int} and $\theta^{NL}_{int^*}$ account for an increase of the nonlinear parameters β_{int} and β^*_{int} in the layers' interfaces between layers of different orientation (i.e. possible clapping mechanisms where the delamination occur). Each damage parameter $\theta_i \in [0, 3]$, with $i = 1, \ldots, 9$, is defined in a dimensionless and logarithmic scale as,

$$\begin{aligned} E_{opt,i} &= E_i e^{-\theta_i} \qquad (i = 1, \ldots, 6) \\ \beta_{opt,i} &= \beta_i e^{\theta_i} \qquad (i = 7, \ldots, 9) \end{aligned} \tag{12.3}$$

Damage parameter estimation

Using the calibrated properties obtained from a calibration step similar to that described in Section 12.2.1, the nonlinear model can be updated for a set of few representative measurements using the model-based estimation procedure depicted in Figure 12.17. The resulting matching between a nonlinear measurements $y_1(n)$ and the numerically predicted model $\tilde{y}_1(n)$ for a low-damaged area of the specimen is depicted in Figure 12.20 (for the nine optimal damage model parameters $\boldsymbol{\theta}$ mentioned above). Even though the minimization is performed in the time-domain, we also represent the matching in the frequency-domain, since it provides a complementary vision of the nonlinear acoustic manifestations. As can be observed, in this case, the damage parameters θ_1 and θ_6 reveal a slight reduction of the stiffness of the interfaces between layers of different orientations due to delaminations, but

the nonlinear properties θ_j ($j = 7, \ldots, 9$) remain unchanged. Again, a fairly good matching is obtained between the experimental and modeled signals.

$$[\mathbf{E}_{opt.}\ \beta_{opt.}] = [4.951\ 11.042\ 11.042\ 11.042\ 11.042\ 2.266\ 308.469\ 173.244\ 173.244]$$

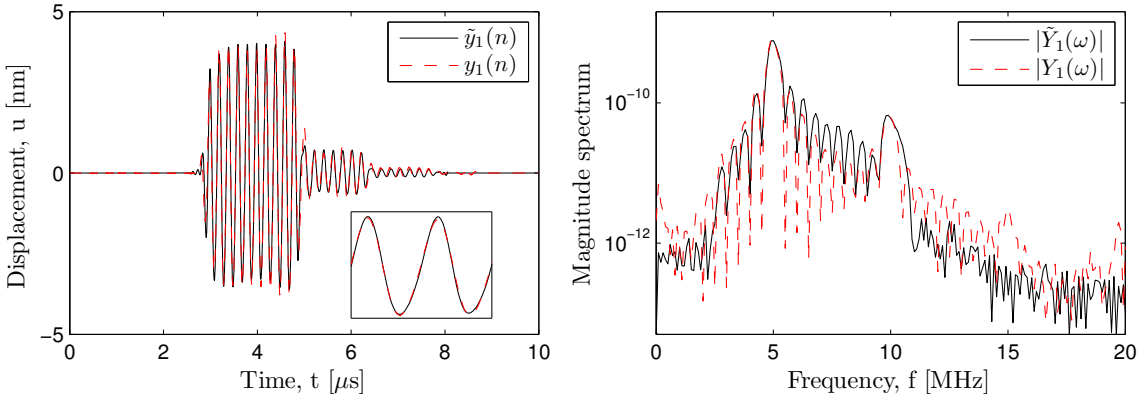

Figure 12.20: *Comparison between a nonlinear measurement and a signal predicted by nonlinear model for a low-damage area.*

An example of the resulting matching between a nonlinear measurement $y_2(n)$ and the numerically predicted nonlinear model $\tilde{y}_2(n)$ for a moderately damaged area of the specimen is depicted in Figure 12.21.

$$[\mathbf{E}_{opt.}\ \beta_{opt.}] = [5.132\ 11.042\ 11.042\ 11.042\ 11.042\ 2.338\ 289.431\ 448.084\ 2326.161]$$

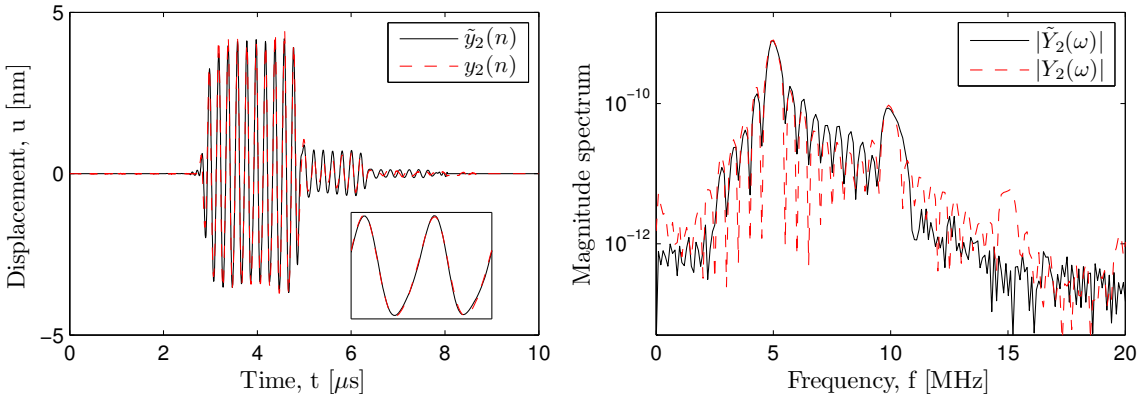

Figure 12.21: *Comparison between a nonlinear measurement and a signal predicted by nonlinear model for a moderately damaged area.*

As can be observed, the damage parameters θ_1 and θ_6 reveal a slight reduction of the stiffness of the interfaces between layers of different orientations due to delaminations. However, in this case, the nonlinear property of the interfaces between the layers of different orientation (i.e. θ_8), and especially that between the two back-wall layers (i.e. θ_9), increases significantly (in a proportion that is much larger than that affecting the stiffness reduction). This phenomenon appears to be consistent with the larger distortion of the waveform and growth of the amplitude of the second-harmonic. Consequently, it seems that the nonlinear properties are more sensitive to this kind of damage than the linear ones. This observation

further supports both the aforementioned hypothesis and the obtained matching between the nonlinear experimental and modeled signals is reasonably good again.

Figure 12.22 depicts an example of the resulting matching between a nonlinear measurement $y_3(n)$ and the numerically predicted nonlinear model $\tilde{y}_3(n)$ for another moderately damaged area of the specimen. In this case, the damage parameter θ_9 corresponding to the nonlinear property of the interface is even larger than in the previous case.

$$[\mathbf{E}_{opt.}\ \beta_{opt.}] = [5.195\ 10.946\ 11.042\ 11.042\ 11.042\ 4.116\ 289.431\ 439.63\ 8830.212]$$

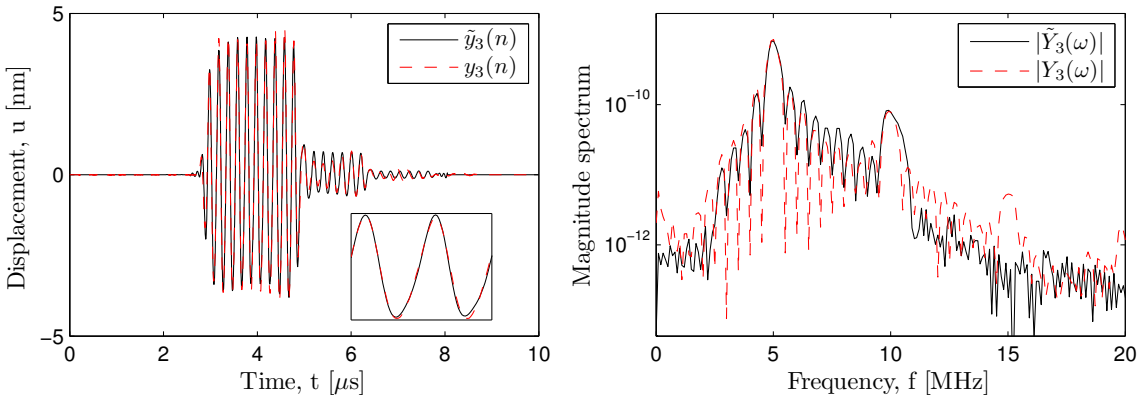

Figure 12.22: *Comparison between a nonlinear measurement and a signal predicted by nonlinear model for another moderately damaged area.*

Finally, an example of the resulting matching between a nonlinear measurement $y_4(n)$ and the numerically predicted nonlinear model $\tilde{y}_4(n)$ for a severe damaged area of the specimen is depicted in Figure 12.23.

$$[\mathbf{E}_{opt.}\ \beta_{opt.}] = [1.33\ 11.042\ 7.251\ 3.603\ 11.042\ 0.259\ 3518.832\ 95.635\ 108.819]$$

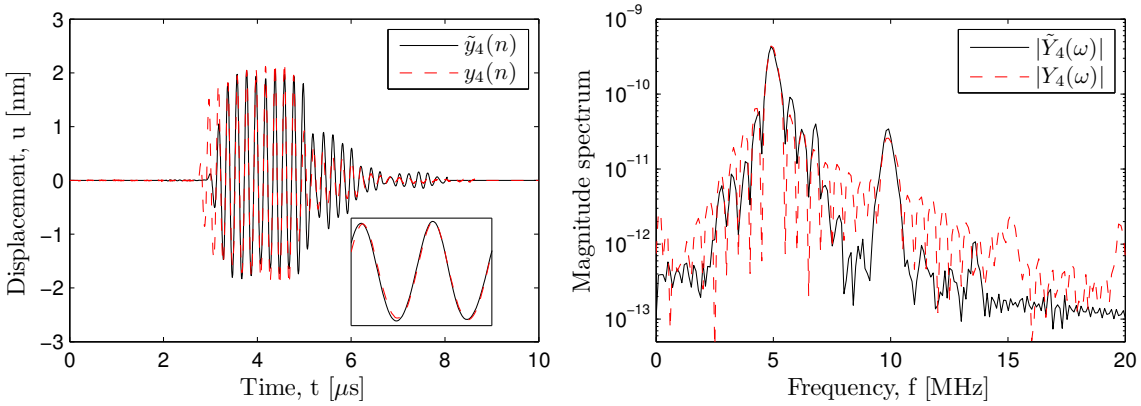

Figure 12.23: *Comparison between a nonlinear measurement and a signal predicted by nonlinear model for a severely damaged area.*

In this case, the matching between the nonlinear experimental and modeled signals is relatively bad. This could be explained as follows: (1) The damage is so large that the chosen damage parametrization does not provide the model sufficient degrees of freedom to fit the experiment, (2) the optimization process, and more concretely the definition of the residual,

is not well-posed for such signals with numerous bursts obtained from a severe damaged area, as it appears that the cross-correlation between the time-domain signals deliver shifted results (see Section 9.3.1).

A further inspection of the modeling error shows that the residuals $e_j(n)$ $(j = 1, 3)$ only contain few components other than measurement noise, but the *approximation error* approximately amounts to 20% of the signal's amplitude, and is larger than in the linear case. It is noteworthy that errors appear both at the fundamental frequency (5 MHz) and twice that frequency (10 MHz). Even though, these results are encouraging and support the potential of this nonlinear model to face up complex wave responses originated from multilayered specimens, whose layers have a classical nonlinear constitutive behavior.

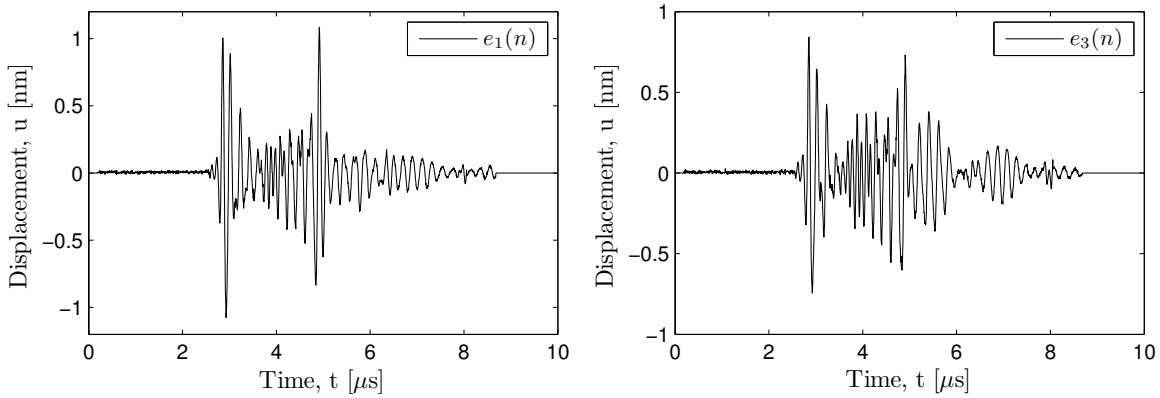

Figure 12.24: *Error between nonlinear measurements and signals predicted by the nonlinear model for a low and moderately damaged area.*

12.3 Discussion

In a first part, the presented framework showed that our digital modeling of the specimen can be inserted in a model-based estimation procedure in a straight-forward way, providing encouraging results at the time of reconstructing the damage parameters corresponding to altered mechanical properties of a CFRP plate subjected to impact and fatigue damage. A compete 3D reconstruction of the stiffness values has been obtained and the results were positively contrasted against other techniques. It particular, it has been demonstrated that the coefficients of the digital model behaves dynamically depending upon the damage state of the material under inspection, that is, both the gains and positions of the coefficients change (this confirms the observations done in Section 11.3). Additionally, it has been observed that damage also affects the length of the modeling-order of the transfer function's denominator. Consequently, it seems to be more adequate to perform such a model-based estimation with a sparse and physics-based digital model with a finite set of damage model parameters (9, in our case) than with an heuristic sparse signal model, whose number of model parameters can *a priori* not be easily determined.

As a drawback, it should be mentioned that neither the preprocessing steps nor the extraction of *cesptral* coefficients described in Chapter 11 result adequate for this experimental case. Indeed, our specimen's digital filter requires a high sampling frequency F_s, so that the rounding of the coefficients is not altered (see discussion in Chapter 7). In addition, such a frequency is also required to compute the nonlinear case (see the oversampled input signal requirement in Chapter 8.1.2). However, this sampling frequency, along with the chosen transducers, plays against alternative domains of representation of the signal, since it introduces components into the spectrum which basically consist of noise (see the frequency-band from 20 to 100 MHz in Figure 12.2). This useless part of the spectrum mixes up with its useful part while applying the IDFT to compute the *cepstrum*, and thus corrupts and invalidates the *cepstra* obtained for the actual optimization task. Furthermore, this noisy part cannot be filtered out, since a multiplication in the frequency-domain corresponds to a sum in the cepstral-domain, and thus the minimization of *cepstral* distances would remain as troublesome as before. Consequently, this incompatibility somehow tells us that the used transducers are maybe not the most suitable ones for inspecting this material, since they focus on a frequency-band which is much smaller than that of the frequency response of the specimen. Notwithstanding, increasing the excitation frequency may lead to higher attenuation of the propagating waves, which could makes the damage identification difficult.

In a second part, a similar framework showed that the NTM formalism can also be inserted in a model-based estimation procedure, providing preliminary results when reconstructing the damage parameters corresponding to altered linear and nonlinear mechanical properties of the CFRP plate mentioned above. In this case, only the stiffness and nonlinearity values of a reduced set of measurements have been computed, suggesting that the nonlinear parameters provide valuable complementary information for early damage detection.

13

Probabilistic inverse problem for ultrasonic monitoring of tissue-engineered materials

The understanding of internal processes that affect the changes of consistency of soft tissue is a challenging problem. For this purpose, an ultrasound-monitoring Petri dish has been designed to monitor the evolution of relevant mechanical parameters during engineered tissue formation processes in real time (see Section 9.2.3). For a better understanding of the measured ultrasonic signals, we propose the use of numerical models for evaluating the ultrasound-tissue interactions. However, many types of uncertainties involved in the modeling of the interactions between ultrasonic waves and tissue, such as excitation, material viscosity, and material heterogeneity are responsible for noise in the output. In this chapter, several models of ultrasound-tissue interactions are developed and contrasted against experimental observations. All assume homogeneous media with varying moduli and energy-dissipation forms that are expressed as attenuation models. High-frequency ultrasound are adopted for analyzing and interacting with small-scale specimens. The minimization between experimental and numerically predicted measurements is addressed by solving a probabilistic inverse problem which incorporates classical signal processing techniques. In addition, a stochastic model-class selection formulation is used to rank which of the proposed interaction models are more plausible. The sensitivity of the system is first verified by monitoring a gelation process, with the purpose of validating the model-class selection algorithm. Such a process is selected, since its behavior is controlled and assumed by the majority of the literature to be viscoelastic [302, 303, 304].

13.1 Monitoring of a gelation process

The proposed methodology combines four elements: (1) The signal acquisition of the ultrasonic signals obtained from the wave interactions with a sample of tissue, a (2) set of alternative attenuation models that simulate the ultrasound-tissue interactions, which is numerically solved by the TM formalism described in Chapter 6, a (3) NDE-oriented signal processing framework that extract relevant features from both the experimental and numerically predicted signals (see Section 4.2), and a (4) stochastic model-class selection formulation used to rank which of the models parametrization are more plausible (see Section 9.3.2). The latter is used to reconstruct the evolution of the relevant mechanical parameters during the culture reaction time.

The experimental system is idealized by a mathematical model of the propagation and interaction of the transmitted ultrasonic waves with all the parts of the system until they are received by the sensor. Damping in tissue can be caused by combinations of physical mechanisms such as thermal flow on both the micro and macro scale, grain boundary viscosity, point-defect relaxations, eddy-current effects, stress induced ordering and electronic effects. Several models are tested here to idealize the removal of energy by dissipation or radiation. Three alternative damping models are used: (i) viscous, (ii) hysteretic, and (iii) proportional to integer time derivatives of the particle movement, based on their fractional time derivatives. The damping is defined in terms of the wave modulus M, which is modified from the undamped one M_0 to generate a dispersive one, which is a frequency-dependent complex modulus $M^*(\omega)$, where ω is the angular frequency if the modulus dispersion is represented by its frequency domain. The viscous model is defined in terms of the frequency-dependent loss factor η, obtained as the ratio between loss and storage moduli [305]. In this context, a specific view of hysteretic damping is taken, where it is expressed as a frequency-independent damping [227]. The last model, based on fractional time derivatives, leads to a damping function that may be expressed as a power law, and thus improves curve-fitting properties for relaxation [305, 227]. These models are selected according to their performance to described such process, as shown in a preliminary study [306]. On the one hand, the viscoelastic and hysteretic models are defined according to Maia *et al.* [307],

$$M^*(\omega) = M^0 \left(1 - j\omega\eta\right) \tag{13.1}$$

and

$$M^*(\omega) = M^0 \left(1 - j\zeta\right) \tag{13.2}$$

where η and ζ are the viscoelastic and hysteretic damping coefficients of tissue, respectively. On the other hand, the fractional time derivative damping is defined as,

$$M^*(\omega) = M^0 \frac{1 + b(j\omega)^\beta}{1 + a(j\omega)^\alpha} \tag{13.3}$$

where a, b, and $\alpha = \beta$ are the fractional derivative constants. The three models are summarized hereafter, highlighting the combination of the considered model parameters,

Tag	Size	Parameters					
1	4	K^{tissue}	ζ	z^{ampl}	z^{time}		
2	4	K^{tissue}	η	z^{ampl}	z^{time}		
3	6	K^{tissue}	a	b	$\alpha = \beta$	z^{ampl}	z^{time}

Table 13.1: Three alternative damping models.

where K^{tissue} denotes the Bulk modulus of tissue. Two additional parameters z^{ampl} and z^{time} are introduced to control the correction of the amplitude and the time-shift of the input signal in the culture, which corrects effects of temperature and other phenomena on the sensors, that affect attenuation and delay on the path from the electronics to the arrival of the signal at the culture specimen.

The mathematical model is approximated by a semi-analytical model of the wave interactions between the Petri dish and the culture based on the TM formalism. It is noteworthy that the experimental configuration used here has two specificities with respect to the usual through-transmission applied over the course of the thesis (see Figure 9.11). Indeed, the sensor disposition in angle position slightly modifies both the transfer matrices and the boundary conditions described in Chapter 6. The first modification can be solved by incorporating the Snell's law within such matrix formulation, whereas the second one is solved by reformulating the boundary conditions (i.e. the Sommerfeld radiation-type condition is now applied to the last layer, by means of a vanishing forward-propagating component, and the wave is detected at position 0).

13.1.1 Measurements

The material evaluated here is the specimen (D) described in Table 9.5. The recorded signals by the ultrasound-monitored Petri dish every 250 seconds are shown in Figure 13.1, without and with specimen, respectively. No clear evolution is detectable by bare visual inspection of the signals. Those are mainly composed of three different waveforms (simplified paths of Figure 9.11), namely (1) the wave front that propagates only through the PMMA layer (labeled as u_1), (2) a wave that crosses both the PMMA layer and the specimen (labeled as u_2), and (3) a wave echo produced by the former wave after crossing twice the specimen (labeled as u_3). It is noteworthy that when the specimen is on place, the majority of the excitation signal (registered without specimen for calibration) is transmitted instead of reflected. Since the wavelength in gel is compatible with the layer thickness, the individual echoes generated by the multiple reflections inside the gel layer can be analyzed separately. We focus our analysis on the two last echoes, since they are those which explicitly interact with the material under inspection.

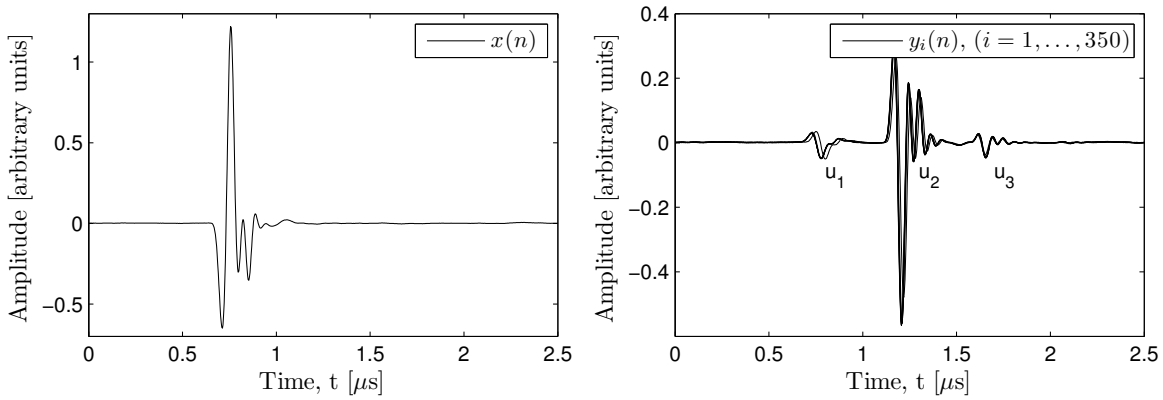

Figure 13.1: *Ahead shifted excitation signal measured without specimen (left); sequence of signals with specimen in-place registered every 250 seconds (right).*

13.1.2 NDE-oriented signal processing

The model-based estimation procedure is performed according to Figure 5.4 and incorporates different signal processing techniques. The signals obtained from the specimen are first preprocessed by making use of a temporal analysis window (Hamming), as in Section 11.1. Then, the minimization is performed in three different domains, namely the time-domain, the frequency-domain and the cepstral-domain. Finally, we define some weighting filters to prioritize some extracted features over others. Indeed, besides the classical residual vector definition of Equation (9.1) (denoted here as $\boldsymbol{r}_0$), we introduce three further definitions to enhance the process evolution. First, a weighted residue $\boldsymbol{r}_1$ which includes the variance of the measurements over the temporal evolution of the reaction process is defined. Thus, the goodness of fit of the model predictions to the experimental values is assessed with a weighted least squares criterion [308]. Additionally, a weighted residue $\boldsymbol{r}_2$ which includes the variance of the measurements over the reaction time of the process is defined. Finally, the last weighted residue $\boldsymbol{r}_3$ incorporated both the aforementioned variances.

Those alternative definitions are assumed to (1) reduce the uncertainties resulting from measurements noise by assuming statistical independence of the errors, and to (2) enhance parts of the signal that may contain information about the reaction process. In a probabilistic sense, residue definitions that take into account variance information can be understood as a prior knowledge on the measurements' quality and/or on the evolution of the reaction process [289].

13.1.3 Signal simulation

The TM formalism is used to generate sample signals, after calibrating the estimated model parameters for the first signal (at the initial evolution time) using the inverse problem described in Section 9.3.1. Note that in such a case, the gel properties at the initial time are close to those of water, and so the model calibration can be performed with BFGS algorithms. Posteriorly, since the number of reaction model parameters (see Table 13.1) is relatively high, the optimization will be performed with GA's. Time-domain signals and magnitude spectra are

shown in Figures 13.2-13.3 for the viscous model (case 2) at an arbitrary time of the reaction process. In those figures, an analysis window (Hamming) has been applied to the signals, and classical and weighted residue definitions are considered, denoted as $\boldsymbol{r}_0$ and $\boldsymbol{r}_3$, respectively.

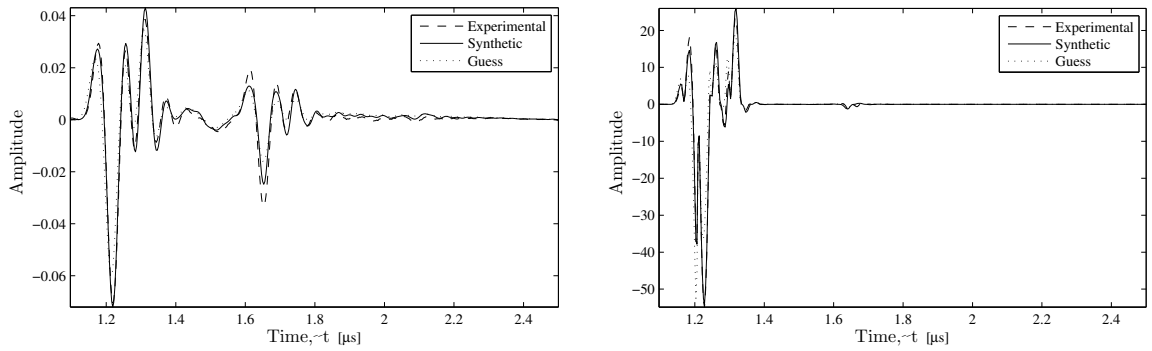

Figure 13.2: *Example of fitting of experimental observations and signals simulated with the viscous model. The minimization has been performed in the time-domain, after preprocessing the signals with a Hamming window, and considering residues $\boldsymbol{r}_0$ (left) and $\boldsymbol{r}_3$ (right).*

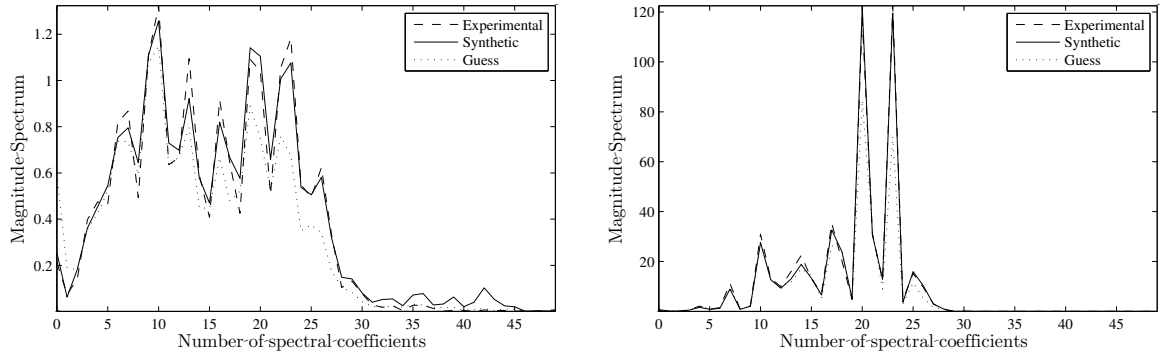

Figure 13.3: *Example of fitting of experimental observations and signals simulated with the viscous model. The minimization has been performed in the frequency-domain, after preprocessing the signals with a Hamming window, and considering residues $\boldsymbol{r}_0$ (left) and $\boldsymbol{r}_3$ (right).*

A significative ability to simulate the system can be observed. As expected, the Hamming window accentuated the detailed spectrum due to the enhanced echoes of the time-domain signals (left plots). Additionally, it seems that the weighted residue $\boldsymbol{r_3}$ allows to remove some variability due to the measurements uncertainties (right plots). In the time-domain, it enhances the signal parts containing information of the reaction process (i.e. here mainly the first echo), while allowing to remove the parts which are invariant to the process evolution (scattering parts). In the frequency-domain, the weighted residue allows to remove the frequency range being insensitive to the reaction process, or being erroneous due to measurements noise.

13.1.4 Posterior probability of the model

The probability density function is computed for the viscous attenuation model (see Section 9.3.2), and some relevant samples issued from the results obtained in the previous section are shown in Figures 13.4-13.6. Since the PDF is a multidimensional function, only a slice along two parameters is represented, namely the Bulk modulus of the tissue and the viscous damping coefficient.

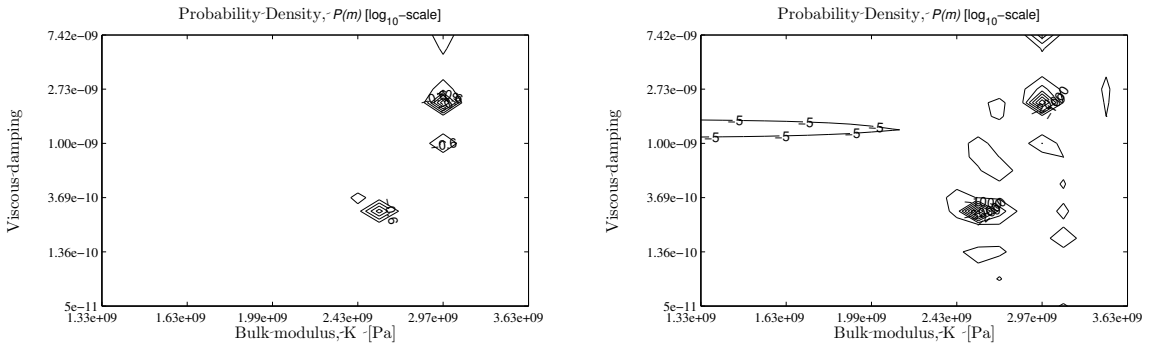

Figure 13.4: *Posterior probability of the viscous model (slice along two parameters). The minimization has been performed in the time-domain, after preprocessing the signals with a Hamming window, and considering residues $\boldsymbol{r}_0$ (left) and $\boldsymbol{r}_3$ (right).*

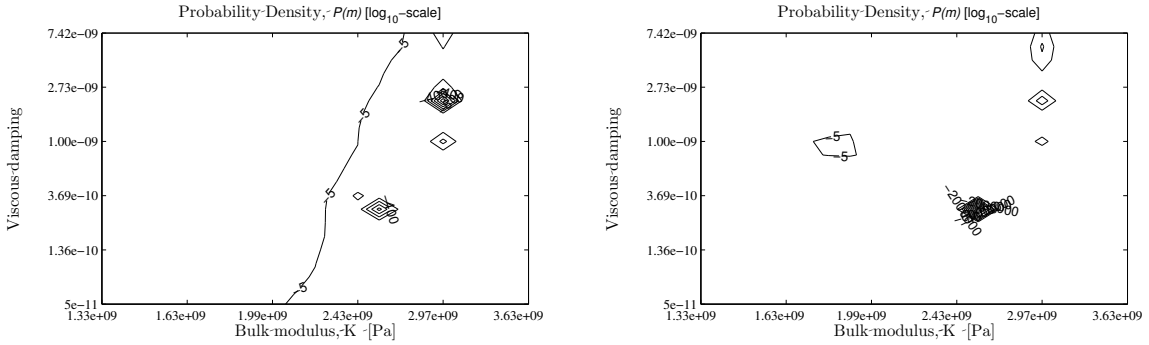

Figure 13.5: *Posterior probability of the viscous model (slice along two parameters). The minimization has been performed in the frequency-domain, after preprocessing the signals with a Hamming window, and considering residues $\boldsymbol{r}_0$ (left) and $\boldsymbol{r}_3$ (right).*

The inspection of these plots reveals several local minima as valleys in the PDF, and variations of several orders of magnitude from good to bad reaction model parameters. This implies a bad conditioning of the reconstruction IP and justifies the use of advanced search algorithms such as GA's. Nonetheless, the use of a weighted residue definition enhance the slope of these local minima, and may thus speed up the convergence of the search algorithm. The other attenuation models present similar trends, but are not displayed here for sake of brevity. Additionally, some irrelevant samples issued from the *cepstral* analysis are depicted in Figure13.6. The inspection of these plots reveals many local minima that approximately have the same values, leading to an ill-conditioned solution space.

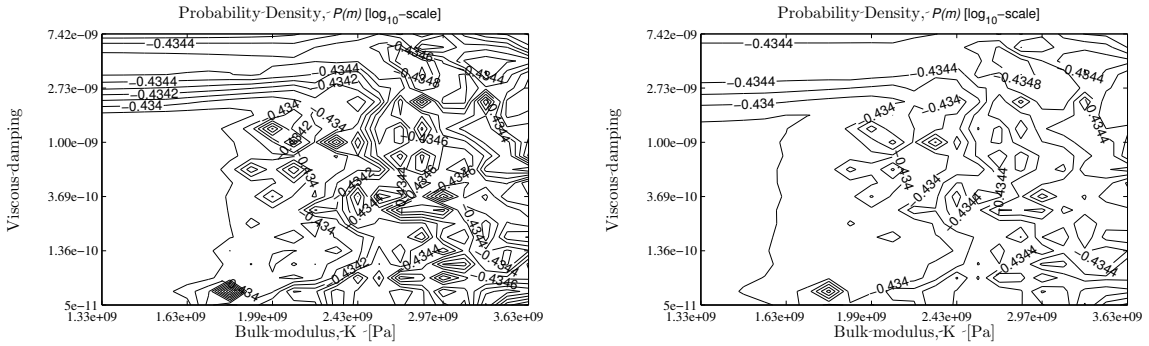

Figure 13.6: *Posterior probability of the viscous model (slice along two parameters). The minimization has been performed in the cepstral-domain, after preprocessing the signals with a Hamming window, and considering residues $\boldsymbol{r}_0$ (left) and $\boldsymbol{r}_3$ (right).*

13.1.5 Model class plausibility

The posterior probability $p(\mathcal{C})$ of every proposed model class $\mathcal{C} \in \mathfrak{C}$ is computed by Quasi Montecarlo integration using 2^{18} Sobol sampling points. Additionally, the estimation of Occam's factor and the certainty metric $\overline{\sigma}$ are summarized in Tables 13.2-13.3 for time-domain signals and magnitude spectra, respectively.

Windowing	Residue	Model class	1	2	3
w_0	$\boldsymbol{r_0}$	$p(\mathcal{C})$ [%]	31.55	32.39	36.06
		Occam $[-log_{10}]$	2.24	4.10	1.90
		Certainty $[log_{10}]$	0.11	0.75	0.37
	$\boldsymbol{r_1}$	$p(\mathcal{C})$ [%]	33.33	33.33	33.33
		Occam $[-log_{10}]$	8.11	7.93	11.93
		Certainty $[log_{10}]$	1.69	1.66	1.97
	$\boldsymbol{r_3}$	$p(\mathcal{C})$ [%]	15.53	**63.10**	21.37
		Occam $[-log_{10}]$	7.34	9.95	14.78
		Certainty $[log_{10}]$	2.23	2.74	2.97
w_1	$\boldsymbol{r_0}$	$p(\mathcal{C})$ [%]	32.45	32.99	34.57
		Occam $[-log_{10}]$	7.14	6.50	7.44
		Certainty $[log_{10}]$	1.40	1.16	1.02
	$\boldsymbol{r_1}$	$p(\mathcal{C})$ [%]	33.33	33.33	33.33
		Occam $[-log_{10}]$	7.93	7.90	13.08
		Certainty $[log_{10}]$	1.83	1.95	∞
	$\boldsymbol{r_3}$	$p(\mathcal{C})$ [%]	34.81	31.57	33.62
		Occam $[-log_{10}]$	4.25	6.17	8.72
		Certainty $[log_{10}]$	1.39	1.79	1.45

Table 13.2: Plausibility of model classes. Time-domain.

The most plausible model-class is shown to be 2, involving K^{tissue}, viscoelastic damping, and temperature and amplitude corrections. It is closely followed by class 1 (hysteretic damping), whereas class 3 does not provide results for all proposed signal processing techniques. The time-domain signal and magnitude spectrum computed with the weighted residue definition $\boldsymbol{r}_3$ show significantly higher posterior probability $p(\mathcal{C})$ (indicated in bold in the tables) than the other domains of representation. It can be shown that the *real cepstrum*

Windowing	Residue	Model class	1	2	3
w_0	r_0	$p(\mathcal{C})$ [%]	29.79	29.39	40.82
		Occam $[-log_{10}]$	0.09	-0.42	-5.17
		Certainty $[log_{10}]$	0.40	0.38	0.71
	r_1	$p(\mathcal{C})$ [%]	49.94	50.06	-
		Occam $[-log_{10}]$	7.71	8.82	-
		Certainty $[log_{10}]$	1.52	1.63	-
	r_3	$p(\mathcal{C})$ [%]	0.02	**56.47**	43.51
		Occam $[-log_{10}]$	4.84	5.88	22.37
		Certainty $[log_{10}]$	1.93	1.89	4.10
w_1	r_0	$p(\mathcal{C})$ [%]	26.90	26.11	46.99
		Occam $[-log_{10}]$	2.47	1.82	-8.55
		Certainty $[log_{10}]$	0.08	0.08	-1.57
	r_1	$p(\mathcal{C})$ [%]	49.98	50.02	-
		Occam $[-log_{10}]$	8.68	7.81	-
		Certainty $[log_{10}]$	1.80	1.49	-
	r_3	$p(\mathcal{C})$ [%]	31.98	44.95	23.07
		Occam $[-log_{10}]$	5.11	4.77	16.15
		Certainty $[log_{10}]$	1.61	1.54	2.85

Table 13.3: Plausibility of model classes. Magnitude spectrum.

also provides bad results for the posterior probability, which is consistent with the observations in the previous section. This evidence further supports the validity of the probabilistic formulation. Hence, the obtained equiprobable values demonstrate its insensitiveness with respect to the selected model classes. This burden probably occurs due to the same reasons than those discussed in Section 12.3. The certainty and the Occam's factor are further metrics used to evaluate the models. The former quantifies the goodness of the model fit, whereas the latter penalizes models with an exceeding number of model parameters.

13.1.6 Monitoring of evolution

The evolution of the relevant reconstructed mechanical properties during the reaction process is shown in Figure 13.7 for the most relevant model class and residue definitions. The value of the reconstructed Bulk modulus at the beginning of the process approximately amounts to 2.385 [GPa]. Under the hypothesis that the gel layer is already in the gelation zone [304] at the initial process time (for such a thin specimen, the gel starts to gelify almost instantaneously), we suppose that the loss and storage moduli at the initial and end process times approximate the ones proposed by Wang *et al.* [304], namely $G_0'' = 1200$ [Pa], $G_0' = 80$ [Pa] and $G_{end}'' = 1800$ [Pa], $G_{end}' = 140$ [Pa], respectively. By making use of the following formula [227],

$$c_p = \sqrt{\frac{(K + \frac{4}{3}G)}{\rho}} \tag{13.4}$$

the wave velocity is found to be 1544 [m/s] at the initial time of the process. The latter is close to the value depicted by other authors for similar materials, among them Norisuye *et al.* [303]. Additionally, the last author suggests that the wave velocity suffers a reduction

of around 3% over the reaction process. Thus, thus Bulk modulus at the end of the process is found to be 2.272 [GPa] (diminution of 5%), and is in agreement with the value obtained with the proposed formalism.

Some parameter evolutions reconstructed using residues and models with low plausibility (not shown here due to space constraints) show larger scattering and instabilities, according to the results discussed in the previous subsections. Those observations further supports the validity of this proposal.

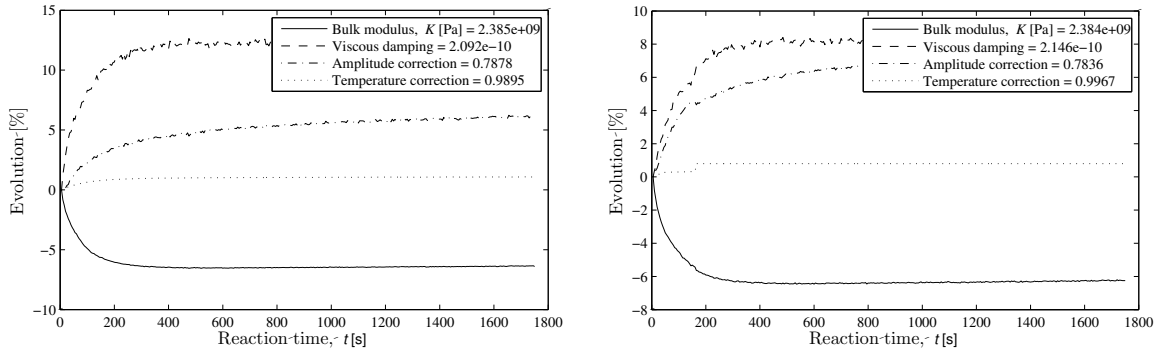

Figure 13.7: *Evolution of the model parameters during reaction for the viscoelastic model. Left figure shows results obtained in the time-domain with the residue definition* $\boldsymbol{r}_0$*, whereas right figure shows results obtained in the frequency-domain with the residue definition* $\boldsymbol{r}_3$*.*

13.2 Conclusions

A numerical method to determine the elastic and dynamic energy dissipation properties during a gelation process has been developed by combining the solution of a probabilistic IP with signal processing techniques, applying genetic algorithms to minimize a cost functional, and using a semi-analytical model of the interactions between ultrasonic waves and tissue. The proposed model-class selection and its subjacent class plausibility have enabled to rank both the models and the suitable residue definitions according to their compatibility with the observations. The resulting trade-off between model simplicity and fitting to observations has demonstrated that the viscous damping model combined with some prior information on the measurements variance over the reaction process evolution, is feasible to characterize the evolution of such a process.

The reconstructed model parameters highlight the following statements. For the viscoelastic models, the Bulk modulus consistently decreases while increasing the damping coefficient. Therefore, both parameters may be associated to the same phenomena, but a careful interpretation has not been carried out at that time. The evolution of the model parameters has a stronger slope during the first 200-300 seconds of the reaction process, and remain almost constant afterwards. This trend validates the observations done *in situ* where the gelation occurred during the first $3-5$ minutes. Consequently, the proposed methodology demonstrates capability to discriminate the process during its early solidification phase.

Part V

CONCLUSIONS AND FUTURE WORKS

14

Conclusions and future works

This chapter presents the most relevant conclusions of the obtained results, along with a discussion regarding the exposed contributions. In addition, some future works currently under development at our laboratory are commented.

Contributions

A first conceptual contribution of this dissertation has been elaborated in **Chapter 5** to provide solutions to several problems that arise in the *model-based estimation procedure* for ultrasonic NDE of layered materials, by making use of digital signal processing and modeling techniques. In particular, we unified the grounds established in the engineering and information theory communities to optimize the performance of such a procedure. It was shown that this approach offers several advantages with respect to classical mode-based inverse problem and system identification approaches: (1) The noise of the captured signals could be reduced, (2) a robust parametrization of the signals, to extract pathology-sensitive model parameters has been introduced, (3) a distance between the observed and modeled features with a mechanical sense has been defined, and (4) an efficient estimation of the damage parameters to identify the pathology has been obtained. The remaining contributions focused on the different models developed over the course of this dissertation, and their use in the model-based estimation procedure.

In **Chapter 7**, we presented a signal-based modeling framework for wave propagation in multilayered materials, which relies on concepts drawn from lattice filter theory. The underlying methodology is based on a physical analysis of the ultrasound-material interactions,

and provides a deeper understanding of the relationship between the material properties and the model parameters. In first place, an analogy between this signal modeling approach and a conventional Transfer Matrix formalism (revisited in Chapter **Chapter 6**) has been established, highlighting the strength and limitations of both methods. Then, a theoretical formalism has been proposed, which efficiently extends the classical recursive framework for Goupillaud-type media to any multilayered (absorbing) structures. The resulting formalism has demonstrated that a through-transmission setup for ultrasonic wave propagation in multilayered structures can be modeled as a classical all-pole filter with sparse coefficients. The strengths of this model are summarized as follows: (1) It is valid for an arbitrary number of absorbing layers of unequal-wave travel time, independent of the digital input signal characteristics (e.g. its central frequency and number of samples), and it is not restricted to any particular boundary conditions, (2) the model parameters are obtained from a rigorous analysis of the physics involved in the wave-material interactions, and thus the sparsity arises naturally and does not rely on heuristic approaches, and (3) this model can be represented as a sparse all-pole digital filter, which has thus obvious practical implications.

Ongoing theoretical work related to this modeling approach includes a further exploitation of concepts drawn from signal theory to study the wave propagation phenomena within multilayered structure under more widen conditions than those used here. Those may involve the study of wave propagation under oblique incidence of the emitted wave (e.g. presence of both longitudinal and transversal waves) and the investigation of more complex layer properties, such as porosity or frequency-dependent attenuation.

In **Chapter 8**, both the digital modeling of the specimen and the TM formalism have been extended to account for the classical nonlinear constitutive behavior of the layers. In first place, a NTM formalism has been successfully developed to account for nonlinear effects up to second harmonics and first-order nonlinearity. In addition, some practical aspects of its implementation have been carefully discussed. Future work may be dedicated to the extension of this nonlinear model up to higher-order harmonics and second-order nonlinearity. Secondly, a nonlinear signal modeling approach has also been developed. Unfortunately, the obtained nonlinear digital signal model, in its proposed form, lacks of practical applicability. Despite this restriction, the obtained theoretical result suggests that the discrete-time transfer function of first-order could be written down as a delayed pole-zero filter with sparse coefficients. Future research in that vein should be conducted, especially on the feasibility of approaching the nonlinear frequency response as a discrete-time transfer function, along with the possibility of representing some missing physical components into the network diagram. Finding a discrete-time transfer function that approximates the nonlinear frequency response for the frequency range of interest in a suitable way is particularly challenging, since the resulting filter might have a large number of coefficients.

Methodology

Chapter 9 was devoted to the obtaining of relevant experimental observations and the development of consistent optimization strategies. In first place, we described a conventional through-transmission technique for measuring the properties of layered materials with known acoustic properties, that served us as a calibration for our experimental devices and provided us fundamental experimental data for validating our models. Secondly, some conventional through-transmission measurements for damage assessment in carbon fiber-reinforced polymers were performed. This configuration has then been modified to investigate the feasibility of measuring the constitutive nonlinearity of such a material using a finite-amplitude through-transmission method. Finally, a novel embedded system for ultrasonic monitoring of tissue-engineered products has been developed. This system has been first ccalibrated on a tissue-equivalent material. A further experiment for monitoring the generation of an artificial tissue culture has then been performed. Unfortunately, the sample under inspection was contaminated after few days of experimentation, and the ultrasonic measurements collected so far were not significative enough to be carefully analyzed. Indeed, for such a tissue culture, it is expected that the cell growth occurs after 4-5 days only.

Future work in that vein may be conducted to support the ongoing theoretical works mentioned above. Thus, other conventional measurements on CFRP under alternative configurations, such as pulse-echo or backscattering approaches, should be performed. The use of nonlinear ultrasound should also be further investigated. On the other hand, the embedded system for ultrasonic monitoring of tissue-engineered products has been meanwhile modified (i.e. the PMMA has been replaced by titanium to improve the biocompatibility) and other design for ultrasonic monitoring of the descellularization process of pig corneal stroma are currently under development. Consequently, future calibration work on real tissue culture is required to provide a rigorous interpretation of the obtained signals.

Results

In **Chapter 10**, we proposed a synthetic comparison between the TM formalism and our digital modeling of the specimen. Then, we presented an experimental validation where the signals predicted by our model were contrasted against signals obtained experimentally from the layered specimens compound of traditional materials. The obtained results proved the potential of our digital model to face up complex wave responses (i.e. numerous and overlapped echoes) originated from multilayered specimens. In addition, it was demonstrated that our model offers numerous advantages with respect to the TM formalism and other proposals based on heuristic signal models (e.g. Bernoulli-Gaussian models). Its strengths are summarized as follows: This model (1) has a very-low complexity, (2) it is valid for any number of layers, and any absorbing layers of unequal wave-travel time, (3) it is suitable for large ”fd-problems”, (4) it does not explicitly depend upon the number of samples of the input signal (and neither on that signal’s appearance), and (5) it enables to represent the material as a sparse digital filter. As a drawback, it should be mentioned

that, formally, the underlying sparse all-pole filter requires integer delays. Nevertheless, increasing the sampling frequency or by applying fractional delay filter formalisms allows to undergo this limitation.

In **Chapter 11**, in an initial approximation, the signal processing and feature extraction procedure applied to the ultrasonic signals provided us some preliminary evidence to select a robust parametrization for such signals in order to identify impact damage in CFRP plates. In particular, the use of a suitable analysis window, the use of an underlying AR model, and the selection of *cepstral* coefficients enabled us to improve the signal analysis and classification. Ongoing works may include advanced extraction/selection techniques such as discriminative transformations of the feature space (by applying LDA or PCA).

In a second part, we showed the capability of our digital modeling of the specimen to identify damage in composite materials, particularly in a CFRP plate subjected to different impact energies. It has been demonstrated that a sparse signal modeling with a reduced number of coefficients provides better results than other common spectrum estimation techniques. In contrast to empirical or heuristic models, the coefficients' position and extent of our model are inherently linked to the material's properties (i.e. stiffness, geometry, etc.), and thus to its health state. Nonetheless, the coefficient positions were fixed according to the digital modeling of an undamaged specimen. To face this unrealistic modeling, a purely heuristic sparse signal model was also considered. From this, it has been confirmed that modeling the complex wave propagation pattern using a sparse transfer function provides better results than other classical spectrum estimation techniques. It has been observed that the non-zero prediction coefficients move dynamically across the filter, depending upon the damage state of the material. Nevertheless, its was shown that the classification results obtained with this heuristic model do not improve the ones obtained with our modeling of the undamaged specimen. By way of conclusion, this characteristic promotes the use of our specimen's digital model, since an heuristic approach suffers from a huge computational costs that makes it almost unviable in IP approaches.

In **Chapter 12**, the presented framework showed that our digital modeling of the specimen can be inserted in a model-based estimation procedure in a straight-forward way, providing encouraging results at the time of reconstructing the damage parameters corresponding to altered mechanical properties of a CFRP plate subjected to impact and fatigue damage. A complete 3D reconstruction of the stiffness values has been obtained and the results were positively contrasted against other techniques, such as radiograph and micrograph. In contrast to other studies, the damage is not identified by considering the time-of-flight or the broadband ultrasound attenuation, but by reconstructing the complete waveform. Moreover, the damage multiplicity does not only appear at several locations (layers) but

simultaneously in different forms (layer degradation and interlaminar debonding). It particular, it has also been demonstrated that the coefficients of the digital model behave dynamically depending upon the damage state of the material under inspection, that is, both the gains and positions of the coefficients change. Additionally, it has been observed that damage also affects the length of the modeling-order of the transfer function's denominator, thus invalidating an approach based on heuristic digital signal models. Future work in that vein should include experimental studies at higher frequencies to take advantage of the complete frequency-range inherently associated to the specimen.

In a second part, a similar framework showed that the NTM formalism can also be inserted in a model-based estimation procedure, providing prospective results when reconstructing the damage parameters corresponding to altered linear and nonlinear mechanical properties of the CFRP plate mentioned above. Future work should be conducted to confirm that the nonlinear properties provide valuable information for early damage detection. For a better understanding of the damage mechanisms, further investigations may be conducted and validated against further NDE techniques. In addition, prospective studies should include the systematic scanning and analysis of CFRP plates submitted to increasing fatigue cycles of loading.

In **Chapter 13**, a numerical method to determine the elastic and dynamic energy dissipation properties during tissue-engineered processes has been developed by combining the solution of a probabilistic inverse problem with signal processing techniques, applying genetic algorithms to minimize a cost function, and using a semi-analytical model of the interaction between ultrasonic waves and tissue. The proposed model-class and residue selection and their underlying class plausibility have enabled a ranking of both the models and suitable residue definitions according to their compatibility with the observations. The resulting trade-off between model simplicity and fitting to observations has demonstrated that the viscous damping models, combined with some prior information on the measurements variance over the reaction process evolution, are feasible to characterize the complex evolution of the process. For a better understanding of ultrasonic tissue monitoring, further *in vitro* studies on real tissue combined with histological studies may be conducted.

15

Conclusiones y trabajos futuros

Este capítulo presenta las conclusiones más relevantes acerca de los resultados obtenidos junto con la discusión sobre las contribuciones expuestas. Asimismo se comentarán algunos trabajos que actualmente están en desarrollo en nuestro laboratorio.

Contribuciones

Una primera contribución conceptual de esta tesis ha sido elaborada en el **Capítulo 5** para ofrecer soluciones a los problemas que se plantean en el *procedimiento de estimación basado en modelo* para la evaluación no destructiva ultrasónica de materiales estratificados, haciendo uso de técnicas de procesamiento y modelado de señales digitales. En concreto, nuestro trabajo unifica los fundamentos implicados en los ámbitos de la ingeniería y de la tecnología de la información, para optimizar el rendimiento de tal procedimiento. Este procedimiento ofrece una serie de ventajas con respecto al problema inverso basado en modelo y a la identificación de sistemas: (1) El ruido de las señales capturadas puede ser reducido, (2) se han introducido una parametrización robusta de las señales, para extraer parámetros del modelo sensibles a las patologías, (3) se ha definido una distancia con un sentido mecánico entre las características observadas y modeladas, y (4) se ha obtenido un modelo eficiente de estimación de parámetros para identificar la patología. Las contribuciones restantes se centran en los diferentes modelos desarrollados a lo largo de esta tesis, y en su uso en el procedimiento de estimación basado en modelos.

En el **Capítulo 7** presentamos un marco de modelado de señales para la propagación de ondas en materiales estratificados, que se basa en conceptos tomados de la teoría de filtros en

celosía. La metodología subyacente se basa en el análisis físico de las interacciones entre los ultrasonidos y el material, y ofrece una comprensión más profunda de las relaciones entre las propiedades del material y los parámetros del modelo. En primer lugar, se ha establecido una analogía entre este planteamiento y el formalismo de la matriz de transferencia (reconsiderado en el **Capítulo 6**), en la que se subrayan los puntos fuertes y las limitaciones de ambos métodos. Seguidamente, se ha propuesto un formalismo teórico que amplía eficazmente el marco recursivo clásico de los media de tipo Goupillaud a cualquier estructura estrátificada. El formalismo resultante ha demostrado que un dispositivo de transmisión de propagación de ondas en estructuras estratificadas se puede modelar como un filtro todopolo clásico con coeficientes *sparse*. Su ventaja se resume a continuación: El modelo (1) es válido para un número arbitrario de capas absorbentes, independiente de las características de la señal de entrada (por ejemplo, su frecuencia central y el número de muestras), y no está restringido a tipo de condiciones de contorno, (2) los parámetros del modelo se obtienen a partir de un riguroso análisis de la física iimplicada en las interacciones onda-material, por lo que la *sparsity* surge naturalmente y no se basa en planteamientos heurísticos, y (3) el modelo puede ser representado como un filtro digital *sparse*, que conlleva obvias implicaciones prácticas.

Futuros trabajos teóricos relacionados con este modelo podrían incluir una mayor explotación de conceptos tomados de la teoría de la señal para estudiar el fenómeno de propagación de ondas en estructuras estratificadas bajo condiciones menos restrictivas que las aquí empleadas. Estas pueden implicar el estudio de la propagación de ondas bajo incidencia oblicua de la onda emitida (suponiendo la presencia de ondas tanto longitudinales como transversales) y la investigación de propiedades más complejas, como la porosidad o la frecuencia dependiente de la atenuación.

En el **Capítulo 8**, tanto el modelado digital del espécimen como el formalismo *TM* han sido ampliados para tener en cuenta el comportamiento constitutivo no-lineal clásico de las capas. En primer lugar, el formalismo *NTM* ha sido desarrollado con éxito para tener en cuenta los efectos no lineales hasta el segundo armónico y la no linealidad de segundo orden. En segundo lugar, se ha desarrollado igualmente un modelado de señal no lineal. Desgraciadamente, este planteamiento, en su forma propuesta, carece de aplicabilidad práctica. A pesar de esta restricción, los resultados teóricos obtenidos sugieren que la función de transferencia en tiempo discreto de primer orden pueda ser descrita como un filtro cero-polo retardado con coeficientes *sparse*.

Futuras investigaciones en esta linea deberían orientarse hacía la viabilidad de expresar la respuesta en frecuencia no lineal como una función de transferencia en tiempo-discreto, así como hacia la posibilidad de representar los componentes físicos ausentes del diagrama de redes. Encontrar una función de transferencia que aproxime la respuesta en frecuencia

no lineal al rango de frecuencia de interés de un modo adecuado es un desafío especialmente interesante, teniendo en cuenta que el filtro resultante puede tener un gran número de coeficientes.

Metodología

El **Capítulo 9** está dedicado a la obtención de observaciones experimentales relevantes, así como al desarrollo de técnicas de optimización consistentes. Por una parte, hemos descrito una técnica convencional de transmisión de ondas ultrasónicas para medir las propiedades de materiales estratificados con propiedades acústicas conocidas. Esta nos proporciona una base para calibrar nuestro dispositivo experimental, así como un conjunto de datos para validar nuestros modelos. Por otra parte, hemos realizados otras medidas a partir de una configuración parecida para identificar defectos en materiales compuestos de fibra de carbono. A continuación, esta configuración ha sido modificada para investigar la posibilidad de medir la no linealidad constitutiva de este material empleando un método de transmisión de amplitud finita. Finalmente, hemos desarrollado un novedoso sistema ultrasónico embebido para la monitorización de muestras de tejidos. Este sistema ha sido primero calibrado en un proceso de solidificación de un gel, y más adelante se usó para caracterizar el desarrollo de un tejido artificial basado en un constructo de fibrina agarosa. Desgraciadamente, esta última muestra se contaminó al cabo de unos pocos días de experimentación, y las señales ultrasónicas capturadas hasta el momento no eran lo suficientemente significativas para ser analizadas más detenidamente. De hecho, para este tipo de tejido, se espera que el crecimiento celular empiece solo a partir del cuarto o quinto día.

En este sentido, serían necesarios otros trabajos experimentales que apoyen las investigaciones teóricas en curso mencionadas previamente. Por tanto, se prevén otras medidas sobre placas de fibra de carbono con una configuración alternativa, como por ejemplo por técnicas de pulso-eco o de retro-dispersión. Se debería considerar igualmente un uso más extenso de técnicas de ultrasonidos no lineales. Por otra parte, el sistema ultrasónico embebido para la monitorización de muestras de tejido ha sido modificado mientras tanto (a saber que el *PMMA* ha sido reemplazado por titanio con el objeto de mejorar la bio-compatibilidad) y otros diseños para la monitorización ultrasónica de córneas, están actualmente en desarrollo. Serían necesarios trabajos de calibración de cultivo celulares reales para proporcionar una interpretación rigurosa de la señales obtenidas.

Resultados

En el **Capítulo 10**, proponemos una comparación sintética entre el formalismo *TM* y nuestro modelado digital del espécimen. Seguidamente, presentamos una validación experimental en la que las señales predichas por nuestro modelo fueron contrastadas con las señales obtenidas experimentalmente sobre el espécmien estratificado compuesto de materiales tradicionales. Los resultados obtenidos muestran el potencial de nuestro modelo digital para hacer frente a respuestas de onda complejas (por ejemplo ecos múltiples y

superpuestos) originadas a partir de especímenes estratificados. Y lo que es más, se ha demostrado que nuestro modelo ofrece muchas ventajas con respecto al formalismo *TM* y otras propuestas basadas en modelos de heurísticos señales (por ej. el modelo *Bernoulli-Gaussian*). Sus puntos fuertes se pueden resumir de la siguiente manera: Este modelo (1) tiene baja complejidad, (2) es válido para cualquier número de capas, y cualquier capa absorbente, (3) es válido para *fd-problems*, (4) no depende explícitamente del número de muestras de la señal de entrada (ni tampoco de la apariencia de dicha señal), y (4) permite representar el material como un filtro digital *sparse*. Como inconveniente, cabe destacar que, formalmente, el el filtro digital subyacente requiere retardos enteros. Sin embargo, ampliando la frecuencia de muestreo o aplicando un *fractional delay filter* permite superar esta limitación.

En el **Capítulo 11**, en una aproximación inicial, el procesado de señal y la extracción de características aplicados a las señales ultrasónicas nos ofrece resultados preliminares para seleccionar una parametrización robusta de tales señales, con el objeto de identificar el daño por impacto en placas de fibra de carbono. En concreto, el uso de una ventana de análisis adecuada, de un modelo autorregresivo subyacente, y la selección de los coeficientes *cepstrales* nos ha permitido mejorar el análisis de señal. Trabajos sucesivos deberían incluir técnicas avanzadas de extracción/selección como transformaciones discriminativas del espacio de características (aplicando *LDA* o *PCA*).

En la segunda parte mostramos la capacidad de nuestro modelado digital del espécimen para identificar daños en materiales compuestos, particularmente en placas de fibra de carbono sometidas a distintas energías de impacto. Se ha demostrado que un modelado de señal *sparse* con un número reducido de coeficientes ofrece mejores resultados que otras técnicas de estimación espectrales. En contraste con los modelos estándares o empíricos, la posición y distribución de los coeficientes de nuestro modelo están vinculadas inherentemente a las propiedades del material (por ejemplo, la rigidez, geometría, etc.), y así a su estado de salud. Sin embargo, las posiciones de los coeficientes se establecen según el modelo digital del especimen no dañado. Para enfrentarse a este modelado poco realista, hemos considerado igualmente un modelado de señal heurístico *sparse*. A partir de este, se ha confirmado que modelar un patrón de propagación complejo usando una función de transferencia *sparse* ofrece mejores resultados que otras técnicas clásicas de estimación de espectros. Además, se ha observado que los coeficientes de predicción se comportan de forma dinámica, dependiendo del estado de daño del material. No obstante, se ha mostrado que la clasificación de resultados obtenidos con este modelo heurístico no mejora a los obtenidos con nuestro modelado del espécimen no dañado. Lo que promueve el uso de nuestro modelo digital del espécimen, sobre todo teniendo en cuenta que el procedimiento heurístico adolece de costos computacionales prohibitivos que lo hacen aún mas inviable.

En el **Capítulo 12**, el planteamiento presentado muestra que nuestro modelado digital del espécimen puede insertarse en un procedimiento de estimación basado en modelo de forma directa, ofreciendo resultados alentadores a la hora de reconstruir los parámetros del daño correspondientes a las propiedades alteradas de una placa de fibra de carbono sometida a impacto y fatiga. Se ha obtenido una reconstrucción completa en 3D de los valores de rigidez, que han sido contrastados positivamente con otras técnicas, como la radiografía y la micrografía. En contraste con otros estudios, el daño no se identifica considerando el tiempo de vuelo o la atenuación ultrasónica de banda ancha, sino reconstruyendo la forma completa de la onda. Y lo que es más, los múltiples mecanismos de daño no sólo aparecen en varios lugares (capas) sino de manera simultánea de diferentes formas (degradación de estratos y delaminación intra-laminar). En concreto, se ha demostrado también que los coeficientes del modelo digital se comparten dinámicamente dependiendo del estado de daño del material examinado, es decir, tanto las ganancias y posiciones de los coeficientes cambian. Además, se ha observado que el daño también afecta a la longitud del orden de modelado. Futuros trabajos en este campo deberían incluir estudios experimentales basados en frecuencias más altas, para aprovechar el rango completo de frecuencias asociado al espécimen.

En una segunda parte, un planteamiento similar muestra que el formalismo *NTM* puede igualmente ser incorporado en un procedimiento de estimación basado en modelo, proporcionando resultados preliminares a la hora de reconstruir los parámetros del daño correspondiente a propiedades mecánicas lineales y no lineales alteradas de la placa de fibra de carbono empleada previamente. Habría que realizar otros trabajos para confirmar que las propiedades no lineales proporcionan una información valiosa a la hora de detectar defectos tempranos. Para mejorar nuestra comprensión de los mecanismos de daño, estas futuras investigaciones deberían ser validadas por otras técnicas de evaluación no destructiva. Por otra parte, otras investigaciones deberían incluir un escaneo y análisis sistemático de placas de fibra de carbono sometidas a crecientes cargas cíclicas de fatiga.

En el **Capitulo 13**, se ha desarrollado un modelo numérico para determinar la elasticidad y las propiedades dinámicas de disipación de la energía durante los procesos evolutivos de cultivos tisulares, combinando la solución de un problema inverso probabilístico con las técnicas de procesado de señal, aplicando algoritmos genéticos para minimizar la función de coste, y usando un modelo semi-analítico de interacción de las ondas ultrasónicas con el tejido. La selección de modelo y de residuo propuesta y la plausibilidad de clase subyacente nos ha permitido clasificar las definiciones de modelos y de residuos respecto a su compatibilidad con las observaciones. En consecuencia, el compromiso entre la simplicidad del modelo y su adaptación a las observaciones ha demostrado que el modelo de atenuación viscosa, combinado con alguna información *a priori* sobre la varianza de las medidas a lo largo del proceso de evolución, son factibles para caracterizar la compleja evolución del proceso.

Para una mejor comprensión de la monitorización ultrasónica del tejido deberán realizarse otros estudios *in vitro* en tiempo real.

Part VI

APPENDICES

A

Derivation of the TM method

This appendix presents a step-by-step derivation of the TM method, by providing the reader the complete equations for establishing the discontinuity and propagation matrices.

A.1 Discontinuity matrix

The continuity of displacement and stress across an arbitrary interface $x = d_i$ ($i = 1, \ldots, M$) is carefully analyzed. The first condition of Equation (6.4) leads to,

$$u_i^f(d_i, \Omega) + u_i^b(d_i, \Omega) \quad = \quad u_{i+1}^f(d_i, \Omega) + u_{i+1}^b(d_i, \Omega) \tag{A.1}$$

whereas the second condition can be written down as,

$$E_i \left[\frac{\partial u_i^f(x, \Omega)}{\partial x} + \frac{\partial u_i^b(x, \Omega)}{\partial x} \right] \Bigg|_{x=d_i} \quad = \quad E_{i+1} \left[\frac{\partial u_{i+1}^f(x, \Omega)}{\partial x} + \frac{\partial u_{i+1}^b(x, \Omega)}{\partial x} \right] \Bigg|_{x=d_i} \tag{A.2}$$

yielding,

$$-jE_i \frac{\Omega}{c_i} \left[u_i^f(d_i, \Omega) - u_i^b(d_i, \Omega) \right] \quad = \quad -jE_{i+1} \frac{\Omega}{c_{i+1}} \left[u_{i+1}^f(d_i, \Omega) - u_{i+1}^b(d_i, \Omega) \right] \tag{A.3}$$

By multiplying Equation (A.3) by the factor $\frac{jc_{i+1}}{\Omega E_{i+1}}$ and adding it to Equation (A.1), an expression for the forward-propagating part of the wave displacement in layer $i+1$ as function

of the forward- and backward-propagating parts of the wave displacement in layer i can be obtained as,

$$u_{i+1}^{f}(d_i,\Omega) = \frac{1}{2}\left(1+\frac{Z_i}{Z_{i+1}}\right)u_i^{f}(d_i,\Omega)+\frac{1}{2}\left(1-\frac{Z_i}{Z_{i+1}}\right)u_i^{b}(d_i,\Omega) \tag{A.4}$$

where $Z_j = \rho_j c_j = E_j/c_j$ denotes the acoustic impedance of a layer j. An expression for the backward-propagating part of the wave displacement in layer $i+1$ can be found accordingly as,

$$u_{i+1}^{b}(d_i,\Omega) = \frac{1}{2}\left(1-\frac{Z_i}{Z_{i+1}}\right)u_i^{f}(d_i,\Omega)+\frac{1}{2}\left(1+\frac{Z_i}{Z_{i+1}}\right)u_i^{b}(d_i,\Omega) \tag{A.5}$$

From Equations (A.4)-(A.5), one can easily recover the discontinuity matrix presented in Equation (6.6).

A.2 Propagation matrix

The derivation of the propagation matrix is trivial. In linear acoustics, it is well-known that the forward- and backward propagating parts do not interact with each others. Thus, considering an harmonic wave propagating in the same homogeneous layer i from position $x = d_{i-1}$ to position $x = d_i$, its transformed displacement at the respective locations can be expressed as,

$$\begin{bmatrix} A_i e^{-j\frac{\Omega}{c_i}d_i} \\ B_i e^{j\frac{\Omega}{c_i}d_i} \end{bmatrix} = \begin{pmatrix} p_i & 0 \\ 0 & p_i^{-1} \end{pmatrix} \begin{bmatrix} A_i e^{-j\frac{\Omega}{c_i}d_{i-1}} \\ B_i e^{j\frac{\Omega}{c_i}d_{i-1}} \end{bmatrix} \tag{A.6}$$

where $p_i = e^{-j\frac{\Omega}{c_i}(d_i-d_{i-1})}$. By inserting the layer's thickness $a_i = d_i - d_{i-1}$, one directly retrieves the propagation matrix presented in Equation (6.8).

B

Outline of the signal modeling approach

This appendix describes in details the demonstrations necessary for establishing the signal modeling approach, and the subsequent digital signal model.

B.1 Distributive property

Equation (7.17) can be proven by deduction. Let us show that Equation (7.17) is correct for $M = 2$, and can thus be extrapolated to an arbitrary number of layers M.

$$\begin{aligned}
&\prod_{i=0}^{M-1} \begin{pmatrix} G_{M-i}^{(A)} e^{-j\omega m_{M-i}} & G_{M-i}^{(B)} e^{j\omega m_{M-i}} \\ G_{M-i}^{(C)} e^{-j\omega m_{M-i}} & G_{M-i}^{(D)} e^{j\omega m_{M-i}} \end{pmatrix} = \begin{pmatrix} G_2^{(A)} e^{-j\omega m_2} & G_2^{(B)} e^{j\omega m_2} \\ G_2^{(C)} e^{-j\omega m_2} & G_2^{(D)} e^{j\omega m_2} \end{pmatrix} \cdot \begin{pmatrix} G_1^{(A)} e^{-j\omega m_1} & G_1^{(B)} e^{j\omega m_1} \\ G_1^{(C)} e^{-j\omega m_1} & G_1^{(D)} e^{j\omega m_1} \end{pmatrix} = \\
&\begin{pmatrix} G_2^{(A)} G_1^{(A)} e^{-j\omega(m_1+m_2)} + G_2^{(B)} G_1^{(C)} e^{-j\omega(m_1-m_2)} & G_2^{(A)} G_1^{(B)} e^{j\omega(m_1-m_2)} + G_2^{(B)} G_1^{(D)} e^{j\omega(m_1+m_2)} \\ G_2^{(C)} G_1^{(A)} e^{-j\omega(m_1+m_2)} + G_2^{(D)} G_1^{(C)} e^{-j\omega(m_1-m_2)} & G_2^{(C)} G_1^{(B)} e^{j\omega(m_1-m_2)} + G_2^{(D)} G_1^{(D)} e^{j\omega(m_1+m_2)} \end{pmatrix} = \\
&\begin{pmatrix} G_2^{(A)} G_1^{(A)} e^{-j\omega(m_1+m_2)} & G_2^{(B)} G_1^{(D)} e^{j\omega(m_1+m_2)} \\ G_2^{(C)} G_1^{(A)} e^{-j\omega(m_1+m_2)} & G_2^{(D)} G_1^{(D)} e^{j\omega(m_1+m_2)} \end{pmatrix} + \begin{pmatrix} G_2^{(B)} G_1^{(C)} e^{-j\omega(m_1-m_2)} & G_2^{(A)} G_1^{(B)} e^{j\omega(m_1-m_2)} \\ G_2^{(D)} G_1^{(C)} e^{-j\omega(m_1-m_2)} & G_2^{(C)} G_1^{(B)} e^{j\omega(m_1-m_2)} \end{pmatrix} = \\
&\begin{pmatrix} \bar{G}_1^{(A)} e^{-j\omega\bar{m}_1} & \bar{G}_1^{(B)} e^{j\omega\bar{m}_1} \\ \bar{G}_1^{(C)} e^{-j\omega\bar{m}_1} & \bar{G}_1^{(D)} e^{j\omega\bar{m}_1} \end{pmatrix} + \begin{pmatrix} \bar{G}_2^{(A)} e^{-j\omega\bar{m}_2} & \bar{G}_2^{(B)} e^{j\omega\bar{m}_2} \\ \bar{G}_2^{(C)} e^{-j\omega\bar{m}_2} & \bar{G}_2^{(D)} e^{j\omega\bar{m}_2} \end{pmatrix} = \sum_{k=1}^{2^{M-1}} \begin{pmatrix} \bar{G}_k^{(A)} e^{-j\omega\bar{m}_k} & \bar{G}_k^{(B)} e^{j\omega\bar{m}_k} \\ \bar{G}_k^{(C)} e^{-j\omega\bar{m}_k} & \bar{G}_k^{(D)} e^{j\omega\bar{m}_k} \end{pmatrix}
\end{aligned} \tag{B.1}$$

where the group delays $\bar{m}_k$, with $k \in \{1, 2\}$, are obtained as a linear combination of the group delays m_{M-i}, namely $\bar{m}_1 = m_1 + m_2$ and $\bar{m}_2 = m_1 - m_2$. On the other hand, the gains labeled with an overscore result from multiplicative combinations of the original gains,

namely:

$$\begin{array}{llll} \bar{G}_1^{(A)} = G_2^{(A)} G_1^{(A)} & , \quad \bar{G}_1^{(B)} = G_2^{(B)} G_1^{(D)} & , \quad \bar{G}_1^{(C)} = G_2^{(C)} G_1^{(A)} & , \quad \bar{G}_1^{(D)} = G_2^{(D)} G_1^{(D)} \\ \bar{G}_2^{(A)} = G_2^{(B)} G_1^{(C)} & , \quad \bar{G}_2^{(B)} = G_2^{(A)} G_1^{(B)} & , \quad \bar{G}_2^{(C)} = G_2^{(D)} G_1^{(C)} & , \quad \bar{G}_2^{(D)} = G_2^{(C)} G_1^{(B)} \end{array} \tag{B.2}$$

B.2 General form

Equation (7.20) can be proven by induction. Thus, assuming that Equation (7.20) is correct for $(M-1)$ layers (the hypothesis is correct and trivial for $M=1$), by multiplying it by another transfer matrix for a layer M, the obtained product may retain the same form with $(M-1)$ increased to M. Hence,

$$\begin{aligned} \boldsymbol{u}_{M+1}(z) &= \frac{G_{\alpha_M} z^{-m_M}}{(1+G_{r_M})} \begin{pmatrix} 1 & G_{r_M} G_{\alpha_M}^{-2} z^{2m_M} \\ G_{r_M} & G_{\alpha_M}^{-2} z^{2m_M} \end{pmatrix} \left(\prod_{i=1}^{M-1} \frac{G_{\alpha_i} z^{-m_i}}{(1+G_{r_i})} \right) \begin{pmatrix} P_{M-1}(G_\alpha, z) & \left(\prod_{i=1}^{M-1} G_{\alpha_i}^{-2} z^{2m_i} \right) Q_{M-1}(G_\alpha^{-1}, z^{-1}) \\ Q_{M-1}(G_\alpha, z) & \left(\prod_{i=1}^{M-1} G_{\alpha_i}^{-2} z^{2m_i} \right) P_{M-1}(G_\alpha^{-1}, z^{-1}) \end{pmatrix} \boldsymbol{u}_1(z) \\ &= \left(\prod_{i=1}^{M} \frac{G_{\alpha_i} z^{-m_i}}{(1+G_{r_i})} \right) \begin{pmatrix} P_{M-1}(G_\alpha, z) + G_{r_M} G_{\alpha_M}^{-2} z^{2m_M} Q_{M-1}(G_\alpha, z) & \left(\prod_{i=1}^{M} G_{\alpha_i}^{-2} z^{2m_i} \right) \left(G_{r_M} P_{M-1}(G_\alpha^{-1}, z^{-1}) + G_{\alpha_M}^2 z^{-2m_M} Q_{M-1}(G_\alpha^{-1}, z^{-1}) \right) \\ G_{r_M} P_{M-1}(G_\alpha, z) + G_{\alpha_M}^{-2} z^{2m_M} Q_{M-1}(G_\alpha, z) & \left(\prod_{i=1}^{M} G_{\alpha_i}^{-2} z^{2m_i} \right) \left(P_{M-1}(G_\alpha^{-1}, z^{-1}) + G_{r_M} G_{\alpha_M}^2 z^{-2m_M} Q_{M-1}(G_\alpha^{-1}, z^{-1}) \right) \end{pmatrix} \boldsymbol{u}_1(z) \\ &= \left(\prod_{i=1}^{M} \frac{G_{\alpha_i} z^{-m_i}}{(1+G_{r_i})} \right) \begin{pmatrix} P_M(G_\alpha, z) & \left(\prod_{i=1}^{M} G_{\alpha_i}^{-2} z^{2m_i} \right) Q_M(G_\alpha^{-1}, z^{-1}) \\ Q_M(G_\alpha, z) & \left(\prod_{i=1}^{M} G_{\alpha_i}^{-2} z^{2m_i} \right) P_M(G_\alpha^{-1}, z^{-1}) \end{pmatrix} \boldsymbol{u}_1(z) \end{aligned} \tag{B.3}$$

where it can be seen that the scaling factor is of the same form with $(M-1)$ changed to M.

B.3 Iterative application

The relationship of Equation (7.23) can be obtained by making use of the recursive scheme described by the polynomial expressions of Equation (7.21),

$$\begin{aligned} & P_M(G_\alpha, z) P_M(G_\alpha^{-1}, z^{-1}) - Q_M(G_\alpha, z) Q_M(G_\alpha^{-1}, z^{-1}) \\ = \; & \left(P_{M-1}(G_\alpha, z) P_{M-1}(G_\alpha^{-1}, z^{-1}) - Q_{M-1}(G_\alpha, z) Q_{M-1}(G_\alpha^{-1}, z^{-1}) \right) (1 - G_{r_M}^2) \\ = \; & \ldots \\ = \; & \left(P_1(G_\alpha, z) P_1(G_\alpha^{-1}, z^{-1}) - Q_1(G_\alpha, z) Q_1(G_\alpha^{-1}, z^{-1}) \right) (1 - G_{r_M}^2) \ldots (1 - G_{r_2}^2) \end{aligned} \tag{B.4}$$

Given the initial conditions of the recursion $P_1(G_\alpha, z) = P_1(G_\alpha^{-1}, z^{-1}) = 1$ and $Q_1(G_\alpha, z) = Q_1(G_\alpha^{-1}, z^{-1}) = G_{r_1}$ yields an iterative application,

$$P_M(G_\alpha, z) P_M(G_\alpha^{-1}, z^{-1}) - Q_M(G_\alpha, z) Q_M(G_\alpha^{-1}, z^{-1}) \;=\; \prod_{i=1}^{M} (1 - G_{r_i}^2) \tag{B.5}$$

which, in analogy to the energy conservation principle, says that for each frequency ω, the energy flowing through the i^{th} layer equals the energy flowing through the $i+1^{th}$ layer.

C

Derivation of the NTM method

This appendix presents a step-by-step derivation of the NTM formalism. First, the obtaining of the elements of the first-order discontinuity and propagation matrices is described (see Equations (8.6) and (8.10)). In a second part, the identities used in Equation (8.17) are proven.

C.1 First-order discontinuity matrix

The continuity of displacement $u^{(1)}(d_i, \Omega)$ and stress $\sigma^{(1)}(d_i, \Omega)$ across an arbitrary interface $x = d_i$ ($i = 1, \ldots, M$) for the first-order perturbation solution is carefully analyzed. For sake of notation simplicity, the argument (d_i, Ω) is omitted along the derivation. The first condition, $u_i^{(1)} = u_{i+1}^{(1)}$ leads to,

$$u_i^{(1),f} + u_i^{(1),b} \quad = \quad u_{i+1}^{(1),f} + u_{i+1}^{(1),b} \tag{C.1}$$

whereas the second condition, $\sigma_i^{(1)} = \sigma_{i+1}^{(1)}$, which can also be written down as,

$$E_i \left[\frac{\partial u_i^{(1)}}{\partial x} + \beta_i \left(\frac{\partial u_i^{(0)}}{\partial x} \right)^2 \right] \Bigg|_{x=d_i} \quad = \quad E_{i+1} \left[\frac{\partial u_{i+1}^{(1)}}{\partial x} + \beta_{i+1} \left(\frac{\partial u_{i+1}^{(0)}}{\partial x} \right)^2 \right] \Bigg|_{x=d_i} \tag{C.2}$$

yields,

$$-2j\frac{\Omega}{c_i}E_i\left(u_i^{(1),f}-u_i^{(1),b}\right)-\frac{1}{2}\beta_i\left(\frac{\Omega}{c_i}\right)^2E_i\left(\left[u_i^{(0),f}\right]^2+\left[u_i^{(0),b}\right]^2-4u_i^{(0),f}u_i^{(0),b}\right)=$$
$$-2j\frac{\Omega}{c_{i+1}}E_{i+1}\left(u_{i+1}^{(1),f}-u_{i+1}^{(1),b}\right)-\frac{1}{2}\beta_{i+1}\left(\frac{\Omega}{c_{i+1}}\right)^2E_{i+1}\left(\left[u_{i+1}^{(0),f}\right]^2+\left[u_{i+1}^{(0),b}\right]^2-4u_{i+1}^{(0),f}u_{i+1}^{(0),b}\right) \tag{C.3}$$

By combining Equation (C.1) with Equation (C.3), an expression for the forward-propagating part of the first-order wave displacement in layer $i+1$ as function of the forward- and backward-propagating parts of the first-order wave displacement in layer i can be found as,

$$\begin{aligned}u_{i+1}^{(1),f} &= \frac{1}{2}\left(1+\frac{Z_i}{Z_{i+1}}\right)u_i^{(1),f}+\frac{1}{2}\left(1-\frac{Z_i}{Z_{i+1}}\right)u_i^{(1),b}\\ &- \frac{j}{4}\beta_i\frac{\Omega}{c_i}\frac{Z_i}{Z_{i+1}}\left(\left[u_i^{(0),f}\right]^2+\left[u_i^{(0),b}\right]^2-4u_i^{(0),f}u_i^{(0),b}\right)\\ &+ \frac{j}{4}\beta_{i+1}\frac{\Omega}{c_{i+1}}\left(\left[u_{i+1}^{(0),f}\right]^2+\left[u_{i+1}^{(0),b}\right]^2-4u_{i+1}^{(0),f}u_{i+1}^{(0),b}\right)\end{aligned} \tag{C.4}$$

Nonetheless, the last term of Equation (C.4) still depends on properties of layer $i+1$. A way to get around it is the use of the linear relations provided by the continuity of displacement and stress for the zero-order solution (see Equations (A.4)-(A.5)). Hence, an expression for the square of the forward-propagating part of the zero-order wave displacement in layer $i+1$ can be found as,

$$\begin{aligned}\left[u_{i+1}^{(0),f}\right]^2 &= \underbrace{\left(\frac{1}{2}\left(1+\frac{Z_i}{Z_{i+1}}\right)\right)^2}_{\mathcal{D}_{i,11}^2}\left[u_i^{(0),f}\right]^2+\underbrace{\left(\frac{1}{2}\left(1-\frac{Z_i}{Z_{i+1}}\right)\right)^2}_{\mathcal{D}_{i,12}^2}\left[u_i^{(0),b}\right]^2\\ &+ \underbrace{\frac{1}{2}\left(1-\left(\frac{Z_i}{Z_{i+1}}\right)^2\right)}_{2\mathcal{D}_{i,11}\mathcal{D}_{i,12}}u_i^{(0),f}u_i^{(0),b}\end{aligned} \tag{C.5}$$

An expression for the square of the backward-propagating part of the zero-order wave displacement in layer $i+1$ can be found accordingly as,

$$\begin{aligned}\left[u_{i+1}^{(0),b}\right]^2 &= \underbrace{\left(\frac{1}{2}\left(1-\frac{Z_i}{Z_{i+1}}\right)\right)^2}_{\mathcal{D}_{i,12}^2}\left[u_i^{(0),f}\right]^2+\underbrace{\left(\frac{1}{2}\left(1+\frac{Z_i}{Z_{i+1}}\right)\right)^2}_{\mathcal{D}_{i,11}^2}\left[u_i^{(0),b}\right]^2\\ &+ \underbrace{\frac{1}{2}\left(1-\left(\frac{Z_i}{Z_{i+1}}\right)^2\right)}_{2\mathcal{D}_{i,11}\mathcal{D}_{i,12}}u_i^{(0),f}u_i^{(0),b}\end{aligned} \tag{C.6}$$

Following the same scheme enables us to find out an expression for the mixed-propagating part of the zero-order wave displacement in layer $i+1$ as,

$$u_{i+1}^{(0),f}u_{i+1}^{(0),b} = \underbrace{\frac{1}{4}\left(1-\left(\frac{Z_i}{Z_{i+1}}\right)^2\right)}_{\mathcal{D}_{i,11}\mathcal{D}_{i,12}}\left(\left[u_i^{(0),f}\right]^2+\left[u_i^{(0),b}\right]^2\right)+\underbrace{\frac{1}{2}\left(1+\left(\frac{Z_i}{Z_{i+1}}\right)^2\right)}_{\mathcal{D}_{i,11}^2+\mathcal{D}_{i,12}^2}u_i^{(0),f}u_i^{(0),b} \tag{C.7}$$

Hence, by inserting Equation (C.5)-(C.7) into Equation (C.4), an expression for the forward-propagating part of the first-order wave displacement in layer $i+1$ can be found as,

$$\begin{aligned} u_{i+1}^{(1),f} &= \underbrace{\frac{1}{2}\left(1+\frac{Z_i}{Z_{i+1}}\right)}_{\mathcal{D}_{i,11}}u_i^{(1),f}+\underbrace{\frac{1}{2}\left(1-\frac{Z_i}{Z_{i+1}}\right)}_{\mathcal{D}_{i,12}}u_i^{(1),b} \\ &- \underbrace{\frac{j}{4}\left(\beta_i\frac{\Omega}{c_i}\frac{Z_i}{Z_{i+1}}+\frac{1}{2}\beta_{i+1}\frac{\Omega}{c_{i+1}}\left(1-3\left(\frac{Z_i}{Z_{i+1}}\right)^2\right)\right)}_{-\mathcal{D}_{i,41}(\Omega)}\left(\left[u_i^{(0),f}\right]^2+\left[u_i^{(0),b}\right]^2\right) \\ &+ \underbrace{j\left(\beta_i\frac{\Omega}{c_i}\frac{Z_i}{Z_{i+1}}-\frac{1}{4}\beta_{i+1}\frac{\Omega}{c_{i+1}}\left(1+3\left(\frac{Z_i}{Z_{i+1}}\right)^2\right)\right)}_{\mathcal{D}_{i,43}(\Omega)}u_i^{(0),f}u_i^{(0),b} \end{aligned} \tag{C.8}$$

An expression for the backward-propagating part of the first-order wave displacement in layer $i+1$ can be found accordingly as,

$$\begin{aligned} u_{i+1}^{(1),b} &= \underbrace{\frac{1}{2}\left(1-\frac{Z_i}{Z_{i+1}}\right)}_{\mathcal{D}_{i,12}}u_i^{(1),f}+\underbrace{\frac{1}{2}\left(1+\frac{Z_i}{Z_{i+1}}\right)}_{\mathcal{D}_{i,11}}u_i^{(1),b} \\ &+ \underbrace{\frac{j}{4}\left(\beta_i\frac{\Omega}{c_i}\frac{Z_i}{Z_{i+1}}+\frac{1}{2}\beta_{i+1}\frac{\Omega}{c_{i+1}}\left(1-3\left(\frac{Z_i}{Z_{i+1}}\right)^2\right)\right)}_{-\mathcal{D}_{i,41}(\Omega)}\left(\left[u_i^{(0),f}\right]^2+\left[u_i^{(0),b}\right]^2\right) \\ &- \underbrace{j\left(\beta_i\frac{\Omega}{c_i}\frac{Z_i}{Z_{i+1}}-\frac{1}{4}\beta_{i+1}\frac{\Omega}{c_{i+1}}\left(1+3\left(\frac{Z_i}{Z_{i+1}}\right)^2\right)\right)}_{\mathcal{D}_{i,43}(\Omega)}u_i^{(0),f}u_i^{(0),b} \end{aligned} \tag{C.9}$$

From those expressions, on can easily retrieve the first-order discontinuity matrix of Equation (8.6), and the linear and nonlinear frequency-dependent elements detailed in Equations (8.7)-(8.8).

C.2 First-order propagation matrix

The derivation of the first-order propagation matrix is not as trivial as for the linear case. Indeed, in nonlinear acoustics, the nonlinear terms (e.g. second harmonics) are generated by frequency-mixing of the fundamental waves, and forward- and backward propagating

parts also can interact with each others. Thus, considering an harmonic wave propagating in the same nonlinear homogeneous layer i from position $x = d_{i-1}$ to position $x = d_i$, its transformed displacement at the respective locations can be expressed as,

$$\begin{bmatrix} \left(A_i e^{-j\frac{\Omega}{c_i}d_i}\right)^2 \\ \left(B_i e^{j\frac{\Omega}{c_i}d_i}\right)^2 \\ A_i B_i \\ \left(\bar{A}_i + \frac{1}{2}\beta_i\left(\frac{\Omega}{c_i}\right)^2 d_i A_i^2\right) e^{-2j\frac{\Omega}{c_i}d_i} \\ \left(\bar{B}_i + \frac{1}{2}\beta_i\left(\frac{\Omega}{c_i}\right)^2 d_i B_i^2\right) e^{2j\frac{\Omega}{c_i}d_i} \end{bmatrix} = \begin{pmatrix} p_i & 0 & 0 & 0 & 0 \\ 0 & p_i^{-1} & 0 & 0 & 0 \\ 0 & 0 & 1 & 0 & 0 \\ \eta_i(\Omega)p_i & 0 & 0 & p_i & 0 \\ 0 & \eta_i(\Omega)p_i^{-1} & 0 & 0 & p_i^{-1} \end{pmatrix} \begin{bmatrix} \left(A_i e^{-j\frac{\Omega}{c_i}d_{i-1}}\right)^2 \\ \left(B_i e^{j\frac{\Omega}{c_i}d_{i-1}}\right)^2 \\ A_i B_i \\ \left(\bar{A}_i + \frac{1}{2}\beta_i\left(\frac{\Omega}{c_i}\right)^2 d_{i-1} A_i^2\right) e^{-2j\frac{\Omega}{c_i}d_{i-1}} \\ \left(\bar{B}_i + \frac{1}{2}\beta_i\left(\frac{\Omega}{c_i}\right)^2 d_{i-1} B_i^2\right) e^{2j\frac{\Omega}{c_i}d_{i-1}} \end{bmatrix} \tag{C.10}$$

where $p_i = e^{-2j\frac{\Omega}{c_i}(d_i - d_{i-1})}$ and $\eta_i(\Omega) = \frac{1}{2}\beta_i\left(\frac{\Omega}{c_i}\right)^2 (d_i - d_{i-1})$. By inserting the layer's thickness $a_i = d_i - d_{i-1}$, one can recover the first-order propagation matrix presented in Equation (8.10). It can be shown that the first-order propagation matrix provided by Yun *et al.* [209], i.e.:

$$\boldsymbol{\mathcal{P}}_i^{Yun}(2\Omega) = \begin{pmatrix} p_i & 0 & 0 & 0 & 0 \\ 0 & p_i^{-1} & 0 & 0 & 0 \\ 0 & 0 & 1 & 0 & 0 \\ p_i & 0 & 0 & \eta_i(\Omega)p_i & 0 \\ 0 & p_i^{-1} & 0 & 0 & \eta_i(\Omega)p_i^{-1} \end{pmatrix}, \tag{C.11}$$

cannot deliver the correct relations between the wave displacements at locations d_i and d_{i-1}.

C.3 First-order transfer matrix

The identities used in Equation (8.17) can be proven by induction. Thus, assuming that Equation (8.17) is correct for $(M-1)$ nonlinear layers, by multiplying it by another first-order transfer matrix for a layer M, the obtained product may retain the same form with $(M-1)$ increased to M. As can be observed in Equation (8.11), this hypothesis is correct and trivial for $M=1$.

$$
\begin{aligned}
\boldsymbol{\mathcal{T}}^{(1)}(\Omega) = \boldsymbol{\mathcal{T}}^{(1)}_{M}(\Omega)\boldsymbol{\mathcal{T}}^{(1)}_{M-1}(\Omega) = &
\begin{pmatrix}
\mathcal{D}^2_{M,11}e^{-2j\frac{\Omega}{c_M}a_M} & \mathcal{D}^2_{M,12}e^{2j\frac{\Omega}{c_M}a_M} & 2\mathcal{D}_{M,11}\mathcal{D}_{M,12} & 0 & 0 \\
\mathcal{D}^2_{M,12}e^{-2j\frac{\Omega}{c_M}a_M} & \mathcal{D}^2_{M,11}e^{2j\frac{\Omega}{c_M}a_M} & 2\mathcal{D}_{M,11}\mathcal{D}_{M,12} & 0 & 0 \\
\mathcal{D}_{M,11}\mathcal{D}_{M,12}e^{-2j\frac{\Omega}{c_M}a_M} & \mathcal{D}_{M,11}\mathcal{D}_{M,12}e^{2j\frac{\Omega}{c_M}a_M} & \mathcal{D}^2_{M,11}+\mathcal{D}^2_{M,12} & 0 & 0 \\
(\mathcal{D}_{M,41}(\Omega)+\eta_M(\Omega)\mathcal{D}_{M,11})\,e^{-2j\frac{\Omega}{c_M}a_M} & (\mathcal{D}_{M,41}(\Omega)+\eta_M(\Omega)\mathcal{D}_{M,12})\,e^{2j\frac{\Omega}{c_M}a_M} & -\mathcal{D}_{M,43}(\Omega) & \mathcal{D}_{M,11}e^{-2j\frac{\Omega}{c_M}a_M} & \mathcal{D}_{M,12}e^{2j\frac{\Omega}{c_M}a_M} \\
(-\mathcal{D}_{M,41}(\Omega)+\eta_M(\Omega)\mathcal{D}_{M,12})\,e^{-2j\frac{\Omega}{c_M}a_M} & (-\mathcal{D}_{M,41}(\Omega)+\eta_M(\Omega)\mathcal{D}_{M,11})\,e^{2j\frac{\Omega}{c_M}a_M} & \mathcal{D}_{M,43}(\Omega) & \mathcal{D}_{M,12}e^{-2j\frac{\Omega}{c_M}a_M} & \mathcal{D}_{M,11}e^{2j\frac{\Omega}{c_M}a_M}
\end{pmatrix}\cdot \\
&
\begin{pmatrix}
\mathcal{T}^{(1)}_{M-1,11}(\Omega) & \mathcal{T}^{(1)}_{M-1,12}(\Omega) & 2\sqrt{\mathcal{T}^{(1)}_{M-1,11}(\Omega)\mathcal{T}^{(1)}_{M-1,12}(\Omega)} & 0 & 0 \\
\mathcal{T}^{(1)}_{M-1,12}(-\Omega) & \mathcal{T}^{(1)}_{M-1,11}(-\Omega) & 2\sqrt{\mathcal{T}^{(1)}_{M-1,11}(-\Omega)\mathcal{T}^{(1)}_{M-1,12}(-\Omega)} & 0 & 0 \\
\sqrt{\mathcal{T}^{(1)}_{M-1,11}(\Omega)\mathcal{T}^{(1)}_{M-1,12}(-\Omega)} & \sqrt{\mathcal{T}^{(1)}_{M,11}(-\Omega)\mathcal{T}^{(1)}_{M-1,12}(\Omega)} & \sqrt{\mathcal{T}^{(1)}_{M-1,11}(\Omega)\mathcal{T}^{(1)}_{M-1,11}(-\Omega)}+\sqrt{\mathcal{T}^{(1)}_{M-1,12}(\Omega)\mathcal{T}^{(1)}_{M-1,12}(-\Omega)} & 0 & 0 \\
\mathcal{T}^{(1)}_{M-1,41}(\Omega) & \mathcal{T}^{(1)}_{M-1,42}(\Omega) & \mathcal{T}^{(1)}_{M-1,43}(\Omega) & \sqrt{\mathcal{T}^{(1)}_{M-1,11}(2\Omega)} & \sqrt{\mathcal{T}^{(1)}_{M-1,12}(2\Omega)} \\
\mathcal{T}^{(1)}_{M-1,42}(-\Omega) & \mathcal{T}^{(1)}_{M-1,41}(-\Omega) & \mathcal{T}^{(1)}_{M-1,43}(-\Omega) & \sqrt{\mathcal{T}^{(1)}_{M-1,12}(-2\Omega)} & \sqrt{\mathcal{T}^{(1)}_{M-1,11}(-2\Omega)}
\end{pmatrix} = \\
&
\begin{pmatrix}
\mathcal{T}^{(1)}_{11}(\Omega) & \mathcal{T}^{(1)}_{12}(\Omega) & 2\sqrt{\mathcal{T}^{(1)}_{11}(\Omega)\mathcal{T}^{(1)}_{12}(\Omega)} & 0 & 0 \\
\mathcal{T}^{(1)}_{12}(-\Omega) & \mathcal{T}^{(1)}_{11}(-\Omega) & 2\sqrt{\mathcal{T}^{(1)}_{11}(-\Omega)\mathcal{T}^{(1)}_{12}(-\Omega)} & 0 & 0 \\
\sqrt{\mathcal{T}^{(1)}_{11}(\Omega)\mathcal{T}^{(1)}_{12}(-\Omega)} & \sqrt{\mathcal{T}^{(1)}_{M,11}(-\Omega)\mathcal{T}^{(1)}_{12}(\Omega)} & \sqrt{\mathcal{T}^{(1)}_{11}(\Omega)\mathcal{T}^{(1)}_{11}(-\Omega)}+\sqrt{\mathcal{T}^{(1)}_{12}(\Omega)\mathcal{T}^{(1)}_{12}(-\Omega)} & 0 & 0 \\
\mathcal{T}^{(1)}_{41}(\Omega) & \mathcal{T}^{(1)}_{42}(\Omega) & \mathcal{T}^{(1)}_{43}(\Omega) & \sqrt{\mathcal{T}^{(1)}_{11}(2\Omega)} & \sqrt{\mathcal{T}^{(1)}_{12}(2\Omega)} \\
\mathcal{T}^{(1)}_{42}(-\Omega) & \mathcal{T}^{(1)}_{41}(-\Omega) & \mathcal{T}^{(1)}_{43}(-\Omega) & \sqrt{\mathcal{T}^{(1)}_{12}(-2\Omega)} & \sqrt{\mathcal{T}^{(1)}_{11}(-2\Omega)}
\end{pmatrix}
\end{aligned}
\tag{C.12}
$$

We will show hereafter that the 19 non-zero elements of the matrix described in Equation (8.16) can be related to the 5 independent elements that arise in the resulting matrix of Equation (C.12). The elements of the first row of that matrix can be written down as,

$$
\begin{aligned}
\mathcal{T}^{(1)}_{11}(\Omega) &= \mathcal{D}^2_{M,11}e^{-2j\frac{\Omega}{c_M}a_M}\mathcal{T}^{(1)}_{M-1,11}(\Omega) + \mathcal{D}^2_{M,12}e^{2j\frac{\Omega}{c_M}a_M}\mathcal{T}^{(1)}_{M-1,12}(-\Omega) \\
&+ 2\mathcal{D}_{M,11}\mathcal{D}_{M,12}\sqrt{\mathcal{T}^{(1)}_{M-1,11}(\Omega)\mathcal{T}^{(1)}_{M-1,12}(-\Omega)} \\
&= \left(\mathcal{D}_{M,11}e^{-j\frac{\Omega}{c_M}a_M}\sqrt{\mathcal{T}^{(1)}_{M-1,11}(\Omega)} + \mathcal{D}_{M,12}e^{j\frac{\Omega}{c_M}a_M}\sqrt{\mathcal{T}^{(1)}_{M-1,12}(-\Omega)}\right)^2,
\end{aligned}
\tag{C.13}
$$

$$
\begin{aligned}
\mathcal{T}^{(1)}_{12}(\Omega) &= \mathcal{D}^2_{M,11}e^{-2j\frac{\Omega}{c_M}a_M}\mathcal{T}^{(1)}_{M-1,12}(\Omega) + \mathcal{D}^2_{M,12}e^{2j\frac{\Omega}{c_M}a_M}\mathcal{T}^{(1)}_{M-1,11}(-\Omega) \\
&+ 2\mathcal{D}_{M,11}\mathcal{D}_{M,12}\sqrt{\mathcal{T}^{(1)}_{M-1,11}(-\Omega)\mathcal{T}^{(1)}_{M-1,12}(\Omega)} \\
&= \left(\mathcal{D}_{M,11}e^{-j\frac{\Omega}{c_M}a_M}\sqrt{\mathcal{T}^{(1)}_{M-1,12}(\Omega)} + \mathcal{D}_{M,12}e^{j\frac{\Omega}{c_M}a_M}\sqrt{\mathcal{T}^{(1)}_{M-1,11}(-\Omega)}\right)^2,
\end{aligned}
\tag{C.14}
$$

and

$$\begin{aligned}
\mathcal{T}_{13}^{(1)}(\Omega) &= 2\mathcal{D}_{M,11}^{2} e^{-2j\frac{\Omega}{c_M}a_(M)} \sqrt{\mathcal{T}_{M-1,11}^{(1)}(\Omega)\mathcal{T}_{M-1,12}^{(1)}(\Omega)} \\
&+ 2\mathcal{D}_{M,12}^{2} e^{2j\frac{\Omega}{c_M}a_(M)} \sqrt{\mathcal{T}_{M-1,11}^{(1)}(-\Omega)\mathcal{T}_{M-1,12}^{(1)}(-\Omega)} \\
&+ 2\mathcal{D}_{M,11}\mathcal{D}_{M,12}\left(\sqrt{\mathcal{T}_{M-1,11}^{(1)}(\Omega)\mathcal{T}_{M-1,11}^{(1)}(-\Omega)} + \sqrt{\mathcal{T}_{M-1,12}^{(1)}(\Omega)\mathcal{T}_{M-1,12}^{(1)}(-\Omega)}\right) \\
&= 2\left(\mathcal{D}_{M,11}e^{-j\frac{\Omega}{c_M}a_M}\sqrt{\mathcal{T}_{M-1,11}^{(1)}(\Omega)} + \mathcal{D}_{M,12}e^{j\frac{\Omega}{c_M}a_M}\sqrt{\mathcal{T}_{M-1,12}^{(1)}(-\Omega)}\right) \\
&\cdot \quad \left(\mathcal{D}_{M,11}e^{-j\frac{\Omega}{c_M}a_M}\sqrt{\mathcal{T}_{M-1,12}^{(1)}(\Omega)} + \mathcal{D}_{M,12}e^{j\frac{\Omega}{c_M}a_M}\sqrt{\mathcal{T}_{M-1,11}^{(1)}(-\Omega)}\right) \\
&= 2\sqrt{\mathcal{T}_{11}^{(1)}(\Omega)\mathcal{T}_{12}^{(1)}(\Omega)}.
\end{aligned} \tag{C.15}$$

As can be observed, the $\mathcal{T}_{13}^{(1)}(\Omega)$-element of the first-order transfer matrix can be expressed by means of the elements $\mathcal{T}_{11}^{(1)}(\Omega)$ and $\mathcal{T}_{12}^{(1)}(\Omega)$. Following this reasoning for the second and third rows enables us to find other elements of that matrix, which also dependent upon those two elements. Hence,

$$\begin{aligned}
\mathcal{T}_{21}^{(1)}(\Omega) &= \mathcal{D}_{M,12}^{2} e^{-2j\frac{\Omega}{c_M}a_M}\mathcal{T}_{M-1,11}^{(1)}(\Omega) + \mathcal{D}_{M,11}^{2} e^{2j\frac{\Omega}{c_M}a_M}\mathcal{T}_{M-1,12}^{(1)}(-\Omega) \\
&+ 2\mathcal{D}_{M,11}\mathcal{D}_{M,12}\sqrt{\mathcal{T}_{M-1,11}^{(1)}(\Omega)\mathcal{T}_{M-1,12}^{(1)}(-\Omega)} \\
&= \left(\mathcal{D}_{M,12}e^{-j\frac{\Omega}{c_M}a_M}\sqrt{\mathcal{T}_{M-1,11}^{(1)}(\Omega)} + \mathcal{D}_{M,11}e^{j\frac{\Omega}{c_M}a_M}\sqrt{\mathcal{T}_{M-1,12}^{(1)}(-\Omega)}\right)^2 \\
&= \mathcal{T}_{12}^{(1)}(-\Omega),
\end{aligned} \tag{C.16}$$

$$\begin{aligned}
\mathcal{T}_{22}^{(1)}(\Omega) &= \mathcal{D}_{M,12}^{2} e^{-2j\frac{\Omega}{c_M}a_M}\mathcal{T}_{M-1,12}^{(1)}(\Omega) + \mathcal{D}_{M,11}^{2} e^{2j\frac{\Omega}{c_M}a_M}\mathcal{T}_{M-1,11}^{(1)}(-\Omega) \\
&+ 2\mathcal{D}_{M,11}\mathcal{D}_{M,12}\sqrt{\mathcal{T}_{M-1,11}^{(1)}(-\Omega)\mathcal{T}_{M-1,12}^{(1)}(\Omega)} \\
&= \left(\mathcal{D}_{M,12}e^{-j\frac{\Omega}{c_M}a_M}\sqrt{\mathcal{T}_{M-1,12}^{(1)}(\Omega)} + \mathcal{D}_{M,11}e^{j\frac{\Omega}{c_M}a_M}\sqrt{\mathcal{T}_{M-1,11}^{(1)}(-\Omega)}\right)^2 \\
&= \mathcal{T}_{11}^{(1)}(-\Omega),
\end{aligned} \tag{C.17}$$

$$
\begin{aligned}
\mathcal{T}_{23}^{(1)}(\Omega) &= 2\mathcal{D}_{M,12}^2 e^{-2j\frac{\Omega}{c_M}a_(M)}\sqrt{\mathcal{T}_{M-1,11}^{(1)}(\Omega)\mathcal{T}_{M-1,12}^{(1)}(\Omega)} \\
&+ 2\mathcal{D}_{M,11}^2 e^{2j\frac{\Omega}{c_M}a_(M)}\sqrt{\mathcal{T}_{M-1,11}^{(1)}(-\Omega)\mathcal{T}_{M-1,12}^{(1)}(-\Omega)} \\
&+ 2\mathcal{D}_{M,11}\mathcal{D}_{M,12}\left(\sqrt{\mathcal{T}_{M-1,11}^{(1)}(\Omega)\mathcal{T}_{M-1,11}^{(1)}(-\Omega)}+\sqrt{\mathcal{T}_{M-1,12}^{(1)}(\Omega)\mathcal{T}_{M-1,12}^{(1)}(-\Omega)}\right) \\
&= 2\left(\mathcal{D}_{M,12}e^{-j\frac{\Omega}{c_M}a_M}\sqrt{\mathcal{T}_{M-1,11}^{(1)}(\Omega)}+\mathcal{D}_{M,11}e^{j\frac{\Omega}{c_M}a_M}\sqrt{\mathcal{T}_{M-1,12}^{(1)}(-\Omega)}\right) \\
&\cdot \quad \left(\mathcal{D}_{M,12}e^{-j\frac{\Omega}{c_M}a_M}\sqrt{\mathcal{T}_{M-1,12}^{(1)}(\Omega)}+\mathcal{D}_{M,11}e^{j\frac{\Omega}{c_M}a_M}\sqrt{\mathcal{T}_{M-1,11}^{(1)}(-\Omega)}\right) \\
&= 2\sqrt{\mathcal{T}_{11}^{(1)}(-\Omega)\mathcal{T}_{12}^{(1)}(-\Omega)},
\end{aligned}
\tag{C.18}
$$

$$
\begin{aligned}
\mathcal{T}_{31}^{(1)}(\Omega) &= \mathcal{D}_{M,11}\mathcal{D}_{M,12}e^{-2j\frac{\Omega}{c_M}a_M}\mathcal{T}_{M-1,11}^{(1)}(\Omega)+\mathcal{D}_{M,11}\mathcal{D}_{M,12}e^{2j\frac{\Omega}{c_M}a_M}\mathcal{T}_{M-1,12}^{(1)}(-\Omega) \\
&+ \left(\mathcal{D}_{M,11}^2+\mathcal{D}_{M,12}^2\right)\sqrt{\mathcal{T}_{M-1,11}^{(1)}(\Omega)\mathcal{T}_{M-1,12}^{(1)}(-\Omega)} \\
&= \left(\mathcal{D}_{M,11}e^{-j\frac{\Omega}{c_M}a_M}\sqrt{\mathcal{T}_{M-1,11}^{(1)}(\Omega)}+\mathcal{D}_{M,12}e^{j\frac{\Omega}{c_M}a_M}\sqrt{\mathcal{T}_{M-1,12}^{(1)}(-\Omega)}\right) \\
&\cdot \quad \left(\mathcal{D}_{M,12}e^{-j\frac{\Omega}{c_M}a_M}\sqrt{\mathcal{T}_{M-1,11}^{(1)}(\Omega)}+\mathcal{D}_{M,11}e^{j\frac{\Omega}{c_M}a_M}\sqrt{\mathcal{T}_{M-1,12}^{(1)}(-\Omega)}\right) \\
&= \sqrt{\mathcal{T}_{11}^{(1)}(\Omega)\mathcal{T}_{12}^{(1)}(-\Omega)},
\end{aligned}
\tag{C.19}
$$

$$
\begin{aligned}
\mathcal{T}_{32}^{(1)}(\Omega) &= \mathcal{D}_{M,11}\mathcal{D}_{M,12}e^{-2j\frac{\Omega}{c_M}a_M}\mathcal{T}_{M-1,12}^{(1)}(\Omega)+\mathcal{D}_{M,11}\mathcal{D}_{M,12}e^{2j\frac{\Omega}{c_M}a_M}\mathcal{T}_{M-1,11}^{(1)}(-\Omega) \\
&+ \left(\mathcal{D}_{M,11}^2+\mathcal{D}_{M,12}^2\right)\sqrt{\mathcal{T}_{M-1,11}^{(1)}(-\Omega)\mathcal{T}_{M-1,12}^{(1)}(\Omega)} \\
&= \left(\mathcal{D}_{M,12}e^{-j\frac{\Omega}{c_M}a_M}\sqrt{\mathcal{T}_{M-1,12}^{(1)}(\Omega)}+\mathcal{D}_{M,11}e^{j\frac{\Omega}{c_M}a_M}\sqrt{\mathcal{T}_{M-1,11}^{(1)}(-\Omega)}\right) \\
&\cdot \quad \left(\mathcal{D}_{M,11}e^{-j\frac{\Omega}{c_M}a_M}\sqrt{\mathcal{T}_{M-1,12}^{(1)}(\Omega)}+\mathcal{D}_{M,12}e^{j\frac{\Omega}{c_M}a_M}\sqrt{\mathcal{T}_{M-1,11}^{(1)}(-\Omega)}\right) \\
&= \sqrt{\mathcal{T}_{11}^{(1)}(-\Omega)\mathcal{T}_{12}^{(1)}(\Omega)},
\end{aligned}
\tag{C.20}
$$

and

$$\begin{aligned}
\mathcal{T}_{33}^{(1)}(\Omega) &= 2\mathcal{D}_{M,11}\mathcal{D}_{M,12}e^{-2j\frac{\Omega}{c_M}a_M}\sqrt{\mathcal{T}_{M-1,11}^{(1)}(\Omega)\mathcal{T}_{M-1,12}^{(1)}(\Omega)} \\
&+ 2\mathcal{D}_{M,11}\mathcal{D}_{M,12}e^{2j\frac{\Omega}{c_M}a_M}\sqrt{\mathcal{T}_{M-1,11}^{(1)}(-\Omega)\mathcal{T}_{M-1,12}^{(1)}(-\Omega)} \\
&+ \left(\mathcal{D}_{M,11}^2+\mathcal{D}_{M,12}^2\right)\left(\sqrt{\mathcal{T}_{M-1,11}^{(1)}(\Omega)\mathcal{T}_{M-1,11}^{(1)}(-\Omega)}+\sqrt{\mathcal{T}_{M-1,12}^{(1)}(\Omega)\mathcal{T}_{M-1,12}^{(1)}(-\Omega)}\right) \\
&= \left(\mathcal{D}_{M,11}e^{-j\frac{\Omega}{c_M}a_M}\sqrt{\mathcal{T}_{M-1,11}^{(1)}(\Omega)}+\mathcal{D}_{M,12}e^{j\frac{\Omega}{c_M}a_M}\sqrt{\mathcal{T}_{M-1,12}^{(1)}(-\Omega)}\right) \\
&\cdot \left(\mathcal{D}_{M,12}e^{-j\frac{\Omega}{c_M}a_M}\sqrt{\mathcal{T}_{M-1,12}^{(1)}(\Omega)}+\mathcal{D}_{M,11}e^{j\frac{\Omega}{c_M}a_M}\sqrt{\mathcal{T}_{M-1,11}^{(1)}(-\Omega)}\right) \\
&+ \left(\mathcal{D}_{M,11}e^{-j\frac{\Omega}{c_M}a_M}\sqrt{\mathcal{T}_{M-1,12}^{(1)}(\Omega)}+\mathcal{D}_{M,12}e^{j\frac{\Omega}{c_M}a_M}\sqrt{\mathcal{T}_{M-1,11}^{(1)}(-\Omega)}\right) \\
&\cdot \left(\mathcal{D}_{M,12}e^{-j\frac{\Omega}{c_M}a_M}\sqrt{\mathcal{T}_{M-1,11}^{(1)}(\Omega)}+\mathcal{D}_{M,11}e^{j\frac{\Omega}{c_M}a_M}\sqrt{\mathcal{T}_{M-1,12}^{(1)}(-\Omega)}\right) \\
&= \sqrt{\mathcal{T}_{11}^{(1)}(\Omega)\mathcal{T}_{11}^{(1)}(-\Omega)}+\sqrt{\mathcal{T}_{12}^{(1)}(\Omega)\mathcal{T}_{12}^{(1)}(-\Omega)}.
\end{aligned} \tag{C.21}$$

This reasoning can be further applied to the lower-right elements of the fourth and fifth rows, leading to:

$$\begin{aligned}
\mathcal{T}_{44}^{(1)}(\Omega) &= \mathcal{D}_{M,11}e^{-2j\frac{\Omega}{c_M}a_M}\sqrt{\mathcal{T}_{M-1,11}^{(1)}(2\Omega)}+\mathcal{D}_{M,12}e^{2j\frac{\Omega}{c_M}a_M}\sqrt{\mathcal{T}_{M-1,12}^{(1)}(-2\Omega)} \\
&= \sqrt{\mathcal{T}_{11}^{(1)}(2\Omega)},
\end{aligned} \tag{C.22}$$

$$\begin{aligned}
\mathcal{T}_{45}^{(1)}(\Omega) &= \mathcal{D}_{M,11}e^{-2j\frac{\Omega}{c_M}a_M}\sqrt{\mathcal{T}_{M-1,12}^{(1)}(2\Omega)}+\mathcal{D}_{M,12}e^{2j\frac{\Omega}{c_M}a_M}\sqrt{\mathcal{T}_{M-1,11}^{(1)}(-2\Omega)} \\
&= \sqrt{\mathcal{T}_{12}^{(1)}(2\Omega)},
\end{aligned} \tag{C.23}$$

$$\begin{aligned}
\mathcal{T}_{54}^{(1)}(\Omega) &= \mathcal{D}_{M,12}e^{-2j\frac{\Omega}{c_M}a_M}\sqrt{\mathcal{T}_{M-1,11}^{(1)}(2\Omega)}+\mathcal{D}_{M,11}e^{2j\frac{\Omega}{c_M}a_M}\sqrt{\mathcal{T}_{M-1,12}^{(1)}(-2\Omega)} \\
&= \sqrt{\mathcal{T}_{12}^{(1)}(-2\Omega)},
\end{aligned} \tag{C.24}$$

and

$$\begin{aligned}
\mathcal{T}_{55}^{(1)}(\Omega) &= \mathcal{D}_{M,12}e^{-2j\frac{\Omega}{c_M}a_M}\sqrt{\mathcal{T}_{M-1,12}^{(1)}(2\Omega)}+\mathcal{D}_{M,11}e^{2j\frac{\Omega}{c_M}a_M}\sqrt{\mathcal{T}_{M-1,11}^{(1)}(-2\Omega)} \\
&= \sqrt{\mathcal{T}_{11}^{(1)}(-2\Omega)},
\end{aligned} \tag{C.25}$$

Finally, the remaining six elements of the fourth and fifth rows which explicitly contain the nonlinear terms can obviously not be directly related to those two elements, and they thus keep their original denomination. Nevertheless, some relations can be established between

them. To this end, let us consider the three first elements of the fourth row. Hence,

$$\begin{aligned}\mathcal{T}_{41}^{(1)}(\Omega) &= (\mathcal{D}_{M,41}(\Omega)+\eta_M(\Omega)\mathcal{D}_{M,11})\,e^{-2j\frac{\Omega}{c_M}a_M}\mathcal{T}_{M-1,11}^{(1)}(\Omega)\\ &+ (\mathcal{D}_{M,41}(\Omega)+\eta_M(\Omega)\mathcal{D}_{M,12})\,e^{2j\frac{\Omega}{c_M}a_M}\mathcal{T}_{M-1,12}^{(1)}(-\Omega)\\ &+ \mathcal{D}_{M,11}e^{-2j\frac{\Omega}{c_M}a_M}\mathcal{T}_{M-1,41}^{(1)}(\Omega)+\mathcal{D}_{M,12}e^{2j\frac{\Omega}{c_M}a_M}\mathcal{T}_{M-1,42}^{(1)}(-\Omega)\\ &- \mathcal{D}_{M,43}(\Omega)\sqrt{\mathcal{T}_{M-1,11}^{(1)}(\Omega)\mathcal{T}_{M-1,12}^{(1)}(-\Omega)},\end{aligned} \tag{C.26}$$

$$\begin{aligned}\mathcal{T}_{42}^{(1)}(\Omega) &= (\mathcal{D}_{M,41}(\Omega)+\eta_M(\Omega)\mathcal{D}_{M,11})\,e^{-2j\frac{\Omega}{c_M}a_M}\mathcal{T}_{M-1,12}^{(1)}(\Omega)\\ &+ (\mathcal{D}_{M,41}(\Omega)+\eta_M(\Omega)\mathcal{D}_{M,12})\,e^{2j\frac{\Omega}{c_M}a_M}\mathcal{T}_{M-1,11}^{(1)}(-\Omega)\\ &+ \mathcal{D}_{M,11}e^{-2j\frac{\Omega}{c_M}a_M}\mathcal{T}_{M-1,42}^{(1)}(\Omega)+\mathcal{D}_{M,12}e^{2j\frac{\Omega}{c_M}a_M}\mathcal{T}_{M-1,41}^{(1)}(-\Omega)\\ &- \mathcal{D}_{M,43}(\Omega)\sqrt{\mathcal{T}_{M-1,11}^{(1)}(-\Omega)\mathcal{T}_{M-1,12}^{(1)}(\Omega)},\end{aligned} \tag{C.27}$$

and

$$\begin{aligned}\mathcal{T}_{43}^{(1)}(\Omega) &= 2\,(\mathcal{D}_{M,41}(\Omega)+\eta_M(\Omega)\mathcal{D}_{M,11})\,e^{-2j\frac{\Omega}{c_M}a_M}\sqrt{\mathcal{T}_{M-1,11}^{(1)}(\Omega)\mathcal{T}_{M-1,12}^{(1)}(\Omega)}\\ &+ 2\,(\mathcal{D}_{M,41}(\Omega)+\eta_M(\Omega)\mathcal{D}_{M,12})\,e^{2j\frac{\Omega}{c_M}a_M}\sqrt{\mathcal{T}_{M-1,11}^{(1)}(-\Omega)\mathcal{T}_{M-1,12}^{(1)}(-\Omega)}\\ &+ \mathcal{D}_{M,11}e^{-2j\frac{\Omega}{c_M}a_M}\mathcal{T}_{M-1,43}^{(1)}(\Omega)+\mathcal{D}_{M,12}e^{2j\frac{\Omega}{c_M}a_M}\mathcal{T}_{M-1,43}^{(1)}(-\Omega)\\ &- \mathcal{D}_{M,43}(\Omega)\left(\sqrt{\mathcal{T}_{M-1,11}^{(1)}(\Omega)\mathcal{T}_{M-1,11}^{(1)}(-\Omega)}+\sqrt{\mathcal{T}_{M-1,12}^{(1)}(\Omega)\mathcal{T}_{M-1,12}^{(1)}(-\Omega)}\right).\end{aligned} \tag{C.28}$$

By making use of the identities $-\mathcal{D}_{i,41}(\Omega) = \mathcal{D}_{i,41}(-\Omega)$, $-\mathcal{D}_{i,43}(\Omega) = \mathcal{D}_{i,43}(-\Omega)$, and $\eta_i(\Omega) = \eta_i(-\Omega)$, $\forall i$, the three first elements of the fifth row can be written down as follows,

$$\begin{aligned}\mathcal{T}_{51}^{(1)}(\Omega) &= (-\mathcal{D}_{M,41}(\Omega)+\eta_M(\Omega)\mathcal{D}_{M,12})\,e^{-2j\frac{\Omega}{c_M}a_M}\mathcal{T}_{M-1,11}^{(1)}(\Omega)\\ &+ (-\mathcal{D}_{M,41}(\Omega)+\eta_M(\Omega)\mathcal{D}_{M,11})\,e^{2j\frac{\Omega}{c_M}a_M}\mathcal{T}_{M-1,12}^{(1)}(-\Omega)\\ &+ \mathcal{D}_{M,12}e^{-2j\frac{\Omega}{c_M}a_M}\mathcal{T}_{M-1,41}^{(1)}(\Omega)+\mathcal{D}_{M,11}e^{2j\frac{\Omega}{c_M}a_M}\mathcal{T}_{M-1,42}^{(1)}(-\Omega)\\ &+ \mathcal{D}_{M,43}(\Omega)\sqrt{\mathcal{T}_{M-1,11}^{(1)}(\Omega)\mathcal{T}_{M-1,12}^{(1)}(-\Omega)}\\ &= \mathcal{T}_{42}^{(1)}(-\Omega),\end{aligned} \tag{C.29}$$

$$\begin{aligned}\mathcal{T}_{52}^{(1)}(\Omega) &= (-\mathcal{D}_{M,41}(\Omega)+\eta_M(\Omega)\mathcal{D}_{M,12})\,e^{-2j\frac{\Omega}{c_M}a_M}\mathcal{T}_{M-1,12}^{(1)}(\Omega)\\ &+ (-\mathcal{D}_{M,41}(\Omega)+\eta_M(\Omega)\mathcal{D}_{M,11})\,e^{2j\frac{\Omega}{c_M}a_M}\mathcal{T}_{M-1,11}^{(1)}(-\Omega)\\ &+ \mathcal{D}_{M,12}e^{-2j\frac{\Omega}{c_M}a_M}\mathcal{T}_{M-1,42}^{(1)}(\Omega)+\mathcal{D}_{M,11}e^{2j\frac{\Omega}{c_M}a_M}\mathcal{T}_{M-1,41}^{(1)}(-\Omega)\\ &+ \mathcal{D}_{M,43}(\Omega)\sqrt{\mathcal{T}_{M-1,11}^{(1)}(-\Omega)\mathcal{T}_{M-1,12}^{(1)}(\Omega)}\\ &= \mathcal{T}_{41}^{(1)}(-\Omega),\end{aligned} \tag{C.30}$$

and

$$\begin{aligned}
\mathcal{T}_{53}^{(1)}(\Omega) &= 2\left(-\mathcal{D}_{M,41}(\Omega)+\eta_M(\Omega)\mathcal{D}_{M,12}\right)e^{-2j\frac{\Omega}{c_M}a_M}\sqrt{\mathcal{T}_{M-1,11}^{(1)}(\Omega)\mathcal{T}_{M-1,12}^{(1)}(\Omega)} \\
&+ 2\left(-\mathcal{D}_{M,41}(\Omega)+\eta_M(\Omega)\mathcal{D}_{M,11}\right)e^{2j\frac{\Omega}{c_M}a_M}\sqrt{\mathcal{T}_{M-1,11}^{(1)}(-\Omega)\mathcal{T}_{M-1,12}^{(1)}(-\Omega)} \\
&+ \mathcal{D}_{M,12}e^{-2j\frac{\Omega}{c_M}a_M}\mathcal{T}_{M-1,43}^{(1)}(\Omega)+\mathcal{D}_{M,11}e^{2j\frac{\Omega}{c_M}a_M}\mathcal{T}_{M-1,43}^{(1)}(-\Omega) \\
&+ \mathcal{D}_{M,43}(\Omega)\left(\sqrt{\mathcal{T}_{M-1,11}^{(1)}(\Omega)\mathcal{T}_{M-1,11}^{(1)}(-\Omega)}+\sqrt{\mathcal{T}_{M-1,12}^{(1)}(\Omega)\mathcal{T}_{M-1,12}^{(1)}(-\Omega)}\right). \\
&= \mathcal{T}_{43}^{(1)}(-\Omega).
\end{aligned} \tag{C.31}$$

From those expressions, we recover all the identities used in Equation (8.17), and show that the 19 non-zero elements of the first-order transfer matrix $\boldsymbol{\mathcal{T}}^{(1)}(\Omega)$ can be expressed using only five elements, namely $\mathcal{T}_{11}^{(1)}(\Omega)$, $\mathcal{T}_{12}^{(1)}(\Omega)$, $\mathcal{T}_{41}^{(1)}(\Omega)$, $\mathcal{T}_{42}^{(1)}(\Omega)$, and $\mathcal{T}_{43}^{(1)}(\Omega)$.

C.4 Relation between the zero and first-order transfer matrices

Let us here show that the system that span the upper left 3×3 sub-matrix of $\mathcal{T}^{(1)}(\Omega)$ in Equation (8.17) corresponds to a quadratic form of the linear transfer matrix. To this end, let us first assume that the linear transfer matrix is correct for $(M-1)$ layers, and thus by multiplying it by another transfer matrix for a layer M, the obtained product may retain the same form with $(M-1)$ increased to M. Then, we will compare the obtained elements to those derived in Appendix C.3.

$$\begin{aligned}
\boldsymbol{\mathcal{T}}^{(0)}(\Omega)=\boldsymbol{\mathcal{T}}_{M}^{(0)}(\Omega)\boldsymbol{\mathcal{T}}_{M-1}^{(0)}(\Omega) &= \begin{pmatrix} \mathcal{D}_{M,11}e^{-j\frac{\Omega}{c_i}a_i} & \mathcal{D}_{M,12}e^{j\frac{\Omega}{c_i}a_i} \\ \mathcal{D}_{M,12}e^{-j\frac{\Omega}{c_i}a_i} & \mathcal{D}_{M,11}e^{j\frac{\Omega}{c_i}a_i} \end{pmatrix}\cdot\begin{pmatrix} \mathcal{T}_{M-1,11}^{(0)}(\Omega) & \mathcal{T}_{M-1,12}^{(0)}(\Omega) \\ \mathcal{T}_{M-1,12}^{(0)}(-\Omega) & \mathcal{T}_{M-1,11}^{(0)}(-\Omega) \end{pmatrix} \\
&= \begin{pmatrix} \mathcal{T}_{11}^{(0)}(\Omega) & \mathcal{T}_{12}^{(0)}(\Omega) \\ \mathcal{T}_{12}^{(0)}(-\Omega) & \mathcal{T}_{11}^{(0)}(-\Omega) \end{pmatrix}
\end{aligned} \tag{C.32}$$

The resulting elements can be written down as,

$$\begin{aligned}
\mathcal{T}_{11}^{(0)}(\Omega) &= \mathcal{D}_{M,11}e^{-j\frac{\Omega}{c_M}a_M}\mathcal{T}_{M-1,11}^{(0)}(\Omega)+\mathcal{D}_{M,12}e^{j\frac{\Omega}{c_M}a_M}\mathcal{T}_{M-1,12}^{(0)}(-\Omega) \\
&= \mathcal{D}_{M,11}e^{-j\frac{\Omega}{c_M}a_M}\sqrt{\mathcal{T}_{M-1,11}^{(1)}(\Omega)}+\mathcal{D}_{M,12}e^{j\frac{\Omega}{c_M}a_M}\sqrt{\mathcal{T}_{M-1,12}^{(1)}(-\Omega)} \\
&= \sqrt{\mathcal{T}_{11}^{(1)}(\Omega)},
\end{aligned} \tag{C.33}$$

$$\begin{aligned}
\mathcal{T}_{12}^{(0)}(\Omega) &= \mathcal{D}_{M,11}e^{-j\frac{\Omega}{c_M}a_M}\mathcal{T}_{M-1,12}^{(0)}(\Omega)+\mathcal{D}_{M,12}e^{j\frac{\Omega}{c_M}a_M}\mathcal{T}_{M-1,11}^{(0)}(-\Omega) \\
&= \mathcal{D}_{M,11}e^{-j\frac{\Omega}{c_M}a_M}\sqrt{\mathcal{T}_{M-1,12}^{(1)}(\Omega)}+\mathcal{D}_{M,12}e^{j\frac{\Omega}{c_M}a_M}\sqrt{\mathcal{T}_{M-1,11}^{(1)}(-\Omega)} \\
&= \sqrt{\mathcal{T}_{12}^{(1)}(\Omega)},
\end{aligned} \tag{C.34}$$

$$\begin{aligned}
\mathcal{T}_{21}^{(0)}(\Omega) &= \mathcal{D}_{M,12}e^{-j\frac{\Omega}{c_M}a_M}\mathcal{T}_{M-1,11}^{(0)}(\Omega) + \mathcal{D}_{M,11}e^{j\frac{\Omega}{c_M}a_M}\mathcal{T}_{M-1,12}^{(0)}(-\Omega) \\
&= \mathcal{D}_{M,12}e^{-j\frac{\Omega}{c_M}a_M}\sqrt{\mathcal{T}_{M-1,11}^{(1)}(\Omega)} + \mathcal{D}_{M,11}e^{j\frac{\Omega}{c_M}a_M}\sqrt{\mathcal{T}_{M-1,12}^{(1)}(-\Omega)} \\
&= \mathcal{T}_{12}^{(0)}(-\Omega) \\
&= \sqrt{\mathcal{T}_{12}^{(1)}(-\Omega)},
\end{aligned} \tag{C.35}$$

and

$$\begin{aligned}
\mathcal{T}_{22}^{(0)}(\Omega) &= \mathcal{D}_{M,12}e^{-j\frac{\Omega}{c_M}a_M}\mathcal{T}_{M-1,12}^{(0)}(\Omega) + \mathcal{D}_{M,11}e^{j\frac{\Omega}{c_M}a_M}\mathcal{T}_{M-1,11}^{(0)}(-\Omega) \\
&= \mathcal{D}_{M,12}e^{-j\frac{\Omega}{c_M}a_M}\sqrt{\mathcal{T}_{M-1,12}^{(1)}(\Omega)} + \mathcal{D}_{M,11}e^{j\frac{\Omega}{c_M}a_M}\sqrt{\mathcal{T}_{M-1,11}^{(1)}(-\Omega)} \\
&= \mathcal{T}_{11}^{(0)}(-\Omega) \\
&= \sqrt{\mathcal{T}_{11}^{(1)}(-\Omega)}.
\end{aligned} \tag{C.36}$$

As can be observed, comparing these elements to those derived in Equations (D.2)-(D.6) enable us to show that Equation (8.21) is a quadratic form of the expression delivered by Equation (6.14).

D

Outline of the nonlinear signal modeling

The identities used in Equation (8.37) can be proven by induction. Thus, assuming that Equation (8.37) is correct for $(M-1)$ layers, by multiplying it by another frequency response of first-order for a layer M, the obtained product may retain the same form with $(M-1)$ increased to M. As can be observed in Equation (8.31), this hypothesis is correct and trivial for $M=1$ since $H_i^{NL}(\omega) = H_i^{NL}(-\omega)$.

$$\boldsymbol{T}^{(1)}(\omega) = \boldsymbol{T}_M^{(1)}(\omega)\boldsymbol{T}_{M-1}^{(1)}(\omega) = \begin{pmatrix} D_{M,11}^2 e^{-2j\omega m_M} & D_{M,12}^2 e^{2j\omega m_M} & 2D_{M,11}D_{M,12} & 0 & 0 \\ D_{M,12}^2 e^{-2j\omega m_M} & D_{M,11}^2 e^{2j\omega m_M} & 2D_{M,11}D_{M,12} & 0 & 0 \\ D_{M,11}D_{M,12}e^{-2j\omega m_M} & D_{M,11}D_{M,12}e^{2j\omega m_M} & D_{M,11}^2 + D_{M,12}^2 & 0 & 0 \\ D_{M,11}H_M^{NL}(\omega)e^{-2j\omega m_M} & D_{M,12}H_M^{NL}(\omega)e^{2j\omega m_M} & 0 & D_{M,11}e^{-2j\omega m_M} & D_{M,12}e^{2j\omega m_M} \\ D_{M,12}H_M^{NL}(\omega)e^{-2j\omega m_M} & D_{M,11}H_M^{NL}(\omega)e^{2j\omega m_M} & 0 & D_{M,12}e^{-2j\omega m_M} & D_{M,11}e^{2j\omega m_M} \end{pmatrix}.$$

$$\begin{pmatrix} T_{M-1,11}^{(1)}(\omega) & T_{M-1,12}^{(1)}(\omega) & 2\sqrt{T_{M-1,11}^{(1)}(\omega)T_{M-1,12}^{(1)}(\omega)} & 0 & 0 \\ T_{M-1,12}^{(1)}(-\omega) & T_{M-1,11}^{(1)}(-\omega) & 2\sqrt{T_{M-1,11}^{(1)}(-\omega)T_{M-1,12}^{(1)}(-\omega)} & 0 & 0 \\ \sqrt{T_{M-1,11}^{(1)}(\omega)T_{M-1,12}^{(1)}(-\omega)} & \sqrt{T_{M,11}^{(1)}(-\omega)T_{M-1,12}^{(1)}(\omega)} & \sqrt{T_{M-1,11}^{(1)}(\omega)T_{M-1,11}^{(1)}(-\omega)} + \sqrt{T_{M-1,12}^{(1)}(\omega)T_{M-1,12}^{(1)}(-\omega)} & 0 & 0 \\ T_{M-1,41}^{(1)}(\omega) & T_{M-1,42}^{(1)}(\omega) & T_{M-1,43}^{(1)}(\omega) & \sqrt{T_{M-1,11}^{(1)}(2\omega)} & \sqrt{T_{M-1,12}^{(1)}(2\omega)} \\ T_{M-1,42}^{(1)}(-\omega) & T_{M-1,41}^{(1)}(-\omega) & T_{M-1,43}^{(1)}(-\omega) & \sqrt{T_{M-1,12}^{(1)}(-2\omega)} & \sqrt{T_{M-1,11}^{(1)}(-2\omega)} \end{pmatrix} =$$

$$\begin{pmatrix} T_{11}^{(1)}(\omega) & T_{12}^{(1)}(\omega) & 2\sqrt{T_{11}^{(1)}(\omega)T_{12}^{(1)}(\omega)} & 0 & 0 \\ T_{12}^{(1)}(-\omega) & T_{11}^{(1)}(-\omega) & 2\sqrt{T_{11}^{(1)}(-\omega)T_{12}^{(1)}(-\omega)} & 0 & 0 \\ \sqrt{T_{11}^{(1)}(\omega)T_{12}^{(1)}(-\omega)} & \sqrt{T_{M,11}^{(1)}(-\omega)T_{12}^{(1)}(\omega)} & \sqrt{T_{11}^{(1)}(\omega)T_{11}^{(1)}(-\omega)} + \sqrt{T_{12}^{(1)}(\omega)T_{12}^{(1)}(-\omega)} & 0 & 0 \\ T_{41}^{(1)}(\omega) & T_{42}^{(1)}(\omega) & T_{43}^{(1)}(\omega) & \sqrt{T_{11}^{(1)}(2\omega)} & \sqrt{T_{12}^{(1)}(2\omega)} \\ T_{42}^{(1)}(-\omega) & T_{41}^{(1)}(-\omega) & T_{43}^{(1)}(-\omega) & \sqrt{T_{12}^{(1)}(-2\omega)} & \sqrt{T_{11}^{(1)}(-2\omega)} \end{pmatrix} \tag{D.1}$$

We will show hereafter that the 19 non-zero elements of the matrix described in Equation (8.28) can be related to the 5 independent elements that arise in the resulting matrix of Equa-

tion (D.1). The elements of the first row of that matrix can be written down as,

$$\begin{aligned} T_{11}^{(1)}(\omega) &= D_{M,11}^2 e^{-2j\omega m_M} T_{M-1,11}^{(1)}(\omega) + D_{M,12}^2 e^{2j\omega m_M} T_{M-1,12}^{(1)}(-\omega) \\ &+ 2D_{M,11}D_{M,12}\sqrt{T_{M-1,11}^{(1)}(\omega)T_{M-1,12}^{(1)}(-\omega)} \\ &= \left(D_{M,11}e^{-j\omega m_M}\sqrt{T_{M-1,11}^{(1)}(\omega)} + D_{M,12}e^{j\omega m_M}\sqrt{T_{M-1,12}^{(1)}(-\omega)}\right)^2, \end{aligned} \tag{D.2}$$

$$\begin{aligned} T_{12}^{(1)}(\omega) &= D_{M,11}^2 e^{-2j\omega m_M} T_{M-1,12}^{(1)}(\omega) + D_{M,12}^2 e^{2j\omega m_M} T_{M-1,11}^{(1)}(-\omega) \\ &+ 2D_{M,11}D_{M,12}\sqrt{T_{M-1,11}^{(1)}(-\omega)T_{M-1,12}^{(1)}(\omega)} \\ &= \left(D_{M,11}e^{-j\omega m_M}\sqrt{T_{M-1,12}^{(1)}(\omega)} + D_{M,12}e^{j\omega m_M}\sqrt{T_{M-1,11}^{(1)}(-\omega)}\right)^2, \end{aligned} \tag{D.3}$$

and

$$\begin{aligned} T_{13}^{(1)}(\omega) &= 2D_{M,11}^2 e^{-2j\omega m_M}\sqrt{T_{M-1,11}^{(1)}(\omega)T_{M-1,12}^{(1)}(\omega)} \\ &+ 2D_{M,12}^2 e^{2j\omega m_M}\sqrt{T_{M-1,11}^{(1)}(-\omega)T_{M-1,12}^{(1)}(-\omega)} \\ &+ 2D_{M,11}D_{M,12}\left(\sqrt{T_{M-1,11}^{(1)}(\omega)T_{M-1,11}^{(1)}(-\omega)} + \sqrt{T_{M-1,12}^{(1)}(\omega)T_{M-1,12}^{(1)}(-\omega)}\right) \\ &= 2\left(D_{M,11}e^{-j\omega m_M}\sqrt{T_{M-1,11}^{(1)}(\omega)} + D_{M,12}e^{j\omega m_M}\sqrt{T_{M-1,12}^{(1)}(-\omega)}\right) \\ &\cdot \left(D_{M,11}e^{-j\omega m_M}\sqrt{T_{M-1,12}^{(1)}(\omega)} + D_{M,12}e^{j\omega m_M}\sqrt{T_{M-1,11}^{(1)}(-\omega)}\right) \\ &= 2\sqrt{T_{11}^{(1)}(\omega)T_{12}^{(1)}(\omega)}. \end{aligned} \tag{D.4}$$

As can be observed, the $T_{13}^{(1)}(\omega)$-element of the frequency response of first-order can be expressed by means of the elements $T_{11}^{(1)}(\omega)$ and $T_{12}^{(1)}(\omega)$. Following this reasoning for the second and third rows enables us to find other elements of that matrix, which also dependent upon those two elements. Hence,

$$\begin{aligned} T_{21}^{(1)}(\omega) &= D_{M,12}^2 e^{-2j\omega m_M} T_{M-1,11}^{(1)}(\omega) + D_{M,11}^2 e^{2j\omega m_M} T_{M-1,12}^{(1)}(-\omega) \\ &+ 2D_{M,11}D_{M,12}\sqrt{T_{M-1,11}^{(1)}(\omega)T_{M-1,12}^{(1)}(-\omega)} \\ &= \left(D_{M,12}e^{-j\omega m_M}\sqrt{T_{M-1,11}^{(1)}(\omega)} + D_{M,11}e^{j\omega m_M}\sqrt{T_{M-1,12}^{(1)}(-\omega)}\right)^2 \\ &= T_{12}^{(1)}(-\omega), \end{aligned} \tag{D.5}$$

$$
\begin{aligned}
T_{22}^{(1)}(\omega) &= D_{M,12}^2 e^{-2j\omega m_M} T_{M-1,12}^{(1)}(\omega) + D_{M,11}^2 e^{2j\omega m_M} T_{M-1,11}^{(1)}(-\omega) \\
&+ 2D_{M,11}D_{M,12}\sqrt{T_{M-1,11}^{(1)}(-\omega)T_{M-1,12}^{(1)}(\omega)} \\
&= \left(D_{M,12}e^{-j\omega m_M}\sqrt{T_{M-1,12}^{(1)}(\omega)} + D_{M,11}e^{j\omega m_M}\sqrt{T_{M-1,11}^{(1)}(-\omega)}\right)^2 \\
&= T_{11}^{(1)}(-\omega),
\end{aligned}
\tag{D.6}
$$

$$
\begin{aligned}
T_{23}^{(1)}(\omega) &= 2D_{M,12}^2 e^{-2j\omega m_M}\sqrt{T_{M-1,11}^{(1)}(\omega)T_{M-1,12}^{(1)}(\omega)} \\
&+ 2D_{M,11}^2 e^{2j\omega m_M}\sqrt{T_{M-1,11}^{(1)}(-\omega)T_{M-1,12}^{(1)}(-\omega)} \\
&+ 2D_{M,11}D_{M,12}\left(\sqrt{T_{M-1,11}^{(1)}(\omega)T_{M-1,11}^{(1)}(-\omega)} + \sqrt{T_{M-1,12}^{(1)}(\omega)T_{M-1,12}^{(1)}(-\omega)}\right) \\
&= 2\left(D_{M,12}e^{-j\omega m_M}\sqrt{T_{M-1,11}^{(1)}(\omega)} + D_{M,11}e^{j\omega m_M}\sqrt{T_{M-1,12}^{(1)}(-\omega)}\right) \\
&\cdot \left(D_{M,12}e^{-j\omega m_M}\sqrt{T_{M-1,12}^{(1)}(\omega)} + D_{M,11}e^{j\omega m_M}\sqrt{T_{M-1,11}^{(1)}(-\omega)}\right) \\
&= 2\sqrt{T_{11}^{(1)}(-\omega)T_{12}^{(1)}(-\omega)},
\end{aligned}
\tag{D.7}
$$

$$
\begin{aligned}
T_{31}^{(1)}(\omega) &= D_{M,11}D_{M,12}e^{-2j\omega m_M}T_{M-1,11}^{(1)}(\omega) + D_{M,11}D_{M,12}e^{2j\omega m_M}T_{M-1,12}^{(1)}(-\omega) \\
&+ \left(D_{M,11}^2 + D_{M,12}^2\right)\sqrt{T_{M-1,11}^{(1)}(\omega)T_{M-1,12}^{(1)}(-\omega)} \\
&= \left(D_{M,11}e^{-j\omega m_M}\sqrt{T_{M-1,11}^{(1)}(\omega)} + D_{M,12}e^{j\omega m_M}\sqrt{T_{M-1,12}^{(1)}(-\omega)}\right) \\
&\cdot \left(D_{M,12}e^{-j\omega m_M}\sqrt{T_{M-1,11}^{(1)}(\omega)} + D_{M,11}e^{j\omega m_M}\sqrt{T_{M-1,12}^{(1)}(-\omega)}\right) \\
&= \sqrt{T_{11}^{(1)}(\omega)T_{12}^{(1)}(-\omega)},
\end{aligned}
\tag{D.8}
$$

$$
\begin{aligned}
T_{32}^{(1)}(\omega) &= D_{M,11}D_{M,12}e^{-2j\omega m_M}T_{M-1,12}^{(1)}(\omega) + D_{M,11}D_{M,12}e^{2j\omega m_M}T_{M-1,11}^{(1)}(-\omega) \\
&+ \left(D_{M,11}^2 + D_{M,12}^2\right)\sqrt{T_{M-1,11}^{(1)}(-\omega)T_{M-1,12}^{(1)}(\omega)} \\
&= \left(D_{M,12}e^{-j\omega m_M}\sqrt{T_{M-1,12}^{(1)}(\omega)} + D_{M,11}e^{j\omega m_M}\sqrt{T_{M-1,11}^{(1)}(-\omega)}\right) \\
&\cdot \left(D_{M,11}e^{-j\omega m_M}\sqrt{T_{M-1,12}^{(1)}(\omega)} + D_{M,12}e^{j\omega m_M}\sqrt{T_{M-1,11}^{(1)}(-\omega)}\right) \\
&= \sqrt{T_{11}^{(1)}(-\omega)T_{12}^{(1)}(\omega)},
\end{aligned}
\tag{D.9}
$$

and

$$\begin{aligned}
T_{33}^{(1)}(\omega) &= 2D_{M,11}D_{M,12}e^{-2j\omega m_M}\sqrt{T_{M-1,11}^{(1)}(\omega)T_{M-1,12}^{(1)}(\omega)} \\
&+ 2D_{M,11}D_{M,12}e^{2j\omega m_M}\sqrt{T_{M-1,11}^{(1)}(-\omega)T_{M-1,12}^{(1)}(-\omega)} \\
&+ \left(D_{M,11}^2 + D_{M,12}^2\right)\left(\sqrt{T_{M-1,11}^{(1)}(\omega)T_{M-1,11}^{(1)}(-\omega)} + \sqrt{T_{M-1,12}^{(1)}(\omega)T_{M-1,12}^{(1)}(-\omega)}\right) \\
&= \left(D_{M,11}e^{-j\omega m_M}\sqrt{T_{M-1,11}^{(1)}(\omega)} + D_{M,12}e^{j\omega m_M}\sqrt{T_{M-1,12}^{(1)}(-\omega)}\right) \\
&\cdot \left(D_{M,12}e^{-j\omega m_M}\sqrt{T_{M-1,12}^{(1)}(\omega)} + D_{M,11}e^{j\omega m_M}\sqrt{T_{M-1,11}^{(1)}(-\omega)}\right) \\
&+ \left(D_{M,11}e^{-j\omega m_M}\sqrt{T_{M-1,12}^{(1)}(\omega)} + D_{M,12}e^{j\omega m_M}\sqrt{T_{M-1,11}^{(1)}(-\omega)}\right) \\
&\cdot \left(D_{M,12}e^{-j\omega m_M}\sqrt{T_{M-1,11}^{(1)}(\omega)} + D_{M,11}e^{j\omega m_M}\sqrt{T_{M-1,12}^{(1)}(-\omega)}\right) \\
&= \sqrt{T_{11}^{(1)}(\omega)T_{11}^{(1)}(-\omega)} + \sqrt{T_{12}^{(1)}(\omega)T_{12}^{(1)}(-\omega)}.
\end{aligned} \tag{D.10}$$

This reasoning can be further applied to the lower-right elements of the fourth and fifth rows, leading to:

$$\begin{aligned}
T_{44}^{(1)}(\omega) &= D_{M,11}e^{-2j\omega m_M}\sqrt{T_{M-1,11}^{(1)}(2\omega)} + D_{M,12}e^{2j\omega m_M}\sqrt{T_{M-1,12}^{(1)}(-2\omega)} \\
&= \sqrt{T_{11}^{(1)}(2\omega)},
\end{aligned} \tag{D.11}$$

$$\begin{aligned}
T_{45}^{(1)}(\omega) &= D_{M,11}e^{-2j\omega m_M}\sqrt{T_{M-1,12}^{(1)}(2\omega)} + D_{M,12}e^{2j\omega m_M}\sqrt{T_{M-1,11}^{(1)}(-2\omega)} \\
&= \sqrt{T_{12}^{(1)}(2\omega)},
\end{aligned} \tag{D.12}$$

$$\begin{aligned}
T_{54}^{(1)}(\omega) &= D_{M,12}e^{-2j\omega m_M}\sqrt{T_{M-1,11}^{(1)}(2\omega)} + D_{M,11}e^{2j\omega m_M}\sqrt{T_{M-1,12}^{(1)}(-2\omega)} \\
&= \sqrt{T_{12}^{(1)}(-2\omega)},
\end{aligned} \tag{D.13}$$

and

$$\begin{aligned}
T_{55}^{(1)}(\omega) &= D_{M,12}e^{-2j\omega m_M}\sqrt{T_{M-1,12}^{(1)}(2\omega)} + D_{M,11}e^{2j\omega m_M}\sqrt{T_{M-1,11}^{(1)}(-2\omega)} \\
&= \sqrt{T_{11}^{(1)}(-2\omega)},
\end{aligned} \tag{D.14}$$

Finally, the remaining six elements of the fourth and fifth rows which explicitly contain the nonlinear terms can obviously not be directly related to those two elements, and they thus keep their original denomination. Nevertheless, some relations can be established between

them. To this end, let us consider the three first elements of the fourth row. Hence,

$$\begin{aligned} T_{41}^{(1)}(\omega) &= D_{M,11}H_M^{NL}(\omega)e^{-2j\omega m_M}T_{M-1,11}^{(1)}(\omega) + D_{M,12}H_M^{NL}(\omega)e^{2j\omega m_M}T_{M-1,12}^{(1)}(-\omega) \\ &+ D_{M,11}e^{-2j\omega m_M}T_{M-1,41}^{(1)}(\omega) + D_{M,12}e^{2j\omega m_M}T_{M-1,42}^{(1)}(-\omega), \end{aligned} \tag{D.15}$$

$$\begin{aligned} T_{42}^{(1)}(\omega) &= D_{M,11}H_M^{NL}(\omega)e^{-2j\omega m_M}T_{M-1,12}^{(1)}(\omega) + D_{M,12}H_M^{NL}(\omega)e^{2j\omega m_M}T_{M-1,11}^{(1)}(-\omega) \\ &+ D_{M,11}e^{-2j\omega m_M}T_{M-1,42}^{(1)}(\omega) + D_{M,12}e^{2j\omega m_M}T_{M-1,41}^{(1)}(-\omega), \end{aligned} \tag{D.16}$$

and

$$\begin{aligned} T_{43}^{(1)}(\omega) &= 2D_{M,11}H_M^{NL}(\omega)e^{-2j\omega m_M}\sqrt{T_{M-1,11}^{(1)}(\omega)T_{M-1,12}^{(1)}(\omega)} \\ &+ 2D_{M,12}H_M^{NL}(\omega)e^{2j\omega m_M}\sqrt{T_{M-1,11}^{(1)}(-\omega)T_{M-1,12}^{(1)}(-\omega)} \\ &+ D_{M,11}e^{-2j\omega m_M}T_{M-1,43}^{(1)}(\omega) + D_{M,12}e^{2j\omega m_M}T_{M-1,43}^{(1)}(-\omega). \end{aligned} \tag{D.17}$$

By making use of the identities $-D_{i,41}(\omega) = D_{i,41}(-\omega)$, $-D_{i,43}(\omega) = D_{i,43}(-\omega)$, and $H_i^{NL}(\omega) = H_i^{NL}(-\omega)$, $\forall i$, the three first elements of the fifth row can be written down as follows,

$$\begin{aligned} T_{51}^{(1)}(\omega) &= D_{M,12}H_M^{NL}(\omega)e^{-2j\omega m_M}T_{M-1,11}^{(1)}(\omega) + D_{M,11}H_M^{NL}(\omega)e^{2j\omega m_M}T_{M-1,12}^{(1)}(-\omega) \\ &+ D_{M,12}e^{-2j\omega m_M}T_{M-1,41}^{(1)}(\omega) + D_{M,11}e^{2j\omega m_M}T_{M-1,42}^{(1)}(-\omega) \\ &= T_{42}^{(1)}(-\omega), \end{aligned} \tag{D.18}$$

$$\begin{aligned} T_{52}^{(1)}(\omega) &= D_{M,12}H_M^{NL}(\omega)e^{-2j\omega m_M}T_{M-1,12}^{(1)}(\omega) + D_{M,11}H_M^{NL}(\omega)e^{2j\omega m_M}T_{M-1,11}^{(1)}(-\omega) \\ &+ D_{M,12}e^{-2j\omega m_M}T_{M-1,42}^{(1)}(\omega) + D_{M,11}e^{2j\omega m_M}T_{M-1,41}^{(1)}(-\omega) \\ &= T_{41}^{(1)}(-\omega), \end{aligned} \tag{D.19}$$

and

$$\begin{aligned} T_{53}^{(1)}(\omega) &= 2D_{M,12}H_M^{NL}(\omega)e^{-2j\omega m_M}\sqrt{T_{M-1,11}^{(1)}(\omega)T_{M-1,12}^{(1)}(\omega)} \\ &+ 2D_{M,11}H_M^{NL}(\omega)e^{2j\omega m_M}\sqrt{T_{M-1,11}^{(1)}(-\omega)T_{M-1,12}^{(1)}(-\omega)} \\ &+ D_{M,12}e^{-2j\omega m_M}T_{M-1,43}^{(1)}(\omega) + D_{M,11}e^{2j\omega m_M}T_{M-1,43}^{(1)}(-\omega) \\ &= T_{43}^{(1)}(-\omega). \end{aligned} \tag{D.20}$$

From those expressions, we recover all the identities used in Equation (8.37), and show that the 19 non-zero elements of the frequency response of first-order $\boldsymbol{T}^{(1)}(\omega)$ can be expressed using only five elements, namely $T_{11}^{(1)}(\omega)$, $T_{12}^{(1)}(\omega)$, $T_{41}^{(1)}(\omega)$, $T_{42}^{(1)}(\omega)$, and $T_{43}^{(1)}(\omega)$.

E

Contributions

The outcomes from this dissertation and other contributions of the PhD fellow are partially reflected in the refereed journals and conference proceedings listed below.

- Refereed journal publications:
  - N. Bochud and G. Rus, Probabilistic inverse problem to characterize tissue-equivalent material mechanical properties, *IEEE Transactions on Ultrasonics, Ferroelectrics and Frequency Control (Special Issue: Novel Embedded Systems for Ultrasonic Imaging and Signal)*, 59(7):1443–1456, 2012 (Journal ranking: SCI – 1.822; 7/31 (Q_1): Acoustics; cited by 1).
  - A. Fahim, R. Gallego, N. Bochud, and G. Rus, Model-based damage reconstruction in composites from ultrasound transmission, *Composites Part B: Engineering*, 45(1):50–62, 2013 (Journal ranking: SCI – 2.143; 7/90 (Q_1): Multi. Eng.; cited by 3).
  - N. Bochud, A. Gomez, G. Rus, and A. Peinado, A sparse digital signal model for ultrasonic nondestructive evaluation of composite materials, *Submitted to IEEE Transactions on Ultrasonics, Ferroelectrics, and Frequency Control (under review)*, 2014 (Journal ranking: SCI – 1.822; 7/31 (Q_1): Acoustics).
  - L. Peralta, N. Bochud, and G. Rus, Mechanical characterization of cervical tissue by ultrasound, *Submitted to the Journal of the Mechanical Behavior of Biomedical Materials (under review)*, 2014 (Journal ranking: SCI – 2.368; 25/79 (Q_2): Biomed. Eng.).

- G. Rus, J. Melchor, N. Bochud, L. Peralta, and W.J. Parnell, A micro-mechanical approach for nonlinear quantitative ultrasound, *Submitted to Ultrasonics (under review)*, 2014 (Journal ranking: SCI – 2.018; 5/31 (Q_1): Acoustics).

- Relevant conference proceedings:
  - N. Bochud, A. Fahim, A. Gomez, and G. Rus, Impact damage characterization in composites using signal processing techniques, *Procedia Engineering of the The Twelfth East Asia-Pacific Conference on Structural Engineering and Construction*, 14:169–176, Hong-Kong, January 2011.
  - N. Bochud, A. Gomez, G. Rus, J. L. Carmona, and A. Peinado, Robust parametrization for non- destructive evaluation of composites using ultrasonic signals, *IEEE International Conference on Acoustics Speech, and Signal Processing*, p. 1789–1792, Praga, May 2011 (cited by 6).
  - B. Fuentes, J. L. Carmona, N. Bochud, A. Gomez, and A. Peinado, Model-based cepstral analysis for ultrasonic non-destructive evaluation of composites, *IEEE International Conference on Acoustics Speech, and Signal Processing*, p. 1717–1720, Tokyo, March 2012 (cited by 3).
  - G. Rus, N. Bochud, J. Melchor, M. Alaminos, and A. Campos, Dispersive model selection and reconstruction for tissue culture ultrasonic monitoring, *International Congress on Ultrasonics*, p. 375–378, Gdansk, September 2012.
  - N. Bochud, A. Gomez, G. Rus, and A. Peinado, Sparse signal model for ultrasonic nondestructive evaluation of CFRP plates, *IEEE International Conference on Acoustics Speech, and Signal Processing*, p. 2844–2847, Vancouver, May 2013.

References

[1] A.M. Khatkhate, A. Ray, and E. Keller. Modelling and system identification of an experimental apparatus for anomaly detection in mechanical systems. *Applied mathematical modelling*, 31(4):734–748, 2007.

[2] M.J.S. Lowe. Matrix techniques for modeling ultrasonic waves in multilayered media. *IEEE Transactions on Ultrasonics, Ferroelectrics and Frequency Control*, 42(4):525–542, 1995.

[3] M.G. Messineo, G.L. Frontini, G.E. Elicabe, and L. Gaete-Garretón. Equivalent ultrasonic impedance in multilayer media. a parameter estimation problem. *Inverse Problems in Science and Engineering*, pages 1–20, 2013.

[4] M. Rielly, V. Humphrey, and F. Duck. A theoretical and experimental investigation of nonlinear ultrasound propagation through tissue mimicking fluids. In *IEEE Ultrasonics Symposium*, volume 2, pages 1355–1358, 2000.

[5] E.R. Hughes, T.G. Leighton, G.W. Petley, and P.R. White. Ultrasonic propagation in cancellous bone: A new stratified model. *Ultrasound in Medicine & Biology*, 25(5):811–821, 1999.

[6] W. Lin, Y.-X. Qin, and C. Rubin. Ultrasonic wave propagation in trabecular bone predicted by the stratified model. *Annals of biomedical engineering*, 29(9):781–790, 2001.

[7] G.-M. Zhang and D.M. Harvey. Contemporary ultrasonic signal processing approaches for nondestructive evaluation of multilayered structures. *Nondestructive Testing and Evaluation*, 27(1):1–27, 2012.

[8] J.D. Achenbach. Quantitative nondestructive evaluation. *International Journal of Solids and Structures*, 37(1):13–27, 2000.

[9] A. Tarantola. *Inverse Problem Theory*. SIAM, 2005.

[10] S. Kubo. Classification of inverse problems arising in field problems and their treatments. In *IUTAM Symposium Tokyo/Japan, 1993*, 1993.

[11] G.P. Singh and S. Udpa. The role of digital signal processing in ndt. *NDT international*, 19(3):125–132, 1986.

[12] T. Wang, J. Saniie, and X. Jin. Analysis of low-order autoregressive models for ultrasonic grain signal characterization. *IEEE Transactions on Ultrasonics, Ferroelectrics and Frequency Control*, 38(2):116–124, 1991.

[13] R. Prakash. Non-destructive testing of composites. *Composites*, 11(4):217–224, 1980.

[14] G.-M. Zhang, C.-Z. Zhang, and D.M. Harvey. Sparse signal representation and its applications in ultrasonic nde. *Ultrasonics*, 52:351–363, 2011.

[15] Q. Shen, M. Omar, and S. Dongri. Ultrasonic nde techniques for impact damage inspection on cfrp laminates. *Journal of materials science research*, 1(1):1–15, 2011.

[16] V.K. Kinra and C. Zhu. Ultrasonic nondestructive evaluation of thin (sub-wavelength) coatings. *The Journal of the Acoustical Society of America*, 93:2454–1467, 1993.

[17] T.C. Hanshaw, C.S. Hsu, and M.J. Anderson. Analysis of ultrasonic non destructive evaluation data using singular value decomposition of the hankel data matrix. In *American Control Conference*, volume 5, pages 3672–3677, 2001.

[18] S.P. Neal and D.O. Thompson. The measurement and analysis of acoustic noise as a random variable in ultrasonic nondestructive evaluation. *The Journal of the Acoustical Society of America*, 86:S94, 1989.

[19] A. Grennberg and M. Sandell. Estimation of subsample time delay differences in narrowband ultrasonic echoes using the hilbert transform correlation. *IEEE Transactions on Ultrasonics, Ferroelectrics and Frequency Control*, 41(5):588–595, 1994.

[20] M.A.G Izquierdo, M.G. Hernández, and J.J. Anaya. Time-varying prediction filter for structural noise reduction in ultrasonic nde. *Ultrasonics*, 44:e1001–e1005, 2006.

[21] S.P. Neal, P.L. Speckman, and M.A. Enright. Flaw signature estimation in ultrasonic nondestructive evaluation using the wiener filter with limited prior information. *IEEE Transactions on Ultrasonics, Ferroelectrics and Frequency Control*, 40(4):347–353, 1993.

[22] S.-K. Sin and C.-H. Chen. A comparison of deconvolution techniques for the ultrasonic nondestructive evaluation of materials. *IEEE Transactions on Image Processing*, 1(1):3–10, 1992.

[23] S.-C. Wooh and C. Wei. Cepstrum-based deconvolution of ultrasonic pulse-echo signals from laminated composite materials. In *Proceedings of the 12th Engineering Mechanics Conference*, pages 1–4, 1998.

[24] A.K. Nandi, D. Mampel, and B. Roscher. Blind deconvolution of ultrasonic signals in nondestructive testing applications. *IEEE Transactions on Signal Processing*, 45(5):1382–1390, 1997.

[25] L. Ghouti and C.H. Chen. Deconvolution of ultrasonic nondestructive evaluation signals using higher-order statistics. In *IEEE International Conference on Acoustics, Speech, and Signal Processing*, volume 3, pages 1457–1460, 1999.

[26] A. Abbate, J. Koay, J. Frankel, S.C. Schroeder, and P. Das. Signal detection and noise suppression using a wavelet transform signal processor: application to ultrasonic flaw detection. *IEEE Transactions on Ultrasonics, Ferroelectrics and Frequency Control*, 44(1):14–26, 1997.

[27] M.A. Malik and J. Saniie. Generalized time-frequency representation of ultrasonic signals. In *IEEE Ultrasonics Symposium*, pages 691–695, 1993.

[28] M. Rodriguez, L. Vergara, and J. Morales. Real-time prototype for microcracks detection on ceramic materials. In *International Symposium on Time-Frequency and Time-Scale Analysis*, pages 469–472, 1996.

[29] G. Wu, J. Su, D. Zhu, H. Gou, W. Sheng, and Y. Li. Ultrasonic nde of thin composite plate based on an enhanced wigner-ville distribution. In *17th World Conference on Nondestructive Testing, Shanghai, China*, 2008.

[30] N.M. Bilgutay, V.L. Newhouse, and E.S. Furgason. Flaw visibility enhancement by split-spectrum processing techniques. In *IEEE Ultrasonics Symposium*, pages 878–883, 1981.

[31] N. Bilgutay, J. Popovics, S. Popovics, and M. Karaoguz. Recent developments in concrete nondestructive evaluation. In *International Conference on Acoustics, Speech, and Signal Processing*, volume 6, pages 3393–3396, 2001.

[32] A. Benammar, R. Drai, and A. Guessoum. Detection of delamination defects in cfrp materials using ultrasonic signal processing. *Ultrasonics*, 48(8):731–738, 2008.

[33] S.C. Ng, N. Ismail, A. Ali, B. Sahari, J.M. Yusof, and B.W. Chu. Non-destructive inspection of multi-layered composite using ultrasonic signal processing. In *IOP Conference Series: Materials Science and Engineering*, volume 17.

[34] A. Messina. Detecting damage in beams through digital differentiator filters and continuous wavelet transforms. *Journal of sound and vibration*, 272(1):385–412, 2004.

[35] W.-X. Yang, J.B. Hull, and M.D. Seymour. A contribution to the applicability of complex wavelet analysis of ultrasonic signals. *NDT & E International*, 37(6):497–504, 2004.

[36] K. Harrouche, J.M. Rouvaen, M. Ouaftouh, M. Ourak, and F. Haine. Signal-processing methods for analysing the structure of carbon-epoxy-resin composite materials. *Measurement Science and Technology*, 11(3):285—-290, 2000.

[37] S. Legendre, J. Goyette, and D. Massicotte. Ultrasonic nde of composite material structures using wavelet coefficients. *NDT & E International*, 34(1):31–37, 2001.

[38] I.M. Johnstone and B.W. Silverman. Wavelet threshold estimators for data with correlated noise. *Journal of the Royal Statistical Society: Series B (Statistical Methodology)*, 59(2):319–351, 1997.

[39] G.-M. Zhang, D.M. Harvey, and D.R. Braden. Signal denoising and ultrasonic flaw detection via overcomplete and sparse representations. *The Journal of the Acoustical Society of America*, 124:2963–2972.

[40] J. Guo, J. Wu, X. Yang, and G. Liu. Ultrasonic nondestructive signals processing based on matching pursuit with gabor dictionary. *Chinese Journal of Mechanical Engineering*, 24(4):591–595, 2011.

[41] F. Boßmann, G. Plonka, T. Peter, O. Nemitz, and T. Schmitte. Sparse deconvolution methods for ultrasonic ndt. *Journal of Nondestructive Evaluation*, 31(3):225–244, 2012.

[42] T. Olofsson and T. Stepinski. Minimum entropy deconvolution of pulse-echo signals acquired from attenuative layered media. *The Journal of the Acoustical Society of America*, 109:2831–2839.

[43] C. Soussen, J. Idier, E. Carcreff, L. Simon, and C. Potel. Ultrasonic non destructive testing based on sparse deconvolution. In *Journal of Physics: Conference Series*, volume 353, page 012018, 2012.

[44] T.J. Case and R.C. Waag. Flaw identification from time and frequency features of ultrasonic waveforms. *IEEE Transactions on Ultrasonics, Ferroelectrics and Frequency Control*, 43(4):592–600, 1996.

[45] J.E. Michaels, A.C. Cobb, and T.E. Michaels. A comparison of feature-based classifiers for ultrasonic structural health monitoring. In *NDE for Health Monitoring and Diagnostics*, pages 363–374, 2004.

[46] A. Peinado and J.C. Segura. *Speech recognition over digital channels*. John Wiley & Sons, 2006.

[47] Á. de la Torre, A.M. Peinado, A.J. Rubio, V.E. Sánchez, and J.E. Díaz. An application of minimum classification error to feature space transformations for speech recognition. *Speech Communication*, 20(3):273–290, 1996.

[48] A. de la Torre, A.M. Peinado, A.J. Rubio, and V. Sánchez. A dfe-based algorithm for feature selection in speech recognition. In *IEEE International Conference on Acoustics, Speech, and Signal Processing*, volume 2, pages 1519–1522, 1997.

[49] E. Meyer and T. Tuthill. Bayesian classification of ultrasound signals using wavelet coefficients. In *IEEE National Aerospace and Electronics Conference*, volume 1, pages 240–243, 1995.

[50] M. Khelil, M. Boudraa, A. Kechida, and R. Drai. Classification of defects by the svm method and the principal component analysis (pca). *Transactions on Engineering, Computing and Technology*, 9:226–231, 2005.

[51] P. Ramuhalli, J. Kim, L. Udpa, and S.S. Udpa. Multichannel signal processing methods for ultrasonic nondestructive evaluation. In *Sensor Array and Multichannel Signal Processing Workshop Proceedings, 2002*, pages 229–233, 2002.

[52] A. Salazar, R. Miralles, A. Parra, L. Vergara, and J. Gosalbez. Ultrasonic signal processing for archaeological ceramic restoration. In *IEEE International Conference on Acoustics, Speech and Signal Processing*, volume 3, pages 1160–1163, 2006.

[53] A. Salazar, J. Gosálbez, J. Igual, R. Llinares, and L. Vergara. Two applications of independent component analysis for non-destructive evaluation by ultrasounds. In *Independent Component Analysis and Blind Signal Separation*, pages 406–413. 2006.

[54] M. Cabrera, X. Castell, and R. Montoliu. Crack detection system based on spectral analysis of a ultrasonic resonance signals. In *IEEE International Conference on Acoustics, Speech, and Signal Processing*, volume 2, pages 605–608, 2003.

[55] R. Miralles, J. Morales, and L. Vergara. An industrial application of signal processing: ceramic microcrack detection. In *IEEE International Conference on Acoustics, Speech, and Signal Processing*, volume 4, pages 2271–2274, 1999.

[56] A. Masnata and M. Sunseri. Neural network classification of flaws detected by ultrasonic means. *NDT & E International*, 29(2):87–93, 1996.

[57] F. Hägglund, J. Martinsson, and J.E. Carlson. Flaw detection in layered media based on parametric modeling of overlapping ultrasonic echoes. In *IEEE Ultrasonics Symposium*, pages 136–139, 2006.

[58] F. Hägglund, J.E. Carlson, and T. Andersson. Ultrasonic classification of thin layers within multi-layered materials. *Measurement Science and Technology*, 21(1):1–10, 2009.

[59] L. Brekhovskikh. *Waves in layered media*. Academic Press, NY, 1960.

[60] Y.-H. Pao, W.-Q. Chen, and X.-Y. Su. The reverberation-ray matrix and transfer matrix analyses of unidirectional wave motion. *Wave Motion*, 44(6):419–438, 2007.

[61] E.L. Adler. Matrix methods applied to acoustic waves in multilayers. *IEEE Transactions on Ultrasonics, Ferroelectrics and Frequency Control*, 37(6):485–490, 1990.

[62] W.T. Thomson. Transmission of elastic waves through a stratified solid medium. *Journal of Applied Physics*, 21(2):89–93, 1950.

[63] N.A. Haskell. The dispersion of surface waves on multilayered media. *Bulletin of the Seismological Society of America*, 43(1):17–34, 1953.

[64] F. Gilbert and G.E. Backus. Propagator matrices in elastic wave and vibration problems. *Geophysics*, 31(2):326–332, 1966.

[65] W.R. Scott and P.F. Gordon. Ultrasonic spectrum analysis for nondestructive testing of layered composite materials. *The Journal of the Acoustical Society of America*, 62:108–116, 1977.

[66] D.L. Folds and C.D. Loggins. Transmission and reflection of ultrasonic waves in layered media. *The Journal of the Acoustical Society of America*, 62:1102–1109, 1977.

[67] P. Cervanka and P. Challande. A new efficient algorithm to compute the exact reflection and transmission factors for plane waves in layered absorbing media (liquids and solids). *The Journal of the Acoustical Society of America*, 89:1579–1589, 1991.

[68] D. Lévesque and L. Piché. A robust transfer matrix formulation for the ultrasonic response of multilayered absorbing media. *The Journal of the Acoustical Society of America*, 92:452–467, 1992.

[69] A.H. Nayfeh. The general problem of elastic wave propagation in multilayered anisotropic media. *Journal of the Acoustical Society of America*, 89(4):1521–1531, 1991.

[70] B. Hosten and M. Castaings. Transfer matrix of multilayered absorbing and anisotropic media. measurements and simulations of ultrasonic wave propagation through composite materials. *The Journal of the Acoustical Society of America*, 94:1488–1495, 1993.

[71] A.H. Nayfeh. *Wave propagation in layered anisotropic media: With application to composites*. North-Holland, 1995.

[72] W. Huang, S.I. Rokhlin, and Y.J. Wang. Effect of fibre-matrix interphase on wave propagation along, and scattering from, multilayered fibers in composites. transfer matrix approach. *Ultrasonics*, 33(5):365–375, 1995.

[73] W. Huang and S.I. Rokhlin. Generalized self-consistent model for composites with functionally graded and multilayered interphases. transfer matrix approach. *Mechanics of materials*, 22(3):219–247, 1996.

[74] A.K. Vashishth and P. Khurana. Waves in stratified anisotropic poroelastic media: a transfer matrix approach. *Journal of sound and vibration*, 277(1):239–275, 2004.

[75] M. Schoenberg. Wave propagation in alternating solid and fluid layers. *Wave motion*, 6(3):303–320, 1984.

[76] C. Potel and J.-F. de Belleval. Propagation in an anisotropic periodically multilayered medium. *The Journal of the Acoustical Society of America*, 93:2669–2677, 1993.

[77] S.E. Hanneman and V.K. Kinra. A new technique for ultrasonic nondestructive evaluation of adhesive joints: Part i. theory. *Experimental mechanics*, 32(4):323–331, 1992.

[78] V.K. Kinra and V.R. Iyer. Ultrasonic measurement of the thickness, phase velocity, density or attenuation of a thin-viscoelastic plate. part i: The forward problem. *Ultrasonics*, 33(2):95–109, 1995.

[79] J.W. Dunkin. Computation of modal solutions in layered, elastic media at high frequencies. *Bulletin of the Seismological Society of America*, 55(2):335–358, 1965.

[80] T. Kundu and A.K. Mal. Elastic waves in a multilayered solid due to a dislocation source. *Wave Motion*, 7(5):459–471, 1985.

[81] *Transmission coefficient of multilayered absorbing anisotropic media. A solution to the numerical limitations of the Thomson-Haskell method. Application to composite materials*, 1993.

[82] M. Castaings and B. Hosten. Delta operator technique to improve the thomson-haskell-method stability for propagation in multilayered anisotropic absorbing plates. *The Journal of the Acoustical Society of America*, 95:1931–1941, 1994.

[83] E.L. Tan. A concise and efficient scattering matrix formalism for stable analysis of elastic wave propagation in multilayered anisotropic solids. *Ultrasonics*, 41(3):229–236, 2003.

[84] B. Hosten. Bulk heterogeneous plane waves propagation through viscoelastic plates and stratified media with large values of frequency domain. *Ultrasonics*, 29(6):445–450, 1991.

[85] K. Balasubramaniam. On a numerical truncation approximation algorithm for transfer matrix method. *The Journal of the Acoustical Society of America*, 107:1053–1056, 2000.

[86] L. Knopoff. A matrix method for elastic wave problems. *Bulletin of the Seismological Society of America*, 54(1):431–438, 1964.

[87] H. Schmidt and F.B. Jensen. A full wave solution for propagation in multilayered viscoelastic media with application to gaussian beam reflection at fluid–solid interfaces. *The Journal of the Acoustical Society of America*, 77:813–825.

[88] H. Schmidt and G. Tango. Efficient global matrix approach to the computation of synthetic seismograms. *Geophysical Journal International*, 84(2):331–359, 1986.

[89] A.K. Mal. Wave propagation in layered composite laminates under periodic surface loads. *Wave Motion*, 10(3):257–266, 1988.

[90] E. Kausel and J.M. Roësset. Stiffness matrices for layered soils. *Bulletin of the Seismological Society of America*, 71(6):1743–1761, 1981.

[91] L. Wang and S.I. Rokhlin. Stable reformulation of transfer matrix method for wave propagation in layered anisotropic media. *Ultrasonics*, 39(6):413–424, 2001.

[92] S.I. Rokhlin and L. Wang. Stable recursive algorithm for elastic wave propagation in layered anisotropic media: Stiffness matrix method. *The Journal of the Acoustical Society of America*, 112:822–834, 2002.

[93] L. Wang and S.I. Rokhlin. Recursive asymptotic stiffness matrix method for analysis of surface acoustic wave devices on layered piezoelectric media. *Applied physics letters*, 81(21):4049–4051, 2002.

[94] L. Wang and S.I. Rokhlin. Modeling of wave propagation in layered piezoelectric media by a recursive asymptotic method. *IEEE Transactions on Ultrasonics, Ferroelectrics and Frequency Control*, 51(9):1060–1071, 2004.

[95] K. Balasubramaniam, V. Mukundan, and M.V. Reddy. A comparison of ultrasonic wave reflection/transmission models from isotropic multilayered structures by transfer-matrix and stiffness-matrix recursive algorithms. In *AIP Conference Proceedings*, volume 657, pages 1095–1102, 2003.

[96] E.L. Tan. Hybrid compliance-stiffness matrix method for stable analysis of elastic wave propagation in multilayered anisotropic media. *The Journal of the Acoustical Society of America*, 119:45–53, 2006.

[97] J.F. Claerbout. *Fundamentals of Geophysical Data Processing, with applications to petroleum prospecting*. Blackwell Scientific Publications, 1985.

[98] G.S. Kino. *Acoustic waves: devices, imaging, and analog signal processing*, volume 107. Prentice-Hall Englewood Cliffs, NJ, 1987.

[99] D. Sjöberg. Analysis of wave propagation in stratified structures using circuit analogues, with application to electromagnetic absorbers. *European Journal of Physics*, 29(4):721–734, 2008.

[100] D. Sjöberg. Circuit analogs for wave propagation in stratified structures. pages 489–508, 2010.

[101] S.R. Ghorayeb, E. Maione, and Va. La Magna. Modeling of ultrasonic wave propagation in teeth using pspice: a comparison with finite element models. *IEEE Transactions on Ultrasonics, Ferroelectrics and Frequency Control*, 48(4):1124–1131, 2001.

[102] R. Challis, F. Blarel, M. Unwin, J. Paul, and X. Guo. Models of ultrasonic wave propagation in epoxy materials. *IEEE Transactions on Ultrasonics, Ferroelectrics and Frequency Control*, 56(6):1225–1237, 2009.

[103] M. Vogt and H. Ermert. Scattering parameters measurement for the determination of layered media properties with 25 mhz ultrasound. In *IEEE Ultrasonics Symposium*, pages 1402–1405, 2006.

[104] S.J. Orfanidis. Electromagnetic waves and antennas. 2008.

[105] P.L. Goupillaud. An approach to inverse filtering of near-surface layer effects from seismic records. *Geophysics*, 26(6):754–760, 1961.

[106] R.J. Freemantle, R.E. Challis, and J.D.H White. A z-transform technique for thin-layer reverberation cancellation applied to ultrasonic ndt of adhered structures. In *Advanced Techniques for Collection and Interpretation of NDT Data*, pages 1–7, 1994.

[107] A.P. Velo, G.A. Gazonas, and T. Ameya. z-transform methods for the optimal design of one-dimensional layered elastic media. *SIAM Journal on Applied Mathematics*, 70(3):762–788, 2009.

[108] G.A. Gazonas and A.P. Velo. Analytical solutions for the resonance response of goupillaud-type elastic media using z-transform methods. *Wave Motion*, doi: 10.1016/j.wavemoti.2011.08.002, 2011.

[109] J.J. Kormylo and J.M. Mendel. Maximum-likelihood seismic deconvolution. *IEEE Transactions on Geoscience and Remote Sensing*, (1):72–82, 1983.

[110] F. Champagnat, Y. Goussard, and J. Idier. Unsupervised deconvolution of sparse spike trains using stochastic approximation. *IEEE Transactions on Signal Processing*, 44(12):2988–2998, 1996.

[111] T. Olofsson and T. Stepinski. Maximum a posteriori deconvolution of sparse ultrasonic signals using genetic optimization. *Ultrasonics*, 37(6):423–432, 1999.

[112] R. Demirli and J. Saniie. Model-based estimation of ultrasonic echoes. part i: Analysis and algorithms. *IEEE Transactions on Ultrasonics, Ferroelectrics and Frequency Control*, 48(3):787–802, 2001.

[113] W. Liang and P.-W. Que. Maximum non-gaussianity parameters estimation of ultrasonic echoes and its application in ultrasonic non-destructive evaluation. *Measurement Science and Technology*, 18(12):3743–3750, 2007.

[114] F. Hägglund, J. Martinsson, J.E. Carlson, and C. Carlander. Model-based characterization of thin layers using pulse-echo ultrasound. In *International Congress on Ultrasonics*, volume 1562, pages 9–12, 2007.

[115] F. Hagglund, J. Martinsson, and J.E. Carlson. Model-based estimation of thin multilayered media using ultrasonic measurements. *Ultrasonics, Ferroelectrics and Frequency Control, IEEE Transactions on*, 56(8):1689–1702, 2009.

[116] J. Martinsson, F. Hägglund, and J.E. Carlson. Complete post-separation of overlapping ultrasonic signals by combining hard and soft modeling. *Ultrasonics*, 48(5):427–443, 2008.

[117] J.E. Dennis and R.B. Schnabel. *Numerical methods for unconstrained optimization and nonlinear equations*, volume 16. SIAM, 1983.

[118] G. Rus and R. Gallego. Optimization algorithms for identification inverse problems with the boundary element method. *Engineering Analysis with Boundary Elements*, 26(4):315–327, 2002.

[119] S.M. Kay. Fundamentals of statistical signal processing: Estimation theory. 1993.

[120] D.W. Marquardt. An algorithm for least-squares estimation of nonlinear parameters. *Journal of the Society for Industrial & Applied Mathematics*, 11(2):431–441, 1963.

[121] J.E. Dennis and J.J. Moré. A characterization of superlinear convergence and its application to quasi-newton methods. *Mathematics of Computation*, 28(126):549–560, 1974.

[122] V.K. Kinra, P.T. Jaminet, C. Zhu, and V.R. Iyer. Simultaneous measurement of the acoustical properties of a thin-layered medium: The inverse problem. *The Journal of the Acoustical Society of America*, 95:3059–3074, 1994.

[123] V.K. Kinra and V.R. Iyer. Ultrasonic measurement of the thickness, phase velocity, density or attenuation of a thin-viscoelastic plate. part ii: The inverse problem. *Ultrasonics*, 33(2):111–122, 1995.

[124] M.J. Maron and R.J. Lopez. *Numerical analysis: a practical approach*. Macmillan New York, 1982.

[125] K. Balasubramaniam and S.C. Whitney. Ultrasonic through-transmission characterization of thick fibre-reinforced composites. *Ndt & E International*, 29(4):225–236, 1996.

[126] B.A. Auld. *Acoustic fields and waves in solids*, volume 1. Wiley New York, 1973.

[127] K. Balasubramaniam and N.S. Rao. Inversion of composite material elastic constants from ultrasonic bulk wave phase velocity data using genetic algorithms. *Composites Part B: Engineering*, 29(2):171–180, 1998.

[128] M. Feder and E. Weinstein. Parameter estimation of superimposed signals using the em algorithm. *IEEE Transactions on Acoustics, Speech and Signal Processing*, 36(4):477–489, 1988.

[129] R. Demirli and J. Saniie. Parameter estimation of multiple interfering echoes using the sage algorithm. In *IEEE Ultrasonics Symposium*, volume 1, pages 831–834, 1998.

[130] I. Ziskind and M. Wax. Maximum likelihood localization of multiple sources by alternating projection. *IEEE Transactions on Acoustics, Speech and Signal Processing*, 36(10):1553–1560, 1988.

[131] R. Demirli and J. Saniie. Model-based estimation of ultrasonic echoes. part ii: Nondestructive evaluation applications. *IEEE Transactions on Ultrasonics, Ferroelectrics and Frequency Control*, 48(3):803–811, 2001.

[132] C.F. Wu. On the convergence properties of the em algorithm. *The Annals of Statistics*, 11(1):95–103, 1983.

[133] P.J. Chung and J.F. Bohme. Comparative convergence analysis of em and sage algorithms in doa estimation. *IEEE Transactions on Signal Processing*, 49(12):2940–2949, 2001.

[134] P. Guillaume and R. Pintelon. A gauss-newton-like optimization algorithm for "weighte" nonlinear least-squares problems. *IEEE Transactions on Signal Processing*, 44(9):2222–2228, 1996.

[135] R. Pintelon and J. Schoukens. *System identification: a frequency domain approach*. John Wiley & Sons, 2001.

[136] R. Fletcher. *Practical methods of optimization*. John Wiley & Sons, 2013.

[137] J. Kormylo and J. Mendel. Maximum likelihood detection and estimation of bernoulli-gaussian processes. *IEEE Transactions on Information Theory*, 28(3):482–488, 1982.

[138] M. Lavielle. Bayesian deconvolution of bernoulli-gaussian processes. *Signal processing*, 33(1):67–79, 1993.

[139] A.E. Yagle and R.R. Joshi. Maximum likelihood estimation with side information of a 1-d discrete layered medium from its noisy impulse reflection response. *IEEE Transactions on Signal Processing*, 48(7):1975–1983, 2000.

[140] H.L. Taylor, S.C. Banks, and J.F. McCoy. Deconvolution with the l_1 norm. *Geophysics*, 44(1):39–52, 1979.

[141] D.A. Lorenz and D. Tredel. Greedy deconvolution of point-like objects. In *Signal Processing with Adaptive Sparse Structured Representations (SPARSE workshop)*, pages 1–5, 2009.

[142] M. Elad. *Sparse and redundant representations: from theory to applications in signal and image processing*. Springer, 2010.

[143] S.G. Mallat and Z. Zhang. Matching pursuits with time-frequency dictionaries. *IEEE Transactions on Signal Processing*, 41(12):3397–3415, 1993.

[144] N. Ruiz-Reyes, P. Vera-Candeas, J. Curpian-Alonso, R. Mata-Campos, and J.C. Cuevas-Martinez. New matching pursuit-based algorithm for snr improvement in ultrasonic ndt. *NDT & E International*, 38(6):453–458, 2005.

[145] N. Ruiz-Reyes, P. Vera-Candeas, J. Curpian-Alonso, J.C. Cuevas-Martinez, and J.L. Blanco-Claraco. High-resolution pursuit for detecting flaw echoes close to the material surface in ultrasonic ndt. *NDT & E International*, 39(6):487–492, 2006.

[146] E. Mor, A. Azoulay, and M. Aladjem. A matching pursuit method for approximating overlapping ultrasonic echoes. *IEEE Transactions on Ultrasonics, Ferroelectrics and Frequency Control*, 57(9):1996–2004, 2010.

[147] J.A. Tropp. Greed is good: Algorithmic results for sparse approximation. *IEEE Transactions on Information Theory*, 50(10):2231–2242, 2004.

[148] T. Peter, D. Potts, and M. Tasche. Nonlinear approximation by sums of exponentials and translates. *SIAM Journal on Scientific Computing*, 33(4):1920–1947, 2011.

[149] J.L. Beck and K.-V. Yuen. Model selection using response measurements: Bayesian probabilistic approach. *Journal of Engineering Mechanics*, 130(2):192–203, 2004.

[150] T.E. Matikas. Damage characterization and real-time health monitoring of aerospace materials using innovative nde tools. *Journal of Materials Engineering and Performance*, 19(5):751–760, 2010.

[151] R.J. Zemp, J. Tavakkoli, and R.S.C. Cobbold. Modeling of nonlinear ultrasound propagation in tissue from array transducers. *The Journal of the Acoustical Society of America*, 113:139–152, 2003.

[152] K. Hokstad. Nonlinear and dispersive acoustic wave propagation. *Geophysics*, 69(3):840–848, 2004.

[153] D.O. Breazeale, M. .and Thompson. Finite-amplitude ultrasonic waves in aluminum. *Applied Physics Letters*, 3(5):77–78, 1963.

[154] R.A. Guyer and P.A. Johnson. Nonlinear mesoscopic elasticity: Evidence for a new class of materials. *Physics today*, 52:30, 1999.

[155] L.A. Ostrovsky and P.A. Johnson. Dynamic nonlinear elasticity in geomaterials. *Rivista del nuovo cimento*, 24(7):1–46, 2001.

[156] L.D. Landau and E.M. Lifshitz. *Theory of Elasticity*. Pergamon press, Oxford, 1959.

[157] R.A. Guyer and P.A. Johnson. *Nonlinear mesoscopic elasticity: the complex behavior of rocks, soil, concrete*. John Wiley & Sons, 2009.

[158] R.A. Guyer, J. TenCate, and P. Johnson. Hysteresis and the dynamic elasticity of consolidated granular materials. *Physical review letters*, 82(16):3280–3283, 1999.

[159] J.A. TenCate, E. Smith, and R.A. Guyer. Universal slow dynamics in granular solids. *Physical review letters*, 85(5):1020–1023, 2000.

[160] L.K. Zarembo and V. I. Timoshenko. Nonlinear acoustics. *Moscow University*, 1, 1984.

[161] Y. Zheng, R.G. Maev, and I.Y. Solodov. Nonlinear acoustic applications for material characterization: A review. *Canadian Journal of Physics*, 77(12):927–967, 2000.

[162] R.T. Beyer. Nonlinear acoustics (naval sea system commands). *Washington DC*, 1974.

[163] L. Germain and J.D.N. Cheeke. Generation and detection of high-order harmonics in liquids using a scanning acoustic microscope. *The Journal of the Acoustical Society of America*, 83:942–949, 1988.

[164] J. Melngailis, A.A. Maradudin, and A. Seeger. Diffraction of light by ultrasound in anharmonic crystals. *Physical Review*, 131(5):1972–1975, 1963.

[165] A. Hikata, B.B. Chick, and C. Elbaum. Effect of dislocations on finite amplitude ultrasonic waves in aluminum. *Applied Physics Letters*, 3(11):195–197, 1963.

[166] L.K. Zarembo and V.A. Krasil'Nikov. Nonlinear phenomena in the propagation of elastic waves in solids. *Physics-Uspekhi*, 13(6):778–797, 1971.

[167] J. Philip and M.A. Breazeale. Temperature variation of some combinations of third-order elastic constants of silicon between 300 and 3°k. *Journal of Applied Physics*, 52(5):3383–3387, 1981.

[168] N. Ichida, T. Sato, and M. Linzer. Imaging the nonlinear ultrasonic parameter of a medium. *Ultrasonic Imaging*, 5(4):295–299, 1983.

[169] W.K. Law, L.A. Frizzell, and F. Dunn. Comparison of thermodynamic and finite amplitude methods of b/a measurement in biological materials. *The Journal of the Acoustical Society of America*, 74:1295–1297, 1983.

[170] X.-F. Gong, Z.-M. Zhu, T. Shi, and J.-H. Huang. Determination of the acoustic nonlinearity parameter in biological media using fais and itd methods. *The Journal of the Acoustical Society of America*, 86:1, 1989.

[171] J.A. TenCate, K.E.A Van Den Abeele, T.J. Shankland, and P.A. Johnson. Laboratory study of linear and nonlinear elastic pulse propagation in sandstone. *The Journal of the Acoustical Society of America*, 100:1383–1391, 1996.

[172] M.F. Hamilton and D.T. Blackstock. *Nonlinear acoustics*. Acoustical Society of America, 1998.

[173] R.N. Thurston and M.J. Shapiro. Interpretation of ultrasonic experiments on finite-amplitude waves. *The Journal of the Acoustical Society of America*, 41:1112–1125, 1967.

[174] R.B. Thompson, O. Buck, and D.O. Thompson. Higher harmonics of finite amplitude ultrasonic waves in solids. *The Journal of the Acoustical Society of America*, 59:1087–1094, 1976.

[175] D. Zhang, X.-F. Gong, and B. Zhang. Second harmonic sound field after insertion of a biological tissue sample. *The Journal of the Acoustical Society of America*, 111:45–48.

[176] X.-F. Zhu, L. Zhou, D. Zhang, and X.-F. Gong. Nonlinear propagation of focused ultrasound in layered biological tissues based on angular spectrum approach. *Chinese Physics*, 14(8):1594–1599, 2005.

[177] B.J. Landsberger and M.F. Hamilton. Second-harmonic generation in sound beams reflected from, and transmitted through, immersed elastic solids. *The Journal of the Acoustical Society of America*, 109:488–500, 2001.

[178] O. Bou Matar, M. Vila, and F.V. Meulen. Experimental and numerical study of the insert-substitution method: application to the measurement of the nonlinear parameter β of solids. In *IEEE Ultrasonics Symposium*, volume 1, pages 709–712, 2001.

[179] G.D. Meegan Jr, P.A. Johnson, R.A. Guyer, and K.R. McCall. Observations of nonlinear elastic wave behavior in sandstone. *The Journal of the Acoustical Society of America*, 94:3387–3391, 1993.

[180] R.A. Guyer, K.R. McCall, and K.E.A. Van Den Abeele. Slow elastic dynamics in a resonant bar of rock. *Geophysical research letters*, 25(10):1585–1588, 1998.

[181] K.E.A Van Den Abeele. Elastic pulsed wave propagation in media with second- or higher-order nonlinearity. part i. theoretical framework. *The Journal of the Acoustical Society of America*, 99:3334–3345, 1996.

[182] K.R. McCall. Theoretical study of nonlinear elastic wave propagation. *Journal of Geophysical Research*, 99(B2):2591–2600, 1994.

[183] K.E.A Van Den Abeele and P.A. Johnson. Elastic pulsed wave propagation in media with second- or higher-order nonlinearity. part ii. simulation of experimental measurements on berea sandstone. *Journal of the Acoustical Society of America*, 99–105(6), 1996.

[184] K.R. McCall and R.A. Guyer. Equation of state and wave propagation in hysteretic nonlinear elastic materials. *Journal of Geophysical Research*, 99(B12):23887–23897, 1994.

[185] K.E.A. Van Den Abeele, P.A. Johnson, R.A. Guyer, and K.R. McCall. On the quasi-analytic treatment of hysteretic nonlinear response in elastic wave propagation. *The Journal of the Acoustical Society of America*, 101:1885–1898, 1997.

[186] V. Aleshin, V. Gusev, and V.Y.U. Zaitsev. Propagation of acoustics waves of nonsimplex form in a material with hysteretic quadratic nonlinearity: analysis and numerical simulations. *Journal of Computational Acoustics*, 12(3):319–354, 2004.

[187] E. Barbieri, M. Meo, and U. Polimeno. Nonlinear wave propagation in damaged hysteretic materials using a frequency domain-based pm space formulation. *International Journal of Solids and Structures*, 46(1):165–180, 2009.

[188] P. Antonaci, C.L.E. Bruno, A.S. Gliozzi, and M. Scalerandi. Evolution of damage-induced nonlinearity in proximity of discontinuities in concrete. *International Journal of Solids and Structures*, 47(11):1603–1610, 2010.

[189] J.H. Cantrell and W.T. Yost. Effect of precipitate coherency strains on acoustic harmonic generation. *Journal of applied physics*, 81(7):2957–2962.

[190] K.-Y. Jhang and K.-C. Kim. Evaluation of material degradation using nonlinear acoustic effect. *Ultrasonics*, 37(1):39–44, 1999.

[191] A.M. Sutin. Nonlinear acoustic nondestructive testing of cracks. *The Journal of the Acoustical Society of America*, 99:2539–2547, 1996.

[192] A.M. Sutin and V.E. Nazarov. Nonlinear acoustic methods of crack diagnostics. *Radiophysics and quantum electronics*, 38(3-4):109–120, 1995.

[193] L.K. Zarembo, V.A. Krasil'nikov, and I.E. Shkol'nik. Nonlinear acoustics in a problem of diagnosing the strength of solids. *Strength of Materials*, 21(11):1544–1551, 1989.

[194] C.L.E. Bruno, A.S. Gliozzi, M. Scalerandi, and P. Antonaci. Analysis of elastic nonlinearity using the scaling subtraction method. *Physical Review B*, 79(6):1–13, 2009.

[195] J.K. Na, W.T. Yost, and J.H. Cantrell. Variation of sound velocity in fatigued aluminum 2024-t4 as a function of hydrostatic pressure. pages 2075–2082, 1993.

[196] J.H. Cantrell and W.T. Yost. Acoustic harmonic generation from fatigue-induced dislocation dipoles. *Philosophical magazine A*, 69(2):315–326, 1994.

[197] I.Y. Solodov. Ultrasonics of non-linear contacts: propagation, reflection and nde-applications. *Ultrasonics*, 36(1):383–390, 1998.

[198] D. Donskoy, A. Sutin, and A. Ekimov. Nonlinear acoustic interaction on contact interfaces and its use for nondestructive testing. *Ndt & E International*, 34(4):231–238, 2001.

[199] I.Y. Solodov, N. Krohn, and G. Busse. Can: an example of nonclassical acoustic nonlinearity in solids. *Ultrasonics*, 40(1):621–625, 2002.

[200] J.M. Richardson. Harmonic generation at an unbounded interface. part i. planar interface between semi-infinite elastic media. *International Journal of Engineering Science*, 17:73–85, 1979.

[201] S. Zhou and Y. Shui. Nonlinear reflection of bulk acoustic waves at an interface. *Journal of applied physics*, 72(11):5070–5080, 1992.

[202] S. Zhou, W. Jiang, and Y. Shui. Nonlinear bulk acoustic waves in anisotropic solids: Propagation, generation, and reflection. *Journal of applied physics*, 78(1):39–46, 1995.

[203] C. Pecorari. An extension of the spring model to nonlinear interfaces. In *AIP Conference Proceedings*, volume 657, pages 49–56, 2003.

[204] C. Pecorari. Nonlinear interaction of plane ultrasonic waves with an interface between rough surfaces in contact. *The Journal of the Acoustical Society of America*, 113:3065–3072, 2003.

[205] A. Berezovski, M. Berezovski, and J. Engelbrecht. Numerical simulation of nonlinear elastic wave propagation in piecewise homogeneous media. *Materials Science and Engineering: A*, 418(1):364–369, 2006.

[206] P.P. Delsanto, S. Hirsekorn, V. Agostini, R. Loparco, and A. Koka. Modeling the propagation of ultrasonic waves in the interface region between two bonded elements. *Ultrasonics*, 40(1):605–610, 2002.

[207] M. Rothenfusser, M. Mayr, and J. Baumann. Acoustic nonlinearities in adhesive joints. *Ultrasonics*, 38(1):322–326, 2000.

[208] R. Williams, E. Cherin, T. Y.J. Lam, J. Tavakkoli, R.J. Zemp, and F.S. Foster. Nonlinear ultrasound propagation through layered liquid and tissue-equivalent media: computational and experimental results at high frequency. *Physics in medicine and biology*, 51(22):5809–5824, 2006.

[209] Y. Yun, G.Q. Miao, P. Zhang, K. Huang, and R.J. Wei. Nonlinear acoustic wave propagating in one-dimensional layered system. *Physics Letters A*, 343(5):351–358, 2005.

[210] K.F. Graff. *Wave Motion in Elastic Solids*. Dover publications, 1975.

[211] C. Pantea, C.F. Osterhoudt, and D.N. Sinha. Determination of acoustical nonlinear parameter β of water using the finite amplitude method. *Ultrasonics*, 53(5):1012–1019.

[212] A.V. Oppenheim and R.W. Schafer. *Discrete-time signal processing*, volume 5. Prentice-Hall, Upper Saddle River, New Jersey, 1989.

[213] F.J. Harris. On the use of windows for harmonic analysis with the discrete fourier transform. 66(1):51–83, 1978.

[214] M.H. Hayes. *Statistical digital signal processing and modeling*. John Wiley & Sons, 1996.

[215] J.G. Proakis and D.G. Manolakis. *Digital Signal Processing: Principles, Algorithms, and Applications*. Prentice-Hall, International, Inc., New Jersey, 1996.

[216] A.V. Oppenheim and R.W. Schafer. From frequency to quefrency: A history of the cepstrum. *IEEE Signal Processing Magazine*, 21(5):95–106, 2004.

[217] J.S. Lim and A.V. Oppenheim. *Advanced Topics in Signal Processing*. Prentice Hall, Englewood Cliffs, New Jersey, 1988.

[218] S.T. Kaplan and T.J. Ulrych. Phase unwrapping: A review of methods and a novel technique. In *CSPG CSEG Convention*, pages 534–537, 2007.

[219] B.P. Bogert, M.J.R. Healy, and J.W. Tukey. The quefrency alanysis of time series for echoes: Cepstrum, pseudo-autocovariance, cross-cepstrum and saphe cracking. In *Proceedings of the Symposium on Time Series Analysis*, pages 209–243, 1963.

[220] D.G. Childers, D.P. Skinner, and R.C. Kemerait. The cepstrum: A guide to processing. 65(10):1428–1443, 1977.

[221] Y. Tohkura. A weighted cepstral distance measure for speech recognition. 35(10):1414–1422, 1987.

[222] J.-C. Junqua and H. Wakita. A comparative study of cepstral lifters and distance measures for all-pole models of speech in noise. In *IEEE International Conference on Acoustics, Speech and Signal Processing*, pages 476–479, 1989.

[223] B.-H. Juang, L. Rabiner, and J. Wilpon. On the use of bandpass liftering in speech recognition. 35(7):947–954, 1987.

[224] N. Bochud. *Signal processing methods for non-destructive evaluation using ultrasonics*. MsC Thesis, Universidad de Granada, 2010.

[225] A.M. Gómez, A.M. Peinado, V. Sánchez, and A.J. Rubio. Recognition of coded speech transmitted over wireless channels. *IEEE Transactions on Wireless Communications*, 5(9):2555–2562, 2006.

[226] N. Cretu and G. Nita. Pulse propagation in finite elastic inhomogeneous media. *Computational materials science*, 31(3):329–336, 2004.

[227] R. Lake. *Viscoelastic materials*. Cambridge University Press, 2009.

[228] S. Treitel and E.A. Robinson. Seismic wave propagation in layered media in terms of communication theory. *Geophysics*, 31(1):17–32, 1966.

[229] V. Valimaki and T.I. Laakso. Principles of fractional delay filters. In *IEEE International Conference on Acoustics, Speech, and Signal Processing*, volume 6, pages 3870–3873, Istanbul, March 2000.

[230] W.R. Sutton. Strategic positioning in composites for global competitiveness. *Moving Forward With 50 Years of Leadership in Advanced Materials*, 39:2373–2384, 1994.

[231] C.E. Bakis, L.C. Bank, V.L. Brown, E. Cosenza, J.F. Davalos, J.J. Lesko, A. Machida, S.H. Rizkalla, and T.C. Triantafillou. Fiber-reinforced polymer composites for construction-state-of-the-art review. *Journal of Composites for Construction*, 6(2):73–87, 2002.

[232] L.C. Hollaway. A review of the present and future utilization of frp composites in the civil infrastructure with reference to their important in-service properties. *Construction and Building Materials*, 24(12):2419–2445, 2010.

[233] R.D. Jamison. The role of microdamage in tensile failure of graphite/epoxy laminates. *Composites Science and Technology*, 24(2):83–99, 1985.

[234] W.J. Cantwell and J. Morton. The impact resistance of composite materials - a review. *composites*, 22(5):347–362, 1991.

[235] S. Abrate. Impact on laminated composites: recent advances. *Applied Mechanics Reviews*, 47:517, 1994.

[236] A. Ruosi, M. Valentino, G. Peluso, and G. Pepe. Analysis of low-velocity impact damage in reinforced carbon fiber composites by hts-squid magnetometers. *Applied Superconductivity, IEEE Transactions on*, 11(1):1172–1175, 2001.

[237] F. Aymerich and S. Meili. Ultrasonic evaluation of matrix damage in impacted composite laminates. *Composites Part B: Engineering*, 31(1):1–6, 2000.

[238] R. Olsson, M.V. Donadon, and B.G. Falzon. Delamination threshold load for dynamic impact on plates. *International journal of solids and structures*, 43(10):3124–3141, 2006.

[239] T. Mitrevski, I.H. Marshall, and R. Thomson. The influence of impactor shape on the damage to composite laminates. *Composite structures*, 76(1):116–122, 2006.

[240] R. Talreja. Damage and fatigue in composites–a personal account. *Composites Science and Technology*, 68(13):2585–2591, 2008.

[241] M. Rheinfurth, N. Kosmann, D. Sauer, G. Busse, and K. Schulte. Lamb waves for non-contact fatigue state evaluation of composites under various mechanical loading conditions. *Composites Part A: Applied Science and Manufacturing*, 43(8):1203–1211, 2012.

[242] H. Schmutzler, M. Alder, N. Kosmann, H. Wittich, and K. Schulte. Degradation monitoring of impact damaged carbon fibre reinforced polymers under fatigue loading with pulse phase thermography. *Composites Part B: Engineering*, 59:221–229, 2014.

[243] A. Rotem and H.G. Nelson. Failure of a laminated composite under tension - compression fatigue loading. *Composites Science and Technology*, 36(1):45–62, 1989.

[244] A. Tropis, M. Thomas, J.L. Bounie, and P. Lafon. Certification of the composite outer wing of the atr72. *Proceedings of the Institution of Mechanical Engineers, Part G: Journal of Aerospace Engineering*, 209(4):327–339, 1995.

[245] T.E. Serdinak. Post-impact fatigue of cross-plied, through-the-thickness reinforced carbon/epoxy composites. *NASA STI/Recon Technical Report N*, 95:31419.

[246] N. Uda, K. Ono, and K. Kunoo. Compression fatigue failure of cfrp laminates with impact damage. *Composites Science and Technology*, 69(14):2308–2314, 2009.

[247] A.S. Chen, D.P. Almond, and B. Harris. Impact damage growth in composites under fatigue conditions monitored by acoustography. *International journal of fatigue*, 24(2):257–261, 2002.

[248] D.D. Symons and G. Davis. Fatigue testing of impact-damaged t300/914 carbon-fibre-reinforced plastic. *Composites science and technology*, 60(3):379–389, 2000.

[249] A. Gagel, D. Lange, and K. Schulte. On the relation between crack densities, stiffness degradation, and surface temperature distribution of tensile fatigue loaded glass-fibre non-crimp-fabric reinforced epoxy. *Composites Part A: Applied Science and Manufacturing*, 37(2):222–228, 2006.

[250] K. Harri, P. Guillaume, and S. Vanlanduit. On-line damage detection on a wing panel using transmission of multisine ultrasonic waves. *NDT & E International*, 41(4):312–317, 2008.

[251] S.-C. Wooh and I.M. Daniel. Three-dimensional ultrasonic imaging of defects and damage in composite materials. *Materials Evaluation*, 52(10), 1994.

[252] M.V. Hosur, C.R.L. Murthy, T.S. Ramamurthy, and A. Shet. Estimation of impact-induced damage in cfrr laminates through ultrasonic imaging. *NDT & E International*, 31(5):359–374, 1998.

[253] M.R. Gorman. Ultrasonic polar backscatter imaging of transverse matrix cracks. *Journal of composite materials*, 25(11):1499–1514, 1991.

[254] K.V. Steiner, R.F. Eduljee, X. Huang, and J.W. Gillespie Jr. Ultrasonic nde techniques for the evaluation of matrix cracking in composite laminates. *Composites science and technology*, 53(2):193–198, 1995.

[255] Langer R. and Vacanti J.P. Tissue engineering. *Science*, 260(5110):920–926, 1993.

[256] R. Archer and D.J. Williams. Why tissue engineering needs process engineering. *Nature biotechnology*, 23(11):1353–1355, 2005.

[257] M.L. Mather, S.P. Morgan, and J.A. Crowe. Meeting the needs of monitoring in tissue engineering. *Regenerative Medicine*, 2(2):145–160, 2007.

[258] K. Kim, C.G. Jeong, and S.J. Hollister. Non-invasive monitoring of tissue scaffold degradation using ultrasound elasticity imaging. *Acta biomaterialia*, 4(4):783–790, 2008.

[259] RM. Williams, W.R. Zipfel, and W.W. Webb. Multiphoton microscopy in biological research. *Current opinion in chemical biology*, 5(5):603–608, 2001.

[260] K. König, K. Schenke-Layland, I. Riemann, and U.A. Stock. Multiphoton autofluorescence imaging of intratissue elastic fibers. *Biomaterials*, 26(5):495–500, 2005.

[261] W. Sun, A. Darling, B. Starly, and J. Nam. Computer-aided tissue engineering: overview, scope and challenges. *Biotechnology and Applied Biochemistry*, 39(1):29–47, 2004.

[262] K.Y. Lee and D.J. Mooney. Hydrogels for tissue engineering. *Chemical reviews*, 101(7):1869–1880, 2001.

[263] N.E. Fedorovich, J. Alblas, J.R. de Wijn, W.E. Hennink, A.J. Verbout, and W.J.A Dhert. Hydrogels as extracellular matrices for skeletal tissue engineering: state-of-the-art and novel application in organ printing. *Tissue engineering*, 13(8):1905–1925, 2007.

[264] E.J. Orwin, M.L. Borene, and A. Hubel. Biomechanical and optical characteristics of a corneal stromal equivalent. *Journal of biomechanical engineering*, 125(4):439–444, 2003.

[265] M. Ahearne, Y. Yang, A.J. El Haj, K.Y. Then, and K.-K. Liu. Characterizing the viscoelastic properties of thin hydrogel-based constructs for tissue engineering applications. *Journal of the Royal Society Interface*, 2(5):455–463, 2005.

[266] Y. Yang, P.O. Bagnaninchi, M. Ahearne, R.K. Wang, and K.-K. Liu. A novel optical coherence tomography-based micro-indentation technique for mechanical characterization of hydrogels. *Journal of The Royal Society Interface*, 4(17):1169–1173, 2007.

[267] K. Hattori, Y. Takakura, H. Ohgushi, T. Habata, K. Uematsu, M. Takenaka, and K. Ikeuchi. Which cartilage is regenerated, hyaline cartilage or fibrocartilage? non-invasive ultrasonic evaluation of tissue-engineered cartilage. *Rheumatology*, 43(9):1106–1108, 2004.

[268] K. Hattori, Y. Takakura, H. Ohgushi, T. Habata, K. Uematsu, and K. Ikeuchi. Novel ultrasonic evaluation of tissue-engineered cartilage for large osteochondral defects – non-invasive judgment of tissue-engineered cartilage. *Journal of orthopaedic research*, 23(5):1179–1183, 2005.

[269] M.A. Rice, K.R. Waters, and K.S. Anseth. Ultrasound monitoring of cartilaginous matrix evolution in degradable peg hydrogels. *Acta biomaterialia*, 5(1):152–161, 2009.

[270] S. Kreitz, G. Dohmen, S. Hasken, T. Schmitz-Rode, P. Mela, and S. Jockenhoevel. Non-destructive method to evaluate the collagen content of fibrin-based tissue engineered structures via ultrasound. *Tissue Engineering Part C: Methods*, 17(10):1021–1026, 2011.

[271] J.E. Carlson, J. Van Deventer, A. Scolan, and C. Carlander. Frequency and temperature dependence of acoustic properties of polymers used in pulse-echo systems. In *IEEE Symposium on Ultrasonics*, volume 1, pages 885–888, 2003.

[272] S.T Moe, K.I Draget, G. Skjåk-Bræ, and O. Simdsrød. Temperature dependence of the elastic modulus of alginate gels. *Carbohydrate polymers*, 19(4):279–284.

[273] K.-I. Kawabata, Y. Waki, T. Matsumura, and S.-I. Umemura. Tissue mimicking phantom for ultrasonic elastography with finely adjustable elastic and echographic properties. In *IEEE Ultrasonics Symposium*, volume 2, pages 1502–1505, 2004.

[274] S.A. Goss, R.L. Johnston, and F. Dunn. Comprehensive compilation of empirical ultrasonic properties of mammalian tissues. *The Journal of the Acoustical Society of America*, 64:423–457, 1978.

[275] R. Ortega, A. Téllez, L. Leija, and A. Vera. Measurement of ultrasonic properties of muscle and blood biological phantoms. *Physics Procedia*, 3(1):627–634, 2010.

[276] A.C. Ximenes Oliveira. *Estudio de la expresión génica en la enfermedad periodontal y obtención de un modelo de matriz biológica descelularizada para la regeneración tisular guiada*. PhD Thesis, Universidad de Granada, 2013.

[277] G. Rus, S.-Y. Lee, and R. Gallego. Defect identification in laminated composite structures by bem from incomplete static data. *International journal of solids and structures*, 42(5):1743–1758, 2005.

[278] R. Palma, G. Rus, and R. Gallego. Probabilistic inverse problem and system uncertainties for damage detection in piezoelectrics. *Mechanics of Materials*, 41(9):1000–1016, 2009.

[279] G. Rus, R. Palma, and J.L. Pérez-Aparicio. Experimental design of dynamic model-based damage identification in piezoelectric ceramics. *Mechanical Systems and Signal Processing*, 26:268–293, 2012.

[280] A.N. Tikhonov and V.Y. Arsenin. Methods for solving ill-posed problems. *Scripta Series in Mathematics*, 1979.

[281] W. Menke. *Geophysical data analysis: discrete inverse theory*, volume 45. 1984.

[282] R.C. Aster, B. Borchers, and C.H. Thurber. *Parameter estimation and inverse problems*. 2005.

[283] H.W. Engl, M. Hanke, and A. Neubauer. *Regularization of inverse problems*, volume 375. 1996.

[284] R. Gallego and G. Rus. Identification of cracks and cavities using the topological sensitivity boundary integral equation. *Computational Mechanics*, 33(2):154–163, 2004.

[285] R. Gallego, L. Comino, and A. Ruiz-Cabello. Material constant sensitivity boundary integral equation for anisotropic solids. *International journal for numerical methods in engineering*, 66(12):1913–1933, 2006.

[286] S.-Y. Lee and S.-C. Wooh. Waveform-based identification of structural damage using the combined finite element method and microgenetic algorithms. *Journal of Structural Engineering*, 131(9):1464–1472, 2005.

[287] D.E. Goldberg and M.P. Samtni. Engineering optimization via the genetic algorithms. *Computers and Structures*, 40:1321–1327, 1991.

[288] G. Rus, R. Palma, and J.L. Pérez-Aparicio. Optimal measurement setup for damage detection in piezoelectric plates. *International Journal of Engineering Science*, 47(4):554–572, 2009.

[289] N. Bochud and G. Rus. Probabilistic inverse problem to characterize tissue-equivalent material mechanical properties. *IEEE Transactions on Ultrasonics, Ferroelectrics and Frequency Control*, 59(7):1443–1456, 2012.

[290] H. Jeffrey. Theory of probability. *Clarendon Press, Oxford*, 1961.

[291] R.T. Cox. *The algebra of probable inference*. Johns Hopkins Press Baltimore, 1961.

[292] A. Elisseeff and M. Pontil. Leave-one-out error and stability of learning algorithms with applications. *Nato Science Series Sub Series III Computer and Systems Sciences*, 190:111–130, 2003.

[293] N. Bochud, A.M. Gomez, G. Rus, J.L. Carmona, and A.M. Peinado. Robust parametrization for non-destructive evaluation of composites using ultrasonic signals. In *International Conference on Acoustics, Speech and Signal Processing*, pages 1789–1792, Prague, May 2011.

[294] B. Fuentes, J.L. Carmona, N. Bochud, A.M. Gomez, and A.M. Peinado. Model-based cepstral analysis for ultrasonic non-destructive evaluation of composites. In *IEEE International Conference on Acoustics, Speech and Signal Processing*, pages 1717–1720, Kyoto, March 2012.

[295] N. Bochud, A.M. Gomez, G. Rus, and A.M. Peinado. Sparse signal model for ultrasonic nondestructive evaluation of cfrp composite plates. In *IEEE International Conference on Acoustics, Speech and Signal Processing*, pages 2844–2847, Vancouver, May 2013. IEEE.

[296] S.W. Huang and P.C. Li. Binary code design for high-frequency ultrasound. *IEEE Transactions on Ultrasonics, Ferroelectrics and Frequency Control*, 54(5):947–956, 2007.

[297] L. Ljung. *System identification: theory for the user*.

[298] A.A. Fahim, R. Gallego, N. Bochud, and G. Rus. Model-based damage reconstruction in composites from ultrasound transmission. *Composites Part B: Engineering*, 45(1):50–62, 2012.

[299] A.M. Peinado, J.L. Carmona, N. Bochud, A.M. Gómez, and G. Rus. Representación cepstral de ultrasonidos para evaluación no-destructiva en placas de fibra de carbono. In *41^{th} National Congress of Acoustics, $6^{t}h$ Iberian Congress of Acoustics*, pages 1–8, Léon, October 2010.

[300] D. Giacobello, M.G. Christensen, M.N. Murthi, S.H. Jensen, and M. Moonen. Sparse linear prediction and its applications to speech processing. *IEEE Transactions on Audio, Speech, and Language Processing*, 20(5):1644–1657, 2012.

[301] J. Koloda, A.M. Peinado, and V. Sánchez. Speech reconstruction by sparse linear prediction. In *Advances in Speech and Language Technologies for Iberian Languages*, pages 247–256, 2012.

[302] S. Cocard, J.-F. Tassin, and T. Nicolai. Dynamical mechanical properties of gelling colloidal disks. *Journal of Rheology*, 44(3):585–594, 2000.

[303] T. Norisuye, A. Strybulevych, M. Scanlon, and J. Page. Ultrasonic investigation of the gelation process of poly (acrylamide) gels. In *Macromolecular symposia*, volume 242, pages 208–215, 2006.

[304] Y.Z. Wang, X.F. Zhang, and J.X. Zhang. New insight into kinetics behavior of the structural formation process in agar gelation. *Rheologica Acta*, 52(1):39–48, 2011.

[305] L. Gaul. The influence of damping on waves and vibrations. *Mechanical systems and signal processing*, 13(1):1–30, 1999.

[306] G. Rus, N. Bochud, J. Melchor, M. Alaminos, and A. Campos. Dispersive model selection and reconstruction for tissue culture ultrasonic monitoring. In *AIP Conference Proceedings*, volume 1433, pages 375–378, 2012.

[307] N.M.M. Maia, J.M.M. Silva, and A.M.R. Ribeiro. On a general model for damping. *Journal of Sound and Vibration*, 218(5):749–767, 1998.

[308] S.C. Constable, R.L. Parker, and C.G. Constable. Occam's inversion: A practical algorithm for generating smooth models from electromagnetic sounding data. *Geophysics*, 52(3):289–300, 1987.